Bosonic many-body systems with topologically nontrivial phases subject to gain and loss

Master thesis submitted by
Felix Dangel

October 27th, 2017

Supervisor:	Priv.-Doz. Dr. Holger Cartarius
Examiner:	Priv.-Doz. Dr. Holger Cartarius
Co-examiner:	Prof. Dr. Udo Seifert

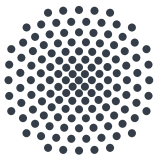

University of Stuttgart
Germany

1. Institut für Theoretische Physik
Universität Stuttgart
Pfaffenwaldring 57, 70550 Stuttgart

Contents

1. Introduction

1.1. Motivation

Long ago, the mathematical area of topology, dealing with the classification of properties of the space that are preserved under continuous deformations [1], has been a subject that was rather unconnected to physical applications. This viewpoint has changed completely with the discovery of the quantum Hall effect [2] in 1986. Ever since, the idea of classifying physical quantities, such as band structures, by means of topology, leading to new exotic phases of matter like topological insulators [3], has attracted numerous scientists. Recently, works in this field have been awarded a Nobel prize.

Mathematically, the notion of a continuous deformation can be reduced to the term of *open sets*. Roughly speaking, neighboring points stay neighbors and edges remain edges under a continuous map, while distances or angles are free to change. Pictorally, two objects are topologically equivalent (*homeomorphic*) when they can be stretched or bent into each other without cutting or gluing. The probably most popular illustrating

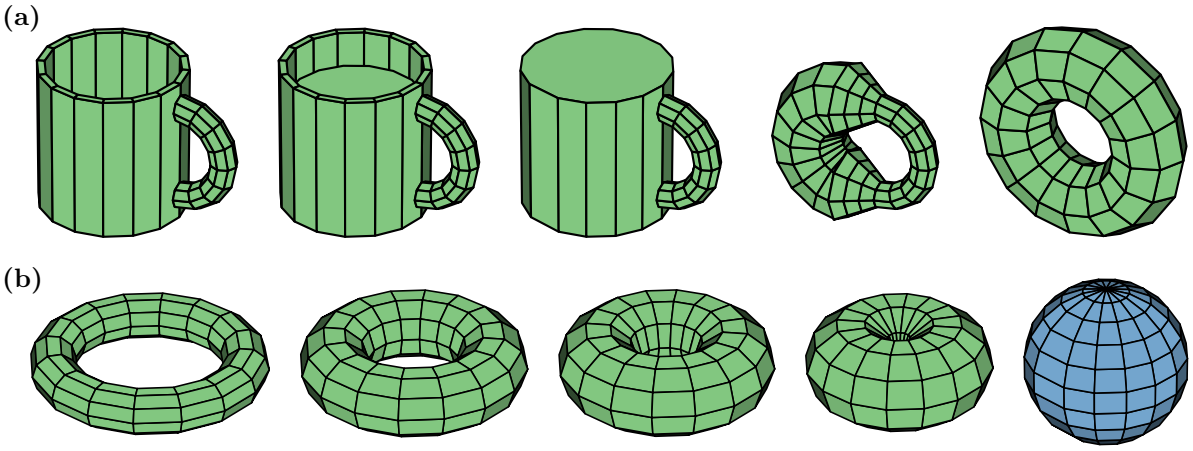

Figure 1.1.: (a) Continuous deformation of a mug into a torus. In the language of topology both objects are homeomorphic such that topological invariants, for instance the number of holes, are identical. (b) The deformation of a torus into a ball can only be achieved by cutting and gluing, which is not a homeomorphism. Thus, the objects are not topologically equivalent and the process corresponds to a topological phase transition with the number of holes changing from zero to one.

example is given by considering a mug and an orange. While the first can be continuously deformed into a torus, the latter is a ball and cannot be transformed into a torus without cutting a hole into it, compare with figure 1.1. Hence, both objects are topologically distinct, meaning that one can find a topological invariant that is not shared between them. In the example, a possible invariant is given by the number of holes, which is one for the mug/torus, but zero for the orange/ball. The important consequence for topological invariants to be preserved under continuous maps implies that the latter are only allowed to change discontinuously.

Physically, topologically protected properties of a system are extremely resistant to a large variation of the system parameters leading to interesting applications, for instance in communication networks [4] and quantum computing [5, 6]. A prominent example for this is the existence of stable edge modes that leads to quantized transport phenomena at the system boundaries. The exhaustive classification scheme of topological insulators and superconductors has been worked out in the *tenfold way* paper by Ryu et al. [7].

Approaches towards a classification of dissipative systems are of recent interest [8, 9], which motivates the subject of this thesis to study effects in dissipative bosonic quantum many-body systems that are known to possess topologically nontrivial phases in the dissipation-free scenario. To do so, extensions of the paradigmatic Su-Schrieffer-Heeger (SSH) model [10] are studied in two different frameworks that allow for the introduction of dissipative effects – complex $\mathcal{PT}$-symmetric on-site potentials [11] and master equations in Lindblad form [12]. Adopting the viewpoint that topological effects are often expressed in interesting edge physics, the description of general edge effects arising in dissipative setups is one of the major goals of this thesis.

The treatment of dissipative quantum many-body systems requires a toolbox of numerical methods. In particular, a density matrix renormalization group (DMRG) algorithm is developed in the course of this thesis. Extending the latter to non-Hermitian Hamiltonians allows for the simulation of systems governed by a $\mathcal{PT}$-symmetric Hamiltonian. Ultimately, the non-Hermitian DMRG procedure is employed in the Liouville space of many-body density matrices for the treatment of master equations in Lindblad form.

Another challenging task involves the comparison of results obtained from both descriptions, which has not been performed so far in the literature. Moreover, the treatment of interacting systems requires advanced techniques that are not necessarily directly available, since in the course of this work ideas of various fields are combined. Using semi-analytical and numerical methods, interesting edge physics in the presence of dissipation will be identified in both frameworks, which can also be brought into accordance, thus dissipative effects can also be effectively studied within a non-Hermitian theory.

1.2. Outline

As extensions of the SSH model are studied within this work, chapter 2 illustrates basic properties of the latter, emphasizing consequences of nontrivial topology and topological expressions. In particular, the occurrence of topologically protected edge states is explained and the topological invariants given by the bulk winding number and the Zak phase [13] are introduced. Moreover, the notion of *adiabatic phases* proposed by Berry [14] is commented on.

Extending the SSH model to bosonic particles leads to the superlattice Bose-Hubbard model (SL-BHM), which is discussed in more detail in chapter 3. It is known to also possess topologically nontrivial phases that host edge states at open boundaries [15]. Interestingly, the SL-BHM is related to the SSH model and therefore most of the topological aspects can be understood as directly inherited. The construction of a topological invariant and reasons for its quantization, which are required for the generalization to the non-Hermitian case, are also contained.

In order to describe dissipative effects, chapter 4 presents the two different methods of imposing $\mathcal{PT}$-symmetric on-site potentials leading to a non-Hermitian Hamiltonian and the description of the system dynamics by master equations in Lindblad form. Both approaches can actually be related in the mean-field limit, which motivates the application of non-Hermitian terms to effectively describe gain and loss also away from this limit. To become familiar with non-Hermitian operators, fundamental quantities that are inevitable for the treatment of the latter are introduced.

Chapter 5 contains an intermezzo on numerical methods to treat bosonic one-dimensional quantum many-body systems described by a local Hamiltonian (or Liouvillean). Starting from a simple build-up procedure of the investigated Hamiltonian, which allows to think of a finite system to be composed of two composite blocks, the idea of properly renormalizing the representation of a block to truncate the basis, thereby keeping the dimension of the problem manageable, the celebrated density matrix renormalization group method (DMRG) [16–18] is introduced and extended to non-Hermitian operators. Ultimately, this allows for the treatment of master equations in Lindblad form by expressing the latter in a vectorized form. A technique to target the *non-equilibrium steady state* (NESS) of a master equation is presented, adopting the language of traditional DMRG.

In chapter 6 the SL-BHM is extended by complex on-site potentials that impose different dissipative patterns on the system. Effects of dissipation are identified in the single-particle picture and related to the many-particle picture which can be accessed by employing the presented DMRG algorithm for non-Hermitian Hamiltonians. In the presence of complex energies a proper interpretation which leads to the most important states resembling the steady states of an equivalent master equation is outlined.

$\mathcal{PT}$-symmetric Hamiltonians are known to possess an entirely real spectrum for certain parameter ranges, where the system is said to be $\mathcal{PT}$-*unbroken* [11, 19, 20]. In chapter 7 the topological invariant introduced for the SL-BHM is formulated in a biorthogonal version which can also be employed in the $\mathcal{PT}$-unbroken regime. The real part of this complex Berry phase is shown to be quantized in integer multiples of π and a simple method for the numerical computation of the generalized winding number (complex Berry phase) is given. The generalization of topological properties to the non-Hermitian case leading to protected edge states at interfaces between two non-Hermitian systems that are characterized by different invariants is also illustrated. Practically, although the interpretation of the complex Berry phase as a topological invariant in the presence of complex eigenvalues does not hold, it can be employed as a local order parameter that encodes entanglement between two neighboring sites, even in the non-quantized case. The effects described in chapter 6 are successfully related to the data for the generalized winding numbers.

The second approach towards introducing gain and loss with master equations in Lindblad form is tackled in chapter 8, where the object of interest is given by the NESS of the system. First, a condition for the total particle number of fermionic and bosonic systems described by a master equation with linear Lindblad couplings is derived. Using the method of *third quantization* for both fermionic [21] and bosonic [22] systems governed by a quadratic Liouvillean, steady state observables can be computed for the dissipative versions of the SSH model and the non-interacting SL-BHM. Taking one step further with the onset of particle interactions, which lead to a non-quadratic Liouville operator that cannot be handled anymore by means of third quantization, the non-Hermitian DMRG algorithm is employed in Liouville space to obtain steady state observables in the interacting dissipative SL-BHM.

Note that each chapter starts with a brief summary of the content and concludes by reviewing the major results and notational aspects. Readers that are already familiar with a certain topic may want to skip a chapter, only reviewing the final summary at the end of each chapter. Expansions of calculations and proofs are contained whenever they were thought to contribute to a better understanding of the text. A detailed discussion of the method of third quantization and considerations about improving the numerical stability of DMRG in Liouville space is contained in the appendices.

2. Su-Schrieffer-Heeger (SSH) model

In the following chapter some of the necessary terminology of topological aspects in one-dimensional quantum systems is introduced and illustrated by investigation of the paradigmatic Su-Schrieffer-Heeger (SSH) model [10, 23] – a tight-binding model, which was originally proposed to describe topological solitons in polyacetylene, a linear polymer $(CH)_x$ consisting of quasi-one-dimensional chains of CH-monomers (see figure 2.1c) with two possible dimerization configurations.

Although the SSH model describes non-interacting fermions, it allows us to introduce the key ideas laying out the foundation for the generalization of topological order to interacting bosonic systems, as will be discussed later on (see chapter 3). Moreover, the approach taken in this work also relies on those ideas, aiming to extend the aforementioned systems by dissipative processes.

Starting off with a discussion of the properties of the bulk (the "interior" part) of a system described by the SSH Hamiltonian, introducing fundamental concepts for the treatment of such Hamiltonians in section 2.1, the text proceeds with the occurrence of topological edge states at system boundaries in section 2.2. Such states are characterized by an exponentially located particle at the edge and emerge if the transition of the boundary is accompanied by a change of the topological invariant. The latter does not change under continuous deformations of the system Hamiltonian, which is the reason for edge states to be robust against a large set of changes of the system parameters.

In case of a gapped system (like the SSH model which models a topological insulator), the concept of adiabatic phases, so called *Berry phases* [14], can be applied and provides a topological invariant that is also referred to as *Zak phase* in one-dimensional systems [13], a subject dealt with in section 2.3.

The material presented throughout this chapter is oriented towards the approach taken in reference [24]. For further reading the reader is also referred to [25].

2.1. Bulk properties

As already mentioned, the SSH model represents a paradigmatic Hamiltonian illustrating the context of topological order in physical systems. In the course of this work the main

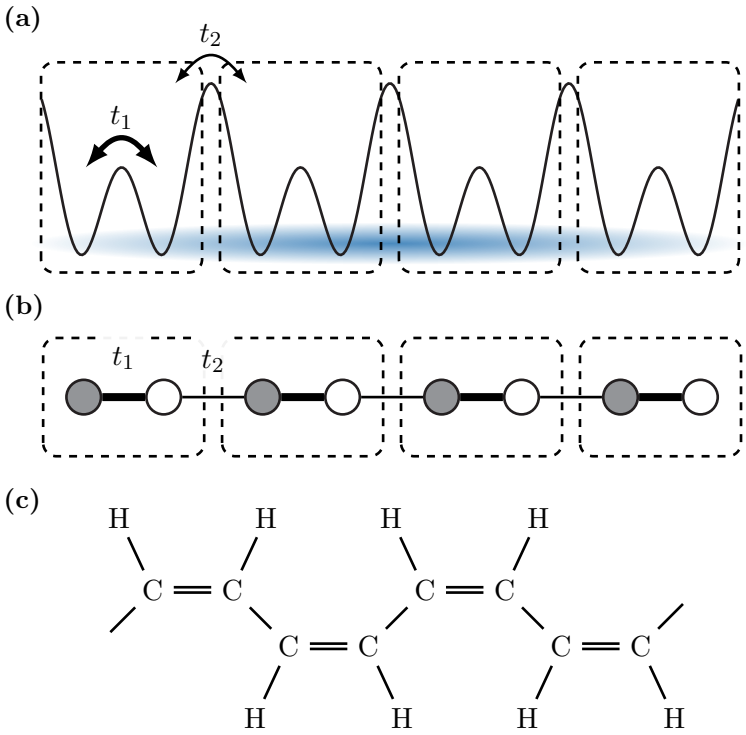

Figure 2.1.: Interpretation and origin of the SSH model. (a) Periodic superlattice potential composed of multiple double-well unit cells (dashed rectangles) with intra-cell tunneling amplitude t_1 and inter-cell tunneling t_2. (b) Scheme of the superlattice in terms of lattice sites (grey circles: sublattice A, white circles: sublattice B) connected by bonds indicating nearest neighbor hopping. The line thickness corresponds to the strength of the related tunneling. (c) Staggered hopping elements model the two dimerization configurations in polyacetylene $(CH)_x$. The trans-dimerization is shown.

focus will be on bosonic lattice systems whose Hamiltonians may easily be engineered and controlled by ultracold atoms in optical lattices [26, 27]. Therefore, the text will frequently adopt the terminology of optical lattices.

Consider a one-dimensional periodic potential of double-wells, which for instance could be created by the superposition of two counter-propagating laser beams (see figure 2.1a). A particle placed into such a superlattice structure may tunnel between two adjacent lattice sites, the rate determined by the potential barrier height. The hopping element of tunneling between two sites of a double-well is denoted by t_1, while the inter-cell tunneling (between two neighboring sites belonging to adjacent double-wells) is described by t_2. As one might already suspect, by varying the ratio of the two tunneling rates, the physical properties of this model change. A common parameterization for the tunneling amplitudes is given by

$$\begin{aligned} t_1 &= t\,(1 + \Delta\cos(\theta))\,, \\ t_2 &= t\,(1 - \Delta\cos(\theta))\,, \end{aligned} \tag{2.1}$$

with an average tunneling t modulated by the dimerization strength Δ. A sweep of the dimerization parameter $\theta \in [0, \pi]$ switches the dominance of inter- and intra-cell tunneling with equal tunnelings at $\theta = \frac{\pi}{2} \Leftrightarrow t_1 = t_2 = t$.

A pictoral way of thinking about those connected double-wells can be made up by considering wells as lattice sites joined by bonds indicating the strength of tunneling.

As indicated by figure 2.1b, thick connections represent strong tunneling, while thin bonds mark weak coupling. One can then imagine the system to be composed of dimers joined together by a small hopping amplitude. This interpretation resembles the original intention to model the two different dimerization configurations in polyacetylene, one of which is sketched in figure 2.1c.

The SSH Hamiltonian for spin-polarized fermions on a one-dimensional chain of L lattice sites labeled by indices $1, 2, \ldots, L$ with staggered hopping elements in second quantization reads

$$H = -\sum_{j=1,3,\ldots}^{L-1} \left(t_1 c_{j+1}^\dagger c_j + \text{h.c.} \right) - \sum_{j=2,4,\ldots}^{L-2} \left(t_2 c_{j+1}^\dagger c_j + \text{h.c.} \right), \tag{2.2}$$

where h.c. denotes Hermitian conjugation, c_j ($c_j^\dagger$) represent fermionic annihilation (creation) operators at site j satisfying the anti-commutation relations

$$\begin{aligned} \{c_j, c_k\} &= \left\{ c_j^\dagger, c_k^\dagger \right\} = 0, \\ \left\{ c_j, c_k^\dagger \right\} &= \delta_{jk}, \end{aligned} \tag{2.3}$$

and real tunneling amplitudes $t_1, t_2 \in \mathbb{R}$ are assumed. Moreover, an integer number of unit cells N implies $L = 2N$ to be even (at least in the course of this chapter).

Since the Hamiltonian (2.2) is quadratic in annihilation and creation operators and therefore there is no interaction between the fermions, it is sufficient to restrict its treatment to the single-particle basis, keeping in mind that a generic many-particle state of the system can be expressed in terms of properly antisymmetrized products of single-particle states. For the purpose of deriving the eigenstates $|\psi_n\rangle$ and energies $E_n, n = 1, 2, \ldots, L$, the Hamiltonian is expressed in the projector notation introduced in [24],

$$H = -\sum_{j=1}^{N} \left(t_1 \left| j, B \right\rangle \left\langle j, A \right| + \text{h.c.} \right) - \sum_{j=1}^{N-1} \left(t_2 \left| j+1, A \right\rangle \left\langle j, B \right| + \text{h.c.} \right), \tag{2.4}$$

where the fact that the chain of double-wells can be separated into two sublattices A and B (compare figure 2.1b) only coupling to one another is used to describe the presence of a particle in unit cell j at the lattice site assigned to sublattice A by $|j, A\rangle$ and so on. The notation in (2.4) emphasizes the two different tunnelings (inter- and intra-cell).

As the main focus is on properties of the bulk periodic boundary conditions are assumed. The Hamiltonian itself is then left invariant by translations $|j, \circ\rangle \to |j + \ell, \circ\rangle, \ell \in \mathbb{Z}, \circ \in \{A, B\}$, by an integer number of unit cells. This periodicity in the degree of freedom labeling the unit cells can be split apart by a Fourier transformation. To to so, one

chooses a representation of $|j,\circ\rangle \equiv |j\rangle \otimes |\circ\rangle$ in terms of the Hilbert spaces of internal (i.e. the single double-well) states $|\circ\rangle \in \mathscr{H}_{\text{internal}}$ and external (i.e. the unit cell index) degrees of freedom $|j\rangle \in \mathscr{H}_{\text{external}}$. Introducing the quasi-momentum state $|k\rangle \in \mathscr{H}_{\text{external}}$, the external degree of freedom is Fourier-transformed according to the relation

$$|k\rangle = \frac{1}{\sqrt{N}} \sum_{j=1}^{N} \mathrm{e}^{\mathrm{i}jk} |j\rangle\,, \qquad \text{where} \qquad k = \frac{2\pi}{N}, \frac{4\pi}{N}, \ldots, 2\pi. \tag{2.5a}$$

Inverting equation (2.5a) leads to

$$|j\rangle = \frac{1}{\sqrt{N}} \sum_{k=\frac{2\pi}{N},\frac{4\pi}{N},\ldots}^{2\pi} \mathrm{e}^{-\mathrm{i}jk} |k\rangle\,, \qquad \text{where} \qquad j = 1, 2, \ldots, N \tag{2.5b}$$

as the correspondence $N\delta_{kk'} = \sum_{j=1}^{N} \mathrm{e}^{-\mathrm{i}(k-k')j}$ holds.

With that said, the external terms stemming from the external degree of freedom in the SSH Hamiltonian (2.4) expressed in momentum state representation read

$$\begin{aligned} \sum_{j=1}^{N} |j\rangle\langle j| &= \frac{1}{N} \sum_{j=1}^{N} \sum_{k=\frac{2\pi}{N},\frac{4\pi}{N},\ldots}^{2\pi} \sum_{k'=\frac{2\pi}{N},\frac{4\pi}{N},\ldots}^{2\pi} \mathrm{e}^{-\mathrm{i}(k-k')j} |k\rangle\langle k'| \\ &= \sum_{k,k'} \delta_{kk'} |k\rangle\langle k'| = \sum_{k} |k\rangle\langle k|\,, \end{aligned} \tag{2.6a}$$

$$\sum_{j=1}^{N} |j+1\rangle\langle j| = \sum_{k} \mathrm{e}^{-\mathrm{i}k} |k\rangle\langle k|\,. \tag{2.6b}$$

Substituting (2.6) into (2.4) (including periodic boundary conditions) yields the following form of the Hamiltonian,

$$\begin{aligned} H &= -t_1 \sum_{j=1}^{N} \left(|j\rangle\langle j| \otimes |A\rangle\langle B| + \text{h.c.}\right) - t_2 \sum_{j=1}^{N} \left(|j+1\rangle\langle j| \otimes |A\rangle\langle B| + \text{h.c.}\right) \\ &= \sum_{k} |k\rangle\langle k| \otimes \underbrace{\left[-\left(t_1 + t_2 \mathrm{e}^{-\mathrm{i}k}\right) |A\rangle\langle B| + \text{h.c.}\right]}_{\equiv H_{\text{Bloch}}(k)}, \end{aligned} \tag{2.7}$$

where the term $H_{\text{Bloch}}(k)$ containing the internal degrees of freedom is referred to as *Bloch Hamiltonian*. Then, the eigenstates can be decomposed by a product ansatz $|\psi_n(k)\rangle = |k\rangle \otimes |u_n(k)\rangle$ with the 2π-periodic Bloch function $|u_n(k)\rangle = a_n(k)\,|A\rangle + b_n(k)\,|B\rangle$. This is nothing but a discrete version of the well-known *Bloch theorem* [28] and such a representation may always be chosen when the system is left invariant by a group of translation operators.

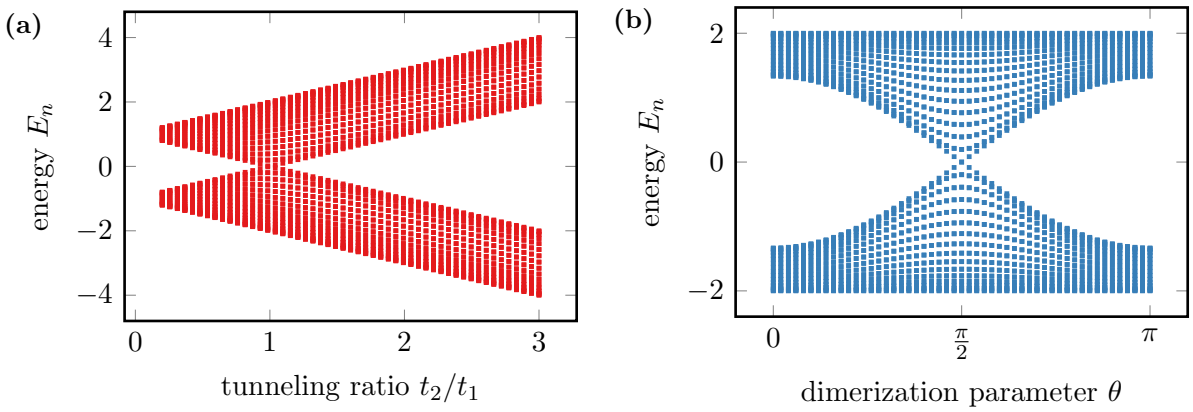

Figure 2.2.: Band structure of the single-particle energies of a finite periodic system of $N = 32$ unit cells for different tunneling ratios obtained numerically by exact diagonalization. (a) Variation of the tunneling ratio keeping $t_1 = 1$. (b) Variation by the parameterization (2.1) with parameters $t = 1, \Delta = 2/3$. The energy gap of the Bloch bands closes at $t_1 = t_2$.

Hence, the eigenvalue problem $H\,|\psi_n\rangle = E_n\,|\psi_n\rangle$ reduces to a much simpler one, namely $H_{\mathrm{Bloch}}(k)\,|u_n(k)\rangle = E_n(k)\,|u_n(k)\rangle$, which can be expressed as a matrix equation,

$$\underbrace{-\begin{pmatrix} 0 & t_1 + t_2 \mathrm{e}^{-\mathrm{i}k} \\ t_1 + t_2 \mathrm{e}^{\mathrm{i}k} & 0 \end{pmatrix}}_{\equiv \boldsymbol{H}_{\mathrm{Bloch}}(k)} \begin{pmatrix} a_n(k) \\ b_n(k) \end{pmatrix} = E_n(k) \begin{pmatrix} a_n(k) \\ b_n(k) \end{pmatrix}, \tag{2.8}$$

with the Bloch Hamiltonian matrix $\boldsymbol{H}_{\mathrm{Bloch}}(k)$ that will be discussed in more detail later on. Finally, after some simple calculus the energy dispersion reads

$$E_{1,2}(k) = \pm\sqrt{t_1^2 + t_2^2 + 2t_1 t_2 \cos(k)} \tag{2.9}$$

and is shown for the two different parameterizations in figure 2.2. The energy spectrum consists of two symmetrically arranged *Bloch bands* around $E = 0$. Thus, the many-particle ground state of the system is given by a fully occupied lower Bloch band. Since both bands are separated by an energy gap, the SSH Hamiltonian describes a (topological) insulator. It is crucial to notice that the staggered hopping is essential for the energy gap to open as the band gap closes for a vanishing dimerization at $t_1 = t_2$ (or equivalently $\theta = \pi/2$).

2.2. Topological edge states

So far the properties of a periodic system (imagine the lattice sites connected in the shape of a ring) without system boundaries have been discussed. However, interesting

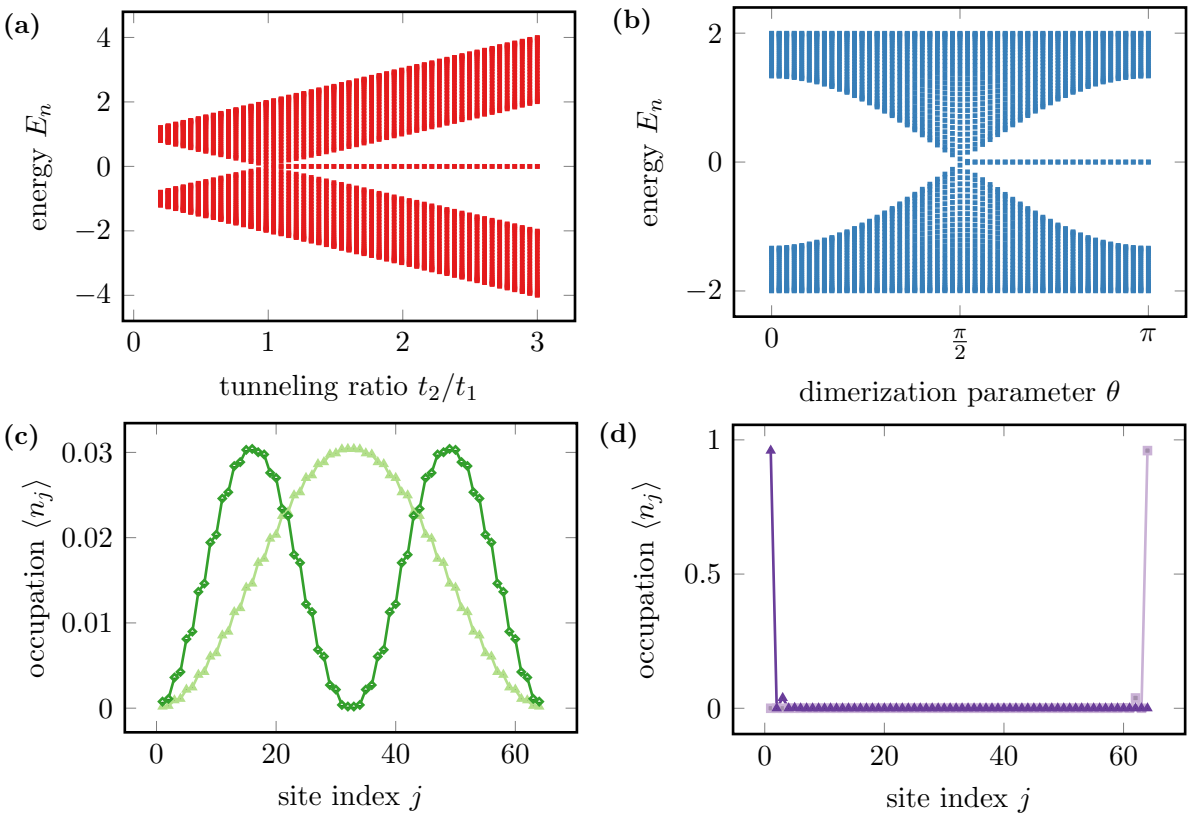

Figure 2.3.: Single-particle energy spectra of an open chain of $N = 32$ unit cells and lattice occupations of some eigenstates. (a) Variation of the tunneling ratio keeping $t_1 = 1$. (b) Variation by the parameterization $t = 1, \Delta = 2/3$. Note the occurrence of zero-energy modes in the regime $t_2 > t_1$. (c) Expectation values of the lattice occupation for two typical bulk states of the lower Bloch band. (d) The mid-gap modes at zero energy are exponentially localized at the system boundary which is why they are called edge states. Note that the edge states are localized on a sublattice only.

features arise when the ring is cut along one bond such that the result is a chain with two open boundaries.

To see this the single-particle energies of a system with identical length as that used in figure 2.2, but this time with open boundaries, is shown in figures 2.3a, 2.3b. While there are still two bands separated by an energy gap that closes at the homogeneous configuration $t_1 = t_2$, the open boundaries cause the emergence of two mid-gap degenerate states at zero energy in the regime where the inter-cell tunneling t_2 dominates the intra-cell hopping t_1. It is not only the energy that distinguishes those zero-energy modes from the rest of the bulk states. In figure 2.3c the lattice occupation $\langle n_j \rangle = \langle c_j^\dagger c_j \rangle$ of two states hosted by the lower Bloch band are shown. As expected a particle delocalizes over the whole bulk described by a Bloch wave. In contrast, the lattice occupation of the zero energy states is strongly concentrated at one of each of the boundaries (compare figure 2.3d). Such states providing a degree of freedom in terms of a localized particle at the

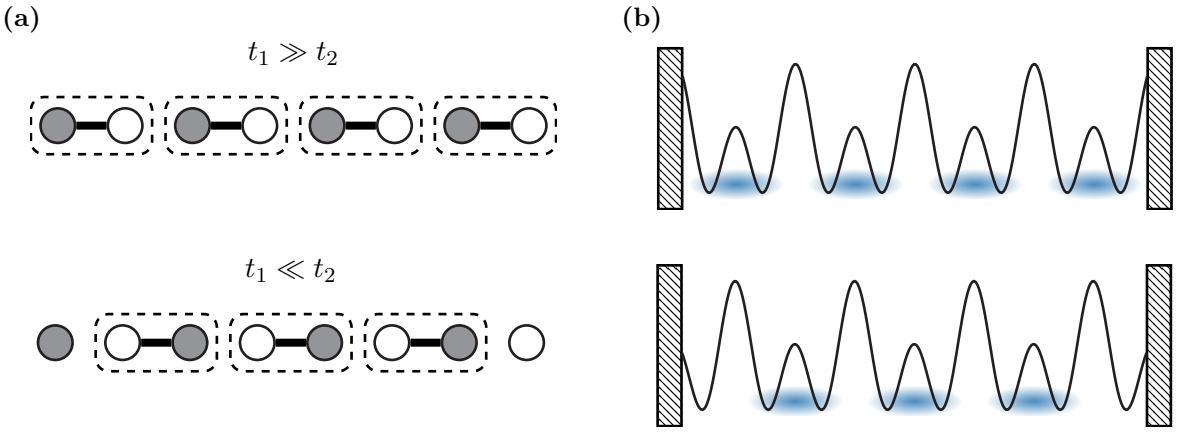

Figure 2.4.: Dimerized limit of the SSH model. (a) Setting either t_2 or t_1 to zero leaves the open chain in a configuration of decoupled double-wells (top panel) or a collection of dimers with completely decoupled single sites at the edges (bottom panel). (b) Same configurations in the superlattice potential picture. The ground state consists of "singlet states" localized on a single double-well (indicated by blue-shaded ellipses) allowing for the possibility of having two isolated sites at the edges a single-particle can be placed on.

edge of the system are called *edge states*.

The occurrence of edge states can be understood by considering the *fully-dimerized limit* of the unit cells shown in figure 2.4a. In the limit $t_1 \gg t_2$ the chain decomposes into N completely decoupled dimers (top panel of figure 2.4a) and the many-particle ground state is composed of singlet-type ground states $\frac{1}{\sqrt{2}}(|j, A\rangle - |j, B\rangle)$ of a double-well, located on a single dimer (top panel of figure 2.4b). The same applies for $t_2 \gg t_1$, except for the lattice sites located at the boundaries (bottom panels of figures 2.4a, 2.4b). However, now there are two lattice sites that are completely isolated from the rest of the chain, which can be filled with a particle without investing any energy (the zero-energy edge states).

However, edge states do not only occur in the strict limit of strongly dimerized double-wells. Rather they are a generic feature of the energy spectrum when $t_2 > t_1$. This robustness originates from the topological properties of the system. Remember that topological properties of a system cannot change under continuous deformations of the system, i.e. as long as the energy gap of the system does not close. Thus, the closing of the energy gap at $t_1 = t_2$ represents a *topological phase transition* and topology protects the edge states from hybridizing with the bulk whenever $t_2 > t_1$.

The topological phase transition can be observed by tracking the topological invariant of the system which is given by a *winding number* ν of the Bloch Hamiltonian matrix

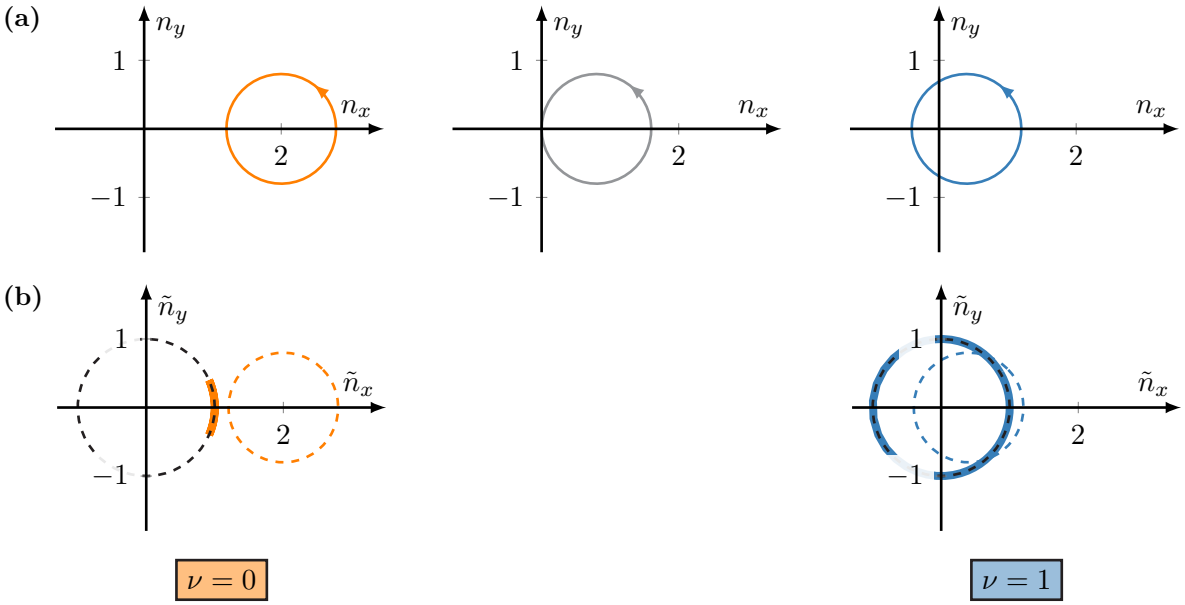

Figure 2.5.: Winding number of the Bloch Hamiltonian of the SSH model. (a) Loop performed by the vector $\underline{n}(k)$ parameterizing $\boldsymbol{H}_{\text{Bloch}}(k)$ for different parameter sets: $t_1 = 2, t_2 = 0.8$ (left), $t_1 = 0.8, t_2 = 0.8$ (center), $t_1 = 0.4, t_2 = 0.8$ (right). The number of times the origin is encircled by the loop, ν, represents a topological invariant which discontinuously changes at the phase transition marked by $t_1 = t_2$ and is accompanied by a closing of the band gap. (b) By projecting the loops (dashed colored lines) onto the unit circle (indicated by dashed black lines), the winding number can also be computed with a standard formula.

$\boldsymbol{H}_{\text{Bloch}}(k)$. By expanding (2.8) in terms of Pauli matrices,

$$\boldsymbol{\sigma}_x = \begin{pmatrix} 0 & 1 \\ 1 & 0 \end{pmatrix}, \qquad \boldsymbol{\sigma}_y = \begin{pmatrix} 0 & -\mathrm{i} \\ \mathrm{i} & 0 \end{pmatrix}, \qquad \boldsymbol{\sigma}_z = \begin{pmatrix} -1 & 0 \\ 0 & 1 \end{pmatrix}, \tag{2.10}$$

the Bloch Hamiltonian can be embedded in a quasi two-dimensional space,

$$\boldsymbol{H}_{\text{Bloch}}(k) = -\underline{n}(k) \cdot \underline{\boldsymbol{\sigma}}, \qquad \underline{n}(k) = \begin{pmatrix} t_1 + t_2 \cos(k) \\ t_2 \sin(k) \\ 0 \end{pmatrix} \tag{2.11}$$

with $\underline{\boldsymbol{\sigma}} = \left(\boldsymbol{\sigma}_x, \boldsymbol{\sigma}_y, \boldsymbol{\sigma}_z\right)^T$ spanned by the x and y components of $\underline{n}(k)$.

Because of the properties of the Pauli matrices the length of the vector $\underline{n}(k)$ corresponds directly to the energy, $|\underline{n}(k)| = |E_{1,2}(k)|$. As the quasi-momentum k sweeps from 0 to 2π the vector $\underline{n}(k)$ performs a loop in the (n_x, n_y)-plain, encircling the point $(n_x = t_1, n_y = 0)$ with a radius of t_2 (compare figure 2.5a). The number of times the loop performed by $\underline{n}(k)$ winds around the origin can simply be read off and it can be checked that the winding number is $\nu = 0$ for $t_1 > t_2$ and changes to $\nu = 1$ for $t_1 < t_2$. At the transition, the loop passes through the origin indicating a closing of the energy gap which, as already

mentioned, represents the only way a topological invariant can change. A standard way of calculating the winding number involves a projection of the loop onto the unit circle, defining $\tilde{\underline{n}}(k) = \underline{n}(k)/\left|\underline{n}(k)\right|$ (see figure 2.5b), computing the oriented area enclosed by $\tilde{\underline{n}}(k)$ and finally dividing this area by the surface of the unit circle [24],

$$\nu = \frac{1}{\pi}\int_0^{2\pi} \frac{1}{2}\left(\tilde{\underline{n}}(k) \times \frac{\partial}{\partial k}\tilde{\underline{n}}(k)\right)_z \mathrm{d}k. \tag{2.12}$$

In the next section, the method of adiabatic phases that provides a more general access to topological invariants of gapped systems will be introduced. The Berry phase (or Zak phase) which represents the topological invariant of the SSH model can be directly associated to the winding number (2.12) [29].

Some final remarks that shall not be kept back are in order. This is the fact that $n_z(k) = 0$ stems from a *chiral symmetry* [24] of the SSH model. The text shall not go too much into detail, but it is worth to be aware of two aspects:

- Chiral symmetry causes the energy spectrum of the SSH model to be antisymmetric, i.e. if E is eigenvalue of H, then $-E$ is another one. Moreover, it can be shown that due to a chiral symmetry, each of the two edge states (left: $|L\rangle$, right: $|R\rangle$) is hosted on one of the sublattices A, B, [24] such that

$$|L\rangle = \sum_{j=1}^{N} a_j \left|j, A\right\rangle, \qquad |R\rangle = \sum_{j=1}^{N} b_j \left|j, B\right\rangle. \tag{2.13}$$

- More generally, nontrivial topological order in one-dimensional systems can only be achieved by a symmetry of the system. Because of that, topological order in one-dimensional systems is often referred to as *symmetry-protected topological order (SPT)* [30].

2.3. Topological invariants – Berry phases

The winding number of the SSH Bloch Hamiltonian provides an illustrative topological invariant, which however cannot be generalized straightforwardly. A more general approach towards the construction of topological invariants for gapped systems is given by the concept of *adiabatic phases*, first introduced by Berry [14] (this text will only present the formalism for one-dimensional systems). The loop performed by the components of $\underline{n}(k)$ can be regarded as a transport of the Hamiltonian $H = H(\underline{n}(k))$ along a closed loop in parameter space $\{\underline{n}, \underline{n} \in \mathbb{R}^3\}$. If the requirements of the *adiabatic theorem*, which will be discussed later on, hold, the ground state of the system will acquire a phase, the Berry phase.

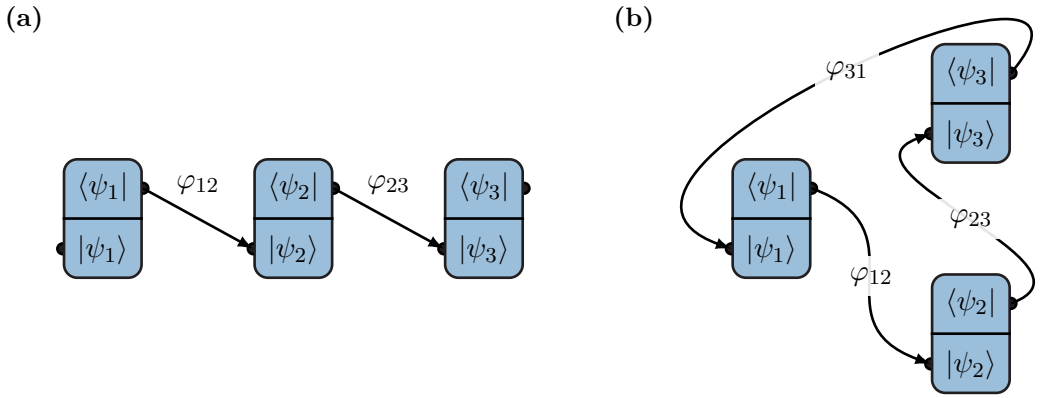

Figure 2.6.: Relative phase between a discrete set of nonorthogonal states. (a) A set of three states assigned to three different locations in parameter space. The phase between to adjacent states can be understood in terms of a contraction of neighboring bras and kets indicated by arrows. Neither of the phases is gauge-invariant. (b) Arranging the states in a closed loop $\mathscr{C}$ yields the quantity $\varphi_{\mathscr{C}} = \varphi_{12} + \varphi_{23} + \varphi_{31}$, which by construction is gauge-invariant.

To see how such a phase can be assigned consider the discrete case first, where a finite set of ground states $\{|\psi_1\rangle, |\psi_2\rangle, \ldots |\psi_M\rangle\}$ (for instance, assigned to points $k_1, k_2, \ldots, k_M$ in parameter space) is given (see figure 2.6a). One might assign a relative phase φ_{12} between two non-orthogonal states $|\psi_1\rangle, |\psi_2\rangle$ by means of the scalar product [24],

$$\varphi_{12} = -\arg\left(\langle\psi_1 \,|\, \psi_2\rangle\right) \quad \Longrightarrow \quad \mathrm{e}^{-\mathrm{i}\varphi_{12}} = \frac{\langle\psi_1 \,|\, \psi_2\rangle}{|\langle\psi_1 \,|\, \psi_2\rangle|}, \tag{2.14a}$$

or, equivalently,

$$\varphi_{12} = -\mathrm{Im}(\ln\left(\langle\psi_1 \,|\, \psi_2\rangle\right)). \tag{2.14b}$$

However, this definition alone is not physically meaningful. This is because the Schrödinger equation is invariant by a *global gauge transformation*,

$$|\psi\rangle \to \mathrm{e}^{\mathrm{i}\alpha}\,|\psi\rangle, \qquad \alpha \in \mathbb{R}, \tag{2.15}$$

as two states that only differ by a global phase α lead to the same evolution of all observables and can therefore be considered equal in quantum mechanics. Note that one could assign any global phase to both of the states in (2.14a) without changing the actual physics, but obviously modifying the outcome of φ_{12} *arbitrarily*. This is also an important aspect for numerical computations as a numerical routine solving for eigenvectors of a Hamiltonian matrix will assign a completely random complex phase to each eigenvector.

Fortunately, this problem can be circumvented if the states used in the computation of the phase are arranged in a closed loop $\mathscr{C}$ (compare figure 2.6b). Then, the Berry phase

$\varphi_{\mathscr{C}}$ of the loop $\mathscr{C}$ reads

$$\begin{aligned}\varphi_{\mathscr{C}} &= \varphi_{12} + \varphi_{23} + \ldots + \varphi_{M1} \\ &= -\arg\left(\langle\psi_1 \,|\, \psi_2\rangle \langle\psi_2 \,|\, \psi_3\rangle \cdots \langle\psi_M \,|\, \psi_1\rangle\right) \\ &= -\mathrm{Im}\left(\ln\left(\prod_{j=1}^{M} \langle\psi_j \,|\, \psi_{j+1}\rangle\right)\right)\end{aligned} \tag{2.16}$$

This form is inherently *gauge-invariant*, as a gauge transformation of any state $|\psi_j\rangle \to \mathrm{e}^{\mathrm{i}\alpha_j} |\psi_j\rangle$ leaves equation (2.16) unchanged because of the simultaneous gauge transformation in the adjoint counterpart $\langle\psi_j| \to \mathrm{e}^{-\mathrm{i}\alpha_j} \langle\psi_j|$. In numerical computations, the parameter space (momentum space for the SSH model) could be discretized in M steps $k_{1,\ldots,M}$ yielding the Bloch states $|\psi_{1,\ldots,M}\rangle$, which can then be used to evaluate (2.16) for the Berry phase.

To represent a topological invariant that can only change discontinuously, an additional property of the Berry phase is quantization, which is caused by a symmetry as already mentioned before. In the following, this will be illustrated for the SSH model. Before doing so some physical requirements that have to be met for equation (2.16) to provide a physically useful quantity are addressed.

The original approach of Berry [14] considers the slow (adiabatic) transport of a quantum system described by a Hamiltonian $H(\underline{R}), \underline{R} \in \mathscr{P}$ parameterized by the parameter space $\mathscr{P}$ around a loop $\mathscr{C}$,

$$\begin{aligned}\mathscr{C}: \quad [0,T) &\to \mathscr{P}, \\ t &\mapsto \underline{R}(t),\end{aligned} \tag{2.17}$$

such that $\underline{R}(0) = \underline{R}(T)$ and T is large enough for the evolution to be slow. The evolution of a state $|\psi(t)\rangle$ is governed by the Schrödinger equation

$$\mathrm{i}\frac{\mathrm{d}}{\mathrm{d}t} |\psi(t)\rangle = H(\underline{R}(t)) |\psi(t)\rangle \tag{2.18}$$

(setting $\hbar = 1$). For any point $\underline{R}(t)$ there exists a natural basis $|n(\underline{R}(t))\rangle$, where

$$H(\underline{R}(t)) |n(\underline{R}(t))\rangle = E_n(\underline{R}(t)) |n(\underline{R}(t))\rangle\,. \tag{2.19}$$

According to the *adiabatic theorem* [31], a system subjected to a slow perturbation remains in its instantaneous eigenstate if the eigenvalue is *gapped* from the rest of the spectrum. Hence, a system initially prepared in a state $|\psi(0)\rangle = |n(\underline{R}(0))\rangle$ and transported slowly enough (see [32] for a rigorous presentation) along the loop in parameter space will at time t be in the state $|n(\underline{R}(t))\rangle$ acquiring two phases,

$$|\psi(t)\rangle = \exp\left(-\mathrm{i}\int_0^t E_n(\underline{R}(t'))\mathrm{d}t'\right) \exp\left(\mathrm{i}\varphi_n(t)\right) |n(\underline{R}(t))\rangle\,. \tag{2.20}$$

The first exponential accounts for the dynamical phase arising from the evolution of the Hamiltonian. The second term can be considered as an effect of the parameter spaces' geometry. Inserting the ansatz (2.20) into (2.18) and solving for the geometric phase $\varphi_n(t)$, one obtains

$$\frac{\mathrm{d}\varphi_n}{\mathrm{d}t} = \mathrm{i}\,\langle n(\underline{R}(t))\,|\,\nabla_{\underline{R}} n(\underline{R}(t))\rangle\cdot\frac{\mathrm{d}\underline{R}}{\mathrm{d}t}. \tag{2.21}$$

Eventually, after performing an adiabatic closed path, the system will end up in the initial state $\sim |n(\underline{R}(0))\rangle$, having picked up a dynamical phase $\int_0^T E_n(\underline{R}(t'))\mathrm{d}t'$ and a geometric phase $\varphi_n(T) = \varphi_n(\mathscr{C})$ that only depends on the loop $\mathscr{C}$,

$$\varphi_n(\mathscr{C}) = \oint_{\mathscr{C}} \langle n(\underline{R})\,|\,\mathrm{i}\nabla_{\underline{R}} n(\underline{R})\rangle\cdot\mathrm{d}\underline{R} \equiv \oint_{\mathscr{C}} \underline{\mathcal{A}}(\underline{R})\cdot\mathrm{d}\underline{R}. \tag{2.22}$$

The integrand of equation (2.22) is called *Berry connection*. It is crucial to be aware of the fact that for the integration in (2.22) to work a smooth gauge has to be chosen for the instantaneous basis. In particular for numerical algorithms this can be an exhausting task [33], making it comfortable to have a gauge-invariant method (equation (2.16)) for computing the Berry phase at hand as well.

The relation between equations (2.16) and (2.22) can be seen by discretizing the loop into M equidistant steps and expressing the gradient term by a finite difference derivative of first order, neglecting higher terms. Assuming a one-dimensional parameter space and a discretized loop $\mathscr{C} = (k_1, k_2, \ldots, k_M)$ with spacing Δk and associated states $(|\psi(k_1)\rangle, |\psi(k_2)\rangle, \ldots, |\psi(k_M)\rangle)$, equation (2.16) can be rewritten by using the following relation from a Taylor expansion of

$$\begin{aligned}\langle\psi(k_j)\,|\,\psi(k_{j+1})\rangle &\approx \langle\psi(k_j)|\left(1+\Delta k\frac{\partial}{\partial k}\right)|\psi(k_j)\rangle\\ &= 1-\mathrm{i}\Delta k\mathcal{A}(k_j)\\ &\approx \exp\left(-\mathrm{i}\Delta k\mathcal{A}(k_j)\right),\end{aligned} \tag{2.23}$$

such that

$$\begin{aligned}\lim_{M\to\infty}\prod_{j=1}^{M}\langle\psi(k_j)\,|\,\psi(k_{j+1})\rangle &= \lim_{M\to\infty}\exp\left(-\mathrm{i}\sum_{j=1}^{M}\Delta k\mathcal{A}(k_j)\right)\\ &= \exp\left(-\mathrm{i}\oint_{\mathscr{C}}\mathcal{A}(k)\mathrm{d}k\right),\end{aligned} \tag{2.24}$$

which reproduces the same result for the Berry phase as (2.22).

The Berry phase obtained by transporting a one-dimensional periodic system along the first Brillouin zone is called *Zak phase*,

$$\varphi_{n,\mathrm{Zak}} = \int_0^{2\pi}\left\langle u_n(k)\,\middle|\,\frac{\partial}{\partial k}u_n(k)\right\rangle\mathrm{d}k \equiv \int_0^{2\pi}\mathcal{A}_n(k)\mathrm{d}k, \tag{2.25}$$

which has also recently been experimentally detected by interferometry [34]. Here, the $|u_n(k)\rangle$ are the Bloch functions introduced in the context of equation (2.8). For the SSH model the Zak phase directly corresponds to the winding number ν of the previous section. Note that due to the form of the Bloch Hamiltonian (equation (2.11)) the Bloch Hamiltonian anti-commutes with the Pauli matrix σ_z,

$$\{H_{\text{Bloch}}(k), \sigma_z\} = 0, \tag{2.26}$$

which is a symmetry property of the model referred to as a *chiral symmetry* leading to the quantization of the Zak phase $\varphi_{\text{Zak}} = 0, \pi \mod 2\pi$. First, by using property (2.26), if $H_{\text{Bloch}}(k)\,|u_+(k)\rangle = E(k)\,|u_+(k)\rangle$ where $|u_+(k)\rangle$ denotes the state of the upper Bloch band, then

$$H_{\text{Bloch}}(k)\sigma_z\,|u_+(k)\rangle = -\sigma_z H_{\text{Bloch}}(k)\,|u_+(k)\rangle = -E(k)\sigma_z\,|u_+(k)\rangle \tag{2.27}$$

implies that $|u_-(k)\rangle = \mathrm{e}^{\mathrm{i}\alpha_-(k)}\sigma_z\,|u_+(k)\rangle$. Thus up to a phase $\alpha_-(k)$ the state $\sigma_z\,|u_+(k)\rangle$ corresponds to the eigenstate in the lower Bloch band with eigenvalue $-E(k)$. It is trivial that the sum over all Zak phases is zero in total, i.e. $\varphi_{+,\text{Zak}} + \varphi_{-,\text{Zak}} = 0 \mod 2\pi$. Moreover, the Berry connection $\mathcal{A}_+(k)$ of a Bloch state in the upper band is related to that in the lower band $\mathcal{A}_-(k)$ by application of the chain rule,

$$\begin{aligned}\mathcal{A}_-(k) &= \left\langle u_-(k) \middle| \mathrm{i}\frac{\partial}{\partial k} u_-(k) \right\rangle = \left\langle u_+(k)\mathrm{e}^{-\mathrm{i}\alpha_-(k)} \middle| \mathrm{i}\frac{\partial}{\partial k}\mathrm{e}^{\mathrm{i}\alpha_-(k)} u_+(k) \right\rangle \\ &= -\frac{\partial}{\partial k}\alpha_-(k) + \mathcal{A}_+(k),\end{aligned} \tag{2.28}$$

which inserted into (2.25) leads to $\varphi_{-,\text{Zak}} - \varphi_{+,\text{Zak}} = 0 \mod 2\pi$. Combining both relations, one arrives at the quantization $\varphi_{\pm,\text{Zak}} = 0, \pi \mod 2\pi$.

Chapter review

- The SSH model describes spin-polarized electrons on a one-dimensional chain of double-wells with alternating nearest neighbor hopping amplitudes t_1 (intra-cell) and t_2 (inter-cell), which may also be expressed by an average tunneling amplitude t, the dimerization strength Δ and a dimerization parameter θ (compare equation (2.1)).
- In the regime $t_2 > t_1$ zero-energy edge states, characterized by an exponentially localized particle appear at an open boundary (or, more generally, at a domain where the topological invariant changes). The emergence of edge states can be understood in the limit of full dimerization and their stability for weaker dimerizations is caused by topology protecting them from hybridizing with the bulk modes.

- The Bloch Hamiltonian (2.8) of the SSH model contains all topological information. The number of times the parametrization vector $\underline{n}(k)$ encircles the origin in parameter space provides a topological invariant, the winding number ν, which may only change when the energy gap between the Bloch bands closes. Berry's method of adiabatic phases [14] provides a more general approach, but for the SSH model the winding number is directly related to the Zak phase φ_{Zak}, given by equation (2.25).
- Each Zak phase of a Bloch band is quantized to $\varphi_{\pm,\text{Zak}} = 0, \pi \mod 2\pi$. This quantization is due to the chiral symmetry of the SSH model. The two topological phases are (i) $t_1 > t_2$ where $\varphi_{\pm,\text{Zak}} = 0$ and (ii) $t_2 > t_1$ where $\varphi_{\pm,\text{Zak}}$. In one-dimensional systems nontrivial topological order is always protected by a symmetry, which for the SSH model is a chiral symmetry.

3. Superlattice Bose-Hubbard model (SL-BHM)

Now that the fundamental aspects of topological order in the SSH model have been laid out, this chapter will present the actual model which will be excessively investigated in what follows – the superlattice Bose-Hubbard model (SL-BHM). The SL-BHM can be considered as a generalization of the SSH model to interacting bosons which reduces to the Hamiltonian of its fermionic predecessor in the limit of hard-core bosons.

Proceeding in a way similar to the previous chapter the text first presents the model Hamiltonian and properties of the bulk in section 3.1 reviewing both numerical [35, 36] and analytical results obtained from perturbative treatment [37, 38]. The phase diagram of the bulk is discussed focussing on the Mott-insulator (MI) phases that are characterized by (half) integer filling of the lattice, some of them hosting topological edge states. A motivation for studying the superlattice Bose-Hubbard model, especially its topological properties, will be given in section 3.2 by outlining its relation to the SSH model. Although the bosonic SL-BHM originates from the fermionic SSH model, there are fundamental differences which become obvious if one attempts to generalize the concept of topological order and the construction of a topological invariant for interacting bosonic systems, which will be addressed in section 3.3.

Note that the details of the SL-BHM's topological properties have already been worked out in reference [15], from which most of the results will be reviewed in this chapter. Moreover, some figures of this publication are reproduced in order to check the validity of the Hermitian density matrix renormalization (DMRG) code (see chapter 5 for more details), which has been implemented in the course of this work.

3.1. Bulk properties and topological edge states

One of the main subjects of the investigations performed in this work involve the one-dimensional superlattice Bose-Hubbard model, whose Hamiltonian for a one-dimensional lattice of length L with sites labeled by $1, 2 \ldots, L$ in the grand-canonical ensemble

reads

$$\begin{aligned} H = &- \sum_{j \text{ odd}} \left(t_1 a_j^\dagger a_{j+1} + \text{h.c.} \right) - \sum_{j \text{ even}} \left(t_2 a_j^\dagger a_{j+1} + \text{h.c.} \right) \\ &+ \frac{U}{2} \sum_j n_j \left(n_j - 1 \right) + \sum_j (\epsilon_j - \mu) n_j, \end{aligned} \tag{3.1}$$

where a_j ($a_j^\dagger$) denote bosonic annihilation (creation) operators satisfying canonical commutation relations,

$$\begin{aligned} [a_j, a_k] = \left[a_j^\dagger, a_k^\dagger \right] = 0, \\ \left[a_j, a_k^\dagger \right] = \delta_{jk}, \end{aligned} \tag{3.2}$$

and $n_j = a_j^\dagger a_j$ is the number operator acting on lattice site j. The first two sums, representing the kinetic term of the Hamiltonian, describe nearest neighbor hopping with alternating tunneling amplitudes $t_1, t_2 \in \mathbb{R}$ that are assumed to be *real, if not explicitely stated differently*. Obviously, the hopping is completely analogous to the SSH case (compare equation (2.2)), except fermionic operators being replaced by bosonic equivalents. As bosons are not governed by Pauli's exclusion principle a site may be populated with multiple bosons, giving rise to interactions. The third term of the Hamiltonian (3.1) accounts for this process and models local on-site interactions (for instance in the spirit of an s-wave scattering interaction potential) described by the on-site interaction U. Throughout the text the energy scale of the model will be fixed by adopting the *convention* $U = 1$. Finally, external potentials may impose a different on-site potential ϵ_j at each lattice site energetically favoring the addition or removal of a particle, and μ denotes the global chemical potential. In most cases the on-site potentials are set to $\epsilon_j = 0$ *unless explicitely stated*.

For $t_1 = t_2$ the SL-BHM reduces to the homogeneous Bose-Hubbard model, which is known to possess gapless superfluid as well as *gapped Mott-insulating (MI)* phases that are characterized by integer occupation per lattice site [37, 39]. Given a fixed value of the tunneling amplitude $t_1 = t_2$ the phase boundaries of MI phases at filling ρ are bounded by the lower and upper chemical potentials $\mu_\rho^\pm$ such that for $\mu_\rho^- \leq \mu \leq \mu_\rho^+$ the ground state is of type MI at filling ρ. Figure 3.1a shows numerical results for the phase boundaries of MI regimes at filling $\rho = 0, 1, 2$ for a finite system with open boundary conditions obtained by DMRG. Note that for $L \to \infty$ the MI phases will be completely absent when t_1 exceeds a critical value – a feature that is not properly reproduced by the finite system, which is considered a finite size effect. The ground state for each of the MI phases shown in figure 3.1a is shown in figure 3.1b.

In the same manner the staggered hopping was essential for the SSH model to open an energy gap between the Bloch bands, it is the main ingredient for the appearance of

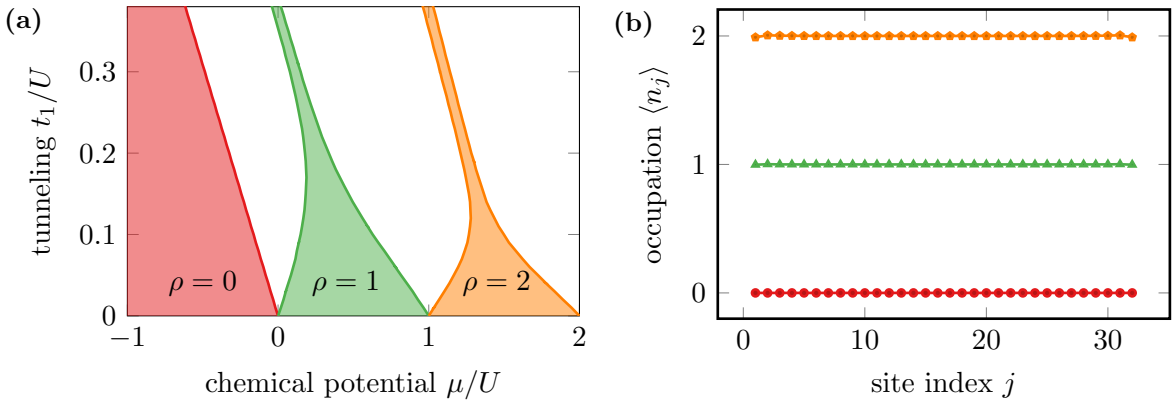

Figure 3.1.: Ground state phase diagram and Mott-insulating phases of the one-dimensional homogeneous Bose-Hubbard model ($t_1 = t_2$). (a) Extract of the phase diagram of a finite system with $L = 16$ lattice sites and open boundaries obtained by DMRG (allowing at most four particles per site, i.e. a local site dimension $D = 5$ and keeping the truncation error $\varepsilon < 10^{-9}$, see chapter 5 for more details). The phase boundaries μ_0^+ (red), $\mu_1^\pm$ (green), and $\mu_2^\pm$ (orange) are determined by a bisection algorithm similar to the method applied in [36] targeting a lattice filling of $\rho = 0, 1, 2$, respectively. Filled areas correspond to the areas of integer filling in the (μ, t_1)-plain. (b) Ground state lattice occupation of the MI phases at filling $\rho = 0, 1, 2$ (red circles, green triangles, orange pentagons, respectively) on a homogeneous lattice ($L = 32$) with open boundaries obtained by DMRG ($D = 5$, $\varepsilon < 10^{-9}$). Model parameters are $t_1/U = 0.1$ and $\mu/U = -0.5, 0.5, 1.4$.

topological order in the SL-BHM. In fact, for alternating hoppings $t_1 \neq t_2$ new features appear in the phase diagram. In addition to Mott regimes of integer occupation separated by superfluid phases, MI phases of half integer occupation emerge [36]. In the phase diagram the loophole shaped areas of such MI phases become more pronounced for a strong staggering and vanish completely as t_1 approaches t_2. Figure 3.2a shows the phase diagram of a finite system with a dimerization of $t_2 = 0.2t_1$ similar to the figure shown in reference [36] obtained by DMRG. The appropriate ground states of the MI phases are plotted as well in figure 3.2b.

In the following, the focus will be on the $\rho = 1/2$ MI phase. In the limit of strong interactions, $t_{1,2}/U \ll 1$ the upper and lower phase boundaries $\mu_{1/2}^\pm$ can be obtained perturbatively up to order $\mathcal{O}\left(t_2^2/U, t_2 t_1^2/U^2\right)$ [15],

$$\begin{aligned} \mu_{1/2}^- &= -\left|t_1 - t_2\right|, \\ \mu_{1/2}^+ &= \left|t_1 - t_2\right| + \frac{U}{2} - \frac{1}{2}\sqrt{16t_1^2 + U^2} - \frac{4t_1 t_2}{U}. \end{aligned} \tag{3.3}$$

A more detailed extract of the phase boundaries $\mu_{1/2}^\pm$ already shown in figure 3.2a is presented in figure 3.3a, the only difference being a swap of the tunneling amplitudes such that $t_2 > t_1$, which does not influence the properties of the bulk when the system is sufficiently large. In this *topologically nontrivial dimerization configuration* the many-particle ground state shows edge features in the $\rho = 1/2$ MI phase. It is the value of

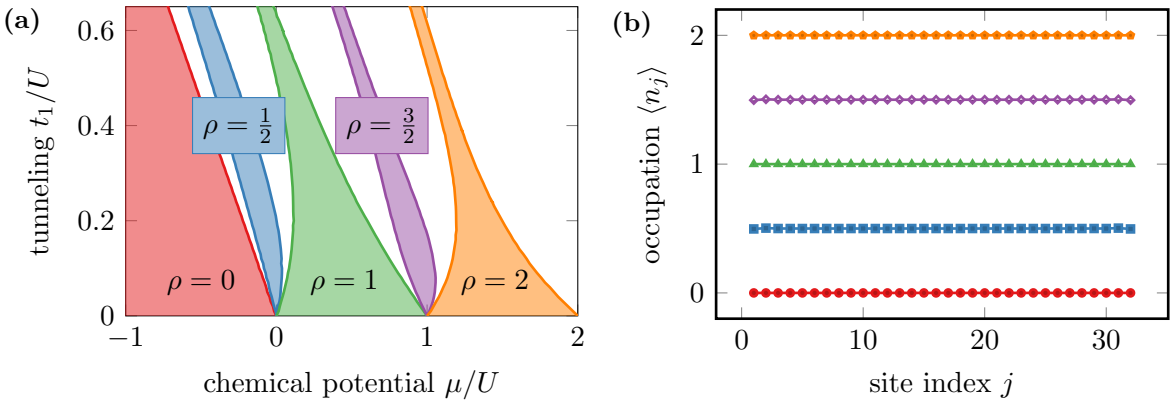

Figure 3.2.: Ground state phase diagram and Mott-insulating phases of the one-dimensional SL-BHM for $t_2 = 0.2t_1$. (a) Extract of the phase diagram of a system with $L = 16$ sites and open boundary conditions showing the phase boundaries $\mu_0^+, \mu_{1/2}^\pm, \mu_1^\pm, \mu_{3/2}^\pm$ and $\mu_2^\pm$ (in red, blue, green, purple, and orange solid lines, respectively). In contrast to the homogeneous Bose-Hubbard model additional MI phases at half integer filling $\rho = 1/2, 3/2, \ldots$ occur when the hopping is alternated. DMRG parameters are chosen identical to that in figure 3.1. (b) Ground state lattice occupation for the MI phases (in the topologically trivial dimerization scheme) at $\rho = 0, 1/2, 1, 3/2, 2$ (red circles, blue squares, green triangles, purple diamonds, and orange pentagons, respectively) in a chain of length $L = 32$. System parameters are $t_1/U = 0.1$ and $\mu/U = -0.5, 0, 0.5, 1.0, 1.4$.

the chemical potential that determines whether the edge state is governed by a localized particle or a localized hole at the boundary as can be seen in figure 3.3b. The transition between hole and particle edge state is marked by a *critical chemical potential* μ_e, such that a hole edge state occurs in the regime $\mu_{1/2} \leq \mu < \mu_e$ while the ground state is a particle edge state when $\mu_e < \mu \leq \mu_{1/2}^+$. An analytical expression of the critical chemical potential can be derived by means of perturbation theory and, in the strongly-interacting limit, is given by the expression [15]

$$\mu_e = -2t_2^2 \frac{U - 2t_1}{(U + t_1)(U - 3t_1)}. \tag{3.4}$$

Note that it has been avoided to overload figure 3.3a by also showing the analytical results (3.3), (3.4), however the validity of numerical values can be verified by taking a look at the original figure in reference [15].

In the latter, it is also shown that the particle edge state vanishes when the tunneling amplitude t_1/U exceeds a critical value. This feature is reproduced within the figure shown in this text as μ_e approaches $\mu_{1/2}^+$ for increasing t_1/U, although this behavior can be seen more clearly when the system size is increased. In fact, when the tunneling is increased, the particle edge state extends more and more into the bulk, until it completely hybridizes with it at the critical value of t_1/U. Figure 3.3c illustrates how the shape of the edge state changes with varying tunneling parameters. For small values of t_1/U, the edge state (particle and hole) is sharply localized at the edge. Increasing the coupling

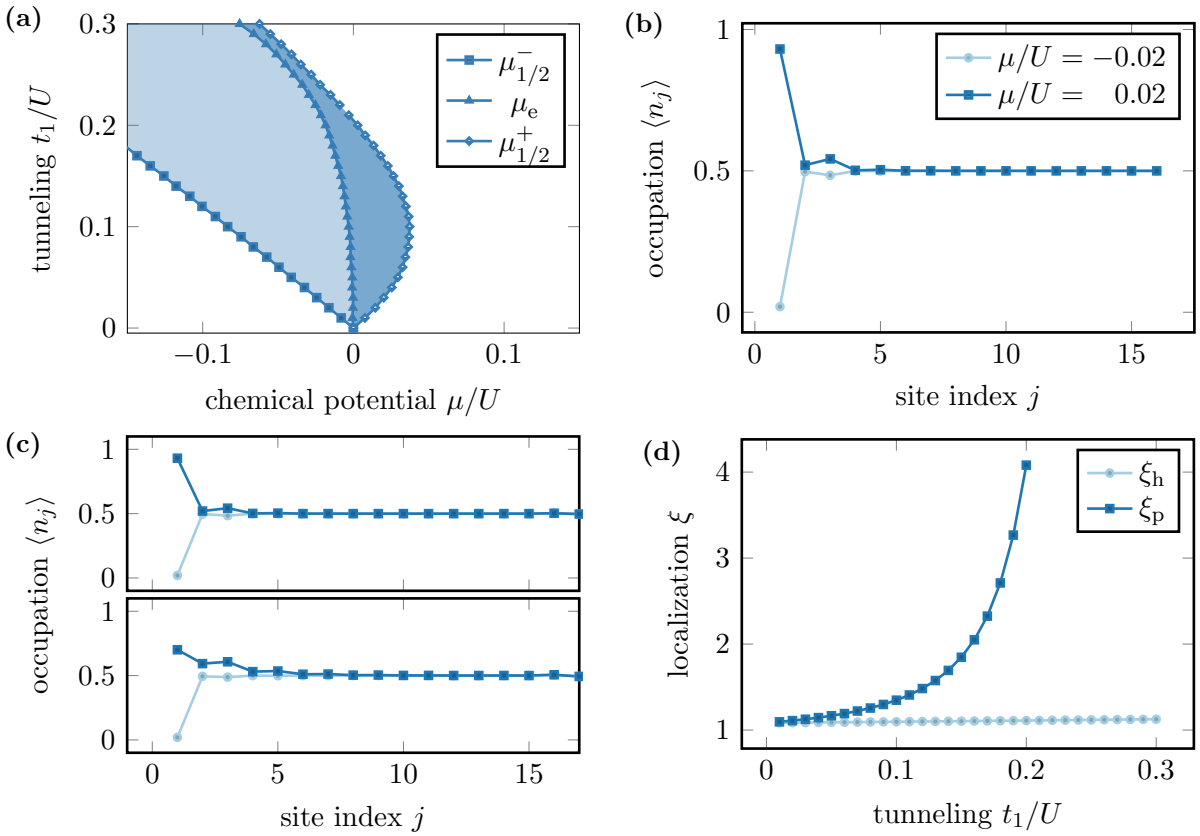

Figure 3.3.: Properties of edge states in the topologically nontrivial $\rho = 1/2$ MI phase of the SL-BHM. (a) Bulk phase boundaries $\mu^{\pm}_{1/2}$ for a system with $L = 16$, open boundaries, and $t_1 = 0.2t_2$. In this dimerization configuration edge states appear in terms of a localized particle or hole at the system boundaries. The phase is split into two regimes separated by the critical chemical potential μ_e, which marks the transition in the many-particle ground state from hole to particle edge state. (b) Lattice occupation of the ground state of a system with $L = 32$ (only the first 16 sites are shown) showing a hole and particle edge state depending on the value of the chemical potential. Additional system parameters are $t_1 = 0.2t_2$ and $t_2 = 0.1$. (c) Shape of the (un)occupied edge states for different values of the tunneling parameter while $t_2 = 0.2t_1$. The values of μ/U are chosen from figure (a) such that the particle state appears if $\mu_e < \mu < \mu^+_{1/2}$ and the hole state is present whenever $\mu^-_{1/2} < \mu < \mu_e$. The system length $L = 17$ is chosen to be odd in order to only obtain edge features at one of the system boundaries. Top panel: $t_1/U = 0.1$, bottom panel: $t_1/U = 0.2$. (d) Localization length (see equation (3.5)) of particle ξ_p and hole ξ_h states for different tunneling amplitudes t_1/U while $t_2 = 0.2t_1$ obtained from a system with $L = 17$ sites.

from the open boundary to the bulk the localization of the occupied edge is blurred, while the hole state stays almost unaffected. A quantitative measure for the localization of an edge state is given by the *localization length* ξ [15],

$$\xi = \left(\sum_j \Delta n_j \right)^2 \Bigg/ \sum_j (\Delta n_j)^2 , \tag{3.5}$$

where $\Delta n_j = |\langle n_j \rangle - 1/2| \, \Theta(\pm(\langle n_j \rangle - 1/2))$ is the difference between the occupation of lattice site j and a generic one in the bulk, $1/2$, and Θ denotes the Heaviside step function. Depending on the type of state (hole or particle) only sites filled with more (+: particle) or less (−: hole) than $1/2$ are used in the determination of ξ_p (particle) and ξ_h (hole). Figure 3.3d shows numerical studies of the localization length of the edge states. The fact that the hole state is nearly unaffected by differing tunneling is underlined by an almost constant localization length, whereas the latter diverges for the particle state at the aforementioned critical tunneling value.

Many properties of the SL-BHM can be related to the SSH model. Therefore the following section is devoted to outlining the parallels of both models.

3.2. Relation to the Su-Schrieffer-Heeger model

The main difference between SL-BHM and SSH model is rooted in the nature of the particles they are describing. While fermions obey Pauli's exclusion principle, forbidding double occupancies of a single lattice site, an arbitrary amount of bosons may be placed on a certain site leading to on-site interactions. However, if one is interested in the low energy physics of the SL-BHM both models can be mapped onto each other in the limit of hard-core bosons $U \to \infty$. In that case the on-site interaction forces the ground state to avoid double occupancies of a lattice site as they would cost plenty of energy.

Hence, the interaction term in (3.1) can be neglected when the hard-core limit $U \to \infty$ is under consideration. Setting $\epsilon_j = 0$ the remaining terms are now transformed by a "fermionization" of the bosonic creation (annihilation) operators $a_j^\dagger$, (a_j), given by a *Jordan-Wigner transformation* [40],

$$\begin{aligned} c_j &= a_j \exp\left(-\mathrm{i}\pi \sum_{k<j} n_k\right), \\ c_j^\dagger &= a_j^\dagger \exp\left(\mathrm{i}\pi \sum_{k<j} n_k\right). \end{aligned} \tag{3.6}$$

It can be checked that the operators $c_j, c_j^\dagger$ satisfy fermionic anti-commutation relations (2.3). Thus the SL-BHM Hamiltonian in the hard-core limit reduces to

$$H_{U\to\infty} = -\sum_{j \text{ odd}} \left(t_1 c_j^\dagger c_{j+1} + \text{h.c.}\right) - \sum_{j \text{ even}} \left(t_2 c_j^\dagger c_{j+1} + \text{h.c.}\right) - \sum_j \mu n_j, \tag{3.7}$$

which, up to the term including the chemical potential, is the SSH Hamiltonian (2.2). Hence, *the SSH model is the hard-core limit of the low-energy physics of the SL-BHM at* $\mu = 0$. That said, some relationships have to be emphasized:

- At $\mu = 0$ the energy spectra of both hard-core SL-BHM and SSH model are encoded in the two Bloch bands (assuming periodic boundaries). The many-particle ground state can be expressed in terms of single-particle states by filling up the entire lower Band, which results in an insulating state at half filling of the lattice that directly corresponds to the $\rho = 1/2$ MI phase in the SL-BHM.
- Following the same argument for a system with open boundaries the emergence of edge states as ground states is a direct consequence of their appearance in the single-particle energy spectrum (compare figure 2.3) whenever $t_2 > t_1$. The term of (3.7) containing the chemical potential can be considered as a shift of the entire single-particle spectrum, such that for $\mu > 0$ the zero-energy edge states of the SSH model are energetically lowered by μ, which leads to a bulk at half filling (completely filled lower Bloch band) with a particle located at each boundary (occupied edge states). For $\mu > 0$ the zero energy modes are shifted towards positive energies and their occupation is avoided by the ground state, which is then given by a bulk with unoccupied edges (the hole state). Hence, the critical chemical potential is $\mu_e = 0$ in the hard-core limit and even in the strongly-interacting limit, see figure 3.3a.
- Similarly, the phase boundaries for the $\rho = 1/2$ MI phase, or equivalently a fully occupied lower Bloch band, can be derived in the hard-core limit. The many-particle ground state is at half filling as long as (i) the upper Bloch band is not lowered below $E = 0$ by the chemical potential term, causing more particles to be filled in the ground state, in this case the upper boundary for the chemical potential is given by the energetic distance between the upper Bloch band and zero implying $\mu^+_{1/2} = |t_1 - t_2|$ (see equation (2.9)) or (ii) the lower Bloch band bulges out of the negative energy domain leading to fewer particles in the ground state and $\mu^-_{1/2} = -|t_1 - t_2|$. Note that this is the limit $U \to \infty$ of equation (3.3) presented earlier.

The emergence of topological edge states in the $\rho = 1/2$ MI phase of the SL-BHM can therefore be interpreted as a remnant of the SSH Bloch band's topology. However, carrying over the topological invariant given by the Zak phase to the bosonic interacting system leads to problems that will be addressed in the next section. Another crucial property of the SSH model is the chiral symmetry, which is spoiled by the interaction term as U becomes finite. The very same symmetry protected the topological order in the SSH model raising the question which symmetry protects topological order in the SL-BHM.

3.3. Topological invariants for interacting systems

The attempt of computing the Zak phase for an interacting system as the SL-BHM fails because the Hamiltonian cannot be represented by a Bloch Hamiltonian and the notion of single-particle states becomes useless. There are different approaches towards generalizing the topological invariants of non-interacting periodic systems usually defined in momentum space, or to define new topological invariants for interacting topological insulators [41–45]. The topological invariant introduced by [15] can be understood as a generalization of the Zak phase (2.25) and applies the concept of *quantized Berry phases as local order parameters* [46] introduced by Hatsugai. This section shall review the steps of Hatsugai's arguments.

As in section 2.3 a Hamiltonian $H(\underline{R})$ parametrized by a number of parameters $\underline{R} \in \mathscr{P}$ spanning the parameter space is assumed. Suppose that, given the normalized unique many-body ground state $|\psi(\underline{R})\rangle$ and a loop $\mathscr{C}$ in $\mathscr{P}$, that the ground state energy is always separated from the rest of the Hamiltonian spectrum. Then one can compute the Berry phase by integration of the Berry connection, see equation (2.22), which is repeated here in adapted notation,

$$\varphi(\mathscr{C}) = \oint_{\mathscr{C}} \langle \psi(\underline{R}) \,|\, \mathrm{i}\nabla_{\underline{R}} \psi(\underline{R}) \rangle \cdot \mathrm{d}\underline{R} \equiv \oint_{\mathscr{C}} \underline{\mathcal{A}}(\underline{R}) \cdot \mathrm{d}\underline{R}. \tag{3.8}$$

A subtle point here is that the ground state is only determined up to a phase such that the Berry connection transforms under a gauge transformation $|\psi(\underline{R})\rangle \to \mathrm{e}^{\mathrm{i}\alpha(\underline{R})} |\psi(\underline{R})\rangle$ by $\underline{\mathcal{A}}(\underline{R}) \to \underline{\mathcal{A}}(\underline{R}) - \nabla_{\underline{R}} \alpha(\underline{R})$ (compare equation (2.28)). A proper *(regular) gauge* may be specified by projecting each ground state to a reference state $|\phi\rangle$, yielding [46]

$$|\psi_\phi(\underline{R})\rangle = |\psi(\underline{R})\rangle \frac{\langle \psi(\underline{R}) \,|\, \phi \rangle}{|\langle \psi(\underline{R}) \,|\, \phi \rangle|}. \tag{3.9}$$

It can be shown that Berry phases obtained by choosing two different reference states $|\phi\rangle, |\phi'\rangle$, both defining regular gauges, are invariant up to integer multiples of 2π,

$$\begin{aligned} \oint_{\mathscr{C}} \underline{\mathcal{A}}_{\psi_\phi}(\underline{R}) \cdot \mathrm{d}\underline{R} &= \oint_{\mathscr{C}} \underline{\mathcal{A}}_{\psi_{\phi'}}(\underline{R}) \cdot \mathrm{d}\underline{R} \mod 2\pi, \\ \varphi(\mathscr{C}, \underline{A}_{\psi_\phi}) &= \varphi(\mathscr{C}, \underline{A}_{\psi_{\phi'}}) \mod 2\pi. \end{aligned} \tag{3.10}$$

The Berry phases' properties become even more interesting when the system possesses a discrete antiunitary symmetry, $[H(\underline{R}), \Theta] = 0$, represented by the operator Θ which is independent from the parameters of the Hamiltonian. The symmetry operator $\Theta = \mathcal{T} U_\Theta$ can be split up into a unitary operation U_Θ, followed by complex conjugation, whose

representation, for the purpose of this text, is given by the time reversal operator $\mathcal{T}$. Expanding the ground state in a fixed orthonormal basis $\{|j\rangle\}$ the action of Θ reads

$$|\psi(\underline{R})\rangle = \sum_j c_j(\underline{R})\,|j\rangle \quad \Longrightarrow \quad \Theta\,|\psi(\underline{R})\rangle \equiv |\psi^\Theta(\underline{R})\rangle = \sum_j c_j^*(\underline{R})\Theta\,|j\rangle\,, \tag{3.11}$$

where the basis $\{\Theta\,|j\rangle\}$ is also assumed to be orthogonal. One can verify that the Berry connections for $|\psi(\underline{R})\rangle\,, \left|\psi^\Theta(\underline{R})\right\rangle$ in a regular gauge are related,

$$\begin{aligned}
\underline{\mathcal{A}}_{\psi^\Theta} &= \left\langle \psi^\Theta(\underline{R}) \,\middle|\, \mathrm{i}\nabla_{\underline{R}}\psi^\Theta(\underline{R})\right\rangle \\
&= \sum_j c_j(\underline{R})\nabla_{\underline{R}}c_j^*(\underline{R}) \\
&= -\sum_j c_j^*(\underline{R})\nabla_{\underline{R}}c_j(\underline{R}) \\
&= -\left\langle \psi(\underline{R}) \,|\, \mathrm{i}\nabla_{\underline{R}}\psi(\underline{R})\right\rangle = -\underline{\mathcal{A}}_\psi,
\end{aligned} \tag{3.12}$$

where the normalization of the ground state $\sum_j |c_j(\underline{R})|^2 = 1$ was used.

However, if the Hamiltonian commutes with Θ and the ground state is always *unique* as assumed, then $\left|\psi^\Theta(\underline{R})\right\rangle$ and $|\psi(\underline{R})\rangle$ can only be related by a gauge transformation. This in addition to the argument urged in equation (3.10) implies that the Berry phases of both Berry connections of equation (3.12) are equal up to an integer multiple of 2π,

$$\varphi(\mathscr{C}, \underline{A}_{\psi^\Theta}) = \varphi(\mathscr{C}, \underline{A}_\psi) \equiv \varphi(\mathscr{C}) \mod 2\pi. \tag{3.13a}$$

Furthermore, the transformation of the Berry connection (3.12) implies

$$\varphi(\mathscr{C}, \underline{A}_{\psi^\Theta}) = -\varphi(\mathscr{C}, \underline{A}_\psi) \mod 2\pi. \tag{3.13b}$$

Ultimately, equations (3.13) state the desired result, namely that "the Berry phase of the antiunitary invariant state is *inevitably* quantized" [46] to

$$\varphi(\mathscr{C}) = 0, \pi \mod 2\pi, \tag{3.14}$$

raising φ to a topological quantity that cannot change continuously because of its strict quantization. Note that this approach requires neither translational symmetry nor periodic boundary conditions and may also be applied to systems with open boundaries governed by an antiunitary symmetry. With that said, one can now define a topological invariant for the SL-BHM that will be called ν in analogy to the winding number of the SSH Hamiltonian back in section 2.3 and in order to separate what follows in notation.

The ground state of the SL-BHM Hamiltonian (3.1) is unique and gapped when the system is in either the half integer or integer MI phase and the system is inversion-symmetric, that is if all sites are mirrored at the centering bond one can think the

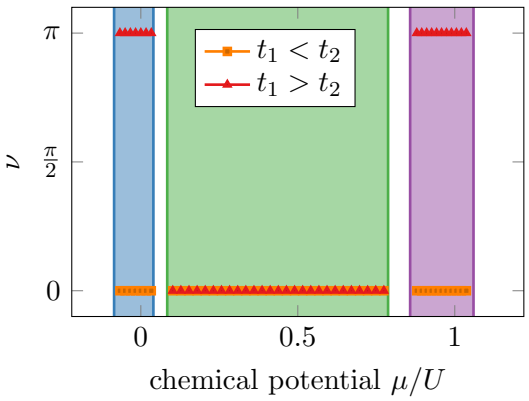

Figure 3.4.: Generalized winding number for different MI phases of the SL-BHM obtained by exact diagonalization ($D = 4$) of a system of $L = 8$ sites (red triangles: $t_1/U = 0.1, t_2/U = 0.02$, orange squares: $t_1/U = 0.02, t_2/U = 0.1$). The loop in parameter space is discretized to 100 equidistant points yielding ν by use of equation (2.16). Regimes of MI phases corresponding to the hopping are filled in the same colors as in figure 3.2a. Note that integer MI are always topologically trivial, while half-integer MI may have $\nu = \pi$ in the nontrivial dimerization configuration in which edge states occur as a consequence.

one-dimensional chain (as sketched in figure 2.1b) to be mapped onto itself. In fact, the antiunitary symmetry is given by the combined action of time inversion $\mathcal{T}$ and space inversion $\mathcal{P}$, also known as parity-time ($\mathcal{PT}$) symmetry,

$$[H, \mathcal{PT}] = 0. \tag{3.15}$$

To define ν consider the sites of the SL-BHM to be periodically connected forming a ring which is cut along one bond to yield the open chain. By introducing a modulated tunneling $t_2 \mathrm{e}^{\mathrm{i}\vartheta}$ (so called *twisted boundary conditions* [15, 41]) at exactly that bond the Hamiltonian parameter space is extended by the modulation parameter ϑ. This exposes the system to a perturbation which, importantly, *respects the symmetry* of the system. This can be understood by investigating only the kinetic term $-t_2 \mathrm{e}^{\mathrm{i}\vartheta} a_L^\dagger a_1 + \text{h.c.}$ with modulated tunneling from last to first site as the rest of the Hamiltonian still anticommutes with $\mathcal{PT}$ (equation (3.15)). The action of $\mathcal{PT}$ on the extension term leaves the latter invariant as well because

$$\begin{aligned} \mathcal{T}: \quad & -t_2 \mathrm{e}^{\mathrm{i}\vartheta} a_L^\dagger a_1 - t_2 \mathrm{e}^{-\mathrm{i}\vartheta} a_1^\dagger a_L \quad \to \quad -t_2 \mathrm{e}^{-\mathrm{i}\vartheta} a_L^\dagger a_1 - t_2 \mathrm{e}^{\mathrm{i}\vartheta} a_1^\dagger a_L, \\ \mathcal{P}: \quad & -t_2 \mathrm{e}^{-\mathrm{i}\vartheta} a_L^\dagger a_1 - t_2 \mathrm{e}^{\mathrm{i}\vartheta} a_1^\dagger a_L \quad \to \quad -t_2 \mathrm{e}^{-\mathrm{i}\vartheta} a_1^\dagger a_L - t_2 \mathrm{e}^{\mathrm{i}\vartheta} a_L^\dagger a_1. \end{aligned} \tag{3.16}$$

Following the argument of the first part of this section, by sweeping the tunneling modulation $\vartheta = 0 \to 2\pi$ the Hamiltonian is transported along a loop in parameter space and the many-particle wave function $|\psi(\vartheta)\rangle$ picks up a Berry phase ν, which according to equation (3.14) is strictly quantized to $\nu = 0, \pi \mod 2\pi$,

$$\nu = \int_0^{2\pi} \left\langle \psi(\vartheta) \middle| \mathrm{i} \frac{\partial}{\partial \vartheta} \psi(\vartheta) \right\rangle \mathrm{d}\vartheta, \tag{3.17}$$

as long as the ground state is unique and gapped during the entire loop.

Figure 3.4 shows numerical results for the generalized winding number of the MI phases of a SL-BHM ($L = 8$) for the two different dimerization configurations. It is easy to

convince oneself of the fact that the ground state of an integer MI phase is always topologically trivial, as it can be written as a product of single-site states – for instance the MI state with $\rho = 1$, $|\psi_1^{\mathrm{MI}}(\vartheta)\rangle = \prod_{j=1}^{L} a_j^\dagger |0\rangle$, which clearly does not pick up any phase when the twisted boundary is modulated, and therefore $\nu = 0$. Similarly, the ground state of the $\rho = 1/2$ MI can be approximated by an (unnormalized) product state of dimers in the "singlet" configuration, given either by $|\psi_{1/2}^{\mathrm{MI}}(\vartheta)\rangle \sim \prod_{j=1}^{M}(a_{2j-1}^\dagger - a_{2j}^\dagger)|0\rangle$ (topologically trivial dimerization, compare upper panel of figure 2.4b), or $|\psi_{1/2}^{\mathrm{MI}}(\vartheta)\rangle \sim \prod_{j=1}^{M}(a_{2j-1}^\dagger - a_{2j}^\dagger)(a_L^\dagger + \mathrm{e}^{\mathrm{i}\vartheta} a_1^\dagger)|0\rangle$ (nontrivial dimerization, see lower panel of figure 2.4b), which picks up a phase of $\nu = \pi$ if the modulated bond corresponds to a strong one that hosts a dimer state.

To illustrate this in more detail consider only one double-well with a twisted tunneling amplitude $t_2 \mathrm{e}^{\mathrm{i}\vartheta}$. In the single-particle limit with basis states $|1,0\rangle, |0,1\rangle$, this is a simple matrix model,

$$\boldsymbol{H} = -\begin{pmatrix} 0 & t_2 \mathrm{e}^{-\mathrm{i}\vartheta} \\ t_2 \mathrm{e}^{\mathrm{i}\vartheta} & 0 \end{pmatrix} \tag{3.18}$$

with ground state $|\psi_-(\vartheta)\rangle = \frac{1}{\sqrt{2}}(|1,0\rangle + \mathrm{e}^{\mathrm{i}\vartheta}|0,1\rangle)$. Computing ν in the sense of equation (3.17) delivers the desired result,

$$\nu = \int_0^{2\pi} \left\langle \psi_-(\vartheta) \middle| \mathrm{i}\frac{\partial}{\partial\vartheta}\psi_-(\vartheta) \right\rangle \mathrm{d}\vartheta = \pi. \tag{3.19}$$

This example demonstrates another aspect leading to a more profound understanding of how the generalization of the Zak phase is accomplished. Note that the model Hamiltonian (3.18) corresponds *directly* to the Bloch Hamiltonian of the SSH model, equation (2.8). Thus, the transport through the Brillouin zone varying the momentum k can also be interpreted as twisting the tunneling amplitudes t_2 of a periodic unit cell.

Physically ϑ corresponds to a magnetic flux threading the system [15] and the complex tunneling amplitudes can be engineered by application of an external magnetic field $\underline{B} = \underline{\nabla} \times \underline{A}$ to an optical lattice modifying the tunneling amplitude t between two lattice sites located at positions $\underline{x}_i, \underline{x}_j$ as

$$t \to t \exp\left(\mathrm{i}\int_{\underline{x}_i}^{\underline{x}_j} \underline{A} \cdot \mathrm{d}\underline{x}\right), \tag{3.20}$$

which is known as *Peierls substitution* [47, 48].

To conclude some comments about a possible experimental realization of a system in which edge states can be observed, as proposed in [15], are in order. Topologically protected edge states may not only arise at an open boundary of a topologically nontrivial system ($\nu \neq 0$), but more generally at any boundary with a change $\Delta\nu$ in the topological

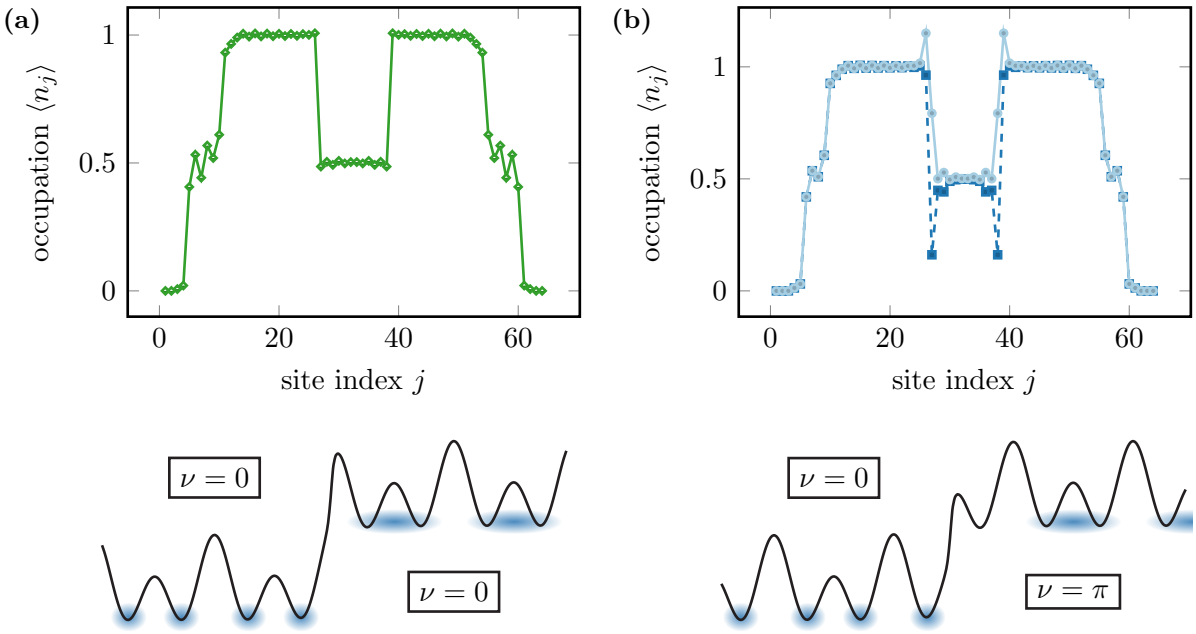

Figure 3.6.: Ground state lattice occupation of an experimentally realizable setup for the observation of edge states at internal domains of MI phases with different topological properties (reproduced from [15]). The system length is $L = 64$ and the on-site potential is a step potential at the centered 12 sites superimposed with a centered harmonic on-site potential $\epsilon_j = \omega(j - j_{\text{center}})^2$ with $\omega/U = 0.001$. DMRG parameters are $D = 5$ and $\Delta\varepsilon < 10^{-9}$. (a) Top panel: $t_1/U = 0.04, t_2/U = 0.2, \Delta\epsilon/U = 0.6$. The interface between the two MI phases in the center does not show edge states. Bottom panel: Sketch of the interface between the $\rho = 1$ (left) and $\rho = \frac{1}{2}$ (right) MI phase. No boundary effects are expected as both phases are topologically trivial. (b) Top panel: $t_1/U = 0.2, t_2/U = 0.04$ for different potential heights $\Delta\epsilon/U = 0.6$ (occupied edge), $\Delta\epsilon/U = 0.7$ (unoccupied edge). The interface is located at a strong bond such that the interior MI phase is topologically nontrivial and edge states appear in form of a localized particle or hole. Bottom panel: Sketch of the situation in terms of potentials. The site at the boundary may be occupied (particle, circular symbols) or unoccupied (hole, rectangular symbols).

invariant. So far a special case under consideration has been the boundary between the vacuum ($\nu = 0$) and a topologically nontrivial system. But it is also possible to observe edge states at internal domain walls, such as a boundary between an integer ($\nu = 0$) and a nontrivial half integer ($\nu = \pi$) MI phase. Such domains form when the SL-BHM is exposed to an external step potential $\epsilon_j = \Delta\epsilon\Theta\left(|j - j_{\text{center}}| - j_{\text{step}}\right)$ governing the $2j_{\text{step}}$ central lattice sites around the center position j_{center}, which could be realized by the admixture of a second species of particles [49]. In figure 3.6 the ground states of such a setup are shown, using the same system parameters as in the original publication [15]. Due to the step potential an internal boundary between two different MI phases arises. If the interface is located at a weak bond, such that the $\rho = 1/2$ MI phase is topologically trivial ($\nu = 0$), no edge states appear (figure 3.6b). If instead the domain wall between the two regimes is located at a strong bond and therefore the interior MI

phase is characterized by $\nu = \pi$, edge states with a localized particle or hole, depending on the potential step height, emerge at the interface (figure 3.6a).

It is the purpose of this work to investigate the influence of dissipative effects on the topological edge states of the SL-BHM. As all systems have so far been described by a Hamiltonian which leads to a unitary evolution in time without dissipation, the following chapter is dedicated to two frameworks that allow for the introduction of dissipation.

Chapter review

- The SL-BHM is the generalization of the SSH model to interacting bosons and reduces to the latter in the limit of hard-core bosons ($U \to \infty$) and low energies. Its ground state phase diagram hosts gapped integer and half-integer MI phases. While the integer MI ground state is always topologically trivial, the half integer MI can possess topological order, which can be regarded as inherited from the SSH model and is indicated by edge states at boundaries at which the topological invariant changes.
- A generalization of the Zak phase for the interacting case can be accomplished by employing twisted boundary conditions on the tunneling amplitude between the first and last site of an open chain, which respects the symmetry of the system. The generalized winding number ν is quantized to $\nu = 0, \pi \mod 2\pi$ because the SL-BHM is inversion-symmetric and thus the appropriate antiunitary symmetry needed to follow the argument of Hatsugai [46] is $\mathcal{PT}$ symmetry.

4. Gain and loss

This chapter presents the methods of how to include dissipative effects in the description of lattice models that are studied in the course of this work.

When dealing with open (in the sense of dissipative) quantum systems the object of interest is usually given by the system's density matrix ρ. Frequently, dissipation is introduced by extending the von Neumann equation governing the unitary evolution of ρ with collapse operators in Lindblad form, which preserve the physical constraints of ρ in the time evolution and model dissipative effects such as many-body recombinations, phase noise or localized particle gain and loss leading to a master equation in Lindblad form. Section 4.1 provides a brief overview of this modification of the unitary evolution, referring the interested reader to the literature [50].

Interestingly the action of the Lindblad operators studied in this work can effectively be replaced by complex on-site potentials in the mean-field limit and offers a way to stay in the wave function picture, however by paying the price of a non-Hermitian Hamiltonian. Since the discovery of Bender and Boettcher [11] that the requirement of a Hermitian Hamiltonian may be relaxed to a weaker condition, namely the Hamiltonian being $\mathcal{PT}$-symmetric, the development of a framework for the treatment of such non-Hermitian Hamiltonians has been triggered [51]. All necessary aspects of this extension of Hermitian quantum mechanics will be discussed in section 4.2.

4.1. Master equations in Lindblad form

The effect of dissipation in a system manifests itself in the evolution of a pure quantum state $|\psi\rangle$. In case of a unitary time evolution generated by a Hermitian Hamiltonian in the Schrödinger equation, the system's exploration of the Hilbert space $\mathscr{H}$ is often severely restricted to the subspace spanned by the contributing eigenvectors in the decomposition of $|\psi\rangle$. On the contrary, this does not hold in the dissipative scenario. An arbitrary state may couple to different dissipative channels that may eventually eliminate any trace of the original quantum state the system has been prepared in. Therefore the description of a quantum state by a wave function has to be extended to a representation that is capable of describing an ensemble of mixed states in the context of open quantum systems.

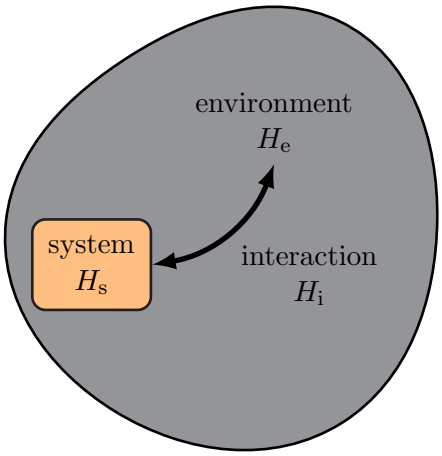

Figure 4.1.: Total system (universe) composed of a system (s) of interest and the remaining part acting as an environment (e). Both building blocks are described by a Hermitian Hamiltonian $H_\mathrm{s}, H_\mathrm{e}$, respectively. As the interest shall only be on the subsystem, the environment can be considered to introduce dissipative effects due to the interaction between system and bath described by the interaction Hamiltonian H_i leading to the form of the total Hamiltonian, see equation (4.5).

The density matrix $\rho \in L(\mathscr{H})$ is a linear positive-semidefinite Hermitian operator on the Hilbert space $\mathscr{H}$. For a finite-dimensional Hamiltonian $H \in L(\mathscr{H})$ with eigenstates $\{|\psi_j\rangle\}$, the most general form of the density matrix is given by

$$\rho = \sum_{j,k} \rho_{jk} \, |\psi_j\rangle\langle\psi_k| \,, \tag{4.1}$$

where the coefficents ρ_{jk} are constrained by $\rho_{jk} = \rho^*_{kj}$ (Hermiticity) and that all eigenvalues of the matrix $\boldsymbol{\rho}$ with $(\boldsymbol{\rho})_{jk} = \rho_{jk}$ are non-negative (positive semi-definite). The density matrix of a statistical ensemble of classically superimposed states with real probabilities p_j completely free of any quantum-mechanical entanglement reads

$$\rho = \sum_{j} p_j \, |\psi_j\rangle\langle\psi_j| \,, \tag{4.2}$$

implying $\mathrm{Tr}\{\rho\} = \sum_j p_j = 1$ because of the probabilistic interpretation. Moreover, the quantity $0 < \mathrm{Tr}\{\rho^2\} = \sum_j p_j^2 \leq 1$ can be employed to classify the purity of the mixed state described by ρ as $\mathrm{Tr}\{\rho^2\} = 1$ for a pure state whereas $\mathrm{Tr}\{\rho^2\} < 1$ in a mixed ensemble. Following the notion of equation (4.2) the expectation value $\langle A\rangle$ of an observable A is evaluated by computing

$$\langle A\rangle = \sum_{j} p_j \, \langle\psi_j \,|\, A\psi_j\rangle = \mathrm{Tr}\{\rho A\} \,. \tag{4.3}$$

To see how dissipative effects can be accounted for in the density matrix formulation consider a total system whose evolution in time is given by a Hamiltonian H (see the sketch in figure 4.1). The actual interest (for instance in observables) shall only be on a small *subsystem* of this *universe* such that the remaining part can be regarded as an *environment*, which due to couplings between bath and system imposes dissipation on

the system of interest. The time evolution of the universe's density matrix ρ is dictated by the *von Neumann equation* (setting $\hbar = 1$),

$$\frac{\mathrm{d}\rho}{\mathrm{d}t} = -\mathrm{i}\,[H, \rho]\,. \tag{4.4}$$

The Hamiltonian acting on the universe's Hilbert space $\mathscr{H}$ that may be decomposed into the system and environmental spaces $\mathscr{H} = \mathscr{H}_\mathrm{s} \otimes \mathscr{H}_\mathrm{e}$ takes the form

$$H = H_\mathrm{s} \otimes \mathbb{1}_\mathrm{e} + \mathbb{1}_\mathrm{s} \otimes H_\mathrm{e} + H_\mathrm{i}. \tag{4.5}$$

Imagine H_s to be given by one of the Hamiltonians presented in chapters 2 and 3. Expectation values of system observables given by operators $A \otimes \mathbb{1}_\mathrm{e}$ are computed via

$$\langle A \otimes \mathbb{1}_\mathrm{e} \rangle = \mathrm{Tr}\{(A \otimes \mathbb{1}_\mathrm{e})\,\rho\} = \mathrm{Tr}_\mathrm{s}\{A\mathrm{Tr}_\mathrm{e}\{\rho\}\} \equiv \mathrm{Tr}_\mathrm{s}\{A\rho_\mathrm{s}\} \tag{4.6}$$

introducing the *reduced density matrix ρ_s of the system*, which is obtained by partially tracing out all degrees of freedom of the environment of ρ, that is $\rho_\mathrm{s} \equiv \mathrm{Tr}_\mathrm{e}\{\rho\}$. It would thus be desirable to compute $\rho_\mathrm{s}(t)$. Partially taking the trace of equation (4.4) over the environment the resulting equation of motion reads

$$\frac{\mathrm{d}\rho_\mathrm{s}}{\mathrm{d}t} = -\mathrm{i}\mathrm{Tr}_\mathrm{e}\{[H, \rho]\}\,. \tag{4.7}$$

Based on assumptions concerning the nature of the reservoir equation (4.7) can be simplified. Without going too much into detail the approximation of a bath with short-lived memory (*Markovian approximation*), which is large enough to stay unaffected over time as well as a weak coupling between system and environment (*Born approximation*) shall be explicitly mentioned here. For a more complete presentation, the interested reader may take a look at reference [50].

Working out all approximations leads to a *master equation in Lindblad form* [12],

$$\frac{\mathrm{d}\rho_\mathrm{s}}{\mathrm{d}t} = -\mathrm{i}\,[H_\mathrm{s}, \rho_\mathrm{s}] + \frac{1}{2}\sum_\mu \left(2L_\mu \rho_\mathrm{s} L_\mu^\dagger - \left\{L_\mu^\dagger L_\mu, \rho_\mathrm{s}\right\}\right) \equiv \hat{\mathcal{L}}\rho_\mathrm{s}, \tag{4.8}$$

which is the most general form preserving the trace and positivity of ρ_s. Note that the first term is equivalent to the von Neumann equation (4.4), thus generating the unitary evolution of the reduced density matrix. The second term models dissipative processes and is parameterized by a number of *Lindblad operators* (or *collapse operators*) L_μ, whose choice may depend on the physical processes they account for. The L_μ are a remnant of the interaction between bath and system, which has effectively been integrated out. Common choices include $L_\mu = \sqrt{\gamma}(a_\mu)^3$ for three-body recombinations, $L_\mu = \sqrt{\gamma}(a_\mu)^2$ for two-body losses by inelastic collisions or $L_\mu = \sqrt{\gamma}a_\mu^\dagger a_\mu$ modeling phase noise (for a complete list and considerations towards experimental realizations see [52]). In this work

the influence of single-particle gain (loss) described by collapse operators $L_\mu = \sqrt{\gamma} a_\mu^\dagger$ ($\sqrt{\gamma} a_\mu$) will be investigated. The coupling strength γ will be referred to as *gain* or *loss parameter*. Before proceeding by reviewing the two simplest models subject to such dissipative processes some more comments about equation (4.8) are made.

First, the influence of the environment on the system can be interpreted in terms of the reservoir *performing measurements* on the system thereby leading to a collapse of the system's wave function, which is called a *quantum jump*. In fact, the adoption of this view has triggered the development of numerical methods for the treatment of dissipative quantum systems such as the quantum Monte Carlo wave function method [53], that stochastically determines the event of a quantum jump by non-Hermitian evolution of a wave function with an effective Hamiltonian $H_{\text{eff}} = H_{\text{s}} - \mathrm{i}/2 \sum_\mu L_\mu^\dagger L_\mu$. Performing many iterations starting off with the same wave function and randomly applying quantum jumps according to the rule of the algorithm yields a set of *quantum trajectories* that can be averaged in order to obtain observables.

Second, the Lindblad equation (4.8) may be viewed as an operator equation in terms of a linear non-Hermitian operator $\hat{\mathcal{L}}$, which is called the *Liouville operator* (or *Liouvillean*) and encodes the information of the open quantum system. There exist interesting analytical approaches for treating ρ_{s} and $\hat{\mathcal{L}}$, two of which have also been employed in the course of this work and are summarized in appendices B and C. Mostly, the interest is on observables of the state that is approached in the long time limit, in which the system has thermalized with the reservoir. This *non-equilibrium steady state (NESS)* can be considered a right eigenstate of the Liouvillean with eigenvalue zero but for now it suffices to be aware of the terminology and more details will be covered in future chapters that deal with the computation and investigation of those states.

Note as well that it is commonly accepted to drop the system indices in equation (4.8) in the context of open quantum systems, which will be done in the following.

Let us now have a look at the two simplest scenarios, which however are of high importance to illustrate the approach taken in the next section – a single site with localized particle loss (gain) as has been worked out in [54, 55]. The Lindblad equation of a single site characterized by a Bose-Hubbard Hamiltonian with particle loss described by a collapse operator $L = \sqrt{\gamma} a$ is given by

$$\frac{\mathrm{d}\rho}{\mathrm{d}t} = \frac{\gamma}{2} \left(2a\rho a^\dagger - a^\dagger a \rho + \rho a^\dagger a \right). \tag{4.9}$$

Inserting the most general allowed ansatz,

$$\rho(t) = \sum_{j=0}^{\infty} p_j(t) \, |j\rangle\langle j| \tag{4.10}$$

with orthogonal Fock states $|j\rangle$ and the constraint that $\sum_j p_j(t) = 1$, leads to the following coupled system of equations,

$$\frac{\mathrm{d}p_j}{\mathrm{d}t} = \gamma\left[(j+1)p_{j+1} - jp_j\right]. \tag{4.11}$$

The total particle number expectation value $n(t) \equiv \mathrm{Tr}\{\rho(t)n\} = \sum_{j=0}^{\infty} jp_j(t)$ on the single site is obtained by inspection of its time derivative using relation (4.11),

$$\frac{\mathrm{d}n}{\mathrm{d}t} = \sum_{j=0}^{\infty}\frac{\mathrm{d}p_j}{\mathrm{d}t}j = \sum_{j=0}^{\infty}\gamma\left[(j-1)jp_j - j^2p_j\right] = -\gamma n, \tag{4.12}$$

implying an exponential decay $n(t) = n(0)\mathrm{e}^{-\gamma t}$ of the particle number.

In the same manner a result for the evolution of the particle number on a single site subject to single-particle gain modeled by a Lindblad operator $L = \sqrt{\gamma}a^\dagger$ can be derived yielding $n(t) = [n(0)+1]\,\mathrm{e}^{\gamma t} - 1$ (see [55]) which is approximately given by $n(t) \approx n(0)\mathrm{e}^{\gamma t}$ in the limit of large initial particle numbers.

It is a crucial point that the mean-field limit of single-particle gain (loss) corresponds to an exponential increase (decay) of the particle number at the rate of the gain (loss) parameter γ. This aspect may be reinterpreted by including the fact that adding a complex potential ${}^{+}_{(-)}\mathrm{i}\gamma/2$ in a discretized Schrödinger equation of a Bose-Einstein condensate, whose wave function is described by a single component $c(t)$, leads to exactly the same behavior as the Schrödinger equation reads

$$\mathrm{i}\frac{\mathrm{d}c}{\mathrm{d}t} = {}^{+}_{(-)}\mathrm{i}\frac{\gamma}{2}c, \tag{4.13}$$

resulting in $n(t) = n(0)\,|c(t)|^2 = n(0)\exp\left({}^{+}_{(-)}\gamma t\right)$. This outcome can be seen as a motivation to study dissipative effects (also away from the mean-field limit) by introduction of *complex on-site potentials* in the model setup. Speaking in terms of the SL-BHM, the Hamiltonian (3.1) in second quantization is to be modified by additional complex on-site terms ϵ_j. However, in doing so the price to be paid is the Hamiltonian losing its Hermiticity. However, Hermiticity is an important property since it guarantees reality of the eigenvalues and physical observables as well as orthogonality of the eigenstates.

4.2. Non-Hermitian quantum mechanics

In the last decades, a lot of progress towards the understanding and extension of quantum mechanics to non-Hermitian theories has been made [19, 20, 56]. In particular, the discovery that the Hermiticity of the Hamiltonian guaranteeing an entirely real eigenvalue spectrum in early quantum mechanics can be relaxed to more general conditions

containing also classes of non-Hermitian operators. For instance a necessary condition for the spectrum of an operator to be entirely real is given by *pseudo-Hermiticity* [57–59].

The family of operators considered in this work contains Hamiltonians that commute with the combined action of parity and time reversal operators $\mathcal{P}$ and $\mathcal{T}$, respectively, which are known as $\mathcal{PT}$*-symmetric Hamiltonians*. A system is said to be $\mathcal{PT}$*-symmetric* if its Hamiltonian commutes with $\mathcal{PT}$,

$$[H, \mathcal{PT}] = 0, \tag{4.14}$$

with the defining actions of the parity-time reversal operator on space $\underline{x}$ and momentum operator $\underline{p}$ as well as the imaginary unit i reading

$$\mathcal{PT} \begin{pmatrix} \underline{x} \\ \underline{p} \\ \mathrm{i} \end{pmatrix} \mathcal{PT} = \begin{pmatrix} -\underline{x} \\ +\underline{p} \\ -\mathrm{i} \end{pmatrix}. \tag{4.15}$$

For one-dimensional lattice systems in second quantization as presented earlier this action translates into $\mathcal{P}$ mirroring all sites (and appropriate annihilation/creation operators) at the center of a chain (compare figure 2.1b) while $\mathcal{T}$ performs a complex conjugation. From equation (4.15) it follows that $(\mathcal{PT})^2 = \mathbb{1}$, and thus the eigenvalues $\lambda = \mathrm{e}^{\mathrm{i}\alpha}$ are located on the unit circle.

If a generic Hamiltonian of the form $H = \underline{p}^2/2m + V(\underline{x})$ with a complex potential $V(\underline{x})$ is investigated, demanding that H commutes with $\mathcal{PT}$ (equation (4.14)) imposes the condition $V(\underline{x}) = V^*(-\underline{x})$ on the potential function. The physical consequences of V being a complex function reveal themselves in the *generalized continuity equation* for a wave function $\psi(\underline{r}, t)$ in position space representation [55] ($\hbar = 1$),

$$\frac{\partial}{\partial t} \left|\psi(\underline{r}, t)\right|^2 + \underline{\nabla} \cdot \underline{j}(\underline{r}, t) = 2 \left|\psi(\underline{r}, t)\right|^2 \mathrm{Im}(V(\underline{r})), \tag{4.16}$$

with $\underline{j} = \mathrm{i}\left(\psi \underline{\nabla} \psi^* - \psi^* \underline{\nabla} \psi\right)/2m$ denoting the current density of probability. Equation (4.16) reduces to the familiar continuity equation if the right side equals zero. One can reinterpret this relation in terms of positive (negative) imaginary parts of V accounting for a source (sink) of the wave function's probability, which corresponds to dissipation.

Interestingly, the eigenvalues of a non-Hermitian Hamiltonian fulfilling equation (4.14) can be real and correspond to stationary modes. To see this, consider the eigenvalue equation $H\left|\psi\right\rangle = E\left|\psi\right\rangle$, where $\left|\psi\right\rangle$ is an eigenvector of the parity-time reversal operator $\mathcal{PT}\left|\psi\right\rangle = \lambda\left|\psi\right\rangle$, multiplied by $\mathcal{PT}$. It follows that

$$\begin{aligned} \mathcal{PT}H\left|\psi\right\rangle &= \left(\mathcal{PT}E\mathcal{PT}\right)\mathcal{PT}\left|\psi\right\rangle, \\ E\lambda\left|\psi\right\rangle &= E^*\lambda\left|\psi\right\rangle, \end{aligned} \tag{4.17}$$

and since $\lambda \neq 0$ the eigenvalue $E = E^*$ is inevitably real, $E \in \mathbb{R}$, for relation (4.17) to hold. Note that this is *not generally* true as $|\psi\rangle$ is required to be an eigenvector of both the Hamiltonian and the $\mathcal{PT}$ operator. In total the following statements hold for a $\mathcal{PT}$-symmetric system [20]:

1. If all eigenstates of a $\mathcal{PT}$-symmetric Hamiltonian (in the sense of equation (4.14)) are also eigenstates of $\mathcal{PT}$, the eigenvalue spectrum is completely real and the $\mathcal{PT}$ symmetry of H is said to be *unbroken*. The inverse of this statement is also valid.

2. In the case of one or more eigenstates of H violating the eigenvalue equation of with $\mathcal{PT}$, the $\mathcal{PT}$ symmetry of H is said to be *broken*.

3. Eigenvalues of a $\mathcal{PT}$-symmetric Hamiltonian come in complex conjugate pairs and respective eigenstates are related by the action of $\mathcal{PT}$, i.e. if $H|\psi\rangle = E|\psi\rangle$, then $\mathcal{PT}|\psi\rangle$ is eigenvector with eigenvalue E^* as $H\mathcal{PT}|\psi\rangle = \mathcal{PT}H|\psi\rangle = E^*\mathcal{PT}|\psi\rangle$.

The approach taken in this work is motivated by the analogy between Lindblad operators and complex on-site potentials in the mean-field limit (see figure 6.1). The introduction of such terms respecting the $\mathcal{PT}$ symmetry of the Hamiltonian is *applied as* an *effective theory* to introduce gain and loss effects, meaning that all quantities (for instance expectation values) are evaluated in the sense of the Hermitian framework. While the regime of unbroken $\mathcal{PT}$ symmetry corresponds to the system having stationary modes stabilized by currents the interpretation of broken $\mathcal{PT}$ symmetry is a subtle point, which has to be carefully investigated and compared to results obtained from Lindblad equations which is left for future chapters.

Before concluding, some final remarks towards the generalization of the treatment of complex non-Hermitian Hamiltonians are necessary to understand what follows. Although the loss of Hermiticity does not necessarily lead to complex observables, an outstanding problem to cure is that the eigenstates lose orthogonality and therefore common projection techniques are spoiled. Moreover, the evolution of a state $|\psi\rangle$ is not unitary in the sense that the norm $\langle\psi(t)\,|\,\psi(t)\rangle$ is conserved. Fortunately, all known concepts like Hermiticity, unitarity, quantum probabilities and the computation of expectation values (to name only a few) can be carried over by working in a biorthogonal basis manifesting the field of *biorthogonal quantum mechanics* [51, 57–59].

In the latter the subject of investigation is a complex finite-dimensional Hamiltonian $K = H - \mathrm{i}\Gamma$ (to distinguish from previous statements) consisting of two Hermitian operators $K = K^\dagger, \Gamma = \Gamma^\dagger$. A necessary condition for the operator to be *biorthogonally Hermitian* (or *η-pseudo-Hermitian*) is given by the relation [51, 57–59]

$$K^\dagger = \eta K \eta^{-1}, \tag{4.18}$$

where η effectively acts as a metric (see text below equation (4.21)). The *right (left) eigenvectors* $|\phi_j\rangle$ ($|\chi_j\rangle$) of K with *right (left) eigenvalues* κ_n (ν_n) are defined by the

relations

$$\begin{aligned} K\,|\phi_j\rangle &= \kappa_j\,|\phi_j\rangle\,, \\ K^\dagger\,|\chi_j\rangle &= \nu_j\,|\chi_j\rangle\,. \end{aligned} \tag{4.19}$$

This is a generalization of the Hermitian scenario where $|\chi_j\rangle = |\phi_j\rangle$. The need to extend the basis of states in this way is triggered by the observation that the orthogonality relation between right eigenstates known from Hermitian quantum mechanics does not hold anymore, that is $\langle\phi_j\,|\,\phi_k\rangle \neq 0$ for $j \neq k$. Of course, the same holds for the left eigenstates. However, if the eigenvalue is assumed to be non-degenerate, then without loss of generality the eigenvalues can be labeled as $\kappa_j = \nu_j^*$ and it may be shown that the following *biorthogonality relation* between left and right eigenvectors holds [51],

$$\langle\chi_j\,|\,\phi_k\rangle = \delta_{jk}\,\langle\chi_j\,|\,\phi_j\rangle\,. \tag{4.20}$$

Taken the same assumptions it can be shown that the eigenstates $|\phi_j\rangle$ are linearly independent and span the Hilbert space $\mathscr{H}$. Equation (4.20) is the key for the aforementioned generalizations of Hermitian quantum mechanics. A detailed description shall be avoided here but the storyline in reference [51] starts from the observation that the operator $\Pi_j = |\phi_j\rangle\langle\chi_j| \,/\, \langle\chi_j\,|\,\phi_j\rangle$ acts as a projector onto the state $|\phi_j\rangle$ and the Hamiltonian K may therefore be expressed as follows,

$$K = \sum_j \kappa_j \Pi_j = \sum_j \kappa_j\,|\phi_j\rangle\langle\chi_j|\,, \tag{4.21}$$

where the normalization convention $\langle\chi_j\,|\,\phi_j\rangle = 1$ has been adopted. Defining a *duality relation* between $\mathscr{H}$ and its dual space $\mathscr{H}^\star$ such that if $|\psi\rangle = \sum_j c_j\,|\phi_j\rangle \in \mathscr{H}$, then the dual element is given by $\langle\tilde{\psi}| = \sum_j c_j^*\,\langle\chi_j| \in \mathscr{H}^\star$ leads to $\langle\psi,\psi\rangle \equiv \langle\tilde{\psi}|\psi\rangle = \langle\psi|\eta\psi\rangle = \sum_j |c_j|^2 = 1$ due to equation (4.20) [51]. Long story short, a generalization of Hermitian quantum mechanics can be performed by properly replacing projectors and scalar products by the respective biorthogonal extensions.

The interested reader is invited to identify the Hermitian equivalents of equations (4.19)-(4.21) as well as in the remaining techniques generalized in reference [51].

Chapter review

- The treatment of open quantum systems is usually based on the density operator, ρ which is capable of describing mixed quantum states.
- The most general form of an equation of motion for a dissipative system preserving positivity and the trace of ρ is given by a master equation in Lindblad form (4.8). It

can be derived by effectively integrating out all environmental effects of a universe system when the interest is only on a small subsystem based on the assumption of a Markovian reservoir and additional approximations.

➢ The mean-field limit of a single lattice site with single-particle gain (loss) with collapse operator $L = \sqrt{\gamma}a^\dagger$ ($\sqrt{\gamma}a$) corresponds to an exponential increase (decay) in particle number at the rate γ. The same behavior is obtained by adding a complex-valued potential ${}_{(-)}^{+}\mathrm{i}\gamma/2$ to a discretized Schrödinger equation. Complex on-site potentials will be used as an effective description for gain and loss also away from the mean-field limit leading to non-Hermitian Hamiltonians.

➢ It is known that non-Hermitian Hamiltonians may also possess entirely real eigenvalues leading to an extension of early quantum mechanics. The family of $\mathcal{PT}$-symmetric operators is a class of Hamiltonians exhibiting such behavior. More generally, the treatment of non-Hermitian Hamiltonians can be formalized by use of a biorthogonal basis consisting of their left and right eigenvectors $|\phi_j\rangle, |\chi_j\rangle$.

5. Numerical treatment of 1D bosonic many-body systems

Despite the fact that it is the process of interaction between particles leading to such a diversity in nature the investigation of such systems both analytically and numerically is complicated for different reasons. In the quantum-mechanical scenario analytical approaches are restricted to special cases or perturbative results – one reason for this being that in the presence of interactions the system properties cannot be analyzed by sole investigation of a single particle but rather the *complete* basis has to be considered. Numerical methods are in most cases restricted to only a few lattice sites as the dimension of the Hilbert space increases exponentially. Nevertheless, this field has pushed its frontiers further in recent decades and by now numerical methods provide promising techniques to gain a deeper understanding of interacting many-body systems. The following chapter presents the most important numerical recipes employed in this work.

Section 5.1 starts with the simplest "brute force" approach of setting up the Hamiltonian matrix from which all system properties can be derived. In fact an iterative scheme of this procedure will be presented, whose limitation however is given by the exponential increase of the problem dimension.

One outcome of attempts to cure the problem of dimensionality is the celebrated *density matrix renormalization group method (DMRG)*, whose understanding and generalization has been under ongoing progress since its proposal by White in 1992 [16]. Therefore, the amount of literature is huge (for reviews see [17, 18] and references therein) and the knowledge required to understand recently developed techniques (formulated in the more general framework of *tensor network states* [60] but roughly pursuing the same goal as the "old-fashioned" algorithm) go beyond the scope of this work. Section 5.2 will give a brief description of the main DMRG techniques for Hermitian Hamiltonians used in this work adopting the language of White, thereby avoiding the terminology of tensor network states or matrix product states (MPS). Interested readers without experience in DMRG may want to consult the very comprehensible introduction [61] and this[1] Python code collection of basic DMRG algorithms consisting of only a few hundred commented lines including the most popular optimization techniques.

[1] https://github.com/simple-dmrg/simple-dmrg

Since one main goal of this work includes the investigation of gain and loss introduced by complex on-site potentials causing the Hamiltonian to be non-Hermitian a possible extension of DMRG to non-Hermitian systems is presented in section 5.3. Works on such extensions are found in quantum chemistry [62, 63] as well as in the study of non-equilibrium systems, which for instance account for diffusive processes [64–68]. To the best of the author's knowledge, this work is the first to deliberately employ the algorithm for the study of $\mathcal{PT}$-symmetric quantum systems.

Practically, having implemented the DMRG method for non-Hermitian operators also allows for the algorithm to be used for the investigation of master equations in Lindblad form. Different methods forming the solid foundation of this goal have been proposed in [69–71] and the purpose itself is still a task under ongoing research and has only recently been tackled in an approach similar to that one taken in this work, but based on the framework of MPS [72]. Section 5.4 presents a method based on the non-Hermitian DMRG algorithm allowing for the investigation of steady state properties of master equations in Lindblad form sticking to the "traditional" terminology of White, thus requiring no prior knowledge of the MPS framework. The focus of both sections 5.3 and 5.4 will be on necessary adaptions of a working Hermitian DMRG code for readers willing to extend their own.

Throughout this chapter the introduced techniques of DMRG will be pointed towards the SL-BHM as it plays the central role in this work. For a more general overview the reader is referred to the reviews [17, 18]. Although effort has been put into finding existing code for reuse and extension, the author is currently not aware of an existing code implementing the presented strategy *without* adopting the terminology of MPS.

5.1. Exact diagonalization

Reconsider the Hamiltonian of the SL-BHM (equation (3.1)),

$$\begin{aligned} H = &- \sum_{j \text{ odd}} \left(t_1 a_j^\dagger a_{j+1} + \text{h.c.} \right) - \sum_{j \text{ even}} \left(t_2 a_j^\dagger a_{j+1} + \text{h.c.} \right) \\ &+ \frac{U}{2} \sum_j n_j \left(n_j - 1 \right) + \sum_j (\epsilon_j - \mu) n_j \\ \equiv &\sum_j T_{j,j+1} + \sum_j V_j, \end{aligned} \tag{5.1}$$

which shall be repeated for completeness here with all terms acting on the same sites collected in the last equality emphasizing the *locality* of the Hamiltonian, as the SL-BHM only consists of nearest neighbor tunneling ($T_{j,j+1}$) and on-site processes (V_j). It is this property which leads to an efficient recursive scheme for building up the Hamiltonian

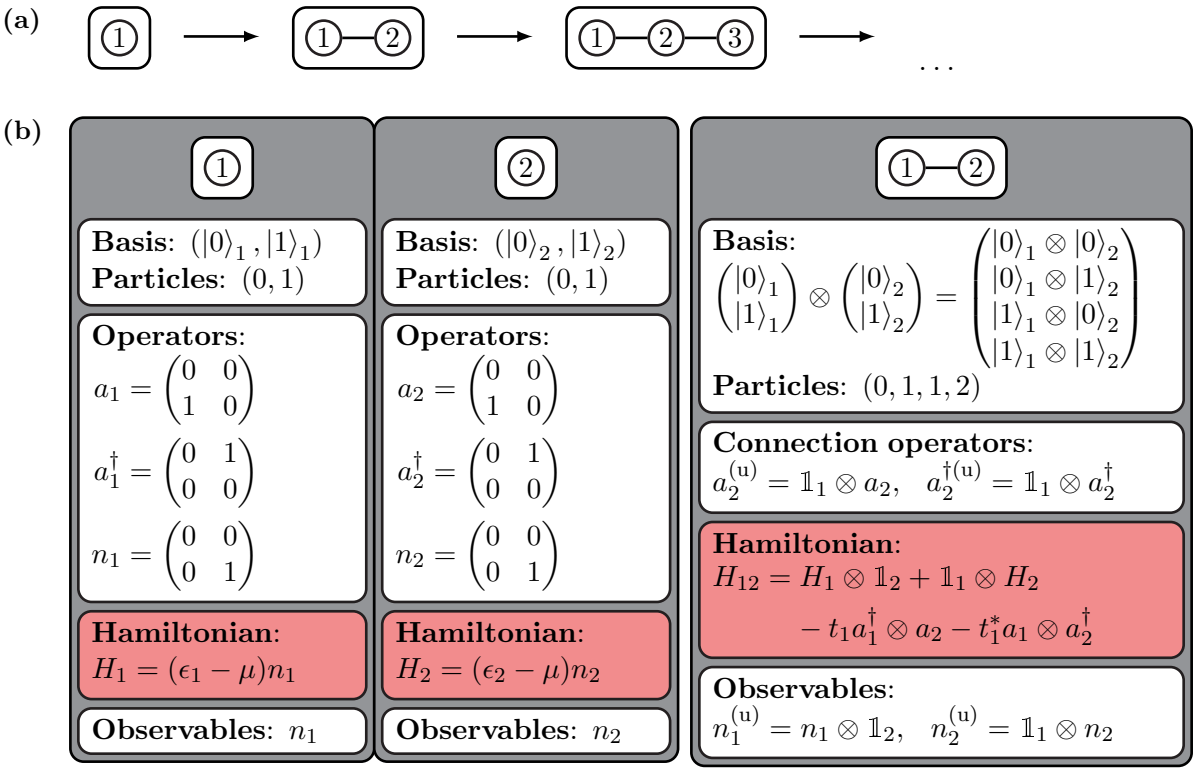

Figure 5.1.: Build-up scheme of lattice sites in exact diagonalization. (a) Starting from a block containing only one lattice site, the latter is consecutively enlarged by adding another single site until the desired system length is reached. (b) Detailed description of an enlargement process with local site dimension $D = 2$ including implementation details such as particle numbers of the basis vectors, operators required for the enlargement and observables to be measured after the build-up. The connection rule for the Hamiltonian is highlighted in red.

matrix of a one-dimensional chain of L lattice sites, as one can imagine this process as starting from a single site adding contiguous sites until the desired system length is reached (compare figure 5.1a). In the language of DMRG one speaks of a *block* consisting of one (or multiple) site(s) being *enlarged* by a single site. The canonical basis to work with is spanned by the single site particle number Fock states $|j\rangle_k$ denoting the presence of j particles at lattice site k.

As an example, consider a single lattice site labeled 1 with a Hamiltonian $H_1 = V_1$ and the basis $\{|j\rangle_1\}$ being enlarged with a single site labeled 2 represented by the Hamiltonian $H_2 = V_2$ in the basis $\{|k\rangle_2\}$. The enlarged block's basis is then spanned by the *product basis* $\{|j\rangle_1 \otimes |k\rangle_2\}$ of sites 1 and 2 and the Hamiltonian is given by $H_{12} = H_1 \otimes \mathbb{1}_2 + \mathbb{1}_1 \otimes H_2 + T_{12}$ with the identity $\mathbb{1}_\ell$ at site ℓ.

Consequently, this procedure can be applied iteratively recycling the quantities from the blocks being connected. For instance, after two enlargements the Hamiltonian of a three-site composite block (compare figure 5.1a) in the product basis $\{|j\rangle_1 \otimes |k\rangle_2 \otimes |\ell\rangle_3\}$

reads $H_{123} = H_{12} \otimes \mathbb{1}_3 + \mathbb{1}_{12} \otimes H_3 + \mathbb{1}_1 \otimes T_{23}$, where only the last term, the *coupling term* T_{23}, cannot be directly constructed by recycling of the former block Hamiltonians.

Numerical treatment requires the introduction of a *cutoff* D of the local Hilbert space dimension. In most scenarios of this work, it suffices to chose $D = 4, 5$ as the low-energy physics of the SL-BHM in the strongly-interacting regime avoid multiple occupation of a single site and D corresponds to the fact that one keeps track of at most $D-1$ particles per site.

To be more illustrative consider another example, namely the enlargement of a single site 1 with local site dimension $D = 2$ represented in the Fock basis $\{|0\rangle_1, |1\rangle_1\}$ by another lattice site 2 with analogous basis as shown in figure 5.1b. With the matrix representation of annihilation, creation and particle number operators at hand their form in the enlarged block 1-2 is simply computed by an outer product "$\otimes$", one representation of which is given by the *Kronecker product*. That said, the coupling term T_{12} in the basis $\{|0\rangle_1 \otimes |0\rangle_2, |0\rangle_1 \otimes |1\rangle_2, |1\rangle_1 \otimes |0\rangle_2, |1\rangle_1 \otimes |1\rangle_2\}$ can be computed by

$$\begin{aligned} T_{12} &= -t_1 a_1^\dagger \otimes a_2 + \text{h.c.} = -t_1 \begin{pmatrix} 0 & 1 \\ 0 & 0 \end{pmatrix} \otimes \begin{pmatrix} 0 & 0 \\ 1 & 0 \end{pmatrix} + \text{h.c.} \\ &= -t_1 \begin{pmatrix} 0 \left(\begin{smallmatrix} 0 & 0 \\ 1 & 0 \end{smallmatrix}\right) & 1 \left(\begin{smallmatrix} 0 & 0 \\ 1 & 0 \end{smallmatrix}\right) \\ 0 \left(\begin{smallmatrix} 0 & 0 \\ 1 & 0 \end{smallmatrix}\right) & 0 \left(\begin{smallmatrix} 0 & 0 \\ 1 & 0 \end{smallmatrix}\right) \end{pmatrix} + \text{h.c.} = -t_1 \begin{pmatrix} 0 & 0 & 0 & 0 \\ 0 & 0 & 1 & 0 \\ 0 & 0 & 0 & 0 \\ 0 & 0 & 0 & 0 \end{pmatrix} + \text{h.c.} \end{aligned} \tag{5.2}$$

and the on-site terms V_1, V_2 as well as the Hamiltonian H_{12} of block 1-2 follow similarly. Continuing this scheme finally leads to the Hamiltonian matrix.

Equation (5.2) already suggests that the final matrix is extremely *sparse* which is (i) due to the locality of the Hamiltonian and (ii) because the Hamiltonian (5.1) conserves the total particle number as it commutes with the operator $\sum_{j=1}^{L} n_j$. The second property causes the Hamiltonian to decompose into block structure, each block only coupling basis states corresponding to the same total particle number. Hence, keeping track of the total particle number of the basis, as indicated in figure 5.1b comes in handy when finally computing for eigenstates of the Hamiltonian matrix employing a *large sparse eigensolver* such as the *implicitly restarted Arnoldi method* provided by the **ARPACK** library [73]. Instead of computing eigenvectors of the entire matrix, cutting and separately diagonalizing the blocks of invariant subspaces leads to a significant speedup.

In view of the next section introducing the idea of DMRG two aspects shall again be stressed before proceeding:

- ➢ The locality of the SL-BHM (equation (5.1)) allows to think of the construction of a system as sticking together single sites or more generally two blocks as indicated by figure 5.2. Whenever two blocks are connected to form a *superblock* of, say length L, the Hamiltonian $H_{1\ldots L}$ of the composite system can be constructed by knowledge of the Hamiltonians $H_{1\ldots\ell}$, $H_{\ell+1\ldots L}$ of both constituents plus the *connection operators*

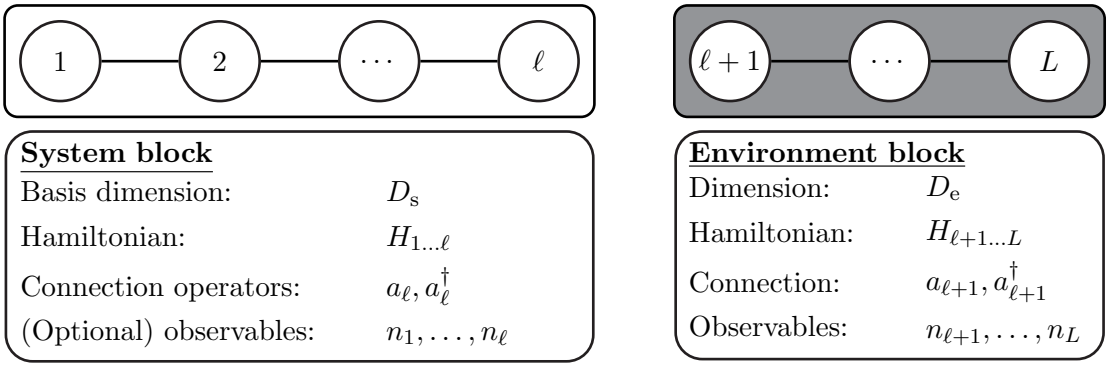

Figure 5.2.: Scheme for connecting two blocks to form a "superblock". For a local Hamiltonian like the SL-BHM the construction of the superblock Hamiltonian $H_{1\ldots L}$ requires knowledge of the composite Hamiltonians $H_{1\ldots\ell}$ and $H_{\ell+1\ldots L}$ as well as the operators contributing in the coupling term $T_{\ell,\ell+1}$. In case of the SL-BHM the hopping term from the left to the right block must have access to the operators $a_\ell, a_\ell^\dagger$ and $a_{\ell+1}, a_{\ell+1}^\dagger$. White blocks will be referred to as *system blocks* in the following, while gray blocks are called *environment blocks* in the spirit of DMRG. The total system is represented by the superblock resulting from the connection of system and environment.

contributing to the coupling term $T_{\ell,\ell+1}$ which are given by the annihilation and creation operators at the sites where the two blocks are joined by a tunneling amplitude, for instance t_1. Consequently this leads to the construction rule

$$H_{1\ldots L} = H_{1\ldots\ell} \otimes \mathbb{1}_{\ell+1\ldots L} + \mathbb{1}_{1\ldots\ell} \otimes H_{\ell+1\ldots L} + \left(t_1 a_\ell^\dagger \otimes a_{\ell+1} + \text{h.c.}\right). \tag{5.3}$$

➢ A drawback of this scheme is that the basis dimension grows rapidly since the Hamiltonian matrix of a chain of length L with single site cutoff D results in D^L basis states corresponding to an *exponentially* increasing problem size. A *compression scheme* has to be found such that the dimensionality stays below numerical limits without losing most of the physical information.

5.2. Hermitian density matrix renormalization group algorithms (DMRG)

The core of DMRG tackles the issue of exact diagonalization from a perspective questioning whether it is necessary to keep all states in a basis when seeking for the ground state of a system. Before justifying that there is indeed a way to truncate the basis without losing important bits of information, the text illustrates underlying ideas first.

Suppose that the total system of interest, a chain of L sites, is constructed by connecting two blocks to a superblock (compare figure 5.2). One block is called the *system block*

while the other is named *environment block*. The state of interest, that is the ground state $|\psi\rangle$ of the superblock, can be expressed in the product basis $|j\rangle_\mathrm{s} \otimes |k\rangle_\mathrm{e} \equiv |j\rangle_\mathrm{s} |k\rangle_\mathrm{e}$ of the system and environment block suppressing the outer product symbol in the following,

$$|\psi\rangle = \sum_{j=1}^{D_\mathrm{s}} \sum_{k=1}^{D_\mathrm{e}} \psi_{jk} |j\rangle_\mathrm{s} |k\rangle_\mathrm{e} , \tag{5.4}$$

with system and environment dimensions $D_\mathrm{s}, D_\mathrm{e}$, respectively. As both dimensions grow exponentially in an exact diagonalization scheme the question to be posed is whether a proper approximation $|\tilde{\psi}\rangle$ of (5.4) can be found by discarding most of the unimportant system block basis states such that the residual norm $\| |\psi\rangle - |\tilde{\psi}\rangle \|^2$ is minimal. The number of *states kept* in the description of the system block is often denoted by m and gives rise to the following form of $|\tilde{\psi}\rangle$ [74],

$$|\tilde{\psi}\rangle = \sum_{\alpha=1}^{m} \sum_{k=1}^{D_\mathrm{e}} \tilde{\psi}_{\alpha k} |\alpha\rangle_\mathrm{s} |k\rangle_\mathrm{e} . \tag{5.5}$$

It turns out that the optimal choice of the states $|\alpha\rangle_\mathrm{s}$ to keep in the description of the system block is given by the orthogonal eigenvectors of the reduced density matrix

$$\begin{aligned} \rho_\mathrm{s} = \mathrm{Tr}_e\{|\psi\rangle\langle\psi|\} &= \sum_{i,j=1}^{D_\mathrm{s}} \sum_{k=1}^{D_\mathrm{e}} \psi_{ik}\psi^*_{jk} |i\rangle_\mathrm{s}\langle j|_\mathrm{s} \\ &\equiv \sum_{i,j=1}^{D_\mathrm{s}} (\boldsymbol{\rho}_\mathrm{s})_{ij} |i\rangle_\mathrm{s}\langle j|_\mathrm{s} \equiv \sum_{\alpha=1}^{D_\mathrm{s}} w_\alpha |\alpha\rangle_\mathrm{s}\langle\alpha|_\mathrm{s} \end{aligned} \tag{5.6}$$

belonging to the m largest eigenvalues $w_{1\ldots m}$, which are assumed to be ordered such that $1 \geq w_1 \geq w_2 \geq \ldots \geq w_{D_\mathrm{s}} \geq 0$ (see also section 4.1 for the properties of the reduced density matrix). This statement can be proofed rigorously (see page 54). Because the eigenvalues satisfy the sum rule $\sum_{\alpha=1}^{D_\mathrm{s}} w_\alpha = 1$, the fidelity of the truncation procedure by discarding all but the first dominant m eigenvalues of ρ_s is given by the *truncation error* ε,

$$\varepsilon = 1 - \sum_{\alpha=m+1}^{D_\mathrm{s}} w_\alpha, \tag{5.7}$$

and if the components ψ_{jk} of the ground state (see equation (5.4)) and analogously $\tilde{\psi}_{jk}$ of the approximation are considered as matrices the residual norm may be evaluated, yielding $\| |\psi\rangle - |\tilde{\psi}\rangle \|^2 = \varepsilon$ [74].

To illustrate this, figure 5.3 shows the eigenvalues of a reduced density matrix of a subsystem with $\ell = 4$ in a total SL-BHM system of $L = 8$ represented exactly (in the

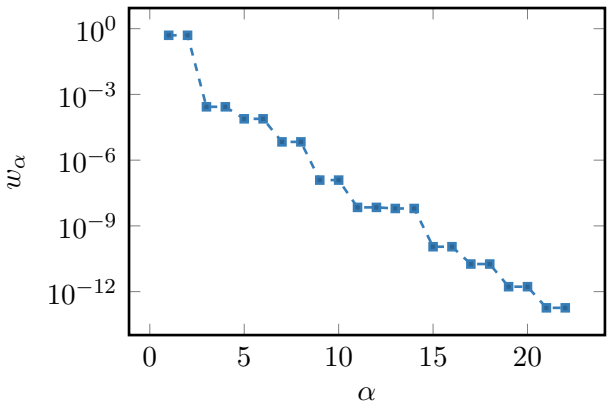

Figure 5.3.: Largest eigenvalues of the reduced density matrix of a subsystem with $\ell = 4$ in a total system of $L = 8$ described by the SL-BHM with system parameters $t_1/U = 0.1, t_2/U = 0.02, \mu/U = 0.02$ and local site dimension $D = 4$. Only the largest of the 64 eigenvalues are shown. The eigenvalues decay rapidly and the system block can be represented to high accuracy by keeping only a fraction of the contributing eigenvectors in the basis.

numerical sense) without prior truncation of the basis and a site cutoff dimension of $D = 4$. It is clearly visible that the eigenvalues decay rapidly such that a truncation of the system basis could be performed very efficiently. Even by keeping $m = 10$ of the 64 states, the truncation error ε can be kept below typical values of 10^{-8} or even less.

The reasons for this behavior are versatile and enlightening in order to get a deeper insight into DMRG, especially when it comes to understanding the limits of the algorithm [60, 74], but go beyond the scope of this text. Nevertheless, one aspect stemming from quantum information theory shall be mentioned here as it has interesting cross connections to topological order. Suppose that an arbitrary system is divided into two subsystems "s" and "e" (system and environment). It can be shown in most cases, that the *von Neumann entanglement entropy*

$$S = -\mathrm{Tr}\{\rho_\mathrm{s} \ln(\rho_\mathrm{s})\} = -\mathrm{Tr}\{\rho_\mathrm{e} \ln(\rho_\mathrm{e})\}, \tag{5.8}$$

or in terms of the eigenvalues $S = -\sum_{\alpha=1}^{D_\mathrm{s}} w_\alpha \ln(w_\alpha)$, which provides a measure of the entanglement between the two subsystems must obey certain *area laws* [75]. As a consequence, the truncation procedure of DMRG discards highly-entangled states between the constituents. Thus the smaller S the fewer states have to be kept in an accurate approximation (for example to deceed a fixed truncation error). As a rule of thumb, the number of states to be kept scales as $m \approx \mathrm{e}^S$ [74]. For ground states of one-dimensional gapped local Hamiltonians with open boundary conditions the appropriate area law states that $S \sim \ln(L)$ and therefore $m \sim L$. This paves the road to success of DMRG in the treatment of one-dimensional quantum systems. Interestingly, the fact that one-dimensional systems obeying the aforementioned criteria are always short-range entangled and the statement that topological order can only be present due to symmetry properties of the system are related to topological order is a consequence of long-range entanglement which cannot occur in a local one-dimensional system [76].

To sum up, the core of DMRG relies on enlarging and connecting system and environment blocks to form a superblock followed by a truncation of the system basis keeping only

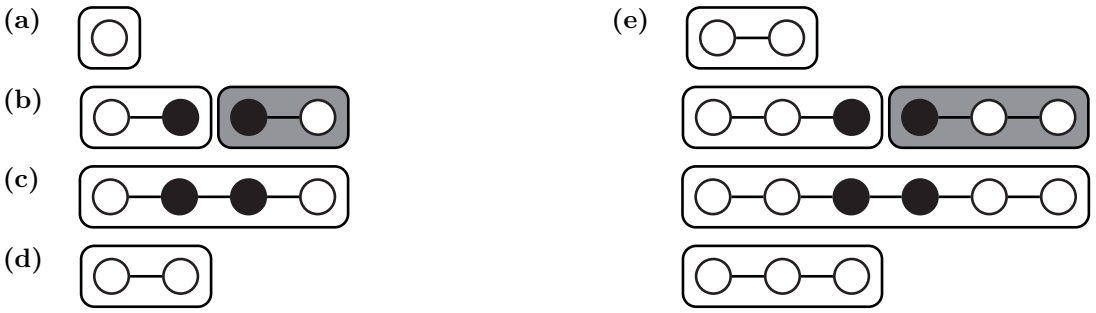

Figure 5.4.: Illustration of the first two steps in the infinite system algorithm. (a) The algorithm starts with a single block. (b) The system block is enlarged by one site and mirrored for the environment block. (c) System and environment block are connected in order to construct the superblock Hamiltonian from which the target ground state is obtained. (d) From the ground state of the superblock the reduced density matrix of the system block is deduced. Finally, the basis of the enlarged system block is truncated by rotating all operators to the new basis given by the m eigenvectors of the reduced density matrix yielding a compressed result of the enlarged block. (e) Continuing the previous steps the system block size is iteratively increased and the algorithm proceeds until the system properties have converged.

the m most contributing eigenvectors $|\alpha\rangle_\mathrm{s}, \alpha = 1, \ldots, m$ of the reduced density matrix. This final step is accompanied by a basis transformation from the former system basis $|j\rangle_\mathrm{s}, j = 1, \ldots, D_\mathrm{s}$ to the compressed basis $|\alpha\rangle_\mathrm{s}$. All internal operators of the system block (Hamiltonian, connection operators, optional observables) have to be rotated to the new basis. Explicitly, an operator $A = \sum_{j,k=1}^{D_\mathrm{s}} A_{jk} |j\rangle_\mathrm{s}\langle k|_\mathrm{s}$ given in the old basis of the system in terms of a $D_\mathrm{s} \times D_\mathrm{s}$ matrix $\boldsymbol{A}$ with $(\boldsymbol{A})_{jk} = A_{jk}$ is transformed to the new basis yielding the truncated rotated form $\tilde{A}$ in the new basis by

$$\begin{aligned} \tilde{A} &= \sum_{\alpha,\alpha'=1}^{m} |\alpha\rangle_\mathrm{s}\langle\alpha|_\mathrm{s} \left(\sum_{j,k=1}^{D_\mathrm{s}} A_{jk} |j\rangle_\mathrm{s}\langle k|_\mathrm{s} \right) |\alpha'\rangle_\mathrm{s}\langle\alpha'|_\mathrm{s} \\ &= \sum_{\alpha,\alpha'=1}^{m} \left(\sum_{j,k=1}^{D_\mathrm{s}} \langle\alpha\,|\,j\rangle_\mathrm{s} A_{jk} \langle k\,|\,\alpha'\rangle_\mathrm{s} \right) |\alpha\rangle_\mathrm{s}\langle\alpha'|_\mathrm{s} \equiv \sum_{\alpha,\alpha'=1}^{m} \tilde{A}_{\alpha\alpha'} |\alpha\rangle_\mathrm{s}\langle\alpha'|_\mathrm{s}\,, \end{aligned} \tag{5.9}$$

which is now characterized by an $m \times m$ dimensional matrix $\tilde{\boldsymbol{A}}$. Numerically this can be achieved by lining up the m eigenvectors of $\boldsymbol{\rho}_\mathrm{s}$ in an $m \times D_\mathrm{s}$ matrix $\boldsymbol{U}$ row per row. Then equation (5.9) translates into

$$\tilde{\boldsymbol{A}} = \boldsymbol{U}\boldsymbol{A}\boldsymbol{U}^\dagger. \tag{5.10}$$

With that said, two common DMRG methods can now be outlined – the *infinite* and the *finite system algorithm*.

Infinite system algorithm: This method was originally intended for obtaining the ground state properties (for instance energy per lattice site) in the thermodynamic limit $L \to \infty$. For an inversion-symmetric system it proceeds as follows (see figure 5.4) [74]:

1. Start by creating a block of one lattice site including all necessary operators such as the Hamiltonian, connection operators and optional observables (figure 5.4a).

2. Enlarge the block by one lattice site (indicated by a black site, see figure 5.4b) updating Hamiltonian and observables. Change the connection operators to the new ones and (optionally) add observables to the enlarged block. Use a mirrored copy of this block as environment (grayish block in figure 5.4b).

3. Connect the enlarged system block and the enlarged environment block to the superblock (figure 5.4c) yielding the superblock Hamiltonian H.

4. Using a large sparse eigensolver, compute the ground state $|\psi\rangle$ of the superblock. The eigenvalue corresponds to the ground state energy. (Optionally) compute expectation values of observables using the ground state and representations of the observable operators in the system and environment block.

5. Construct the reduced density matrix $\boldsymbol{\rho}_\mathrm{s}$ of the system block using $|\psi\rangle$. To do so, reshape the components ψ_{jk} (compare equation (5.4)) into a $D_\mathrm{s} \times D_\mathrm{e}$ matrix $\boldsymbol{\psi}$ such that the row index corresponds to the system basis whereas column indices are associated with environment basis elements. Then according to equation (5.6) the matrix $\boldsymbol{\rho}_\mathrm{s}$ is obtained by $\boldsymbol{\rho}_\mathrm{s} = \boldsymbol{\psi}\boldsymbol{\psi}^\dagger$. Diagonalize the matrix $\boldsymbol{\rho}_\mathrm{s}$ and yield the D_s eigenvalues w_α in descending order with the appropriate eigenvectors $|\alpha\rangle_\mathrm{s}$.

6. Choose the number of basis vectors to keep after the truncation (for instance set $m = \text{const}$ or choose m dynamically by keeping the truncation error ε (equation (5.7)) below a specified threshold). Line up the components of the m most contributing eigenvectors in a $m \times D_\mathrm{s}$ matrix $\boldsymbol{U}$.

7. Truncate the system block by applying equation (5.10) to all internal operators thereby reducing the basis dimension of the block from D_s to m. Note that the length of the enlarged truncated system block has increased by one (figure 5.4d).

8. Continue with step 2. After one DMRG step, this yields a truncated system block of increased length (figure 5.4e). Iterate the scheme until the system properties (observables, energy per lattice site) have converged.

In order to treat systems without inversion symmetry step 2 has to be modified since the mirrored version of the enlarged block cannot serve as environment. Therefore two species of blocks representing the left and right half of the total system have to be grown separately using the other complement as environment block. It shall be emphasized that steps 2-7 represent the core of DMRG and are referred to as a *DMRG step*, which is also the foundation of the finite size algorithm.

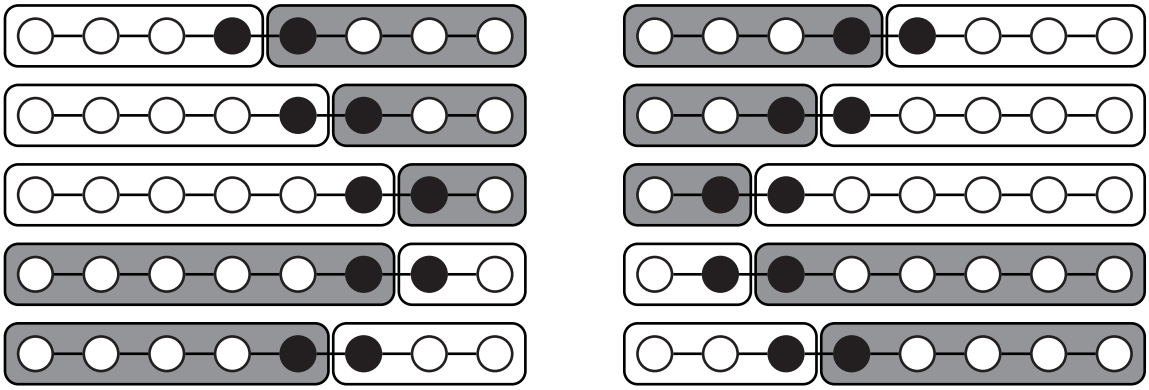

Figure 5.5.: Illustration of a sweep in the finite system DMRG for a system of total length $L = 8$ (from top to bottom, from left to right). The sweep starts in the symmetric configuration, where the left block of length $\ell = L/2-1$ is chosen as system block whereas the environment corresponds to the right block of length $L - \ell - 1$. Iterating to the right, the role of system and environment are reversed and the system growth proceeds from right to left until reaching the left boundary of the system is reached. Finally the system returns to the initial situation and another sweep can be performed.

Finite system algorithm: In contrast to the infinite size algorithm which often leads to poor results, the formulation of the finite size algorithm can achieve a much higher accuracy. The limited fidelity of the infinite system algorithm arises from the fact that each bond at which the superblock is cut into system and environment is only optimized once. Thus later truncation steps cannot affect the previously performed steps. This reasoning in the finite size algorithm introduces the notion of *sweeping* (see figure 5.5). The algorithm is performed in the following steps [74]:

1. Start from a single lattice site and apply the infinite system algorithm until the block length reaches $L/2 - 1$. During this procedure store the interim left and right blocks in a list for later reuse. Finishing this build-up the list of intermediate blocks should contain left and right blocks from length 1 to $L/2 - 1$.

2. Perform a *sweep* (best illustrated by an example, compare figure 5.5). To do so, take for instance the left block of length $\ell = L/2-1$ as system block which implies that the environment block is given by the right block of length $L-\ell-1$ (compare to the top left configuration of figure 5.5). After performing the DMRG step (usually without measuring observables), store the resulting left block of length $\ell+1$ in the block list and proceed with the latter choosing the appropriate environment block from the list. When the system block reaches length $L - 2$, reverse direction by taking the right block as system and the appropriate left block as environment. Continue this scheme until the initial configuration with the system given by the left block of length $L/2 - 1$ is reached. This situation is called the *symmetric configuration*, in which observables can be computed most accurately.

3. Apply multiple sweeps until the system properties (energy per lattice site, expectation values) have converged to the desired accuracy.

The sweeping procedure is essential as former variations are capable of influencing later truncations and vice versa leading to a tremendous increase in accuracy.

Instead of only optimizing for the ground state (*target state*) it is also possible to target multiple states in step 4. For instance if the interest is on the k lowest states of the system, one solves for the appropriate target states $|\psi_1\rangle, |\psi_2\rangle, \ldots, |\psi_k\rangle$ and constructs the reduced density matrix

$$\rho_\mathrm{s} = \sum_{j=1}^{k} w_j \mathrm{Tr}_\mathrm{e}\{|\psi_j\rangle\langle\psi_j|\}\,, \tag{5.11}$$

where the weight factors w_j are usually chosen equal, that is $w_j = 1/k$.

We conclude this section by commenting on aspects about pushing the performance of DMRG (see also [17, 74]). Generally the computationally most demanding task in a DMRG step is given by employing the large sparse solver for finding the target state(s) of the superblock Hamiltonian. Two of the most powerful techniques to improve the runtime of this step are mentioned here as they have also been included in the code:

- State prediction: Common large sparse eigensolver routines usually rely on iterative schemes (for instance the Lanczos algorithm [77]) that converge towards the desired eigenvector after a number of iterations. Providing a proper guess state in the initialization therefore speeds up the solver as convergence takes fewer iterations. A prediction state can be computed in a sweep using the target state of the previous step and the transformation matrices $\boldsymbol{U}$ of the system and environment blocks in order to transform the latter into the new basis.

- Symmetries of the model: As already mentioned in section 5.1 the SL-BHM is particle-conserving, which is a consequence of its $U(1)$-symmetry. Hence the superblock Hamiltonian decomposes into block structure and each block assigned to an invariant subspace of same total particle number can be diagonalized separately. The very same argument leads to a block structure of the reduced density matrix $\boldsymbol{\rho}$ and the transformation matrix $\boldsymbol{U}$, and is practical as the block structure of internal block quantities is not spoiled by numerical inaccuracies. This saves a lot of memory in the sparse representation due to the huge number of exact zeros. Note that in order to exploit the particle number conservation, the particle number of each basis vector of a block has to be kept track of in a DMRG step.

Although the aforementioned techniques speed up the diagonalization of the superblock Hamiltonian this task still takes most of the computational time in the algorithm.

5.3. DMRG for non-Hermitian Hamiltonians

After the basic DMRG techniques for Hermitian Hamiltonians have been outlined, this section aims at generalizing the procedure in order to deal with non-Hermitian Hamiltonians, especially the previously mentioned $\mathcal{PT}$-symmetric Hamiltonians.

Recap that while a Hermitian operator $H = \sum_j E_j \left|\psi_j\right\rangle\!\left\langle\psi_j\right| = H^\dagger$ can be expressed solely by knowledge of its eigenvectors $\left|\psi_j\right\rangle$ with real eigenvalues E_j, a non-Hermitian operator $K \neq K^\dagger$ may only be written in this form using the left and right eigenvectors $\left|\chi_j\right\rangle, \left|\phi_j\right\rangle$ respectively (see equations (4.19), (4.21)) with eigenvalues κ_j, that is $K = \sum_j \kappa_j \left|\phi_j\right\rangle\!\left\langle\chi_j\right|$. Thus it seems reasonable that a non-Hermitian formulation of DMRG requires left and right eigenvectors as well.

It will turn out that only slight changes of the Hermitian algorithms have to be implemented. Instead of computing only the (right) target state $\left|\psi\right\rangle \equiv \left|\phi\right\rangle$ of the non-Hermitian superblock Hamiltonian, the left eigenstate $\left|\chi\right\rangle$ is required as well. Then the residual norm

$$\left|\left|\phi\right\rangle - \left|\tilde{\phi}\right\rangle\right|^2 + \left|\left|\chi\right\rangle - \left|\tilde{\chi}\right\rangle\right|^2 \tag{5.12}$$

relative to the approximations $\left|\tilde{\phi}\right\rangle, \left|\tilde{\chi}\right\rangle$ with a truncated system is minimized by keeping the m most contributing eigenvectors of the density matrix [66]

$$\rho_\mathrm{s} = \frac{1}{2}\mathrm{Tr}_\mathrm{e}\{\left|\phi\right\rangle\!\left\langle\phi\right| + \left|\chi\right\rangle\!\left\langle\chi\right|\}\,. \tag{5.13}$$

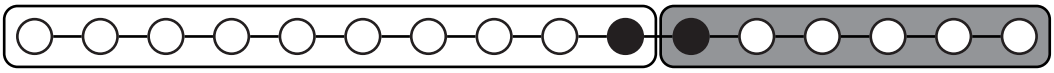

1.	Use enlarged system and environment to construct the superblock Hamiltonian H (K)	
2.	Solve the eigenvalue equation $H\left\|\psi\right\rangle = E\left\|\psi\right\rangle$ for the desired target state (for instance the ground state)	Solve the eigenvalue equations $K\left\|\phi\right\rangle = \kappa\left\|\phi\right\rangle$ and $K^\dagger\left\|\chi\right\rangle = \kappa^*\left\|\chi\right\rangle$ for the desired target states
3.	Construct the reduced density matrix $\rho_\mathrm{s} = \mathrm{Tr}_\mathrm{e}\{\left\|\psi\right\rangle\!\left\langle\psi\right\|\}$	Construct the reduced density matrix $\rho_\mathrm{s} = 1/2\ \mathrm{Tr}_\mathrm{e}\{\left\|\phi\right\rangle\!\left\langle\phi\right| + \left|\chi\right\rangle\!\left\langle\chi\right|\}$
4.	Compute the eigenvectors $\left\|\alpha\right\rangle_\mathrm{s}, \alpha = 1, \ldots, D_\mathrm{s}$ with eigenvalues w_α, order them descendingly and keep m eigenvectors associated with the largest eigenvalues	
5.	Line up the eigenvectors in an $m \times D_\mathrm{s}$ matrix $\boldsymbol{U}$ and transform all operators of the enlarged system block, for instance $\boldsymbol{A} \to \tilde{\boldsymbol{A}} = \boldsymbol{U}\boldsymbol{A}\boldsymbol{U}^\dagger$ to perform the truncation	

Figure 5.6.: Comparison between a DMRG step of a Hermitian (blue) and a non-Hermitian (orange) system. Note that most of the steps are identical whereas changes only appear in two substeps.

This choice of the density matrix can also be understood by considering the Hermitian scenario with multiple target states (equation (5.11)) but this time left and right eigenstates have to be targeted for a proper representation of the system Hamiltonian, compare equation (4.21).

Figure 5.6 illustrates the modifications to a Hermitian DMRG code that have to be made in order to add the capability of handling non-Hermitian systems.

To further illustrate the choice of eigenvectors of the density matrix (5.13) minimizing equation (5.12) the proof of the Hermitian equivalent shall be given here following references [17, 66], from which the non-Hermitian version follows immediately but requires a lengthily notation.

Suppose the representation of the ground state of a superblock expressed in the product basis of system and environment is given (compare equation (5.4)),

$$|\psi\rangle = \sum_{j=1}^{D_\mathrm{s}} \sum_{k=1}^{D_\mathrm{e}} \psi_{jk} \, |j\rangle_\mathrm{s} \, |k\rangle_\mathrm{e} \,, \tag{5.14}$$

and we are seeking for an optimal representation of the system in terms of m orthogonal vectors $|\alpha\rangle_\mathrm{s} = \sum_j u_{\alpha j} \, |j\rangle_\mathrm{s}$ such that the approximation of $|\psi\rangle$ (equation (5.5)),

$$|\tilde{\psi}\rangle = \sum_{\alpha=1}^{m} \sum_{k=1}^{D_\mathrm{e}} \tilde{\psi}_{\alpha k} \, |\alpha\rangle_\mathrm{s} \, |k\rangle_\mathrm{e} \,, \tag{5.15}$$

minimizes the distance $| \, |\psi\rangle - |\tilde{\psi}\rangle \, |^2$. Inserting the expansion of both states using the normalization of $|\psi\rangle$ one finds (throughout assuming *real components* for simplicity)

$$| \, |\psi\rangle - |\tilde{\psi}\rangle \, |^2 = 1 - 2 \sum_{\alpha,j,k} \tilde{\psi}_{\alpha k} u_{\alpha j} \psi_{jk} + \sum_{\alpha,k} \tilde{\psi}_{\alpha k}^2 \stackrel{!}{=} \min \tag{5.16}$$

for the expression to be minimized. Taking the partial derivative of (5.16) with respect to one of the variational parameters $\tilde{\psi}_{\alpha k}$ and demanding for it to vanish in the global minimum leads to

$$-2 \sum_j u_{\alpha j} \psi_{jk} + 2 \tilde{\psi}_{\alpha k} = 0 \quad \Longrightarrow \quad \sum_j u_{\alpha j} \psi_{jk} = \tilde{\psi}_{\alpha k}. \tag{5.17}$$

Eliminating the $\tilde{\psi}_{jk}$ from equation (5.16) with this relation leads to an expression de-

pending on the coefficients $u_{\alpha j}$ which has to be minimized,

$$\begin{aligned} \left| \left|\psi\right\rangle - \left|\tilde{\psi}\right\rangle \right|^2 &= 1 - 2\sum_{\alpha,j,k}\left(\sum_{\ell} u_{\alpha\ell}\psi_{\ell k}\right) u_{\alpha j}\psi_{jk} + \sum_{\alpha,k}\left(\sum_{j,\ell} u_{\alpha j}\psi_{jk}u_{\alpha\ell}\psi_{\ell k}\right) \\ &= 1 - \sum_{\alpha,j,\ell} u_{\alpha j}\left(\sum_{k}\psi_{jk}\psi_{\ell k}\right) u_{\alpha\ell} \\ &= 1 - \sum_{\alpha,j,\ell} u_{\alpha j}\left(\boldsymbol{\rho}_{\mathrm{s}}\right)_{j\ell} u_{\alpha\ell}, \end{aligned} \tag{5.18}$$

where quite naturally the components of the reduced density matrix (equation (5.6)) appear. Because of the positivity and Hermiticity of $\boldsymbol{\rho}_{\mathrm{s}}$ equation (5.18) is minimized by setting the $u_{\alpha j}$ to the components of the eigenvectors belonging to the m largest eigenvalues w_α and therefore the $\left|\alpha\right\rangle_{\mathrm{s}}$ correspond to those eigenvectors, which concludes the proof. Note as well that equation (5.7) follows immediately.

Carrying over this proof to the non-Hermitian case, it can be argued that in order to target both left and right eigenstates $\left|\phi\right\rangle, \left|\chi\right\rangle$ one seeks proper approximations $\left|\tilde{\phi}\right\rangle, \left|\tilde{\chi}\right\rangle$,

$$\left|\tilde{\phi}\right\rangle = \sum_{j=1}^{m}\sum_{k=1}^{D_{\mathrm{e}}} \tilde{\phi}_{\alpha k}\left|\alpha\right\rangle_{\mathrm{s}}\left|k\right\rangle_{\mathrm{e}}, \qquad \left|\tilde{\chi}\right\rangle = \sum_{j=1}^{m}\sum_{k=1}^{D_{\mathrm{e}}} \tilde{\chi}_{\alpha k}\left|\alpha\right\rangle_{\mathrm{s}}\left|k\right\rangle_{\mathrm{e}}, \tag{5.19}$$

which minimize equation (5.12). Following the steps of the above proof for this case then leads to the result that the $\left|\alpha\right\rangle_{\mathrm{s}}$ are best chosen as the m eigenvectors belonging to the largest eigenvalues of the reduced density matrix given by equation (5.13).

5.4. DMRG in Liouville space

With the non-Hermitian DMRG algorithms at hand the field of physically accessible problems has widened. Our code can treat non-Hermitian Hamiltonians, for instance find the "ground state" (that is the eigenstate with lowest real part of the eigenvalue), but the interest shall also be on a comparison between results from $\mathcal{PT}$-symmetric Hamiltonians and dissipation introduced by a master equation in Lindblad form,

$$\frac{\mathrm{d}\rho}{\mathrm{d}t} = -\mathrm{i}\left[H,\rho\right] + \sum_{\mu}\left(2L_\mu\rho L_\mu^\dagger - \left\{L_\mu^\dagger L_\mu,\rho\right\}\right) \equiv \hat{\mathcal{L}}\left|\rho\right\rangle_{\#}, \tag{5.20}$$

where the last equality will be explained in a moment. Note that the Lindblad operators have been rescaled in comparison to equation (4.8) in order to be consistent with the references [21, 22] aiming at an analytical approach towards the solution of this equation (see also appendices B and C).

The idea of how to include the capability of handling equation (5.20) in our non-Hermitian DMRG code relies on the construction and enlargement rule of a Liouville operator (instead of a Hamiltonian) for a single site. Similar to the build-up procedure of the SL-BHM Hamiltonian in section 5.1, an iterative enlargement procedure can be found, which is presented in the following. Using the non-Hermitian DMRG method allows us to optimize the basis representation of a system for the desired target state.

First, consider the construction of $\hat{\mathcal{L}}$ for only a single site with a Hilbert space $\mathscr{H}$ restricted to D states, that is at most $D-1$ particles. $\mathscr{H}$ is spanned by the Fock states $|j\rangle, j = 0, \ldots, D-1$ denoting the presence of j particles at that site. As the Liouville operator is acting on the density matrix $\rho \in \mathscr{L}$ living in the *Liouville space* $\mathscr{L} = L(\mathscr{H})$, the basis to work with is given by the D^2 standard basis vectors $|i\rangle \otimes \langle j| = |i\rangle\langle j|, i, j = 0, \ldots, D-1$ spanning the single site Liouville space, and ρ may be expressed as follows,

$$\rho = \sum_{i,j=0}^{D-1} c_{ij} \, |i\rangle\langle j| \, . \tag{5.21}$$

Similar to the Fock basis being orthogonal with respect to the scalar product $\langle \circ \,|\, \blacktriangle \rangle$, the standard Liouvillean basis is trace-orthogonal,

$$\mathrm{Tr}_{\mathscr{H}} \Big\{ \left(|i\rangle\langle j|\right)^\dagger |k\rangle\langle \ell| \Big\} = \delta_{ik}\delta_{j\ell}. \tag{5.22}$$

One can then adopt a vectorized "superket" notation of the density matrix,

$$\rho = \sum_{i,j=1}^{D-1} \rho_{ij} \, |i\rangle\langle j| \quad \rightarrow \quad |\rho\rangle_{\#} = \sum_{i,j=1}^{D-1} \rho_{ij} \Big| \, |i\rangle\langle j| \, \Big\rangle_{\#}, \tag{5.23}$$

such that "superket" states are still orthonormal in the sense of equation (5.22). In the more general case of L lattice sites $1, \ldots, L$, whose total Liouville space $\mathscr{L}_{\mathrm{tot}}$ is spanned by the single site Liouville spaces $\mathscr{L}_i$,

$$\mathscr{L}_{\mathrm{tot}} = \bigotimes_{i=1}^{L} \mathscr{L}_i, \tag{5.24}$$

the vectorized density matrix can be expanded as

$$|\rho\rangle_{\#} = \sum_{i_1,j_1} \sum_{i_2,j_2} \cdots \sum_{i_L,j_L} \rho_{i_1 j_1, i_2 j_2, \ldots, i_L j_L} \Big| \, |i_1\rangle_1\langle j_1|_1 \otimes |i_2\rangle_2\langle j_2|_2 \otimes \ldots \otimes |i_L\rangle_L\langle j_L|_L \, \Big\rangle_{\#}. \tag{5.25}$$

Practically, this notation allows us to express the action of $\hat{\mathcal{L}}$ onto the vectorized $|\rho\rangle_{\#}$ in terms of a matrix (compare to the Hamiltonian matrix acting on a vector wave function).

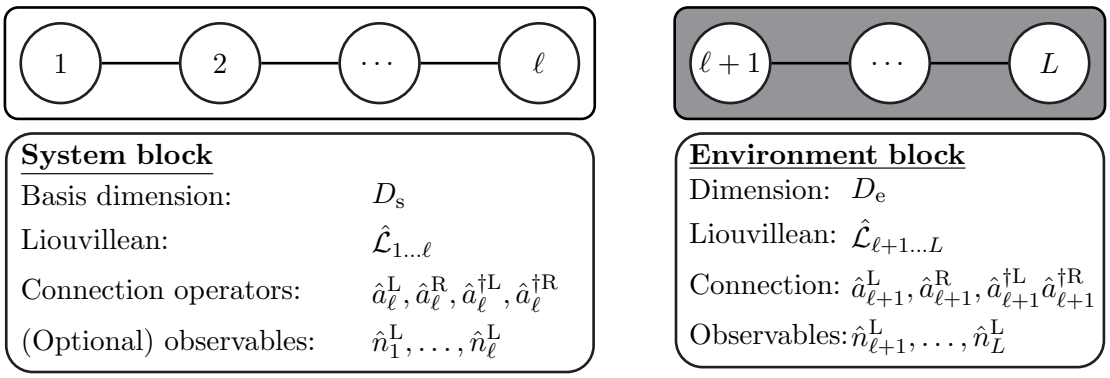

Figure 5.7.: Scheme for the connection of two dissipative blocks to form a superblock. In the dissipative framework both blocks are described by Liouvillean operators $\hat{\mathcal{L}}_{1\dots\ell}, \hat{\mathcal{L}}_{\ell+1\dots L}$, respectively. The superblock Liouvillean $\hat{\mathcal{L}}_{1\dots L}$ needs access to both Liouville operators as well as the connection operators at the bond, that is $a^\mathrm{L}_\ell, a^\mathrm{R}_\ell, a^{\dagger\mathrm{L}}_\ell, a^{\dagger\mathrm{R}}_\ell$ and $a^\mathrm{L}_{\ell+1}, a^\mathrm{R}_{\ell+1}, a^{\dagger\mathrm{L}}_{\ell+1}, a^{\dagger\mathrm{R}}_{\ell+1}$, see equation (5.28).

To do so, left and right bosonic annihilation and creation operators $\hat{a}^\mathrm{L}, \hat{a}^\mathrm{R}, \hat{a}^{\dagger\mathrm{L}}, \hat{a}^{\dagger\mathrm{R}}$ are introduced by the following action on the vectorized density matrix [22],

$$\begin{aligned} \hat{a}^\mathrm{L} |\rho\rangle_\# &= |a\rho\rangle_\# , & \hat{a}^{\dagger\mathrm{L}} |\rho\rangle_\# &= \left|a^\dagger\rho\right\rangle_\# , \\ \hat{a}^\mathrm{R} |\rho\rangle_\# &= |\rho a\rangle_\# , & \hat{a}^{\dagger\mathrm{R}} |\rho\rangle_\# &= \left|\rho a^\dagger\right\rangle_\# . \end{aligned} \tag{5.26}$$

Using those operators equation (5.20) translates into

$$\begin{aligned} \hat{\mathcal{L}} |\rho\rangle_\# &= -\mathrm{i}\left(|H\rho\rangle_\# - |\rho H\rangle_\#\right) + \sum_\mu \left(2\left|L_\mu \rho L_\mu^\dagger\right\rangle_\# - \left|L_\mu^\dagger L_\mu \rho\right\rangle_\# - \left|\rho L_\mu^\dagger L_\mu\right\rangle_\#\right) \\ &\equiv -\mathrm{i}\left(\hat{H}^\mathrm{L} - \hat{H}^\mathrm{R}\right)|\rho\rangle_\# + \left(\sum_\mu 2\hat{L}^\mathrm{L}_\mu \hat{L}^{\dagger\mathrm{R}}_\mu - \hat{L}^{\dagger\mathrm{L}}_\mu \hat{L}^\mathrm{L}_\mu - \hat{L}^\mathrm{R}_\mu \hat{L}^{\dagger\mathrm{R}}_\mu\right)|\rho\rangle_\# \\ &\equiv \left(\hat{\mathcal{L}}^{(\mathrm{uni})} + \hat{\mathcal{L}}^{(\mathrm{diss})}\right)|\rho\rangle_\# , \end{aligned} \tag{5.27}$$

where $\hat{H}^\mathrm{L}, \hat{H}^\mathrm{R}$ denote the Hamilton operators in which bosonic annihilation/creation operators have been replaced by the left and right equivalents of equation (5.26), respectively (the same holds for the Lindblad terms). The unitary term $\hat{\mathcal{L}}^{(\mathrm{uni})}$ of the Liouvillean is obviously a local operator as it contains the Hamiltonian, which is assumed to possess this property (see section 5.1). If the Lindblad operators L_μ are also chosen to be local (which is the case in this work as single-particle gain and loss on single sites is investigated), the dissipative term $\hat{\mathcal{L}}^{(\mathrm{diss})}$ of the Liouvillean is also local. Thus a simple connection/enlargement rule between two blocks can be formulated in terms of the operators (5.26) (see figure 5.7):

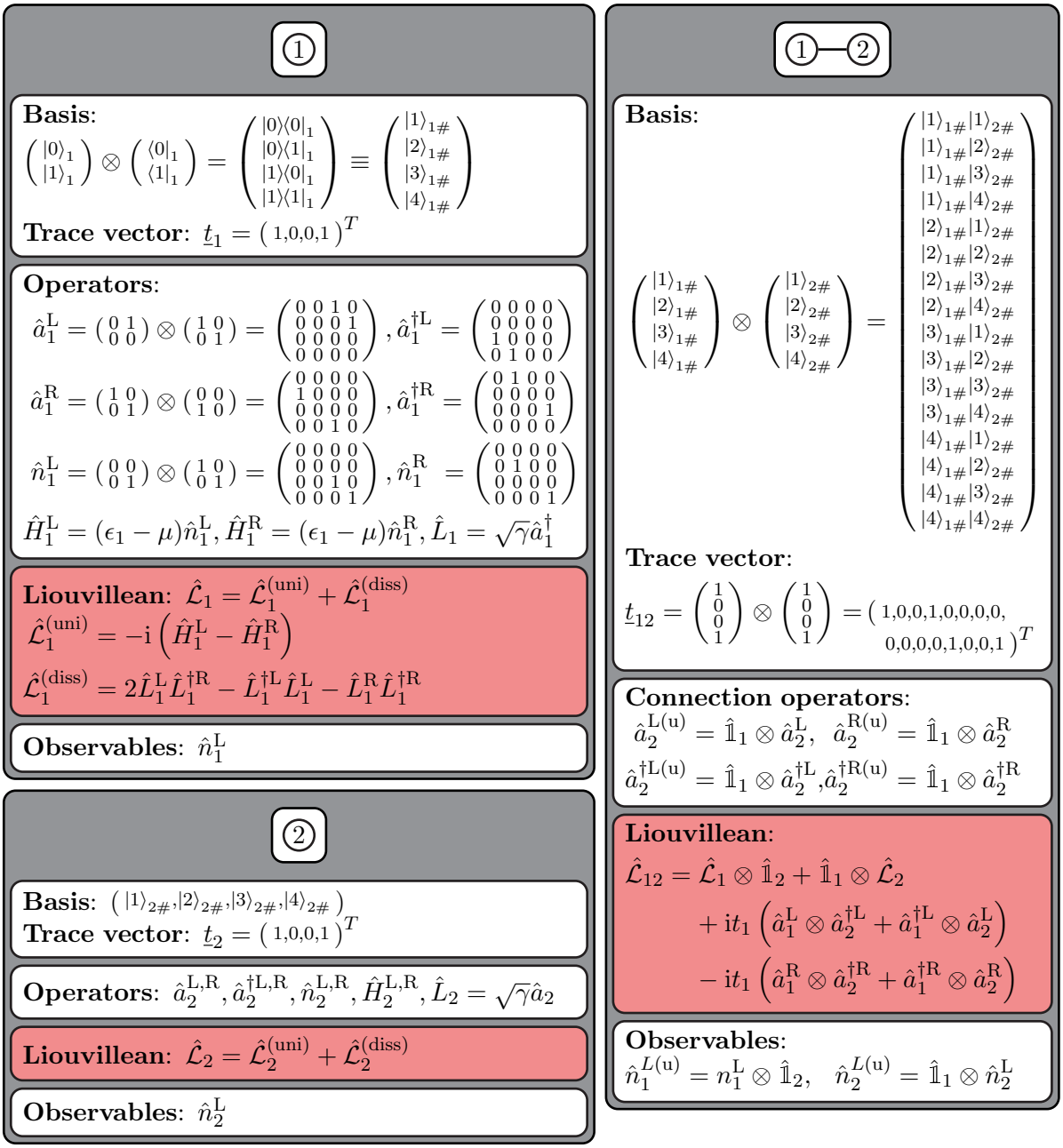

Figure 5.8.: Illustration of the enlargement procedure of a single site dissipative block 1 with local Hilbert space dimension $D = 2$, that is $D^2 = 4$ degrees of freedom for the single site density matrix. The matrix representations for left and right bosonic annihilation and creation operators have been explicitly computed to show that operators from the Hamiltonian routine (compare figure 5.2) may in principle be reused. The connection rule for the construction of the Liouville operator of the connected block is highlighted and for simplicity $t_1 \in \mathbb{R}$ has been assumed. The trace vector contains information about the contribution of a basis vector to the trace and is required in the computation of expectation values. A generalization of this scheme to $D > 2$ is straightforward.

➢ Given a system block of length ℓ which is to be connected with a tunneling amplitude $t_1 \in \mathbb{R}$ to the environment block of length $L-\ell$ where both blocks are described by a Liouvillean $\hat{\mathcal{L}}_{1\ldots\ell}, \hat{\mathcal{L}}_{\ell+1\ldots L}$, respectively, the *superblock Liouvillean* $\hat{\mathcal{L}}_{1\ldots L}$ is given by

$$\begin{aligned}\hat{\mathcal{L}}_{1\ldots L} = \hat{\mathcal{L}}_{1\ldots\ell} \otimes \hat{\mathbb{1}}_{\ell+1\ldots L} + \hat{\mathbb{1}}_{1\ldots\ell} \otimes \hat{\mathcal{L}}_{\ell+1\ldots L} \\ + \mathrm{i}t_1 \left(\hat{a}_\ell^{\mathrm{L}} \otimes \hat{a}_{\ell+1}^{\dagger\mathrm{L}} + \hat{a}_\ell^{\dagger\mathrm{L}} \otimes \hat{a}_{\ell+1}^{\mathrm{L}}\right) - \mathrm{i}t_1 \left(\hat{a}_\ell^{\mathrm{R}} \otimes \hat{a}_{\ell+1}^{\dagger\mathrm{R}} + \hat{a}_\ell^{\dagger\mathrm{R}} \otimes \hat{a}_{\ell+1}^{\mathrm{R}}\right),\end{aligned} \tag{5.28}$$

where the second line is caused by the coupling between both blocks in the unitary term $\hat{\mathcal{L}}^{(\mathrm{uni})}$ and the case $L-\ell = 1$ corresponds to enlarging a dissipative block of length ℓ by one lattice site.

To illustrate the growth of a dissipative system block further, the enlargement process of a single site with $D = 2$ is shown in figure 5.8. For the construction of left and right annihilation/creation operators the appropriate matrices from the Hamiltonian method can be recycled.

With that said, one concludes that the Liouvillean has now been successfully integrated in the class of operators that can be handled by non-Hermitian DMRG. The locality of the Liouville operator (equation (5.27)) induces a block scheme which is required for DMRG techniques that heavily rely on blocking. For the purpose of writing equation (5.20) as matrix equation where the Liouvillean is represented by a matrix, a "superket" notation for the vectorized density matrix $|\rho\rangle_{\#}$ is introduced. Due to the orthogonality of the basis states (equation (5.22)) all substeps in the DMRG algorithm, for instance the construction of the "reduced superket density matrix of the system", work safely. An interesting state of the Liouville operator is given by the eigenstate $|\rho_{\mathrm{ness}}\rangle_{\#}$ associated with eigenvalue zero since

$$\hat{\mathcal{L}}\,|\rho_{\mathrm{ness}}\rangle_{\#} = 0\,|\rho_{\mathrm{ness}}\rangle_{\#} \tag{5.29}$$

in addition with the master equation (5.20) implies $|\rho_{\mathrm{ness}}(t)\rangle_{\#} = \mathrm{const}$, and thus $|\rho_{\mathrm{ness}}\rangle_{\#}$ corresponds to the *non-equilibrium steady state* (*NESS*) towards which the system converges in the long-time limit. Targeting the eigenvalue zero in the diagonalization of the superblock Liouvillean in a DMRG step leads to a representation of $|\rho_{\mathrm{ness}}\rangle_{\#}$.

So far one subtle aspect has been withheld from the discussion since it requires some additional treatment, namely the computation of expectation values. Evaluating the latter for an observable $\hat{A}$ requires a *"superket" representation of the trace*, compare equation (4.3). This representation is implemented by keeping track of the identity $\mathbb{I}_{1\ldots\ell}$ in the Hilbert space of a block of length ℓ,

$$\mathbb{I}_{1\ldots\ell} = \sum_{i_1,i_2,\ldots,i_\ell} |i_1\rangle_1\langle i_1|_1 \otimes |i_2\rangle_2\langle i_2|_2 \otimes \ldots \otimes |i_\ell\rangle_\ell\langle j_\ell|_\ell\,, \tag{5.30a}$$

whose "superket" representation reads

$$|\mathbb{I}_{1\dots\ell}\rangle_{\#} = \sum_{i_1,i_2,\dots,i_\ell} \Big| \, |i_1\rangle_1\langle i_1|_1 \otimes |i_2\rangle_2\langle i_2|_2 \otimes \dots \otimes |i_\ell\rangle_\ell\langle j_\ell|_\ell \, \Big\rangle_{\#}. \tag{5.30b}$$

Effectively, the components of the vector $|\mathbb{1}_{1\dots\ell}\rangle_{\#}$ expressed in the system "superket" basis $|i\rangle_{\mathrm{s}\#}, i = 1, \dots, D_{\mathrm{s}}$ stored in the so called *trace vector* $\underline{t}_{1\dots\ell}$ contain the contribution of a basis state to the trace in the Hilbert space (compare figure 5.8 for an example),

$$|\mathbb{I}_{1\dots\ell}\rangle_{\#} = \sum_{i=1}^{D_{\mathrm{s}}} t_i \, |i\rangle_{\mathrm{s}\#} \, . \tag{5.30c}$$

In a DMRG step the basis of the system is rotated by the transformation matrix $\boldsymbol{U}$ and all operators of the block represented by matrices transform according to equation (5.10). Carrying the notion of equation (5.9) over to the trace vector $\underline{t}$ (equation (5.30c)) leads to the following transformation in the truncation procedure,

$$\begin{aligned} t_i \, |i\rangle_{\mathrm{s}\#} \to \sum_{\alpha=1}^{m} t_i \, \langle\alpha \,|\, i\rangle_{\mathrm{s}\#} \, |\alpha\rangle_{\mathrm{s}\#} = \sum_{\alpha=1}^{m} t_i u_{\alpha i} \, |\alpha\rangle_{\mathrm{s}\#} \equiv \sum_{\alpha=1}^{m} \tilde{t}_\alpha \, |\alpha\rangle_{\mathrm{s}\#} \\ \implies \underline{t} \to \underline{\tilde{t}} = \boldsymbol{U}\underline{t}. \end{aligned} \tag{5.31}$$

Ultimately, the computation of an expectation value can be formulated as follows:

➢ Given the right target state $|\rho\rangle_{\#} = \sum_{i=1}^{D_{\mathrm{s}}D_{\mathrm{e}}} \rho_i \, |i\rangle_{\#}$, the trace vector and an observable $\hat{A}$ in the superblock basis $|i\rangle_{\#}$ described by the vectors $\underline{\rho}, \underline{t}$ and the matrix $\boldsymbol{A}$ respectively, the expectation value

$$\langle\hat{A}\rangle = \frac{\mathrm{Tr}\Big\{\hat{A}\,|\rho\rangle_{\#}\Big\}}{\mathrm{Tr}\Big\{|\rho\rangle_{\#}\Big\}} \qquad \text{is evaluated by} \qquad \langle\hat{A}\rangle = \frac{\underline{t}\cdot\boldsymbol{A}\underline{\rho}}{\underline{t}\cdot\underline{\rho}}. \tag{5.32}$$

Equation (5.32) is best understood by recapitulating that the vector $\underline{t}$ contains information about the contribution of the respective basis state to the trace such that multiplying $\underline{t}$ with another quantity results in the trace of the latter.

Finally, a non-Hermitian DMRG step (compare figure 5.6 for the formulation in the Hamiltonian framework) in the language of the Liouvillean is presented in figure 5.9.

There are some more subtleties to be aware of, which are also mentioned in [72] presenting a similar MPS-based algorithm. Our method does neither ensure that the target density matrix is (i) positive-semidefinite nor (ii) Hermitian. While the second aspect can be circumvented by a more sophisticated choice of the local Liouville space basis in terms of Hermitian *generalized Gell-Mann matrices*, which is commented on in appendix D, the

1. Use the enlarged system and environment to construct the superblock Liouvillean $\hat{\mathcal{L}}$

2. Solve the eigenvalue equations $\hat{\mathcal{L}}\,|\phi\rangle_{\#} = \kappa^*\,|\phi\rangle_{\#}$, $\hat{\mathcal{L}}^\dagger\,|\chi\rangle_{\#} = \kappa\,|\chi\rangle_{\#}$ for the desired target ($\kappa = 0$ for the NESS). The state $|\phi\rangle_{\#}$ ($= |\rho\rangle_{\#}$ in the text) corresponds to the vectorized "superket" representation of the density matrix which is sought

3. Construct the "reduced superket density matrix" (does *not* correspond to a physically meaningful quantity but rather provides the opimal basis representation of the system to approximate the target states) $\rho_{\mathrm{s}} = 1/2\ \mathrm{Tr}_{\mathrm{e}}\Big\{|\phi\rangle_{\#}\langle\phi|_{\#} + |\chi\rangle_{\#}\langle\chi|_{\#}\Big\}$

4. Compute the eigenvectors $|\alpha\rangle_{\mathrm{s}\#}, \alpha = 1, \ldots, D_{\mathrm{s}}$ with eigenvalues w_α, order them descendingly and keep m eigenvectors associated with the largest eigenvalues

5. Construct the transformation matrix $\boldsymbol{U}$ and truncate all operators (the trace vector) of the system according to the scheme $\boldsymbol{A} \to \tilde{\boldsymbol{A}} = \boldsymbol{U}\boldsymbol{A}\boldsymbol{U}^\dagger$ ($\underline{t} \to \underline{\tilde{t}} = \boldsymbol{U}\underline{t}$)

Figure 5.9.: Non-Hermitian DMRG step in the terms of the Liouvillean. Note that all steps can directly be adopted from the Hamiltonian method (figure 5.6) the only difference being a different basis, which however is still orthogonal in the sense of equation (5.22) and is required for the outlined DMRG algorithm to work. A small adaption, namely the transformation of the trace vector originates from the modified computation of expectation values.

first point cannot be straightforwardly implemented. Therefore one has to rely on the assumption that the mathematical properties of ρ are physically meaningful. Moreover, in chapter 8 a condition for the expectation value of the particle number in the steady state will be derived and can be used as additional check for the validity of the results obtained from simulations.

Chapter review

- Interacting bosonic systems are difficult to investigate numerically as the dimension of the Hilbert space is infinite-dimensional, that is a single lattice site can host an arbitrary number of bosons. Usually, the degrees of freedom of a single are restricted to D states (at most $D-1$ particles per site), which still comes at a price of exponential growth of the dimension.
- Since the Hamiltonians under investigation are local, a representation of a finite system can be generated iteratively by starting from a single site providing a proper enlargement rule for adding an additional site. DMRG makes use of this building procedure but also provides a truncation procedure to effectively reduce the dimensionality of the problem. In many cases, especially in one-dimensional local gapped quantum systems, this truncation procedure is highly effective which

is one of the reasons for the success of DMRG. Errors of numerical simulations (for instance energy or expectation values) are usually on the order of the truncation error ε.

➢ For the purpose of this work, a basic DMRG code for Hermitian operators has been implemented. Moreover, in order to deal with $\mathcal{PT}$-symmetric Hamiltonians the algorithm has been extended to non-Hermitian Hamiltonians.

➢ Using non-Hermitian DMRG allows us to study dissipative systems not only in the framework of $\mathcal{PT}$-symmetric Hamiltonians but also by targeting the steady state properties of a master equation in Lindblad form. The technique resembles recently developed MPS-based algorithms but does not require prior knowledge of this framework as we formulate it in the *traditional* language of DMRG. Thus we believe it may provide a very comprehensible approach for readers familiar with DMRG that do not (yet) want to get involved with MPS. All adaptions can be included in a working Hermitian DMRG code without much effort.

6. The $\mathcal{PT}$-symmetric SL-BHM

This chapter gives an overview of the effects arising in the SL-BHM extended by complex $\mathcal{PT}$-symmetric potentials such that the Hamiltonian *always* satisfies equation (4.14). Before doing so, a physical motivation why such an extension is of interest is given. In chapter 3 it was outlined that the gapped Mott-insulator (MI) phases are characterized by a topological invariant given by the generalized Zak phase ν (see equation (3.17)), which is quantized due to the $\mathcal{PT}$ symmetry of the Hermitian Hamiltonian (considerations on how to carry over the generalized Zak phase to the non-Hermitian scenario are given in chapter 7). Extending the latter by addition of non-Hermitian on-site terms which however respect the symmetry of the Hamiltonian can be employed as an *effective* theory to introduce single-particle gain and loss, see chapter 4. In particular, the class of non-Hermitian $\mathcal{PT}$-symmetric operators is capable of possessing entirely real eigenvalues for a certain range in parameter space corresponding to stationary modes, which can be interpreted as stable although the system is *subject to gain and loss*. The interpretation in the $\mathcal{PT}$-broken (see page 39) regime is more complicated as complex eigenvalues lead to an exponential (de)amplification of a bosonic system, which finally ends up entirely empty or keeps on filling with particles due to gain and loss effects.

It is therefore desirable to study the existence of parameter ranges in which the SL-BHM is stable despite of dissipative effects. Even more interesting the question how topological order, which quite generically is accompanied by the occurrence of edge modes, translates into the dissipative case can be posed. Pushing this idea further there could exist topological phase transitions that are driven by dissipation and a problem under recent investigation addresses the topological classification of open quantum systems (for an approach to fermionic systems, see reference [9]).

In section 6.1 the complex on-site potentials, which have already been partially used for studying the relation between $\mathcal{PT}$ symmetry and topological phases in different fermionic models [78–81] are presented including a discussion of the single-particle spectra.

Section 6.2 investigates the low-energy spectrum of the SL-BHM extended by complex on-site potentials focussing on the identification of features in the edge states that are caused by dissipation, which may serve as an indicator for topological effects.

6.1. Complex on-site potentials

In the following, the SL-BHM Hamiltonian (3.1), which is denoted by H_0 from now on, will be extended by a non-Hermitian potential U such that the total Hamiltonian

$$H = H_0 + U \tag{6.1}$$

effectively describes a dissipative version of the SL-BHM with different gain and loss patterns dictated by U. In total four different on-site potentials are considered on a chain of L lattice sites, all of which are sketched in figure 6.1.

A simple dissipative setup is given by setting the first site of a one-dimensional SL-BHM chain to act as a sink for particles, while bosons are filled into the system at the last site acting as a source. Such a situation can be realized when the chain (for instance a quantum wire) is in contact with two different baths (e.g. heat [82, 83] or particle reservoirs) at its outer boundaries. The potential describing this situation is abbreviated by U_1 and reads

$$U_1 = -\mathrm{i}\gamma n_1 + \mathrm{i}\gamma n_L \tag{6.2a}$$

parameterized by the gain/loss strength γ. Physically one expects U_1 to induce currents through the entire system from source to sink.

Placing single-particle gain and loss on two directly adjacent sites in the center of the chain results in the "centered" version of U_1 denoted as $U_1^{(\mathrm{c})}$,

$$U_1^{(\mathrm{c})} = -\mathrm{i}\gamma n_{L/2-1} + \mathrm{i}\gamma n_{L/2}, \tag{6.2b}$$

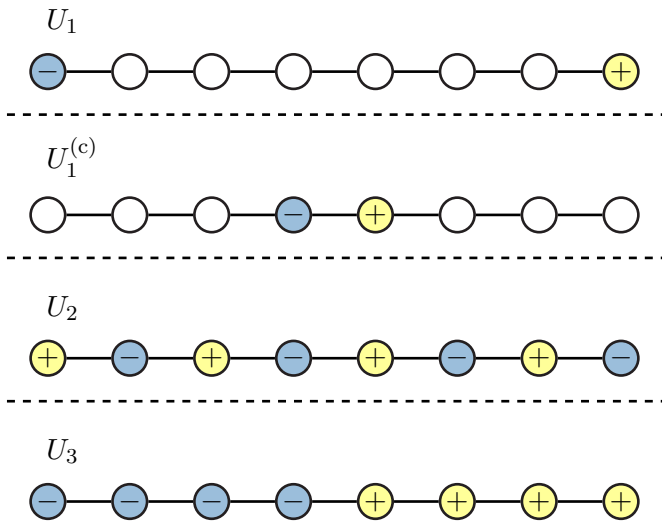

Figure 6.1.: Sketch of the complex on-site potentials (equations (6.2)) accounting for different dissipative setups of single-particle gain and loss on a linear chain with $L = 8$ sites. While white lattice sites are not directly affected by dissipation (no complex on-site potential), blue sites $(-)$ are subject to loss effects by an imaginary potential of $-\mathrm{i}\gamma$ and yellow circles $(+)$ mark sites where particles are coupled into the system corresponding to a potential value of $+\mathrm{i}\gamma$. The dimerization of the chain is suppressed in this illustration as the focus is on the on-site terms.

which can be regarded as a dissipative impurity in the system and has only recently also been investigated in [84]. In particular, the centered construction is advantageous compared to U_1 as it allows for tracking the quantized topological order parameter between two adjacent dissipative sites (see chapter 7).

Moving away from only single sites acting as sinks and sources for particles, the next potentials are characterized by a fully dissipative chain, that is each lattice site is subject to either gain or loss. If both effects are introduced in an alternating fashion, the unit cell structure will be conserved allowing for an analytical approach of the fermionic SSH version of the model. The appropriate on-site potential is called U_2,

$$U_2 = \sum_{j=1,3,\dots} \mathrm{i}\gamma n_j + \sum_{j=2,4,\dots} (-\mathrm{i}\gamma) n_j. \tag{6.2c}$$

Finally, in order to investigate the consequence of identical dissipative processes among a large number of sites a potential overlaying gain or loss on an entire half of the chain will be considered,

$$U_3 = \sum_{j=1}^{L/2} (-\mathrm{i}\gamma) n_j + \sum_{j=L/2+1}^{L} \mathrm{i}\gamma n_j, \tag{6.2d}$$

which can be imagined by a chain embedded into two two-dimensional reservoirs.

The behavior of a single particle in an SSH chain of unit cells subject to adjacent gain and loss described by U_2 shall be derived analytically as it emphasizes the existence of real eigenvalues in the spectrum and the hard-core bosonic SL-BHM model maps onto the latter in the strongly-interacting regime at $\mu = 0$ (see chapter 3). Considering the Hamiltonian (2.2) extended by the potential term (6.2c), the same steps as in chapter 2 can be carried out to yield the Bloch Hamiltonian of the periodic system,

$$\begin{aligned} \boldsymbol{H}_{\mathrm{Bloch}}(k) = -\begin{pmatrix} -\mathrm{i}\gamma & t_1 + t_2 \mathrm{e}^{-\mathrm{i}k} \\ t_1 + t_2 \mathrm{e}^{\mathrm{i}k} & \mathrm{i}\gamma \end{pmatrix} \equiv -\underline{n}(k) \cdot \underline{\boldsymbol{\sigma}}, \\ \text{with} \qquad \underline{n}(k) = \begin{pmatrix} t_1 + t_2 \cos(k) \\ t_2 \sin(k) \\ \mathrm{i}\gamma \end{pmatrix}, \end{aligned} \tag{6.3}$$

compare with equations (2.8), (2.10) and (2.11). Solving for the eigenvalues $E_n(k)$ of the matrix (6.3) by use of the Pauli matrices' properties leads to $\boldsymbol{H}_{\mathrm{Bloch}}(k)^2 = \underline{n}(k) \cdot \underline{n}(k) \mathbb{1} = E_n^2 \mathbb{1}$, and thus the energy dispersion reads as follows,

$$E_n(k) = \pm \sqrt{t_1^2 + t_2^2 + 2 t_1 t_2 \cos(k) - \gamma^2}, \tag{6.4}$$

compare equation (2.9). The behavior of the eigenvalues can best be studied in the "worst case", where $k = \pi$, and the tunneling-dependent strictly positive term of the

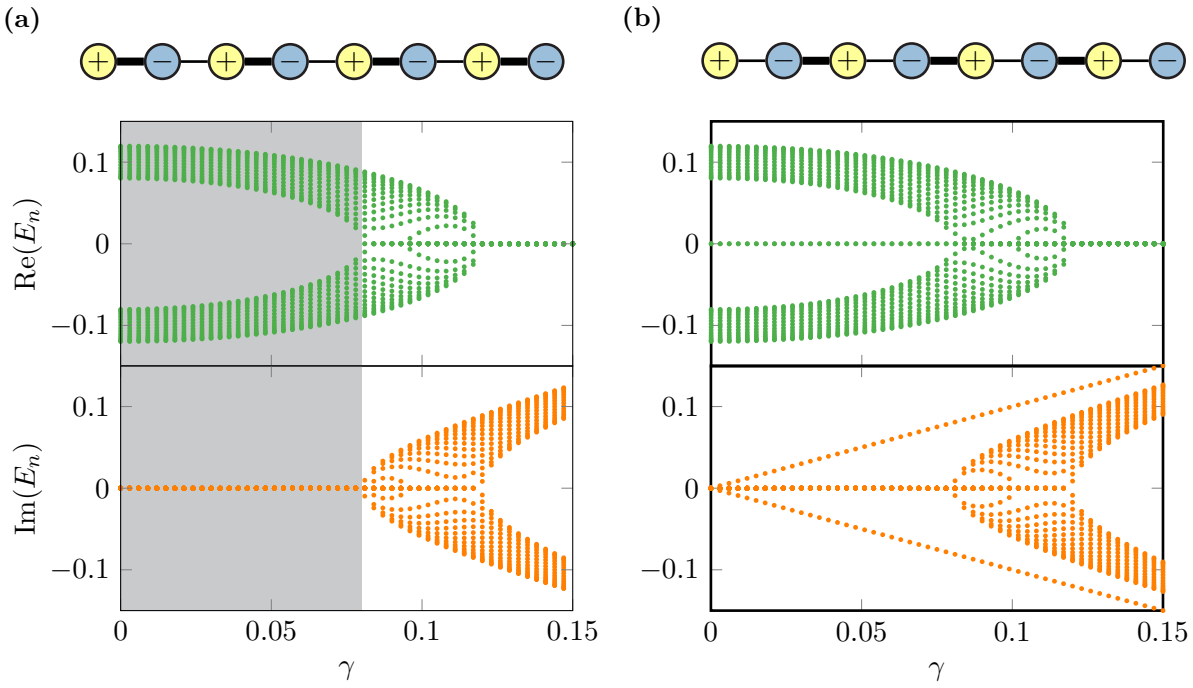

Figure 6.2.: Real and imaginary parts of the single-particle energies of an open chain with $L = 32$ and U_2. The $\mathcal{PT}$-unbroken phase is marked by a gray-shaded area. (a) The trivial phase ($t_1 = 0.1, t_2 = 0.02$) correctly reproduces equations (6.4) and (6.5) ($\gamma_c^{(U_2)} = 0.08$). (b) In the nontrivial dimerization ($t_1 = 0.02, t_1 = 0.1$) that hosts zero-energy edge modes, the bulk states act as expected by the analytical result, while the edge states do not correspond to eigenstates of $\mathcal{PT}$ and immediately break the $\mathcal{PT}$ symmetry of the Hamiltonian.

square root's argument is minimal. Since $E_n(k = \pi) = \pm\sqrt{(t_1 - t_2)^2 - \gamma^2}$, the critical value $\gamma_c^{(U_2)}$ at which the eigenvalues change their property from entirely real to imaginary is given by

$$\gamma_c^{(U_2)} = |t_1 - t_2|. \tag{6.5}$$

Figure 6.2 shows real and imaginary parts of the single-particle energies of a chain with open boundaries and $L = 32$ in both the topologically trivial and nontrivial dimerization. In the first, the spectrum reproduces the expected behavior of equation (6.4) (see figure 6.2b) as the missing weak bond from last to first site in the periodic system may be neglected without significant effects. In addition to this behavior, the edge states occurring in the open chain with nontrivial dimerization (compare zero-energy modes in figure 6.2b) immediately break the $\mathcal{PT}$ symmetry of the Hamiltonian while the remaining bulk states act like in the trivial phase. This is trivially obtained, using the shape of an edge state (see figure 2.3d) and the statement on page 39 that eigenstates of an entirely real spectrum of a non-Hermitian Hamiltonian are necessarily eigenstates of $\mathcal{PT}$ as reference, because an edge state is obviously not an eigenstate of the latter. Thus, the $\mathcal{PT}$ symmetry of the nontrivial phase is broken for finite values of γ.

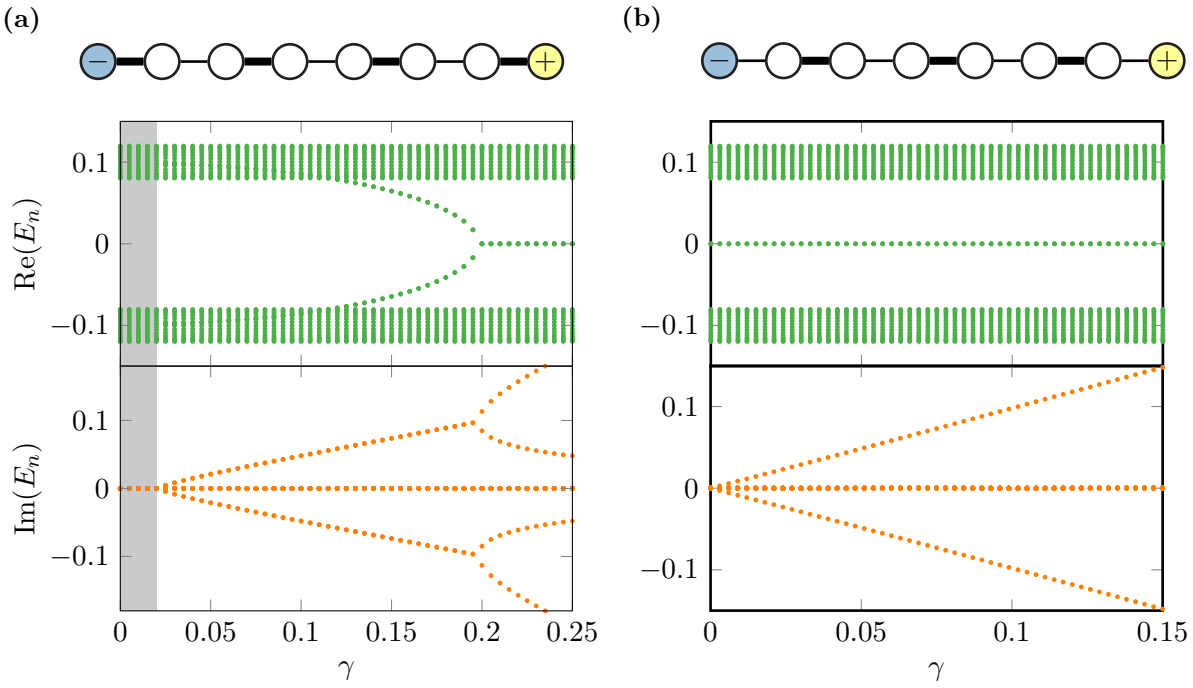

Figure 6.3.: Real and imaginary parts of the single-particle energies of an open chain with $L = 32$ and U_1 with $\mathcal{PT}$-unbroken phases shaded in gray. (a) In the trivial dimerization ($t_1 = 0.1, t_2 = 0.02$) the real part of the energies of all but four bulk states is independent from the gain/loss parameter γ. The aforementioned states start to separate from the Bloch bands accompanied by a breaking of $\mathcal{PT}$ symmetry and finally become purely imaginary after a bifurcation. (b) The imaginary part of the bulk and edge states in the nontrivial dimerization pattern ($t_1 = 0.02, t_2 = 0.1$) is completely unaffected by γ, while edge states again break the $\mathcal{PT}$ symmetry for finite γ.

Moreover, the potentials U_1 and $U_1^{(c)}$ which unfortunately do not allow to be treated analytically also lead to a stable $\mathcal{PT}$-unbroken phase in the nontrivial dimerization under small perturbations parameterized by γ (see figures 6.3 and 6.4). Instead of the whole Bloch band bending towards the imaginary axis leading to purely imaginary energies in the case of U_2, the real part of all but a fixed number of states in the Bloch band is not affected by the dissipation described by both potentials. Though not analytically accessible, many aspects of the single-particle spectra can be explained by adopting the view of the fully-dimerized limit (compare figure 2.4), which is to a certain extent fulfilled by the choice of the tunneling amplitudes in figures 6.3, 6.4. Then, the similarity of the spectra in the trivial dimerization, figures 6.3a, 6.4a follows directly as both systems contain $(L-4)/2$ Hermitian double-wells and two non-Hermitian double-wells, either with gain or loss, all of which are weakly coupled. Note however that this does not mean that the states bending towards zero real part are the same in both scenarios, as will become clear in the next section, in which the many-particle perspective will be tackled. In the same fashion, the critical value $\gamma_c^{U_1}$ for the trivially dimerized configuration with $U_1^{(c)}$ can be derived when gain and loss are located on a strongly coupled dimer which

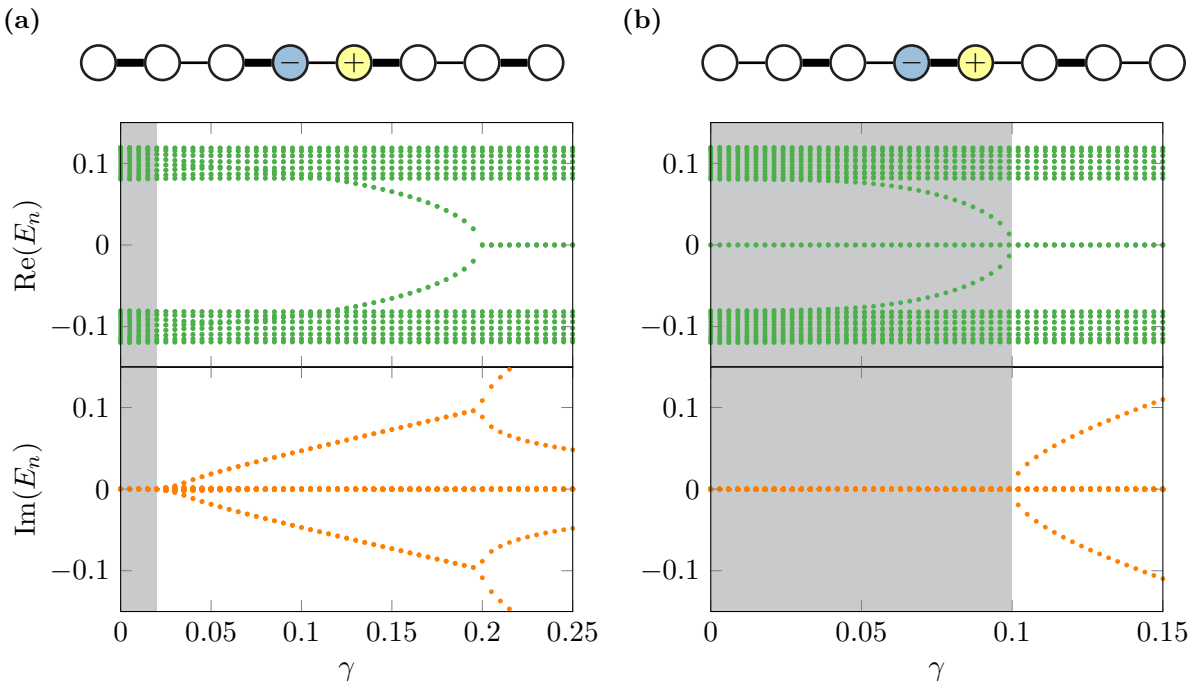

Figure 6.4.: Single-particle energies of an open chain with $L = 32$ and $U_1^{(c)}$ with the $\mathcal{PT}$-unbroken phase highlighted in gray. (a) The trivial dimerization ($t_1 = 0.1, t_2 = 0.02$) exhibits the same behavior as in the case of U_1, compare with figure 6.3b. The reason for this will become clearer in the many-particle picture, see section 6.2. (b) In the nontrivial dimerization ($t_1 = 0.02, t_2 = 0.1$) two bulk states bend to zero real part, which is accompanied by breaking of the $\mathcal{PT}$ symmetry after their arrival and can be understood by a simple dissipative double-well model. Interestingly, the edge states from the Hermitian case still have real eigenvalues as they are only supported at the boundaries and do not reach into the bulk, where the dissipative impurity is located.

can be treated separately besides its Hermitian equivalents, as is the case for the system in figure 6.4b. To do so, one may again employ the familiar double-well matrix model introduced in equation (3.18), but now with a real tunneling amplitude t_1 and single-particle loss (gain) at the left (right) well. The Hamiltonian of such a dissipative dimer is given by

$$\boldsymbol{H} = -\begin{pmatrix} \mathrm{i}\gamma & t_2 \\ t_2 & -\mathrm{i}\gamma \end{pmatrix} \tag{6.6}$$

with eigenvalues $E_\pm = \pm\sqrt{t_2^2 - \gamma^2}$ that are real as long as $|t_2| < |\gamma|$. Consequently, when all dimers of the chain can approximately be regarded as decoupled the critical value is $|\gamma_c^{(U_1)}| \approx |t_2|$, which is in perfect agreement with the illustration 6.4b.

In addition, a unique feature in the nontrivial dimerization pattern appears for $U_1^{(c)}$ as particle gain and loss are located in the interior of the system. Hence, the Hermitian zero-energy edge modes which are located only at the boundaries of the system are

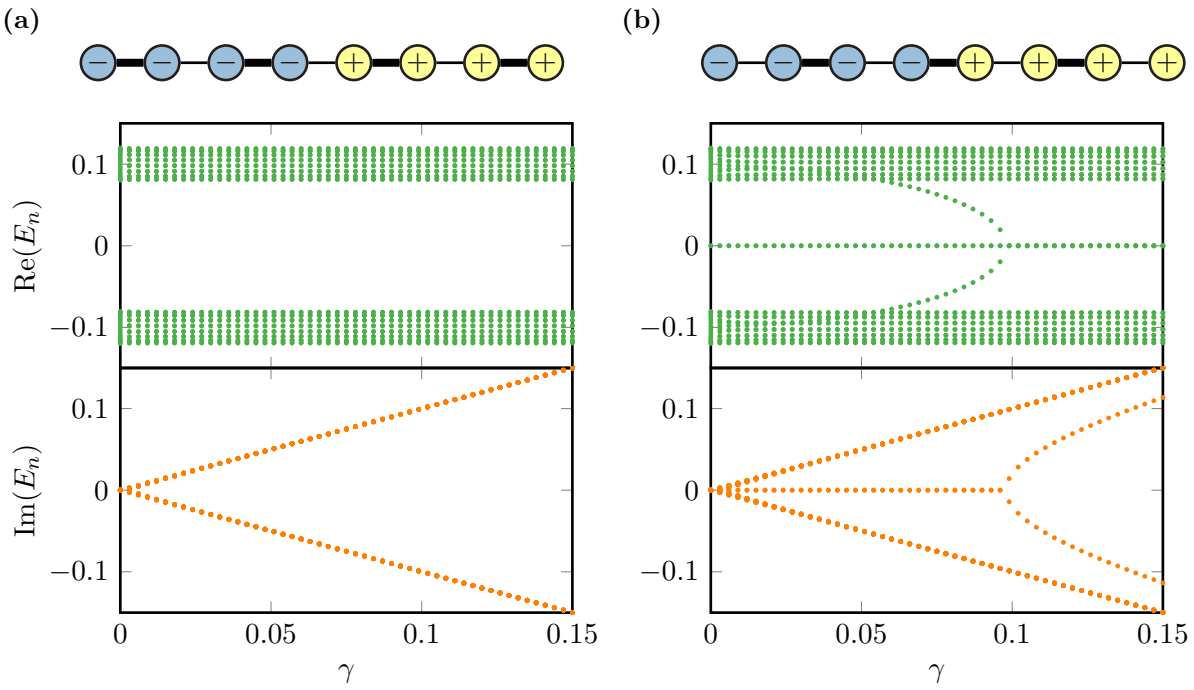

Figure 6.5.: Real and imaginary parts of the single-particle spectra of a system with $L = 32$ and U_3. (a) In the trivial dimerization ($t_1 = 0.1, t_2 = 0.02$) all real parts of the bulk states are resistant to γ but the $\mathcal{PT}$ symmetry breaks immediately. (b) Two bulk states bend towards the imaginary axis in the nontrivial dimerization ($t_1 = 0.02, t_1 = 0.1$) leading to additional "zero-energy" modes.

effectively uninfluenced by the dissipative impurity in the center, and therefore do *not* correspond to imaginary energies, contrary to the scenarios of the other potentials in which gain and loss are always present at the system boundaries.

The only potential immediately breaking the Hamiltonian's $\mathcal{PT}$ symmetry in both dimerizations is given by U_3, see figure 6.5. While the real parts of almost all the Bloch band energies are unaffected by γ, two states bend towards real part zero in the nontrivial dimerization (figure 6.5b), which can be identified with the analogous process for $U_1^{(c)}$ (figure 6.4b) caused by the centering double-well with adjacent gain and loss.

If one temporarily ignores the imaginary parts of the energies, three different scenarios can be identified in the spectra of the potentials U_1, $U_1^{(c)}$ and U_3, compare figures 6.3a, 6.4a, 6.4b and 6.5b: (i) for small values of the gain/loss parameter γ all bulk states are stable, (ii) intermediate values of γ lead to several bulk states bending towards zero energy and (iii) increasing γ to a critical value those bulk states arrive at zero energy where they remain for larger values of the gain/loss strength. In other words, the influence of gain and loss can lead to *additional* zero-energy modes triggering the speculation that the topology of the system's many-body "ground state" (whose definition in the non-equilibrium case is not obvious) might be affected as well.

Thus, if a way to interpret the imaginary parts of the spectrum is found, which in the case of hard-core bosons (or fermions) can be accomplished by interpreting $\mathrm{Im}(E_n)$ as a *decay rate*, one may speak of "dissipatively driven zero-energy modes" in the system.

6.2. Low-energy spectra for different potentials

As outlined in the previous section the different complex on-site potentials considered in the single-particle picture show varying effects depending on both the dimerization of the chain and the strength of particle gain/loss. Now, the many-particle view will be assumed in order to relate both investigations. To do so, some comments about the physical constraints underlying the interpretation of results in this section are inevitable.

Since bosons are not restricted by Pauli's exclusion principle, adding particle gain on a single lattice site can in principle lead to the system infinitely filling up with particles. Besides the fact that such an *amplification* spoils any trace of the system properties (for instance edge states or other topological effects), it contradicts to the approximation of a weak coupling between the system and reservoir, which builds the foundation for the master equations in Lindblad form and is therefore also deeply rooted in the motivation of using complex on-site potentials away from the mean-field limit. The following investigations will thus be restricted to the low-energy regime (no amplification) of the non-Hermitian SL-BHM in the strongly-interacting regime. Although those assumptions seem to be very restrictive, they lead to an impressive agreement with results obtained in the treatment of hard-core bosons in the framework of master equations in Lindblad form (see chapter chapter 8). The amplification problem will be targeted in sections 8.3, 8.4 and can basically be reduced to the problem of finding a proper setup of Lindblad operators guaranteeing for a compensation between gain and loss effects.

Throughout this section, the non-Hermitian DMRG code presented in section 5.3 is employed using the local site cutoff $D = 5$ and a dynamical adaption of the number of states kept in the truncation to keep the truncation errors $\varepsilon < 10^{-9}$ during the build-up procedure and improving the accuracy by decreasing the latter to $\varepsilon < 10^{-10}$ in the sweeping process, which should yield accurate results (an online article dealing with the proper choice of DMRG hyper-parameters such as the truncation error or the number of sweeps can be found on the homepage of the Itensor C++ library[1]). As an incidental remark, note that for smaller systems the accordance of the non-Hermitian DMRG code with results from exact diagonalization has been verified.

The interest is on the effects on the topologically interesting $\rho = 1/2$ MI phase of the SL-BHM. Instead of studying consequences of varying chain dimerization (see chapter 2), the tunneling amplitude ratio is kept fixed, sweeping the gain/loss parameter γ.

[1] http://itensor.org/index.html

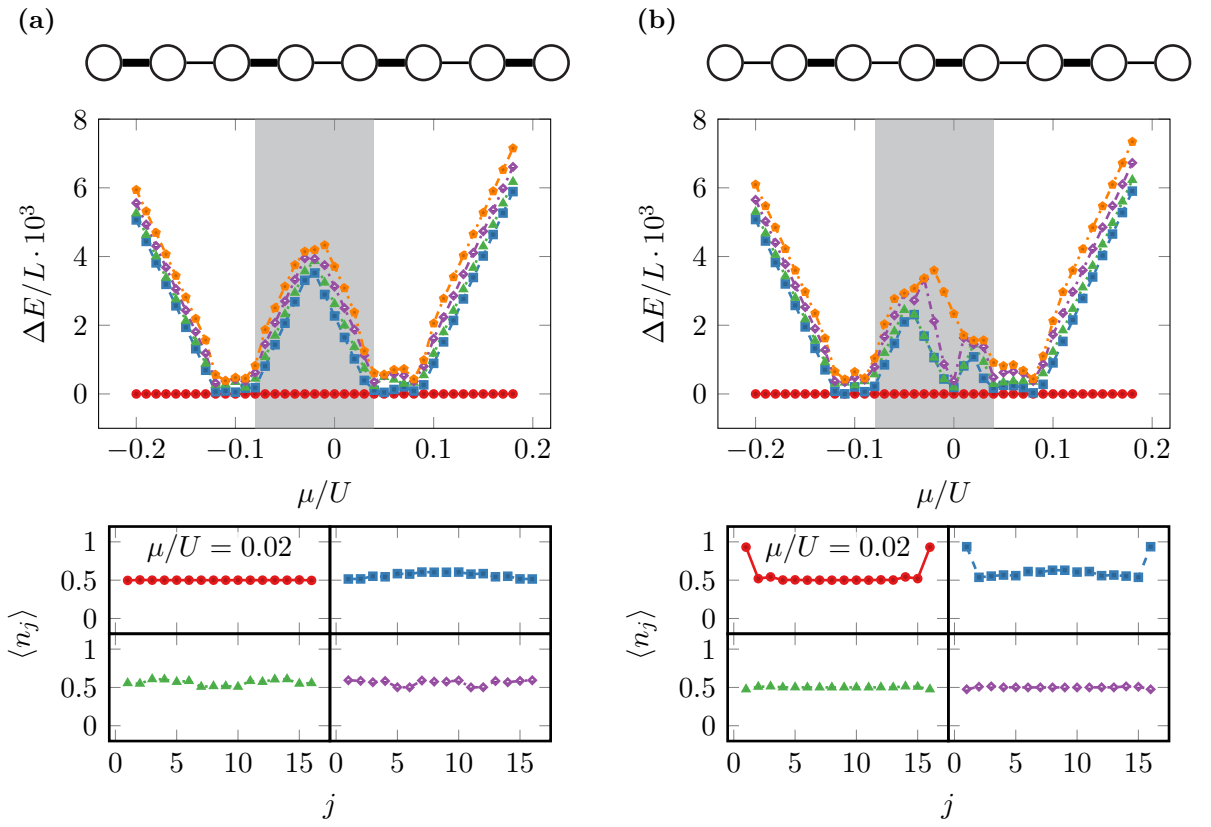

Figure 6.6.: Low-energy spectrum and states of the SL-BHM (open chain with $L = 16$) around $\mu/U = 0$ for (a) the trivial $(t_1/U = 0.1, t_2/U = 0.02)$ and (b) the nontrivial dimerization pattern $(t_1/U = 0.01, t_2/U = 0.1)$. Top panel: Sketch of both systems for $L = 8$ and energy gap $\Delta E/L$ per lattice site between the ground (red circles) and the first few excited states. The gapped $\rho = 1/2$ MI phase is highlighted in gray. Bottom panels: Particle number expectation values of the first excited states at $\mu/U = 0.02$. Colors and markers correspond to those of the energies in the top panels.

In particular, the two dimerizations are chosen to be $t_1/U = 0.1, t_2/U = 0.02$ (trivial pattern) and $t_1/U = 0.02, t_2/U = 0.1$ (nontrivial scheme). Figure 6.6 contains sketches of both system setups in the Hermitian case where thick lines that join two sites are associated with the larger tunneling amplitude.

The low-energy spectrum, or more precisely the energy gap (per lattice site) between the many-particle ground state and the first few excited states obtained by DMRG is shown for the trivial (figure 6.6a) and nontrivial dimerization (figure 6.6b) of a chain with $L = 16$. The closing and reopening of the energy gap associated with the phase transition of the model from $\rho = 0$ MI to superfluid to $\rho = 1/2$ MI to superfluid to $\rho = 1$ MI is clearly visible (see also figure 3.2a for the phase diagram). In the chemical potential regime of the $\rho = 1/2$ MI phase highlighted in gray the gap closes once more at $\mu/U \approx 0$ in the nontrivial dimerization, in which the topological edge states in the

ground state change from hole to particle type. Choosing a fixed chemical potential value of $\mu/U = 0.02$ results in the ground state represented by a flat $\rho = 1/2$ MI state in the trivial and an edge state with both occupied boundaries for the nontrivial dimerization as can be seen in the lower panels of figure 6.6, which show the lattice occupation of the ground and the first excited states. The excited states of the trivial phase are given by adding another particle to the bulk that delocalizes over the entire lattice in form of Bloch waves. The same applies to the nontrivial dimerization where interestingly the edge feature is still present in the first excited state and higher states are also obtained by removing a particle from the edge such that the system is half-filled.

The interpretation of the following spectra is somewhat difficult as complex energies, especially in the bosonic case, would lead to an amplification of the system for states corresponding to energies with positive imaginary part and a decay for the negative equivalent. With the restrictions on the spectrum explained above, the investigated regime should therefore properly reproduce the behavior of the system for time scales during which the reservoir does not heat up the system too much (small real part of the energy) such that occupations with multiple bosons are avoided. Chapter 8 will illustrate that this interpretation in most cases leads to the same effects that are observed in the steady state of an equivalent master equation in Lindblad form.

One subtle aspect has to be addressed before moving on: the aforementioned approach towards the interpretation of complex spectra induces that the states contributing most to the dissipative low-energy behavior are constraint to (i) small real parts and (ii) large imaginary parts of the respective energies. Using DMRG only one constraint, namely the first is realized by targeting a number of ~ 10 states associated with the lowest lying real parts in the spectrum. Such a small number of states may not be sufficient to obtain the state satisfying the second condition as well. Therefore the investigation of the different gain/loss patterns shall rather serve as an indicator of generic features appearing in the system. In fact, combining additional information about the properties of the steady state, exact diagonalization studies realizing both constraints can be performed and one finds the desired states from the description with complex on-site potentials to *correctly reproduce* the steady state of the equivalent master equation, which represents a *remarkable* result that is left for the end of this chapter.

To start off with the many-particle description of the SL-BHM with complex on-site potential U_1, figure 6.7 shows the real and imaginary parts of the energies in the low-energy regime for varying strengths of gain and loss. As in the single-particle case of nontrivial dimerization (compare figure 6.3b), in which the real parts of the energies are completely unaffected by the dissipation introduced within U_1 and only the zero-energy edge modes break the $\mathcal{PT}$ symmetry, the real part of the spectrum in the interacting many-particle case neither shows a strong dependence on γ nor a crossing of states (top panels of figure 6.7b). A $\mathcal{PT}$-symmetric many-body state with two occupied edges represents the "ground state" of the system whose stability however is questionable as the

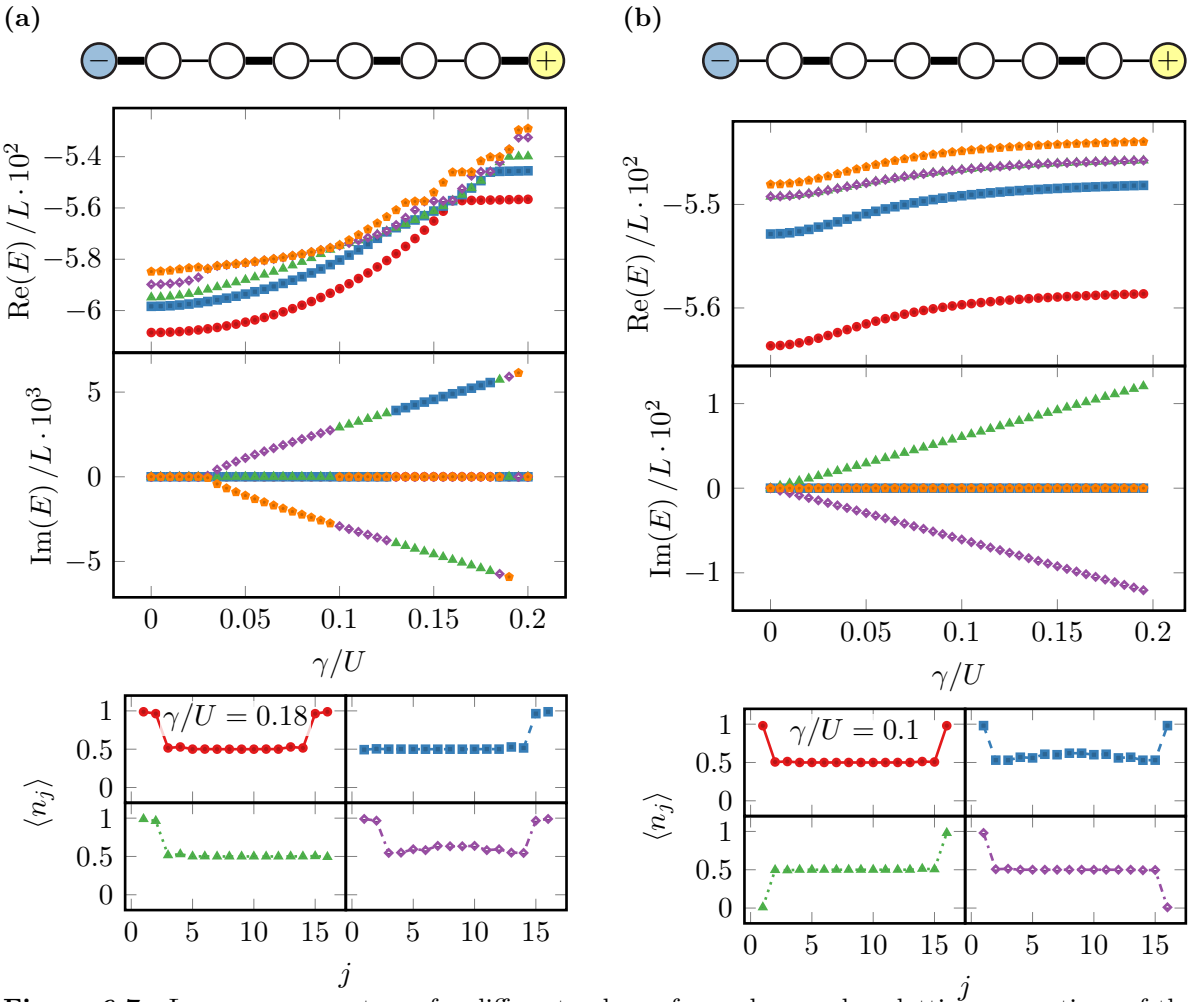

Figure 6.7.: Low-energy spectrum for different values of γ and exemplary lattice occupations of the first excited states of an SL-BHM chain with length $L = 16$ and $\mu/U = 0.02$ superposed with U_1. (a) In the trivial dimerization ($t_1/U = 0.1, t_2/U = 0.02$) the $\mathcal{PT}$ symmetry of the shown fraction of states is unbroken up to $\gamma/U \approx 0.02$. The $\mathcal{PT}$-broken states are given by edge states in the Hermitian nontrivially dimerized subsystem (white sites only), while the sites subject to gain and loss effectively decouple from the rest of the system. The plots are sorted for ascending real part leading to sudden color changes in the imaginary part. (b) The nontrivially dimerized phase ($t_1/U = 0.02, t_2/U = 0.1$) immediately breaks the $\mathcal{PT}$ symmetry with gain and loss favoring the occupation of an edge indicated by a positive imaginary part of the energy (green triangles).

spectrum is complex for finite γ. The two $\mathcal{PT}$-broken states (green triangles and purple diamonds) result from an occupied and an unoccupied edge. As one would expect, the favored state associated with a positive imaginary part of the energy belongs to a configuration with occupied right edge and empty left boundary. In the trivial dimerization, the $\mathcal{PT}$ symmetry of the system is unbroken for small values of γ in the part of the spectrum shown in figure 6.7a (top panel), which is consistent with the observation in the single-particle spectrum (figure 6.3a). The transition to the $\mathcal{PT}$-broken phase is

accompanied by the occurrence of states that are characterized by a fixed occupation of the sites subject to gain and loss combined with an edge state in the interior system. This effect can be interpreted as an *effective decoupling* of the dissipative sites from the rest of the Hermitian system, which is then a nontrivial chain with edge states whose occupations are influenced by the dissipative sites. Thus, the states bending towards zero real part in the single-particle energy spectrum are given by the edge modes of the Hermitian subsystem of sites 2 to $L-2$.

This leads to the following reinterpretation of the three stages mentioned in the last section (page 71): (i) for small coupling strengths γ gain and loss processes induce currents, which however can be compensated by the system that is therefore still $\mathcal{PT}$-unbroken, (ii) at a certain point the currents cannot be balanced by the system anymore and the dissipative sites start to fill or empty. Simultaneously, the sites more and more decouple from the system and are solely influenced by the dissipative effects located on them. If the remaining subsystem is given by a nontrivially dimerized chain this triggers some of the original bulk states to deform into edge states of the latter and (iii) when the decoupling of the dissipative sites is completed, the remaining system possesses zero (real part) energy modes given by the empty or filled isolated dissipative sites *plus* edge modes of the Hermitian subsystem which also have an energy real part of zero. The imaginary parts give some indication about whether the dissipative setup leads to an occupation of the state or not.

Carrying over this notion to the case of $U_1^{(\mathrm{c})}$, one expects new edge states to emerge in the spectrum whenever the Hermitian subsystem obtained by neglecting the dissipative sites of the chain possesses a nontrivial boundary, which is the case for a total chain of trivial dimerization shown in figure 6.8a. Indeed after the $\mathcal{PT}$ phase transition at $\gamma/U \approx 0.02$ $\mathcal{PT}$-broken states with edge features at the neighboring sites of the dissipative impurity appear (blue squares and green triangles). While the occupation of the edge state located on the subsystem adjacent to the gain site is favored (positive imaginary part), the equivalent next to the loss site will decay leaving an empty edge (negative imaginary part). In the single-particle picture of figure 6.4a the four bending states are given by particles directly localized on the two dissipative sites and two edge states located at the arising nontrivial boundaries in the Hermitian remainders of the chain. Contrary to this, the decomposition of the nontrivially dimerized chain subject to $U_1^{(\mathrm{c})}$ does not lead to further nontrivial boundaries hosting edge states. The $\mathcal{PT}$-broken states only show features directly on the dissipative sites (compare figure 6.8b). In consistence to that, only two instead of four states represented by the two degrees of freedom on the dissipative impurity bend towards the imaginary axis in the single-particle picture, see figure 6.4b. Note that the spectrum of figure 6.8b illustrates that the many-particle DMRG simulation is not capable of resolving the entire spectrum which is expressed in the artifacts around $\gamma/U \approx 0.01$ to 0.09 that indicate the $\mathcal{PT}$ phase transition although a subset of entirely real eigenvalues is obtained from $\gamma/U \approx 0.09$ to 0.15.

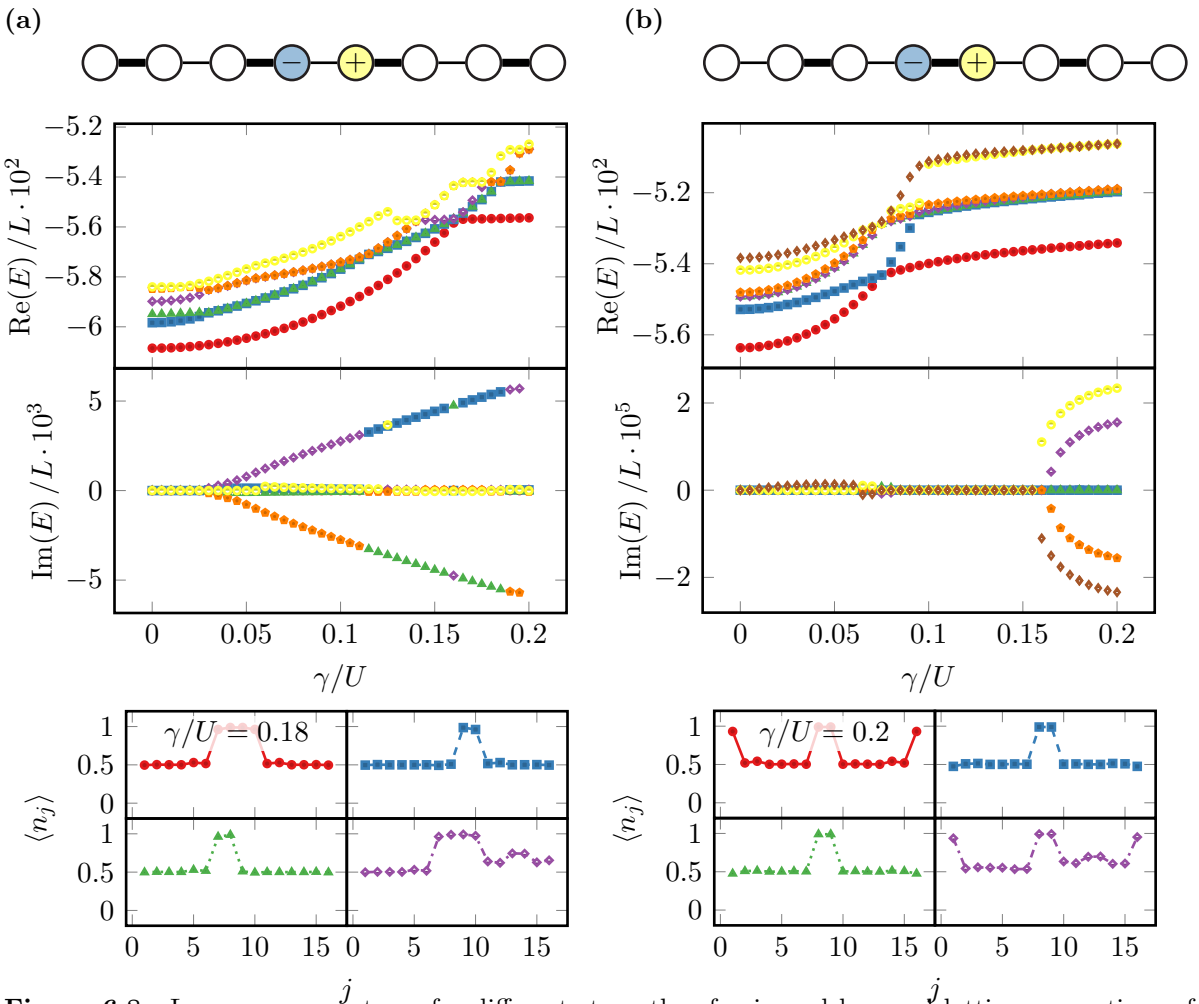

Figure 6.8.: Low-energy spectrum for different strengths of gain and loss and lattice occupations of the excited states of an SL-BHM chain with length $L = 16$ and chemical potential $\mu/U = 0.02$, superposed with $U_1^{(c)}$. (a) The trivial chain with a dissipative impurity is $\mathcal{PT}$-unbroken up to $\gamma/U \approx 0.02$. After the $\mathcal{PT}$ transition edge features appear at the Hermitian subsystem and are clearly visible in the low-energy states. The imaginary part of the spectrum leads to the conclusion that the occupation of the edge state on the left half will be avoided while the filling of the equivalent on the right subsystem is preferred. (b) In the nontrivial chain the Hermitian remainder does not possess an additional nontrivial boundary. Hence no additional edge features emerge, except for the occupation of the dissipative sites.

This problem becomes even more intriguing for the case of the complex on-site potential U_2. Although such a system may possess a large $\mathcal{PT}$-unbroken regime, the phase transition in the single-particle picture is accompanied by a change of the eigenvalues from entirely real to *purely imaginary*, compare figure 6.2. Such a behavior fits into the list of effects observed so far for the other potentials as now all sites are subject to dissipation, thus *all* bulk states will deform to result in localized particle states at one site each for large values of γ. Hence a band structure with almost degenerate real parts

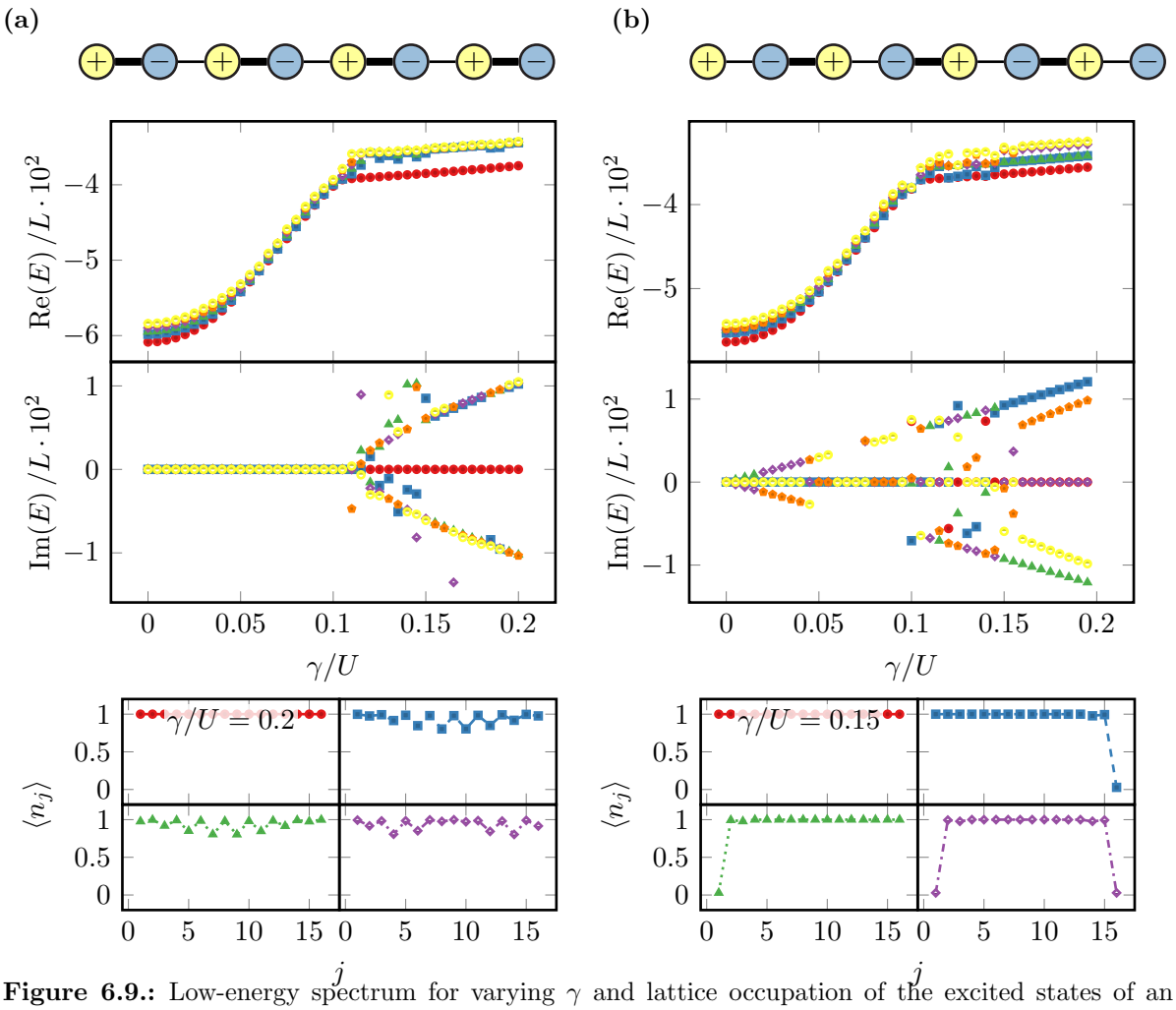

Figure 6.9.: Low-energy spectrum for varying γ and lattice occupation of the excited states of an SL-BHM chain with length $L = 16$, $\mu/U = 0.02$ and alternating gain and loss described by U_2. (a) The trivial chain is $\mathcal{PT}$-unbroken until $\gamma/U \approx 0.1$ and after the $\mathcal{PT}$ transition the states start to fill up with particles, which is a consequence of the inadequate target sector of DMRG and does not lead to the expected behavior. Note however that the bulk staggering in the excited states is a very well expected feature. (b) In the nontrivial chain the filling of the bulk is also an incorrect feature produced by the limitations of DMRG. At least the edge features in the excited states give rise to a different behavior in comparison to the trivial chain.

is expected in the interacting many-body $\mathcal{PT}$-broken regime of a chain with alternating gain and loss, which lets the DMRG algorithm struggle when targeting for the lowest real parts. Indicators of this behavior are given by the noisy imaginary parts of the spectra in figure 6.9, which nevertheless have been included at this point for completeness. The large $\mathcal{PT}$-unbroken parameter regime of the trivial chain (figure 6.9a) up to $\gamma/U \approx 0.1$ is still correctly produced by DMRG, and encourages the statement that the effects observed in the lattice occupation of the excited states in the $\mathcal{PT}$-broken phase are *not* in accordance with the Lindblad scenario. This can be traced back to the lim-

itations of realizing the second constraint mentioned above within DMRG. While one expects the chain to fill up with particles on the gain sites with loss sites simultaneously emptying in the $\mathcal{PT}$-broken phase leading to a staggered occupation of the chain, the states shown in the lower panel of figure 6.9a do not exhibit this behavior. At least a sign of staggered occupation is visible in the excited states (blue squares, green triangles, purple diamonds). Consequently, the states shown in figure 6.9 are not the most important configurations in the dissipative behavior of the system. The results obtained for the nontrivially dimerized chain shown in figure 6.9b lead so a similar conclusion: the excited states in the $\mathcal{PT}$-broken regime simply do not represent the most important states as DMRG is not capable of simultaneously targeting smallest real *and* largest imaginary parts.

It is a general observation that the explained problem occurs whenever a large number of single-particle states breaks the $\mathcal{PT}$ symmetry, as is the case for U_2 and U_3, see figures 6.2, 6.5. In the single-particle picture many complex eigenvalues lead to many degrees of freedom to get a complex energy in the many-body view. In such cases the states with largest imaginary part are not accessible to the DMRG setup chosen in this section, which may then only be employed to investigate a fraction of the spectrum in order to obtain hints whether the system is in the $\mathcal{PT}$-unbroken phase or not.

With that said, it is not surprising that the states representing the first excited states in the dissipative system subject to U_3 (lower panels of figure 6.10) do not possess the expected filling of the right half of the system while emptying the left half completely. In accordance with the single-particle picture, the $\mathcal{PT}$ symmetry of both configurations is immediately broken. Nevertheless, the notion of a bipartitioning of the system for increasing gain/loss strength is still present in the lattice occupations (see for instance the lower panel of figure 6.10a). Similar to the effects shown for $U_1^{(c)}$, there may be additional edge modes when the boundary between gain and loss is located on a strong bond (compare figure 6.10b), which is also illustrated by the two bulk states bending towards zero real part in the single-particle representation, figure 6.5a.

Unfortunately, the huge number of many-body states in the low real part regime of the spectrum does not allow for DMRG to access all states because it is restricted to a number of ~ 10 target states. Now, the dimensionality of the system will effectively be broken down until it is manageable by exact diagonalization since the large sparse eigensolver employed in the latter is capable of computing ~ 50 eigenstates for a sufficiently small dimension of the problem and one might then choose the state with largest imaginary part from this subset to yield the most dominating state of the system.

To do so, the site dimension of the system is cut to $D = 2$ as low real parts in the energy spectrum in the strongly-interacting limit can only be realized by avoiding multiple occupations of a single site. Moreover, for the steady state of a system with at most one particle per site one can derive the condition that the number of particles located

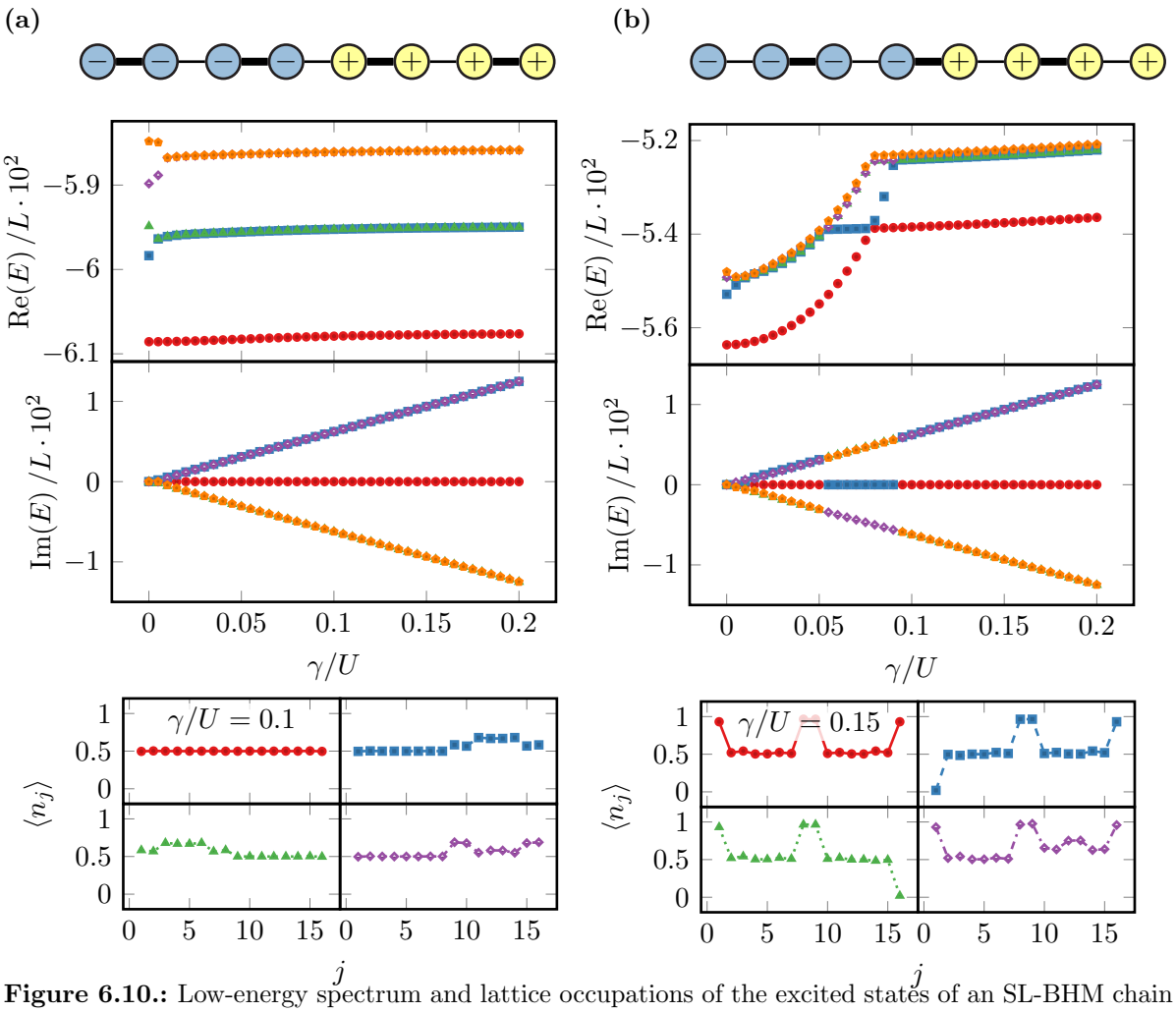

Figure 6.10.: Low-energy spectrum and lattice occupations of the excited states of an SL-BHM chain with length $L = 16$ and $\mu/U = 0.02$ subject to U_3. Both configurations break the $\mathcal{PT}$ symmetry for finite γ. (a) The states shown for the trivial chain are not the most important configurations in the dissipative behavior but still contain the idea of a bipartitioning of the system at the boundary between gain and loss. (b) In consistence with the single-particle picture where bulk states bend towards the imaginary axis, edge effects appear in the states when the boundary of gain and loss is located on a strong bond.

on the loss sites is equal to the number of holes on the gain sites for identical gain and loss parameters (see equation (8.15) in chapter 8), that is

$$\sum_{j_{\mathrm{gain}}} \left(1 - \langle n_{j_{\mathrm{gain}}} \rangle\right) = \sum_{j_{\mathrm{loss}}} \langle n_{j_{\mathrm{loss}}} \rangle \,, \tag{6.7}$$

where $j_{\mathrm{gain}}, j_{\mathrm{loss}}$ denote the indices of the sites subject to gain and loss respectively. For U_2 and U_3 where all sites are exposed to gain and loss this directly leads to the

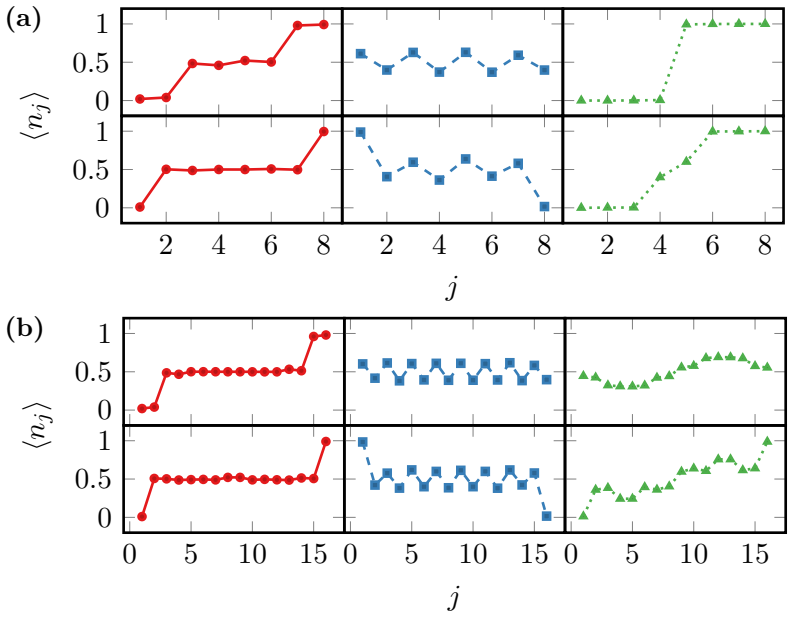

Figure 6.11.: Lattice occupation of the low-energy states with largest imaginary part at half filling obtained by exact diagonalization (by picking the desired state from the lowest 70) for the trivial (top rows) and nontrivial dimerization (bottom rows) where the system parameters are chosen equal to the previous spectra. The potentials are U_1 (left column), U_2 (center column) and U_3 (right column) with $\gamma/U = 0.1$. Additional parameters are (a) $L = 8$, $D = 4$ and (b) $L = 16$, $D = 2$.

condition

$$\frac{L}{2} = \sum_{j_{\text{loss}}} \langle n_{j_{\text{loss}}} \rangle + \sum_{j_{\text{gain}}} \langle n_{j_{\text{gain}}} \rangle = \sum_{j} \langle n_j \rangle = \langle N \rangle \,, \tag{6.8}$$

which means that the steady state is *at half filling* of the lattice and the diagonalization procedure can thus be restricted to only this invariant particle number subspace.

Under those assumptions figure 6.11 contains the lattice occupations of the state with the largest imaginary part obtained from the computation of the 70 lowest lying states (real part) within exact diagonalization for an intermediate dissipative strength of $\gamma/U = 0.1$ of the complex potentials U_1, U_2 and U_3 in the two distinct dimerization patterns. Two different system lengths and site dimensions are chosen such that both figure 6.11a and 6.11b illustrate all effects that are also observed in the steady state computation performed in chapter 8. The system properties of the different dissipative patterns can be summed up as follows:

- The lattice occupation profile of the Hermitian subsystem in a total system subject to U_1 (red circles) is still flat with $\rho = 1/2$ and the occupations of the gain (loss) sites at the open boundaries are fixed to 1 (0). In the trivial dimerization (top row of each subfigure) where the subsystem is nontrivially dimerized, additional edge modes whose occupation is fixed by the outer dissipative sites appear in the state.

- In case of the potential U_2 (blue squares) the bulk occupation becomes staggered and the staggering increases for larger values of γ. The trace of the edge modes in

the nontrivial chain, whose occupation is determined by the type of dissipation on the most outer sites is still present.

➢ U_3 (green triangles) leads to different shapes of the most important state depending on the gain/loss strength and system size. While there are wave-like excitations in the left and right half of the system where the features of edge modes are still clearly visible (figure 6.11b), there exists also a phase in which all dissipative sites are completely filled or empty and only the occupation of the centered double-well in the transition from gain to loss can still be balanced (compare figure 6.11b).

Chapter review

➢ Different complex on-site potentials are employed to study dissipative effects on the $\rho = 1/2$ MI phase of the SL-BHM. While the interpretation of the $\mathcal{PT}$-unbroken phase is straightforward, the $\mathcal{PT}$-broken phase requires additional treatment.

➢ Since a bosonic system may in principle suffer from an infinite amplification by gain processes, the investigation of the dissipative behavior is restricted to weak couplings (low real parts in the energies, i.e. no double occupancies) of the reservoir.

➢ In the single-particle picture, it is observed that for the potentials $U_1, U_1^{(c)}$ and U_3 a limited number of bulk states is deformed towards energy real part zero for increasing strengths of the gain/loss parameter γ. Working in the many-particle picture, those states are identified as (i) localized particles at dissipative sites and (ii) zero-energy edge modes of the remaining Hermitian subsystem(s). This process is interpreted in terms of the dissipative sites *effectively decoupling* from the rest of the system, which shall be investigated in more detail in the next chapter. If the imaginary part of the energy of such a state is positive, its occupation is favored by dissipation, while a negative imaginary part leads to an unoccupied state.

➢ For potentials with only a few dissipative sites, non-Hermitian DMRG can be employed successfully to study the important states of the system, that is the low-energy states with largest imaginary part. For the potentials U_2, U_3 with a large number of dissipative sites only one constraint (small real part) can be ensured and DMRG is limited to only a small number of states such that the important ones may not be contained in the targeted subset. After additional assumptions about the properties of the steady state in the Lindblad master equation framework, the same states can also be obtained by exact diagonalization, see chapter 8.

7. Topological invariant for the $\mathcal{PT}$-symmetric SL-BHM

In this chapter the topological invariant ν for the SL-BHM introduced in chapter 3 is generalized to the non-Hermitian case. This is done by carrying over the arguments employed in sections 2.3 and 3.3 leading to a quantized *complex Berry phase* whose quantization is protected by $\mathcal{PT}$ symmetry giving rise to topologically protected edge states in the $\mathcal{PT}$-unbroken phase. Such states have already been found in optical structures that obey equations analogous to those of $\mathcal{PT}$-symmetric quantum systems [4]. Their construction, together with the generalization of ν are the subject of section 7.1.

Practically, the construction of ν relies on Hatsugai's proposal [46] to use Berry phases as local order parameters. Even in the non-quantized scenario those quantities can be employed to describe the correlation between adjacent sites, which is used in section 7.2 to follow the decoupling process of the dissipative lattice sites for increasing strengths of gain and loss observed in the previous chapter.

7.1. Complex Berry phase for interacting systems

In order to extend the concept of Berry's phase to non-Hermitian Hamiltonians one can adopt the view taken in section 2.3 where the Hamiltonian $H_0(\underline{R}) = H_0^\dagger(\underline{R})$ parameterized by a set of parameters $\underline{R} \in \mathscr{P}$ is transported along a closed loop $\mathscr{C}$ in parameter space $\mathscr{P}$ [85]. Since the Berry phase describes a geometric phase that is picked up by the ground state of the Hamiltonian during the transport along $\mathscr{C}$ one is left with finding an expression for the relative phase between the ground states at two infinitesimally distant points in parameter space in a version of $\mathscr{C}$ discretized into M points $\underline{R}_1, \underline{R}_2, \ldots, \underline{R}_M$ with $\underline{R}_{M+1} \equiv \underline{R}_1$ and $M \to \infty$.

For a Hermitian Hamiltonian, this phase between say $\underline{R}_1$ and $\underline{R}_2$ (see equation (2.14a)) required only knowledge of the right ground states $|\psi_{1,2}\rangle$, from which the dual representations $\langle\psi_{1,2}|$ are trivially obtained and the normalization conditions $\langle\psi_{1,2}\,|\,\psi_{1,2}\rangle = 1$ ensure that a gauge-transformation (equation (2.15)) does not affect the phase picked up on a *closed* loop. Those properties of the *Hermitian phase* between nonorthogonal states on a closed loop is nicely illustrated by figure 2.6b.

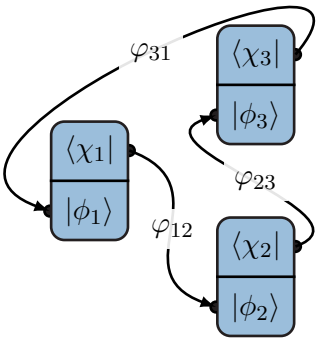

Figure 7.1.: Relative non-Hermitian phase $\varphi_{\mathscr{C}} = \varphi_{12} + \varphi_{23} + \varphi_{31}$ between a discrete set of three states arranged on a loop $\mathscr{C}$. Phases between neighboring points are evaluated by contraction between the states that are joined by arrows. By construction $\varphi_{\mathscr{C}}$ is a gauge-invariant quantity. Note the unmistakable resemblance to figure 2.6b.

In case of a non-Hermitian Hamiltonian $H(\underline{R}) \neq H^\dagger(\underline{R})$, the dual representation of a (right) ground state $|\phi\rangle$ is given by the left ground state $\langle\chi|$ (see equation (4.19)) with the normalization condition

$$\langle\chi\,|\,\phi\rangle = 1. \tag{7.1}$$

This motivates the following relation for the phase φ_{12} between two ground states $(|\phi_1\rangle, \langle\chi_1|)$ and $(|\phi_2\rangle, \langle\chi_2|)$ represented by the left and right eigenvectors $|\phi_i\rangle, \langle\chi_i|$ at the points $\underline{R}_1, \underline{R}_2$ in parameter space, respectively,

$$\varphi_{12} = -\arg(\langle\chi_1\,|\,\phi_2\rangle) \quad \Longrightarrow \quad \mathrm{e}^{-\mathrm{i}\varphi_{12}} = \frac{\langle\chi_1\,|\,\phi_2\rangle}{|\,\langle\chi_1\,|\,\phi_2\rangle\,|}, \tag{7.2a}$$

or, in the same manner as equation (2.14a),

$$\varphi_{12} = -\mathrm{Im}(\ln(\langle\chi_1\,|\,\phi_2\rangle))\,. \tag{7.2b}$$

Again, φ_{12} is not gauge-invariant, but when the non-Hermitian phase $\varphi_{\mathscr{C}}$ of the states $(|\phi_1\rangle, \langle\chi_1|), \ldots, (|\phi_M\rangle, \langle\chi_M|)$ arranged on the loop $\mathscr{C} = (\underline{R}_1, \ldots, \underline{R}_M, \underline{R}_{M+1} = \underline{R}_1)$ is computed by (compare equation (2.16))

$$\begin{aligned}\varphi_{\mathscr{C}} &= \varphi_{12} + \varphi_{23} + \ldots + \varphi_{M1} \\ &= -\arg\left(\langle\chi_1\,|\,\phi_2\rangle\,\langle\chi_2\,|\,\phi_3\rangle\cdots\langle\chi_M\,|\,\phi_1\rangle\right) \\ &= -\mathrm{Im}\left(\ln\left(\prod_{j=1}^{M}\langle\chi_j\,|\,\phi_{j+1}\rangle\right)\right),\end{aligned} \tag{7.3}$$

a gauge-invariant quantity is obtained since the normalization convention (7.1) acts similarly to the Hermitian case and compensates a gauge transformation $|\phi_j\rangle \to \mathrm{e}^{\mathrm{i}\alpha_j}\,|\phi_j\rangle$ in the dual state $\langle\chi_j| \to \mathrm{e}^{-\mathrm{i}\alpha_j}\,\langle\chi_j|$. An example for a loop of three points is shown in figure 7.1 and the reader is invited to identify the analogy to figure 2.6b. Roughly speaking, the extension of the Hermitian to the non-Hermitian Berry phase is performed

by the assignments

$$\begin{aligned} |\psi(\underline{R})\rangle &\rightarrow |\phi(\underline{R})\rangle\,, \\ \langle\psi(\underline{R})| &\rightarrow \langle\chi(\underline{R})|\,, \\ \langle\psi(\underline{R})\,|\,\psi(\underline{R})\rangle = 1 &\rightarrow \langle\chi(\underline{R})\,|\,\phi(\underline{R})\rangle = 1, \end{aligned} \tag{7.4a}$$

where the states fulfill the following eigenvalue equations,

$$\begin{aligned} H_0(\underline{R})\,|\psi(\underline{R})\rangle = E_0(\underline{R})\,|\psi(\underline{R})\rangle &\rightarrow H(\underline{R})\,|\phi(\underline{R})\rangle = E(\underline{R})\,|\phi(\underline{R})\rangle\,, \\ \langle\psi(\underline{R})|\,H_0(\underline{R}) = E_0(\underline{R})\,\langle\psi(\underline{R})| &\rightarrow \langle\chi(\underline{R})|\,H(\underline{R}) = E^*(\underline{R})\,\langle\chi(\underline{R})|\,. \end{aligned} \tag{7.4b}$$

Hence, the definition of the *non-Hermitian Berry connection* $\underline{\mathcal{A}}(\underline{R})$ reads

$$\underline{\mathcal{A}}(\underline{R}) \equiv \left\langle \chi(\underline{R}) \,\middle|\, \mathrm{i}\underline{\nabla}_{\underline{R}}\phi(\underline{R})) \right\rangle. \tag{7.5}$$

Working through the steps of equations (2.23) and (2.24) in exactly the same manner but using the non-Hermitian substitution rules (7.4) it is straighforward to show that on a loop discretized into equidistant intervals $\underline{R}_1, \underline{R}_2, \ldots, \underline{R}_M$, the following limit holds,

$$\begin{aligned} \lim_{M\to\infty} \prod_{j=1}^{M} \left\langle \chi(\underline{R}_j) \,\middle|\, \phi(\underline{R}_{j+1}) \right\rangle &= \lim_{M\to\infty} \exp\left(-\mathrm{i} \sum_{j=1}^{M} \Delta\underline{R} \cdot \underline{\mathcal{A}}(\underline{R}) \right) \\ &= \exp\left(-\mathrm{i} \oint_{\mathscr{C}} \underline{\mathcal{A}}(\underline{R}) \cdot \mathrm{d}\underline{R} \right), \end{aligned} \tag{7.6}$$

such that equation (7.3) allows for the computation of the non-Hermitian Berry phase

$$\varphi_{\mathscr{C}} = \oint_{\mathscr{C}} \left\langle \chi(\underline{R}) \,\middle|\, \mathrm{i}\underline{\nabla}_{\underline{R}}\phi(\underline{R}) \right\rangle \cdot \mathrm{d}\underline{R}. \tag{7.7}$$

While the Hermitian Berry phase $\tilde{\varphi}_{\mathscr{C}}$ is real,

$$\begin{aligned} \tilde{\varphi}_{\mathscr{C}} &= \oint_{\mathscr{C}} \left\langle \psi(\underline{R}) \,\middle|\, \mathrm{i}\underline{\nabla}_{\underline{R}}\psi(\underline{R}) \right\rangle \cdot \mathrm{d}\underline{R} \\ &= \oint_{\mathscr{C}} \mathrm{i} \left(\underline{\nabla}_{\underline{R}} \langle \psi(\underline{R}) \,|\, \psi(\underline{R}) \rangle - \left\langle \underline{\nabla}_{\underline{R}}\psi(\underline{R}) \,\middle|\, \psi(\underline{R}) \right\rangle \right) \cdot \mathrm{d}\underline{R} \\ &= \oint_{\mathscr{C}} \mathrm{i} \left(0 - \left\langle \psi(\underline{R}) \,\middle|\, \underline{\nabla}_{\underline{R}}\psi(\underline{R}) \right\rangle^* \right) \cdot \mathrm{d}\underline{R} \\ &= \tilde{\varphi}^*_{\mathscr{C}}, \end{aligned} \tag{7.8}$$

the non-Hermitian equivalent is not necessarily real, which can be understood from the interpretation of the Berry phase as geometric phase picked up in the adiabatic transport of an eigenstate of the Hamiltonian along a closed loop while the system stays in this state such that the norm is *conserved*. In the Hermitian case this leads to $|\psi\rangle \rightarrow \mathrm{e}^{\mathrm{i}\tilde{\varphi}_{\mathscr{C}}}\,|\psi\rangle$

(neglecting the kinetic phase) and the conserved norm $\langle\psi|\psi\rangle = 1$ automatically fixes $\tilde{\varphi}^*_{\mathscr{C}} = \tilde{\varphi}_{\mathscr{C}}$. However, in the case of a non-Hermitian $\mathcal{PT}$-symmetric Hamiltonian in the $\mathcal{PT}$-unbroken phase with entirely real eigenvalues and eigenstates that can physically be regarded as stationary modes of the system, the conserved norm is given by $\langle\chi|\phi\rangle = 1$. Thus, if $|\phi\rangle$ picks up the *complex phase* $\gamma_{\mathscr{C}}$ it can only be stated that $\langle\chi|$ picks up the phase $-\gamma_{\mathscr{C}}$ in an adiabatic evolution.

In the case of resonances in the spectrum indicated by complex eigenvalues, the adiabatic evolution cannot be regarded as solely governed by acquiring of a phase. In fact, a non-Hermitian version of the adiabatic theorem has to be employed [86] leading to higher order corrections [87] with equation (7.7) representing only the lowest order.

In the same fashion the quantization of the Hermitian Berry phase follows from an antiunitary symmetry $\Theta = \mathcal{T}U_\Theta$ consisting of a complex conjugation $\mathcal{T}$ and a unitary operation Θ (see section 3.3), it can be shown that the *real part* of the *complex Berry phase* of a $\mathcal{PT}$-symmetric Hamiltonian is quantized in integer multiples of $\pi \mod 2\pi$, that is

$$\mathrm{Re}(\varphi_{\mathscr{C}}) = 0, \pi \mod 2\pi, \tag{7.9}$$

if the unique transported state is also an eigenstate of $\Theta = \mathcal{PT}$. The sketch for the proof of this statement runs as follows [33]: Expressing the transported right eigenstate $|\phi(\underline{R})\rangle$ and its dual partner $|\chi(\underline{R})\rangle$ in a stationary orthonormal basis $\{|j\rangle\}$ with $\langle j|k\rangle = \delta_{jk}$,

$$|\phi(\underline{R})\rangle = \sum_j c_j(\underline{R})\,|j\rangle\,, \qquad |\chi(\underline{R})\rangle = \sum_j d_j(\underline{R})\,|j\rangle\,, \tag{7.10}$$

the norm $\langle\chi(\underline{R})|\phi(\underline{R})\rangle = 1$ constrains the coefficients to $\sum_j d^*_j(\underline{R})c_j(\underline{R}) = 1$. A gauge transformation with $\alpha(\underline{R}) \in \mathbb{R}$ leads to $|\phi(\underline{R})\rangle \to \mathrm{e}^{\mathrm{i}\alpha(\underline{R})}\,|\phi(\underline{R})\rangle$, and thus $|\chi(\underline{R})\rangle \to \mathrm{e}^{\mathrm{i}\alpha(\underline{R})}\,|\chi(\underline{R})\rangle$, causing the transformation of the complex Berry connection (7.5) according to $\underline{\mathcal{A}}(\underline{R}) \to \underline{\mathcal{A}}(\underline{R}) - \underline{\nabla}_{\underline{R}}\alpha(\underline{R})$ and thus the condition

$$\varphi_{\mathscr{C}} = \oint_{\mathscr{C}} \underline{\mathcal{A}}(\underline{R}) \cdot \mathrm{d}\underline{R} \quad \to \quad \varphi'_{\mathscr{C}} = \oint_{\mathscr{C}} \underline{\mathcal{A}}(\underline{R}) \cdot \mathrm{d}\underline{R} - \oint_{\mathscr{C}} \left(\underline{\nabla}_{\underline{R}}\alpha(\underline{R})\right) \cdot \mathrm{d}\underline{R} \tag{7.11a}$$

follows. The latter relates two complex Berry phases in different gauges,

$$\varphi_{\mathscr{C}} = \varphi'_{\mathscr{C}} + 2\pi m, \qquad \text{or} \qquad \mathrm{Re}(\varphi_{\mathscr{C}}) = \mathrm{Re}(\varphi'_{\mathscr{C}}) \mod 2\pi \tag{7.11b}$$

with $m \in \mathbb{Z}$ (compare equation (3.10)). Regarding the antiunitary symmetry $\mathcal{PT}$ of the system, another property of the complex Berry connection can be derived. To do so, the action of the symmetry operator $\mathcal{PT}$ is defined by

$$\begin{aligned} \mathcal{PT}\,|\phi(\underline{R})\rangle &\equiv |\phi^{\mathcal{PT}}(\underline{R})\rangle = \sum_j c^*_j(\underline{R})\,|j\rangle\,, \\ \mathcal{PT}\,|\chi(\underline{R})\rangle &\equiv |\chi^{\mathcal{PT}}(\underline{R})\rangle = \sum_j d^*_j(\underline{R})\,|j\rangle\,, \end{aligned} \tag{7.12}$$

compare equation (3.11). By using equations (7.10) and (7.12) it follows that the complex Berry connection (7.5) satisfies the relation

$$\begin{aligned}\underline{\mathcal{A}}_{\mathcal{PT}}(\underline{R}) &= \left\langle \chi^{\mathcal{PT}}(\underline{R}) \,\middle|\, \mathrm{i}\underline{\nabla}_{\underline{R}}\phi^{\mathcal{PT}}(\underline{R})\right\rangle \\ &= \mathrm{i}\sum_j d_j(\underline{R})\underline{\nabla}_{\underline{R}}c_j^*(\underline{R}) = \mathrm{i}\sum_j \left(d_j^*(\underline{R})\underline{\nabla}_{\underline{R}}c_j(\underline{R})\right)^* \\ &= -\left\langle \chi(\underline{R}) \,\middle|\, \mathrm{i}\underline{\nabla}_{\underline{R}}\phi(\underline{R})\right\rangle^* = -\underline{\mathcal{A}}^*(\underline{R}),\end{aligned} \tag{7.13}$$

compare equation (3.12) for the equivalent version in an orthogonal basis. Integrating equation (7.13) over a loop $\mathscr{C}$, the Berry phase $\varphi_{\mathscr{C}}^{\mathcal{PT}}$ obtained from the transport of $|\phi^{\mathcal{PT}}(\underline{R})\rangle$ and the equivalent quantity $\varphi_{\mathscr{C}}$ for the transport of $|\phi(\underline{R})\rangle$ are connected by

$$\varphi_{\mathscr{C}} = -\varphi_{\mathscr{C}}^{\mathcal{PT}*} \tag{7.14}$$

Both relations (7.11b) and (7.14) can only be combined when the application of $\mathcal{PT}$ on the state $|\phi(\underline{R})\rangle \to |\phi^{\mathcal{PT}}(\underline{R})\rangle$ corresponds to a *gauge-transformation*. This is the case if the transported state $|\phi(\underline{R})\rangle$ is unique and an eigenstate of $\mathcal{PT}$ whose eigenvalues are known to be located on the complex unit circle (see page 38). Incorporating the known properties of $\mathcal{PT}$-symmetric Hamiltonians (see page 39) the conclusion to be drawn reads as follows: If the state $|\phi(\underline{R})\rangle$ does not break the Hamiltonian's $\mathcal{PT}$ symmetry,

$$\begin{aligned} & H(\underline{R})\,|\phi(\underline{R})\rangle = E(\underline{R})\,|\phi(\underline{R})\rangle\,, \qquad E(\underline{R}) \in \mathbb{R}, \\ \Longrightarrow\ & \left|\phi^{\mathcal{PT}}(\underline{R})\right\rangle = \mathrm{e}^{\mathrm{i}\alpha(\underline{R})}\,|\phi(\underline{R})\rangle\,, \end{aligned} \tag{7.15}$$

both conditions on the complex Berry phase picked up by the state apply and

$$\varphi_{\mathscr{C}} = \varphi_{\mathscr{C}}^{\mathcal{PT}} + 2\pi m = -\varphi_{\mathscr{C}}^* + 2\pi m \quad \Longrightarrow \quad 2\mathrm{Re}(\varphi_{\mathscr{C}}) = 2\pi m \tag{7.16}$$

with $m \in \mathbb{Z}$. Finally, using equation (7.11b) once more this yields the desired result $\mathrm{Re}(\varphi_{\mathscr{C}}) = 0, \pi \mod 2\pi$ (equation (7.9)), constituting the biorthogonal version of equation (3.14). This result is not surprising as the conserved biorthogonal norm $\langle\chi(\underline{R})|\phi(\underline{R})\rangle$ allows for both states to pick up an arbitrary imaginary phase with opposite sign for the dual partner such that the norm is conserved and the quantization rule applies only to the real part of the phase, which can be considered a consequence of the biorthogonal basis.

With that said, one can directly introduce the *generalized winding number* ν for the dissipative SL-BHM by substituting the non-Hermitian equivalents (equation (7.4)) in equation (3.17) resulting in

$$\nu = \int_0^{2\pi} \left\langle \chi(\vartheta) \,\middle|\, \mathrm{i}\frac{\partial}{\partial\vartheta}\phi(\vartheta)\right\rangle \mathrm{d}\vartheta, \tag{7.17}$$

where $\langle\chi(\vartheta)|\,, |\phi(\vartheta)\rangle$ are the left and right ground states of the SL-BHM Hamiltonian $H(\theta) = H_0(\vartheta) + U$ extended by one of the complex potentials U introduced in chapter

6 with twisted boundary conditions (see page 28). The $U(1)$-variation imposed by the twisted tunneling term $-t_2 e^{i\vartheta} a_L^\dagger a_1 + \text{h.c.}$ respects the $\mathcal{PT}$ symmetry of the non-Hermitian Hamiltonian (see also equation (3.16)), and therefore the necessary conditions for the real part of the complex Berry phase to be quantized may in principle be fulfilled.

In particular, equation (7.17) provides the non-Hermitian generalization of the topological invariant for the Hermitian SL-BHM when the Hamiltonian's $\mathcal{PT}$ symmetry is *unbroken*. Its computation is straightforward:

1. Impose a $U(1)$ twist on an arbitrary tunneling element $t \to te^{i\vartheta}, \vartheta \in [0, 2\pi)$ on the non-Hermitian Hamiltonian of a periodic or open chain. Divide the loop $\mathscr{C}$ given by the interval of ϑ into M equidistant steps, $\mathscr{C} = (\vartheta_1 = 0, \vartheta_2, \ldots, \vartheta_M, \vartheta_{M+1} = 2\pi = \vartheta_1)$.
2. For each $\vartheta_j, j = 1, \ldots, M$ compute the left and right ground states $|\phi(\vartheta_j)\rangle \equiv |\phi_j\rangle, |\chi(\vartheta_j)\rangle \equiv |\chi_j\rangle$ associated with the smallest eigenvalue of the Hamiltonian $H(\vartheta_j)$ with twisted tunneling amplitude $te^{i\vartheta_j}$.
3. Use equation (7.3) to obtain ν by

$$\nu = \lim_{M\to\infty} -\text{Im}\left(\ln\left(\prod_{j=1}^{M} \langle \chi_j \,|\, \phi_{j+1}\rangle\right)\right). \tag{7.18}$$

Note that the outlined procedure may in principle be applied to *any* tunneling amplitude in the system, but only when the discussed assumptions are met ν will be rigorously quantized and can serve as a topological invariant. Even in the non-quantized scenario, ν can be used as a local order parameter to follow the decoupling process of the dissipative sites discussed in chapter 6. This aspect is left for the next section.

Recap from the last chapter that the complex potentials U_1, $U_1^{(c)}$ and U_2 do not immediately break the $\mathcal{PT}$ symmetry of the extended SL-BHM in the single-particle picture where the entire spectrum can be scanned. Therefore the computation of ν shall first be restricted to periodic chains subject to those dissipative patterns, in which U_1 and $U_1^{(c)}$ do not have to be distinguished in a periodic system. For the interpretation of ν as a topological invariant to hold, the computed values always have to be considered in relation to the energy spectrum, which must not contain complex eigenvalues.

Figure 7.2a shows numerical results of ν on a small periodic chain with length $L = 8$ and the complex potential U_2 where the additional parameters are chosen as before. In fact there are eight quantized Berry phases $v^{(A)}, \ldots, v^{(H)}$ obtained from twisting each of the enumerated bonds (A) to (H) separately, but as the ring is invariant under translations among two lattice sites only two different values are taken by the latter, which is the reason why only two phases are shown for the variation of bonds (A) and (B). The reader is invited to convince him- or herself of the fact that the performed twists conserve the

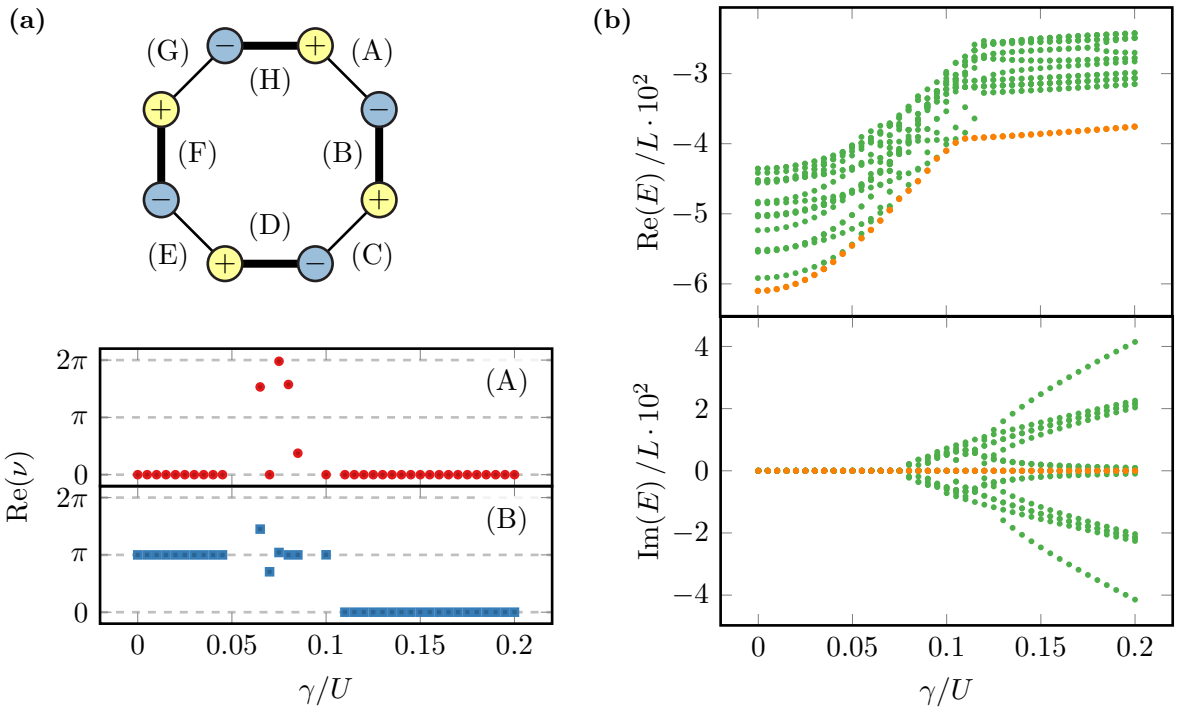

Figure 7.2.: Real part of the generalized winding number ν and low-energy spectrum of a periodic chain subject to U_2 obtained by exact diagonalization. System parameters are $t_1/U = 0.02, t_2/U = 0.1, \mu/U = 0.02$ and the local site dimension is restricted to $D = 4$. (a) Model sketch with enumerated bonds that are varied in a $U(1)$ twist where the interval $[0, 2\pi)$ is split up into $M = 100$ equidistant steps to obtain the winding number ν in the lower panels. Because of the translation symmetry of the ring only two phases are shown as the others behave in the same way. (b) Real and imaginary parts of the lowest 20 states of the system with the ground state (lowest real part) highlighted in orange. The $\mathcal{PT}$ phase transition takes place near $\gamma/U \approx 0.8$.

system's $\mathcal{PT}$ symmetry during the entire loop. In the panels of the winding numbers, two regimes in which the quantity is perfectly quantized can be detected, separated by a region in which no results or non-quantized values are obtained. The reason for that can be traced back to the appearance of the system's low-energy spectrum shown in figure 7.2b. As expected by the analytical result for the non-interacting case (equation (6.5)), the $\mathcal{PT}$ phase transition takes place near $\gamma_c^{(U_2)}/U = |t_1 - t_2|/U = 0.08$. Around this transition the spectrum becomes almost gapless in the regime from $\gamma/U \approx 0.05$ to 0.1, which is the reason for the spoiled quantization of ν. The ground state is not unique during the entire loop as the twist of the tunneling leads to an intermediate energy crossing. Often, the particle number of the ground state changes within such a crossing such that *exact* zeros are obtained in the argument of the logarithm in equation (7.18) leading to undefined results corresponding to void areas in the winding number plots.

Depending on whether a strong or a weak bond in the periodic chain with U_2 is varied, the winding number in the $\mathcal{PT}$-unbroken phase evaluates to $\nu = \pi$ or $\nu = 0$ respectively.

This result is consistent to the Hermitian case where the bulk of a periodic system in the $\rho = 1/2$ MI phase is characterized by a trivial (nontrivial) value of ν when the system is cut along a weak (strong) bond to yield an open chain. The presented biorthogonal formulation (7.17) of the winding number therefore constitutes a topological invariant for the interacting non-Hermitian $\mathcal{PT}$-unbroken MI phases of the extended SL-BHM.

A similar formulation for the non-interacting analytically accessible scenario that is equivalent to a non-Hermitian formulation of the Zak phase for the SSH model consisting of non-Hermitian dimers is tackled in references [88, 89] and an algorithm for computing the complex Berry phase, which is even capable of following the ground state through a crossing leading to much smoother data for ν, is proposed in [33, 90] and also contains further example models.

The theoretical observation that topologically protected edge states may still arise even in dissipative non-Hermitian systems has also triggered interesting experimental works, for instance in photonic systems [91], which allow for the realization of quasi $\mathcal{PT}$-symmetric systems in coupled waveguides [92]. Topologically protected edge modes can be employed as stable guiding channels for light and therefore have interesting applications, e.g. for robust communication systems. By wiggling a waveguide, the refractive index can be modulated leading to the desired loss effects in the non-Hermitian description. In a passive non-Hermitian system realizing a loss profile similar to that of U_2 a topological phase transition was observed experimentally [93] by tracking the propagation of light in the array, where the winding number is effectively given by the mean displacement.

Borrowing the idea of the construction of a $\mathcal{PT}$-symmetric defect originating from reference [4], topologically protected edge states can also be observed in the SL-BHM version of a chain subject to U_2 in the $\mathcal{PT}$-unbroken phase. Figure 7.3*a* illustrates the system configuration: starting with two chains composed of dissipative dimers with strong and weak bonds (green and gray boxes, respectively), both are connected with a weak bond. According to figure 7.2a, the two different joined subsystems result from cutting a SL-BHM ring subject to U_2 at a strong (weak) bond. Therefore the winding numbers of the cut bonds differ, as a strong bond leads to $\nu = \pi$ whereas a weak one is classified by $\nu = 0$ in the $\mathcal{PT}$-unbroken phase. Thus the connection between the two topologically distinct chains emulates an interface at which the topological invariant changes, leading to localized topologically protected edge states (compare chapter 3). As an incidental remark, note that in order for the total system to be $\mathcal{PT}$-symmetric, the dissipation of the central site has to be removed such that the system is invariant under inversion at the latter followed by a complex conjugation that effectively swaps gain and loss.

The interface states emerging as ground states of an SL-BHM system with U_2 and a defect with a total system length of $L = 33$ are shown in figure 7.3b together with the first excited states for a value of the gain/loss parameter where the system is expected to be in the $\mathcal{PT}$-unbroken phase (compare figure 7.2b). As is the case for the Hermitian SL-BHM, the type of the edge state is determined by the value of the chemical potential μ/U which

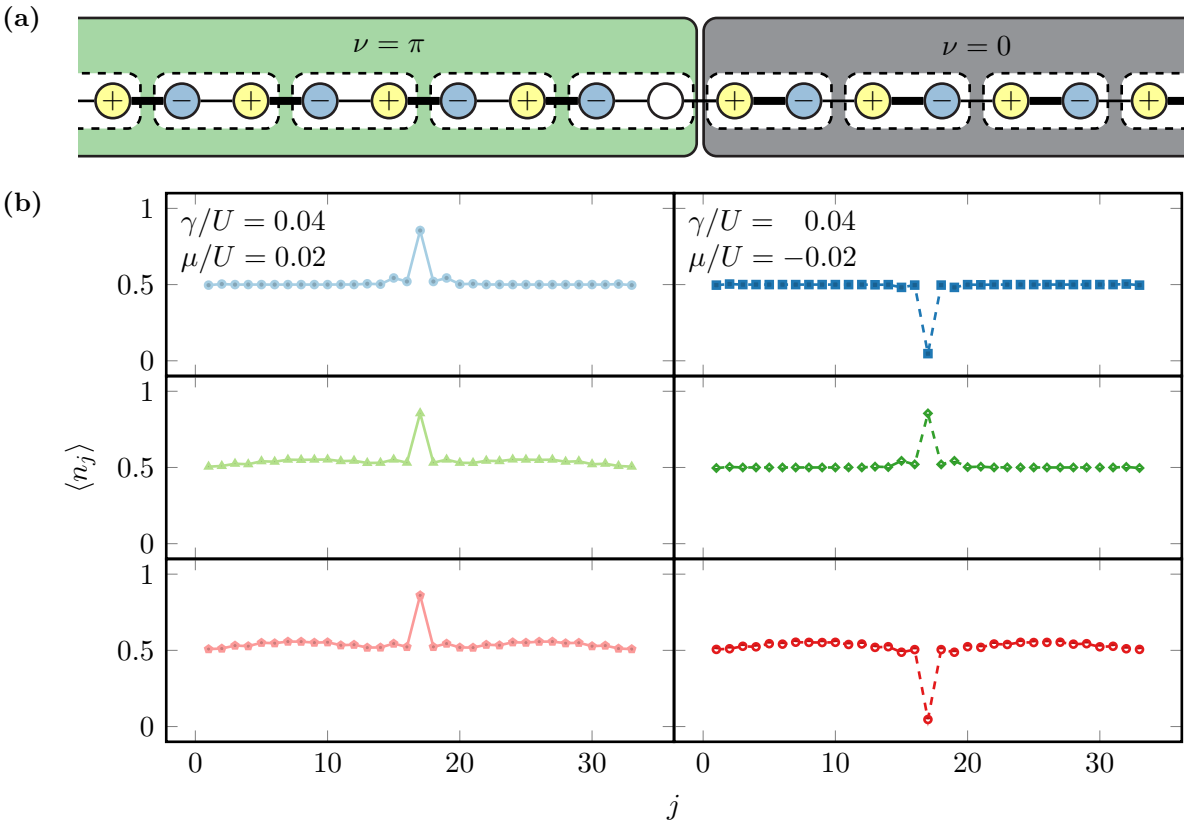

Figure 7.3.: Topologically protected interface states at a boundary between two topologically distinct non-Hermitian systems. (a) Extract of a sketch of the system configuration. The total system consists of two open chains (green and gray boxes), which are made up of strongly or weakly bound dissipative dimers. Both chains can be imagined as a result of cutting a ring with alternating gain and loss at a strong or a weak bond. The bond along which the system is cut represents a topological invariant which differs for the two subsystems leading to topologically protected interface states. For the total system to be $\mathcal{PT}$-symmetric, the dissipative effect on the central site has to be removed. (b) Ground state (top panel) and first excited states (center and bottom panel) of the sketched non-Hermitian defect system with $L = 33$ obtained by non-Hermitian DMRG (hyper-parameters like in section 6.2) for different values μ/U of the chemical potential. Additional system parameters are $t_1/U = 0.1$ (strong bonds), $t_2/U = 0.02$ (weak bonds) and $\gamma/U = 0.04$.

was chosen such that both particle and hole configuration with a flat bulk at $\rho = 1/2$ appear. Excited states are distinguished by excitations of the bulk, where interestingly the feature of a localized particle at the interface is still present. Alternatively, an empty interface can also be filled up with a particle to yield an excited state.

This concludes the outline that topological effects can also be expected and classified in non-Hermitian bosonic interacting $\mathcal{PT}$-unbroken systems.

Unfortunately, exact diagonalization studies of periodic systems of $L = 8$ subject to $U_1, U_1^{(c)}$ and U_3 reveal that the $\mathcal{PT}$ symmetry is immediately broken, which spoils the

interpretation of the introduced winding number in the sense of falling back to the framework of topological order in Hermitian systems. Nevertheless, the introduced Berry phase represents an interesting quantity even in the non-quantized case and in the $\mathcal{PT}$-broken regime, as will be addressed in the next section.

7.2. Local order parameters as indicator for decoupling

To see how the real part of the complex Berry phase can still be used as an indicator for the decoupling process between the dissipative sites from the rest of the system, taking one step back to the Hermitian case is quite helpful.

In case of a periodic Hermitian SL-BHM sketched in figure 7.4a, the winding numbers are exactly quantized (see the argument of section 3.3) and transporting the many-body ground state of a $\rho = 1/2$ MI along a loop in parameter space results in $\nu = 0$ ($\nu = \pi$) when a weak (strong) bond is twisted. The reason for this is that the ground state approximately consists of singlet configurations that are entangled on a strong bond. Therefore, the entanglement between two sites is encoded in the winding number resulting from a $U(1)$ twist of the connecting bond.

With this interpretation at hand it follows immediately that although the requirements for the quantization of ν are violated when an arbitrary tunneling element of an open chain is twisted, the obtained value of ν is still close to the quantized value in the periodic

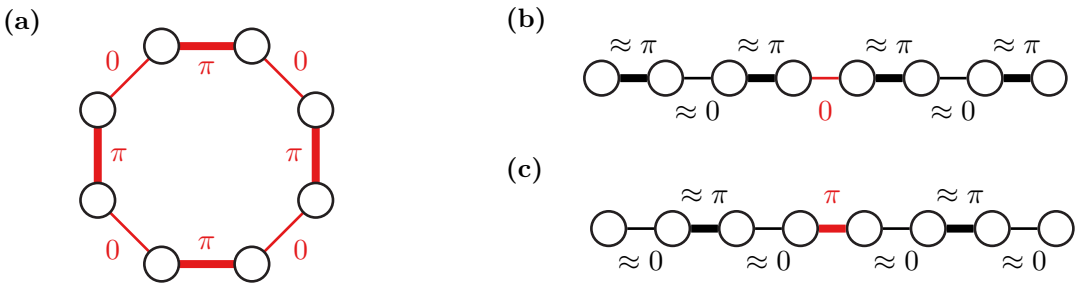

Figure 7.4.: Interpretation of the winding number as a local order parameter encoding the entanglement between neighboring sites in the many-body ground state of the $\rho = 1/2$ MI phase of the SL-BHM. Exactly quantized winding numbers are highlighted in red. (a) A $U(1)$ variation of an arbitrary tunneling element in the periodic system leads to a quantized winding number. The ground state consists of singlets located on strongly-coupled double-wells with $\nu = \pi$ while weak bonds pick up a phase of $\nu = 0$. (b) In the open chain a twist does not respect the symmetries of the system leading to non-quantized values of ν. Though no quantization is present, the winding numbers are still close to the expectation in the periodic system as the ground state of the latter is a good approximation. (c) Also in the nontrivial chain the interpretation of ν containing information about the entanglement of the singlets located on the strong bonds holds to a large extent.

system indicated in the two different dimerization configurations in figures 7.4b, 7.4c. Interestingly, the inversion-symmetric bond at the center of the open chain still leads to an exactly quantized value of ν as the variation of the tunneling amplitude respects the $\mathcal{PT}$ symmetry of the system which guarantees the quantization.

Extending this interpretation of ν to the non-Hermitian SL-BHM allows us to follow the behavior of entanglement between the lattice sites using ν as a local order parameter. To do so, the *ground state*, that is the eigenstate associated with the smallest real part, is classified by computing the complex Berry phase for each tunneling element by use of the procedure presented in the previous section. This has two practical reasons: (i) As the reader may verify, in the many-body DMRG computations for all complex potentials the ground state's eigenvalue is *always* real-valued, thus the ground state is an eigenstate of $\mathcal{PT}$ which can in principle lead to a quantized winding number (the required conditions for this to hold were outlined in the previous section). (ii) Although the classified state is not stationary in the presence of complex eigenvalues in the spectrum, it nevertheless contains the desired features of effects caused by dissipation such as additional edge modes in Hermitian subsystems, compare figures 6.7 to 6.10.

For the following discussion, open SL-BHM chains with $L = 8$ extended by the complex potentials presented in chapter 6 are studied within exact diagonalization setting the local Hilbert space dimension to $D = 4$. The chemical potential is set to $\mu/U = 0.02$ and the trivial (nontrivial) dimerization corresponds to $t_1/U = 0.1, t_2/U = 0.02$ ($t_1/U = 0.02, t_2 = 0.1$). This choice is in consistence with the spectra shown in the previous chapter except for the system length. The computation of ν for a certain bond is performed by use of equation (7.18), where the interval $[0, 2\pi)$ is split into $M = 100$ equidistant steps. For brevity, the system parameters will be suppressed for the rest of this section, only adopting the terminology of a *trivial* or a *nontrivial* chain. As the imaginary part of ν will not be considered, the terms $\mathrm{Re}(\nu)$ and ν are used equivalently without differentiating. Similarly, the terms *complex Berry phase* and *winding number* are used synonymously as was already done before.

Figure 7.5 shows the winding numbers $\nu^{(\mathrm{A})}, \ldots, \nu^{(\mathrm{G})}$ resulting from a twist of the enumerated bonds (A) to (G) for an open SL-BHM chain of length $L = 8$ extended by U_1 in both dimerization configurations. It is clearly visible that the winding numbers are always near a value of 0 or $\pi \mod 2\pi$ (values of $\nu \approx 0$ and $\nu \approx 2\pi$ are to be considered equal). Note as well that for $\gamma/U = 0$ the Hermitian case is accurately reproduced with strong (weak) bonds picking up $\nu = \pi$ ($\nu = 0$). The general statement that the winding number is almost unaffected by γ/U can be established for bonds between two Hermitian sites. In addition to that, $\nu^{(\mathrm{D})}$ is exactly quantized as the appropriate twist respects the model symmetry. For the nontrivial chain (compare figure 7.5a) the winding numbers expected from the non-Hermitian model remain perfectly at this value up to $\gamma/U \approx 0.16$, where the strong bonds (A), (F) infected by gain and loss also become trivial. At this transition, a crossing of the ground state takes place in the real part of

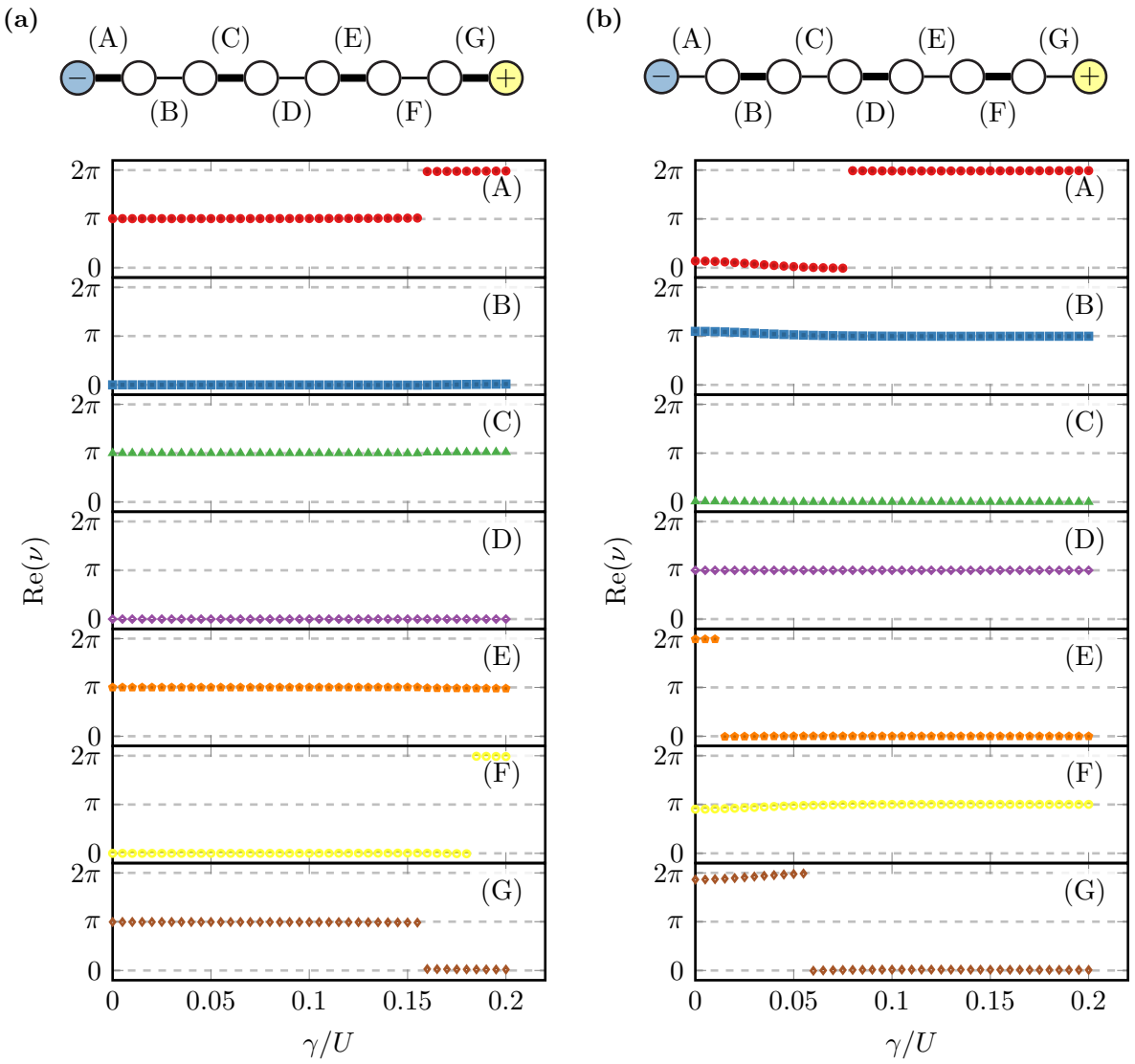

Figure 7.5.: Real part of the complex Berry phase for the different bonds of a trivially and nontrivially dimerized SL-BHM extended by U_1 for varying strength of the gain/loss parameter. (a) The bonds between two Hermitian sites in the trivial chain are almost unaffected by γ. As a consequence of symmetry, $\nu^{(\mathrm{D})}$ is exactly quantized. The bonds with a dissipative site show a significant change from $\nu^{(\mathrm{A})} \approx \pi \approx \nu^{(\mathrm{G})}$ to $\nu^{(\mathrm{A})} \approx 0 \approx \nu^{(\mathrm{G})} \mod 2\pi$ at $\gamma/U \approx 0.16$. (b) In the trivial chain all bonds are more or less unaffected by γ. Again, symmetry forces the exact quantization of $\nu^{(\mathrm{D})}$.

the energy spectum, see figure 6.7a, and the dissipative sites decouple from the rest of the chain such that the ground state shows features of internal edge modes. Speaking in terms of entanglement, the dissipative bonds become *unentangled* at a critical value of γ/U which is tracked by the transition from $\nu^{(A,G)} \approx \pi$ to approximately zero. This is already the case in the ground state of the nontrivial chain (compare figure 7.5b), where no crossing in the real part of the spectrum occurs (see figure 6.7b) such that all Berry

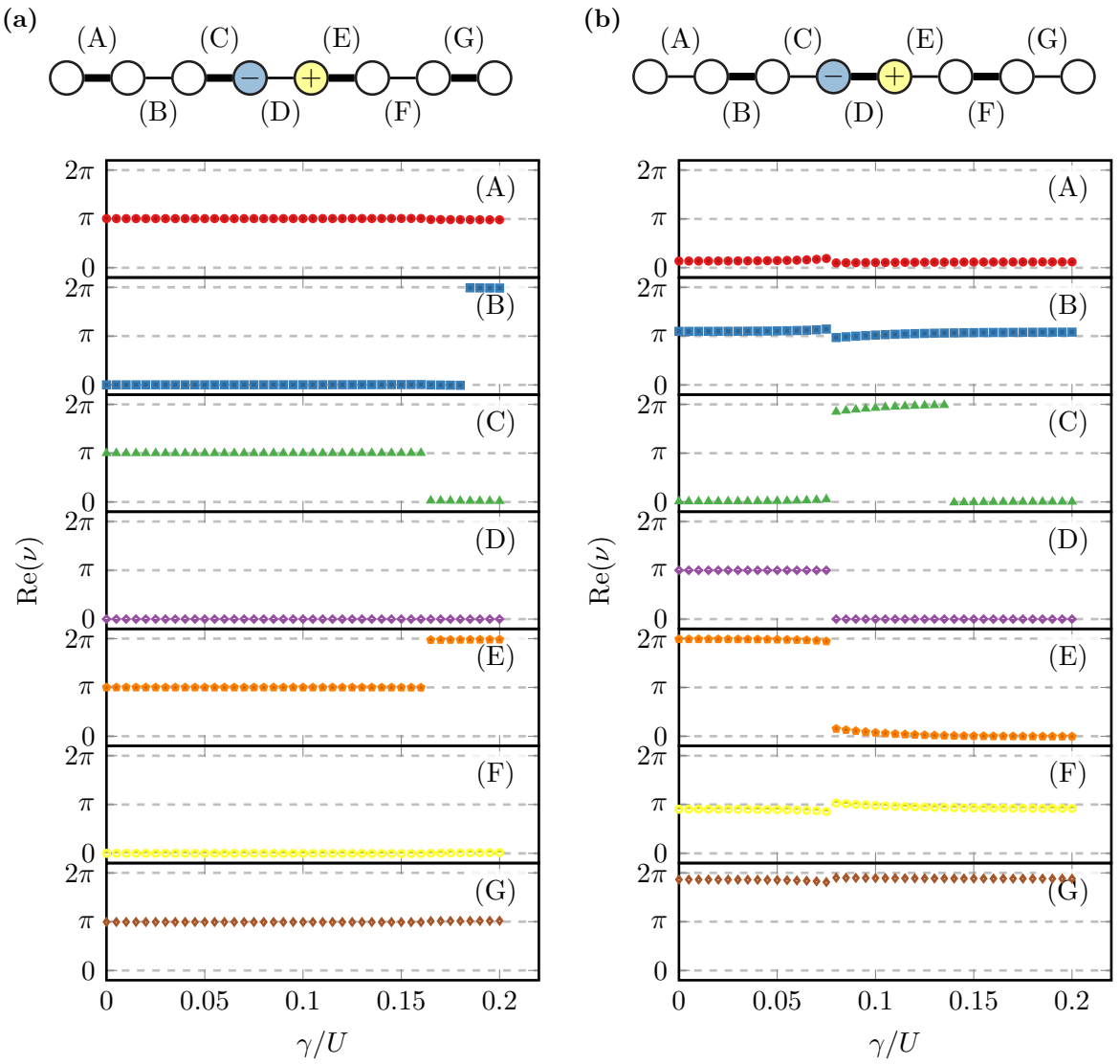

Figure 7.6.: Winding number for all bonds in an SL-BHM chain subject to $U_1^{(c)}$. (a) The two strong links (C), (E), that are directly affected by gain and loss in the trivial chain, change their Berry phase from $\nu \approx \pi$ to $\nu \approx 0$ at $\gamma/U \approx 0.16$ leading to an internal boundary that hosts edge states. (b) The central bond's Berry phase changes from $\nu = \pi$ to $\nu = 0$ in the nontrivial chain at $\gamma/U \approx 0.07$ indicating that the entanglement between the two dissipative sites is lost in the new ground state.

phases more or less remain at the original values modulo 2π.

This reasoning can directly be carried over to the scenario in which the open chain is subject to $U_1^{(c)}$ shown in figure 7.6. In a trivial chain in which the dissipative impurity is located on a weak bond, the investigation of the low-energy regime shows additional edge features appearing in the ground state as the decomposition of the Hermitian system

from the dissipative sites creates two additional nontrivial boundaries (compare figure 6.8a). The decoupling between the dissipative sites and their Hermitian neighbors is encoded in the winding numbers of the strong bonds (C), (E) at the center shown in figure 7.6a changing from approximately π to zero at a value of $\gamma/U \approx 0.16$ according to the crossing in the ground state spectrum. The loss of entanglement between two dissipative sites coupled by a strong link can also be observed in the trivial chain shown in figure 7.6b. The central bond (D) becomes unentangled at $\gamma/U \approx 0.07$ where the ground state of the system changes according to the spectrum (figure 6.8b). Note however that the directly adjacent sites are now still entangled via the bonds (B), (F), which still take values of approximately π such that no additional edge modes appear in the subsystems in accordance with the expectation of no additional nontrivial boundaries resulting from the decoupling process. An interesting consequence of the central position of the dissipative impurity is that the change of an exactly quantized Berry phase can be observed. However, this winding number $\nu^{(\mathrm{D})}$ has its limitations in a physical interpretation as an adiabatic phase because the spectrum is complex and therefore the transported ground state to obtain the phase cannot be considered stationary, spoiling the assumptions of the adiabatic theorem.

For the case of alternating gain and loss imposed on the system by U_2, three regions can be identified in the parameter regime shown in figure 7.7 similar to the periodic case in the previous section. Up to a value of $\gamma/U \approx 0.05$ the chain is $\mathcal{PT}$-unbroken with a *gapped* ground state such that the exactly quantized winding numbers $\nu^{(\mathrm{D})}$ yield results similar to those shown in figure 7.2a. The region from $\gamma/U \approx 0.05$ to 0.1, in which the $\mathcal{PT}$ phase transition also occurs, again corresponds to a gapless spectrum. In this range the complex Berry phases are far away from the quantized values and the transition to $\nu \approx 0$ appears to happen in a stage-like fashion. In fact, the plots in figures 7.7a, 7.7b allow for the identification of three intermediate stages. They can be understood by considering the shape of the ground state shown within figure 6.9. In the gapless regime the ground state is filled up from $\rho = 1/2$ to $\rho = 1$ MI which for a system with $L = 8$ corresponds to three intermediate values between a total particle number of $L/2$ and L. In contrast to the periodic case, those intermediate ground states are not driven through a crossing in the $U(1)$ twist what results less scattered data.

It is interesting that although the transported $\rho = 1$ MI ground state in the case of U_2 does not represent the most important state showing a staggered occupation (compare the states shown in the center column of figure 6.11), the interpretation of decoupling dissipative sites, that is all $\nu \approx 0$ is obviously valid for the staggered state. This can be justified by borrowing the relation of the model to the single-particle limit whose properties are inherited to the many-body case in the limit of strong interactions. From the single-particle spectrum (figure 6.2) it is obvious that all states are driven towards real part zero corresponding to local degrees of freedom on each dissipative site. As those states are solely supported on a single site there cannot be any entanglement in

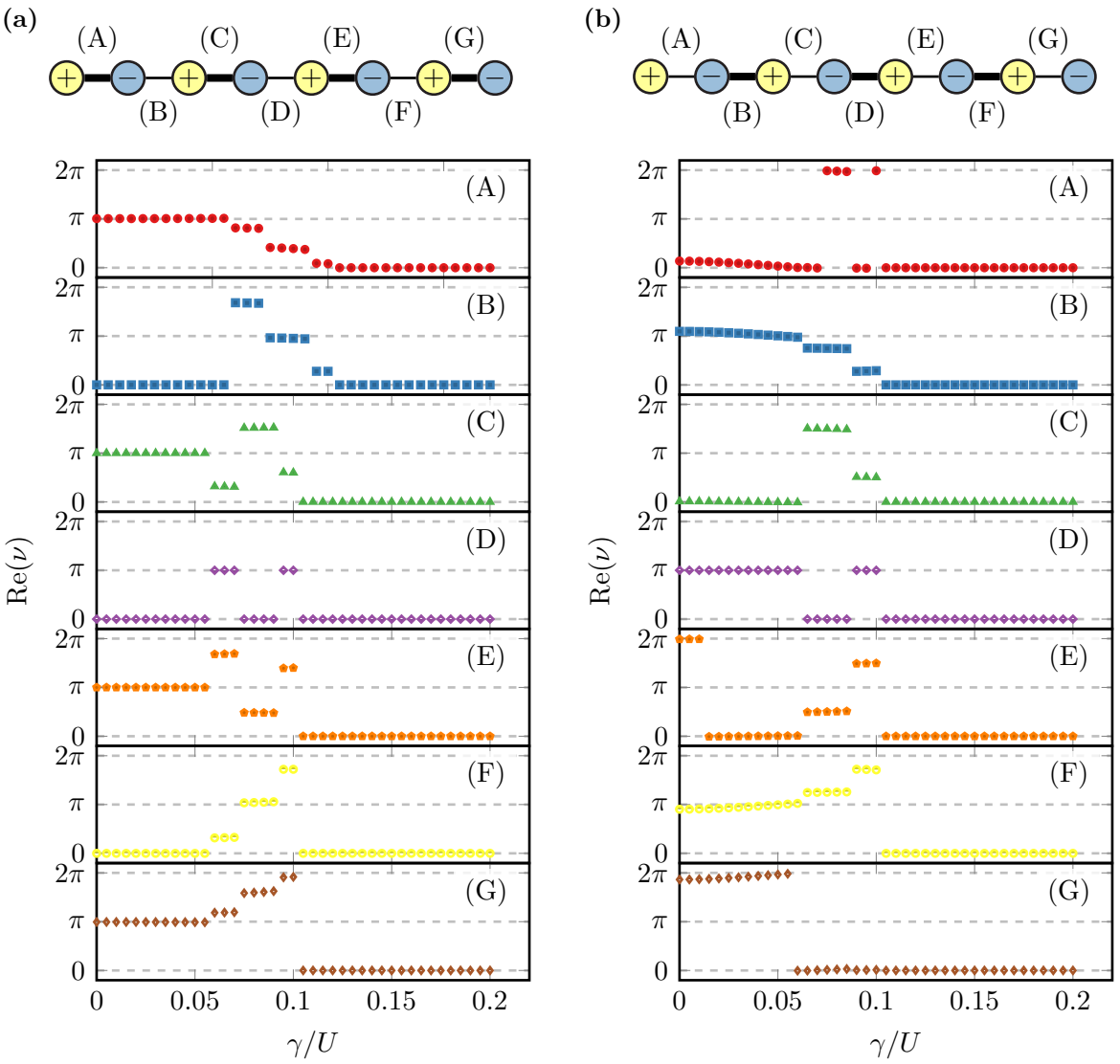

Figure 7.7.: Real part of the complex Berry phases for an open SL-BHM chain subject to U_2. The quantized numbers $\nu^{(\mathrm{D})}$ (in the gapped regime) directly correspond to the values of the twist of a weak and strong bond in a periodic ring, see figure 7.2a. A discussion of the three regimes is included in the text. Winding numbers of strong bonds are driven to ν=0 for both (a) the trivial and (b) the nontrivial chain. This can also be understood by a recapitulation of the fact that the transported state changes from $\rho = 1/2$ MI to $\rho = 1$ MI in the non-Hermitian description.

a many-body state, thus all ν are approximately 0. The transported state then has the wrong filling of single-particle states but nevertheless produces the expected result.

The results for the winding numbers for U_3 are withheld for brevity as they would lead to redundancy of what has already been said so far. Moreover, they can easily be derived by considering the behavior and lattice occupation of the ground state in the spectrum

of the system shown in figure 6.10 and a comparison with the data for $U_1^{(c)}$, which in the limit of $L = 2$ is equal to U_3.

To conclude, note that the entanglement interpretation of the complex Berry phase motivated by the singlet product structure of the $\rho = 1/2$ MI ground state reproduces a feature that is quite peculiar in dissipative quantum systems. In the limit of strong dissipation all winding numbers of dissipative bonds are eventually driven to approximately zero such that the ground state is completely unentangled. Entanglement expresses itself in correlations in the many-body quantum state that are unveiled by performing measurements. As mentioned in chapter 4 the influence of a reservoir on a system can be understood in terms of the bath performing measurements on the system therefore leading to quantum jumps. This formulation fits nicely into the picture of a reservoir performing many measurements in the case of strong dissipation, thereby destroying any correlations in the system's quantum state which can thus not be entangled.

Chapter review

- A biorthogonal formulation of the SL-BHM generalized winding number (3.17) can be employed to yield the complex Berry phase (7.17) whose real part is quantized to $\mathrm{Re}(\nu) = 0, \pi \mod 2\pi$ for the gapped ground state of a $\mathcal{PT}$-unbroken Hamiltonian when the applied perturbation respects the $\mathcal{PT}$ symmetry of the model and the transported state is unique during the entire loop.
- For the complex potential U_2 which exhibits a $\mathcal{PT}$-unbroken regime the notion of topological order can be carried over to the non-Hermitian scenario leading to localized interface states at boundaries between to topologically distinct non-Hermitian systems.
- Even in the case in which the quantization of ν is spoiled for different reasons, it can still be employed as a local order parameter detecting the entanglement between the two lattice sites joined by the twisted bond. The effects of decoupling dissipative lattice sites originally described in chapter 6 are illustrated by the appropriate winding numbers being driven from $\nu \approx \pi$ to $\nu \approx 0$.
- In the limit of strong dissipation all winding numbers of dissipative bonds are driven to $\nu \approx$ in consistence with the picture of a reservoir performing frequent measurements on the system leading to a collapse of correlations/entanglement in the many-body quantum state.

8. Dissipation by master equations in Lindblad form

In this last chapter some of the previously described effects that are observed in the formulation of gain and loss with of complex on-site potentials are compared to results obtained from a description with master equations in Lindblad form. The object of interest is given by the non-equilibrium steady state (NESS), towards which the system converges in the long-time limit regardless of its initial configuration if there are no further decoherence-free subspaces. Under circumstances that have to be specified, such states may correspond to physically interesting states, for instance topologically protected states, which has triggered ideas of deliberately using engineered dissipation to condense a system into the steady state exploiting this process as a preparation procedure [8, 9]. The topological classification of steady states, or more generally mixed states described by density matrices represents a question which is under current investigation [9, 94–96]. Without going too much into detail, the idea of a ground state that is topologically protected by an energy gap in the non-dissipative Hamiltonian framework carries over to two different gaps in the dissipative framework of a *Gaussian* master equation, namely a *dissipative gap* (that is the smallest decay rate of the other modes) and a *purity gap* (that is the purity of the state, which can be introduced by $\mathrm{Tr}\{\rho^2\}$, compare chapter 4).

In contrast to this, the pragmatic view that topological effects are almost always accompanied by the occurrence of edge states is adopted in this chapter, which motivates the approach to study edge effects in the lattice occupation of steady states. As the lattice occupation of various NESS will be investigated in this chapter, a condition for the expectation values of the particle numbers of steady states in both fermionic (hard-core bosonic) and bosonic systems with linear Lindblad operators is derived in section 8.1.

In the case of a non-interacting system with linear Lindblad couplings is described by terms that are at most quadratic in the bosonic/fermionic annihilation and creation operators, the method of *third quantization* [21, 22] provides a powerful and efficient way for computing observables of the steady state. For brevity, the outline of this procedure for both the fermionic and bosonic case is excluded in this presentation, referring the interested reader to appendices B and C that also contain remarks about the numerical realization for the case of the SSH and the non-interacting SL-BHM models.

Employing the fermionic method of third quantization, section 8.2 studies the steady states of the dissipative SSH model. It can be interpreted as a hard-core bosonic version of the SL-BHM Hamiltonian which does not suffer from the problem of amplification as only one particle is allowed per lattice site, similar to the physical restrictions imposed in the extended $\mathcal{PT}$-symmetric SL-BHM in chapter 6. The bosonic formulation of third quantization is used in section 8.3 to study the non-interacting SL-BHM. Finally, the interacting dissipative SL-BHM is tackled in section 8.4 using the non-Hermitian DMRG procedure presented in chapter 5.

Before proceding, a few remarks on notation are in order.

Preliminaries and conventions: In chapter 4 the form (4.8) of the master equation in Lindblad form used in [54, 55] was adopted to outline that a Lindblad operator $\tilde{L} = \sqrt{\tilde{\gamma}}a$ ($\tilde{L} = \sqrt{\tilde{\gamma}}a^\dagger$) on a single site may effectively be replaced by a complex on-site potential ${}^{(+)}_{(-)}\mathrm{i}\tilde{\gamma}/2$ in the mean-field limit. Absorbing the factor $1/2$ led to the complex on-site potentials $\varepsilon_j = {}^{(+)}_{(-)}\mathrm{i}\gamma$ introduced in chapter 6, that is $\tilde{\gamma}/2 \leftrightarrow \gamma$,

$$\tilde{L} = \sqrt{\tilde{\gamma}}a_j^{(\dagger)} \quad \leftrightarrow \quad \epsilon_j = {}^{(+)}_{(-)}\mathrm{i}\frac{\tilde{\gamma}}{2} \equiv {}^{(+)}_{(-)}\mathrm{i}\gamma. \tag{8.1}$$

In this chapter however (except for the next section where the convention does not matter anyways), the convention

$$\frac{\mathrm{d}\rho}{\mathrm{d}t} = -\mathrm{i}\,[H,\rho] + \sum_\mu \left(2L_\mu \rho L_\mu^\dagger - \left\{L_\mu^\dagger L_\mu, \rho\right\}\right) \tag{8.2}$$

stemming from the discussion [21, 22] of third quantization will be used in combination with Lindblad operators describing single-particle loss (gain) by $L = \sqrt{\gamma'}a$ ($L = \sqrt{\gamma'}a^\dagger$). Comparing the different conventions leads to the relation $\tilde{\gamma}/2 \leftrightarrow \gamma'$ and thus the substitutions $\gamma' \leftrightarrow \tilde{\gamma}/2 \leftrightarrow \gamma$ hold.

Thus, the master equations in Lindblad form with collapse operators parameterized by the gain/loss strength γ' used in this chapter are "equivalent" to the complex on-site potential description of chapter 4 with a gain/loss parameters γ,

$$\gamma' \leftrightarrow \gamma. \tag{8.3}$$

Note however that this substitution is *not* rigorous because it only holds in the mean-field limit. Nevertheless both formalisms are expected to exhibit similar effects when the respective gain/loss parameters take values of the same magnitude, $\gamma \sim \gamma'$.

8.1. Expectation value conditions for the steady state

A necessary condition to be fulfilled by the steady state observables $\langle n_j \rangle$, which may be employed to check whether the result of a simulation corresponds to a physically meaningful quantity can be derived by demanding the expectation value $\langle N \rangle$ of the total particle operator $N = \sum_{j=1}^{L} n_j = \sum_{j=1}^{L} a_j^\dagger a_j$ to be constant in time, that is $\mathrm{d}/\mathrm{d}t \langle N \rangle = 0$ or expressed in terms of the density matrix ρ using equation (4.3),

$$\begin{aligned} \frac{\mathrm{d}\langle N \rangle}{\mathrm{d}t} &= \frac{\mathrm{d}}{\mathrm{d}t}\left(\sum_{j=1}^{L} \langle n_j \rangle\right) = \frac{\mathrm{d}}{\mathrm{d}t}\left(\sum_{j=1}^{L} \mathrm{Tr}\{\rho n_j\}\right) \\ &= \sum_{j=1}^{L} \mathrm{Tr}\left\{\frac{\mathrm{d}\rho}{\mathrm{d}t} n_j + \rho \frac{\mathrm{d}n_j}{\mathrm{d}t}\right\} = \sum_{j=1}^{L} \mathrm{Tr}\left\{\frac{\mathrm{d}\rho}{\mathrm{d}t} n_j\right\} = \mathrm{Tr}\left\{\frac{\mathrm{d}\rho}{\mathrm{d}t} N\right\} \overset{!}{=} 0. \end{aligned} \tag{8.4}$$

Inserting the master equation in Lindblad form (4.8) for the equation of motion of the density matrix ρ leads to two terms,

$$\begin{aligned} \frac{\mathrm{d}\langle N \rangle}{\mathrm{d}t} &= \mathrm{Tr}\left\{ N \left[-\mathrm{i}\,[H, \rho] + \frac{1}{2} \sum_{\mu} \left(2 L_\mu \rho L_\mu^\dagger - \left\{ L_\mu^\dagger L_\mu, \rho \right\} \right) \right] \right\} \\ &= -\mathrm{i}\mathrm{Tr}\{NH\rho - N\rho H\} + \frac{1}{2} \sum_{\mu} \mathrm{Tr}\left\{ 2 N L_\mu \rho L_\mu^\dagger - N L_\mu^\dagger L_\mu \rho - N \rho L_\mu^\dagger L_\mu \right\} \\ &= -\mathrm{i}\mathrm{Tr}\{NH\rho - HN\rho\} + \frac{1}{2} \sum_{\mu} \mathrm{Tr}\left\{ 2 L_\mu^\dagger N L_\mu \rho - N L_\mu^\dagger L_\mu \rho - L_\mu^\dagger L_\mu N \rho \right\} \\ &= -\mathrm{i}\,\langle NH - HN \rangle + \frac{1}{2} \sum_{\mu} \left\langle 2 L_\mu^\dagger N L_\mu - N L_\mu^\dagger L_\mu - L_\mu^\dagger L_\mu N \right\rangle \\ &= -\mathrm{i}\,\langle NH - HN \rangle + \frac{1}{2} \sum_{\mu} \left\langle L_\mu^\dagger \,[N, L_\mu] - \left[N, L_\mu^\dagger\right] L_\mu \right\rangle, \end{aligned} \tag{8.5}$$

where linearity and cyclicity of the trace have been used. The first term can be evaluated by making use of the fact that the Hamiltonian conserves the total particle number and therefore $NH = HN$. This can also be explicitly derived by writing both operators in terms of bosonic creation and annhilation operators using the canonical commutation relations of the latter. Hence, the first term vanishes and one is left with

$$\frac{\mathrm{d}\langle N \rangle}{\mathrm{d}t} = \frac{1}{2} \sum_{\mu} \left\langle L_\mu^\dagger \,[N, L_\mu] - \left[N, L_\mu^\dagger\right] L_\mu \right\rangle, \tag{8.6}$$

where up to this point the choice of the Lindblad operators is *arbitrary* and is now replaced by the *linear* collapse operators employed in this work.

For the following discussion, the two commutation relations are quite helpful,

$$[a_j, N] = -[N, a_j] = \sum_k \left[a_j, a_k^\dagger a_k\right] = \left[a_j, a_j^\dagger\right] a_j = a_j, \tag{8.7a}$$

$$\left[a_j^\dagger, N\right] = -\left[N, a_j^\dagger\right] = \sum_k \left[a_j^\dagger, a_k^\dagger a_k\right] = a_j^\dagger \left[a_j^\dagger, a_j\right] = -a_j^\dagger. \tag{8.7b}$$

Considering the case of single-particle gain at site j with a gain parameter γ_j, that is $L = \sqrt{\gamma_j} a_j^\dagger$, the respective term in the sum of equation (8.6) simplifies to

$$\begin{aligned} \frac{1}{2}\gamma_j \left\langle a_j \left[N, a_j^\dagger\right] - [N, a_j]\, a_j^\dagger \right\rangle &= \frac{1}{2}\gamma_j \left\langle a_j a_j^\dagger + a_j a_j^\dagger \right\rangle \\ &= \gamma_j \left\langle 1 + a_j^\dagger a_j \right\rangle = \gamma_j \left(1 + \langle n_j \rangle\right). \end{aligned} \tag{8.8a}$$

The same calculation for single site loss on site j with $L = \sqrt{\gamma_j} a_j$ results in

$$\frac{1}{2}\gamma_j \left\langle a_j^\dagger [N, a_j] - \left[N, a_j^\dagger\right] a_j \right\rangle = \frac{1}{2}\gamma_j \left\langle -a_j^\dagger a_j - a_j^\dagger a_j \right\rangle = -\gamma_j \langle n_j \rangle . \tag{8.8b}$$

Piecing equation (8.6) together for a system with loss at the sites labeled by j_{loss} and analogously j_{gain} for sites with gain, by using equations (8.8) it follows that

$$\frac{\mathrm{d}\langle N \rangle}{\mathrm{d}t} = \sum_{j_{\text{gain}}} \gamma_{j_{\text{gain}}} \left(1 + \langle n_{j_{\text{gain}}} \rangle\right) - \sum_{j_{\text{loss}}} \gamma_{j_{\text{loss}}} \langle n_{j_{\text{loss}}} \rangle . \tag{8.9}$$

Ultimately, the steady state condition (8.4) for the expectation value of the total particle number being stationary leads to a relation for the occupation of the dissipative sites,

$$\sum_{j_{\text{gain}}} \gamma_{j_{\text{gain}}} \left(1 + \langle n_{j_{\text{gain}}} \rangle\right) = \sum_{j_{\text{loss}}} \gamma_{j_{\text{loss}}} \langle n_{j_{\text{loss}}} \rangle , \tag{8.10}$$

that holds for the steady state of a bosonic system described by arbitrary linear Lindblad operators parameterized by vectors $\underline{l}_\mu, \underline{k}_\mu$ such that $L_\mu = \underline{l}_\mu \cdot \underline{a} + \underline{k}_\mu \cdot \underline{a}^\dagger$ with the annihilation (creation) operators aligned in vectors $\underline{a}$ ($\underline{a}^\dagger$).

Steady state condition for hard-core bosons/fermions: Performing the same computation for hard-core bosons, the bosonic creation and annihilation operators $a_j^\dagger, a_j$ can effectively be replaced by their fermionic equivalents $c_j^\dagger, c_j$. The procedure is completely analogous to the previous computation up to equation (8.6), which however is better rewritten in terms of anticommutators,

$$\begin{aligned} \frac{\mathrm{d}\langle N \rangle}{\mathrm{d}t} &= \frac{1}{2}\sum_\mu \left\langle 2L_\mu^\dagger N L_\mu - N L_\mu^\dagger L_\mu - L_\mu^\dagger L_\mu N \right\rangle \\ &= \frac{1}{2}\sum_\mu \left\langle 2L_\mu^\dagger N L_\mu - \left\{N, L_\mu^\dagger L_\mu\right\} \right\rangle . \end{aligned} \tag{8.11}$$

Useful relations are given by

$$\left\{N, c_j^\dagger c_j\right\} = \left\{c_j^\dagger c_j, N\right\} = \{n_j, N\} = 2n_j N = 2N n_j, \tag{8.12a}$$

$$\left\{N, c_j c_j^\dagger\right\} = \left\{c_j c_j^\dagger, N\right\} = \left\{1 - c_j^\dagger c_j, N\right\} = 2N - 2n_j N, \tag{8.12b}$$

and

$$N c_j = \sum_k c_k^\dagger c_k c_j = -\sum_k c_k^\dagger c_j c_k = -\sum_k (\delta_{jk} - c_j c_k^\dagger) c_k = c_j (N-1), \tag{8.12c}$$

$$N c_j^\dagger = \sum_k c_k^\dagger c_k c_j^\dagger = \sum_k c_k^\dagger (\delta_{jk} - c_j^\dagger c_k) = c_j^\dagger + \sum_k c_j^\dagger c_k^\dagger c_k = c_j^\dagger (1+N), \tag{8.12d}$$

where canonical anticommutation relations were used.

Single-site gain with $L = \sqrt{\gamma_j} c_j^\dagger$ leads to the following contribution in (8.11),

$$\begin{aligned} \frac{1}{2}\gamma_j \left\langle 2c_j N c_j^\dagger - \left\{N, c_j c_j^\dagger\right\} \right\rangle &= \frac{1}{2}\gamma_j \left\langle 2c_j c_j^\dagger (1+N) - (2N - 2n_j N) \right\rangle \\ &= \frac{1}{2}\gamma_j \left\langle 2(1-n_j)(1+N) - (2N - 2n_j) \right\rangle \\ &= \gamma_j \left(1 - \langle n_j \rangle\right). \end{aligned} \tag{8.13a}$$

In the same fashion for single site loss on site j with $L = \sqrt{\gamma_j} c_j$ one obtains

$$\begin{aligned} \frac{1}{2}\gamma_j \left\langle 2c_j^\dagger N c_j - \left\{N, c_j^\dagger c_j\right\} \right\rangle &= \frac{1}{2}\gamma_j \left\langle 2n_j (N-1) - 2N n_j \right\rangle \\ &= -\gamma_j \langle n_j \rangle . \end{aligned} \tag{8.13b}$$

Consequently, the change of the total particle number expectation value of a system affected by both single site gain and loss at sites j_{gain}, j_{loss} respectively is given by

$$\frac{\mathrm{d}\langle N \rangle}{\mathrm{d}t} = \sum_{j_{\text{gain}}} \gamma_{j_{\text{gain}}} \left(1 - \left\langle n_{j_{\text{gain}}} \right\rangle\right) - \sum_{j_{\text{loss}}} \gamma_{j_{\text{loss}}} \left\langle n_{j_{\text{loss}}} \right\rangle , \tag{8.14}$$

which states the hard-core bosonic (fermionic) equivalent of equation (8.9). Thus, the steady state of a hard-core bosonic (fermionic) system with linear Lindblad couplings that can most generally be parameterized by $L_\mu = \underline{l}_\mu \cdot \underline{c} + \underline{k}_\mu \cdot \underline{c}^\dagger$ obeys the relation

$$\sum_{j_{\text{gain}}} \gamma_{j_{\text{gain}}} \left(1 - \left\langle n_{j_{\text{gain}}} \right\rangle\right) = \sum_{j_{\text{loss}}} \gamma_{j_{\text{loss}}} \left\langle n_{j_{\text{loss}}} \right\rangle . \tag{8.15}$$

8.2. Steady states of the SSH model

In order to circumvent the amplification problem bosonic systems may suffer from, the discussion of the extended SL-BHM in chapter 6 was restricted to the low-energy regime which corresponds to the strongly-interacting scenario, where multiple occupations of a single site are avoided and the hard-core bosons can effectively be considered as fermions. This analogy is used as a motivation to study the dissipative SSH Hamiltonian (2.1) corresponding to the hard-core limit of the SL-BHM Hamiltonian (3.1) around $\mu = 0$.

Because the Hamiltonian of interest does not contain interaction terms but only quadratic contributions and the Lindblad couplings are linear, $L = \sqrt{\gamma'}a^{(\dagger)}$, the method of third quantization for quadratic fermionic systems [21] can be applied to compute observable expectation values of the steady state. An outline of the general procedure complemented with the application onto the dissipative SSH model is given in appendix B. The main advantage of this method compared to exact diagonalization or DMRG procedures in the 4^L-dimensional Liouville space is that NESS properties can be obtained from a $4L \times 4L$-dimensional *shape matrix* which allows for much larger system sizes. In order to perform a comparison to the description of gain and loss with complex on-site potentials, the results shown in this section are limited to $L = 16$.

With that said, the dissipative patterns imposed by the complex on-site potentials in chapter 6 will now be discussed. Again, the tunnelings are set to $t_1 = 0.1, t_2 = 0.02$ ($t_1 = 0.02, t_1 = 0.1$), referring to the configuration as trivial (nontrivial) chain.

Figure 8.1 shows the steady state lattice occupation of a system with $L = 16$ subject to a dissipative pattern similar to U_1. In the trivial chain (figure 8.1a) the entire system possesses a flat occupation for dissipation strengths up to $\gamma' \approx 0.02$. The currents induced by gain and loss at the right and left boundary can be balanced by the system until the couplings exceed the maximum current that is determined by the tunneling amplitudes. At this point the dissipative sites start to fill/empty. Note however that instead of influencing the entire bulk of the system, only the sites close to the sink/source are affected by a change in occupation. This behavior can be understood by making oneself aware of the fact that fermions are governed by Pauli's exclusion rule forbidding the presence of two fermions at the same lattice site. Consequently, when the site subject to gain has been completely filled up with particles, the exclusion principle prevents more fermions from being coupled into the system. In accordance to the results obtained in the description with complex on-site potentials (compare figure 6.7), the dissipative sites are entirely filled up (or emptied) and decouple from the remaining system as no more particles can be coupled into or out of the system. The Hermitian subsystem has nontrivial boundaries leading to the occurrence of edge states whose occupation is favored or avoided by dissipation.

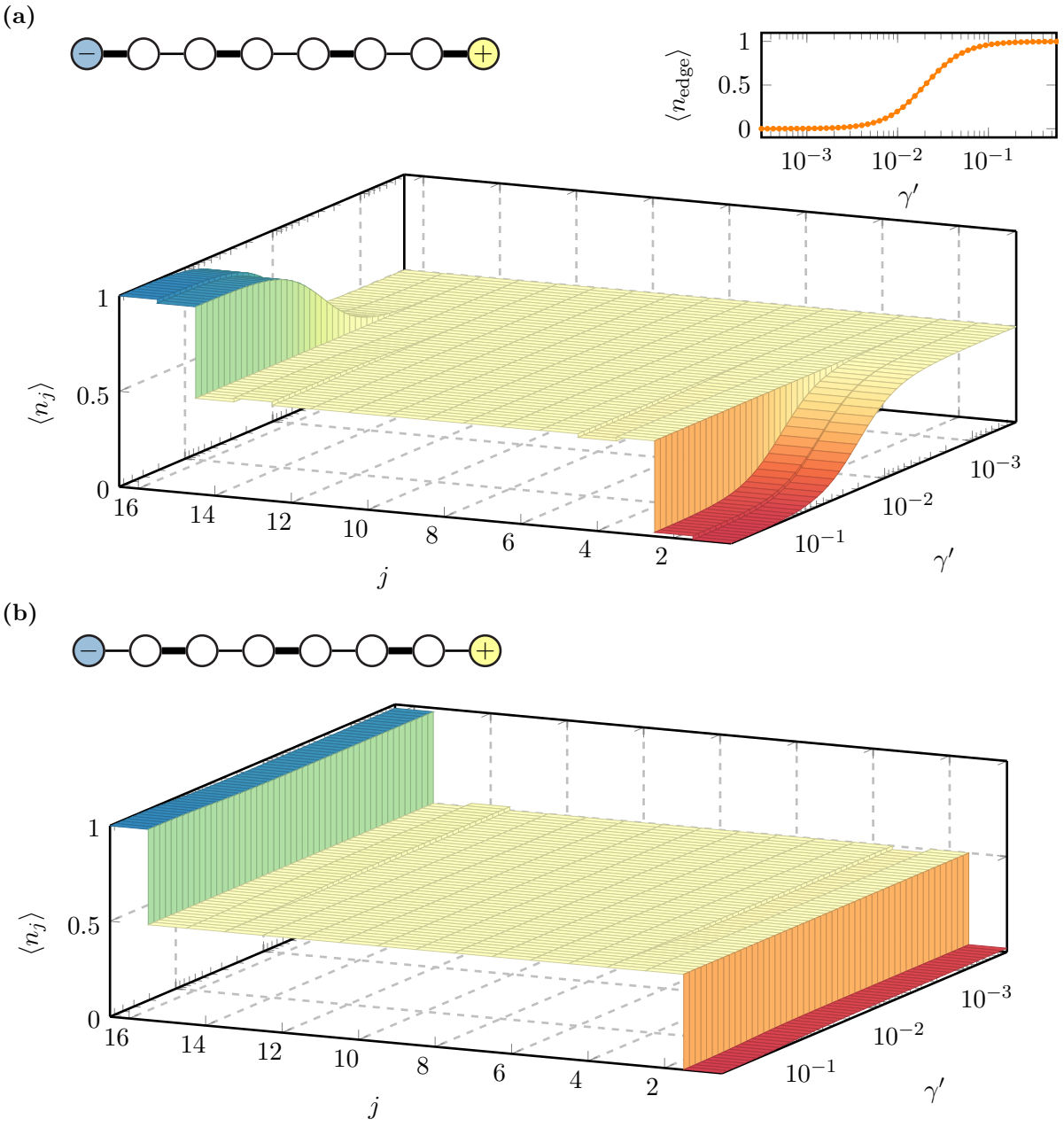

Figure 8.1.: Steady state lattice occupation for an SSH chain with $L = 16$ and a dissipation pattern similar to U_1 for varying dissipation strength (colors do not carry information and are rather used for reasons of visibility). (a) In the trivially dimerized chain a transition from a completely flat to a steady state with edge features occurs. To follow this transition in more detail, the quantity $\langle n_{\mathrm{edge}}\rangle = \sum_{j=L-4}^{L}(\langle n_j\rangle - 1/2)$ where the difference of the occupation of the four most outer sites at the gain boundary and a flat $\rho = 1/2$ bulk is summed. The observed behavior is consistent with the description with complex on-site potentials, where the dissipative sites decouple from the Hermitian subsystem and induce edge states in the nontrivially dimerized remnant. (b) The nontrivial chain is almost unaffected by dissipation for parameter ranges varying over four magnitudes with gain (loss) favoring (avoiding) the occupation of a boundary.

To follow the transition from a flat steady state to one with edge features, the particle numbers of the outer four sites at the gain edge, subtracted from the bulk occupation 1/2 are summed to yield a quantity that describes the presence of edge features,

$$\langle n_{\mathrm{edge}} \rangle = \sum_{j=L-4}^{L} \left(\langle n_j \rangle - 1/2 \right), \tag{8.16}$$

which is also shown in figure 8.1a and exhibits a sharp transition around the mentioned value of γ'.

In contrast to this, the steady state of the nontrivial chain is almost unaffected by a sweep of the gain/loss parameter, compare figure 8.1b. For finite values of γ', the edge mode located at the lossy boundary is emptied while the occupation of its opponent at the gain boundary is favored. Again, the interpretation that the remaining subsystem is trivially dimerized and therefore does not exhibit edge modes is in accordance with the behavior observed in chapter 6.

Figure 8.2 presents the NESS occupations of open chains subject to adjacent gain and loss in the spirit of the complex on-site potential U_2. The bulks of both the trivial (figure 8.2a) and nontrivial (figure 8.2b) chain remain flat at half filling up to values of $\gamma' \approx 0.1$. This is in exact correspondence to the expected behavior of the system in the description with complex on-site potentials, where the $\mathcal{PT}$ phase transition up to which the system is stationary occurs at $\gamma_{\mathrm{c}}^{(U_2)} = |t_1 - t_2| = 0.08$. Only when this critical value of the gain/loss strength is exceeded, dissipative effects start to influence the configuration of the bulk, which becomes staggered with gain sites being completely filled with fermions while loss sites are emptied. In order to keep track of the steady state staggering, especially at the system boundaries, the quantity

$$\langle n_{\mathrm{stagg}} \rangle = -1/4 \sum_{j=1}^{4} (-1)^j (\langle n_j \rangle - 1/2) \tag{8.17}$$

is defined and takes a value of $\langle n_{\mathrm{stagg}} \rangle = 0$ for a flat and $\langle n_{\mathrm{stagg}} \rangle = 1$ for a perfectly staggered configuration of the steady state. The equivalent of the transition from the $\mathcal{PT}$-unbroken to the $\mathcal{PT}$-broken regime in the Lindblad scenario is presented in the plots of $\langle n_{\mathrm{stagg}} \rangle$. It shall be emphasized here that the staggering of the steady state can also be understood by interpreting the imaginary parts of the energies shown in the single-particle treatment of U_2 (compare figure 6.2) as decay rates. As all states are driven towards real part zero corresponding to local degrees of freedom on a single site with a negative (positive) imaginary part for loss (gain), the long-time behavior of the system is given by all modes with positive (negative) imaginary part filling up (emptying), which leads to the observed staggering. However, for small values of γ' the nontrivial chain shows clear edge features described by $\langle n_{\mathrm{stagg}} \rangle = 1/4$ while the bulk remains flat.

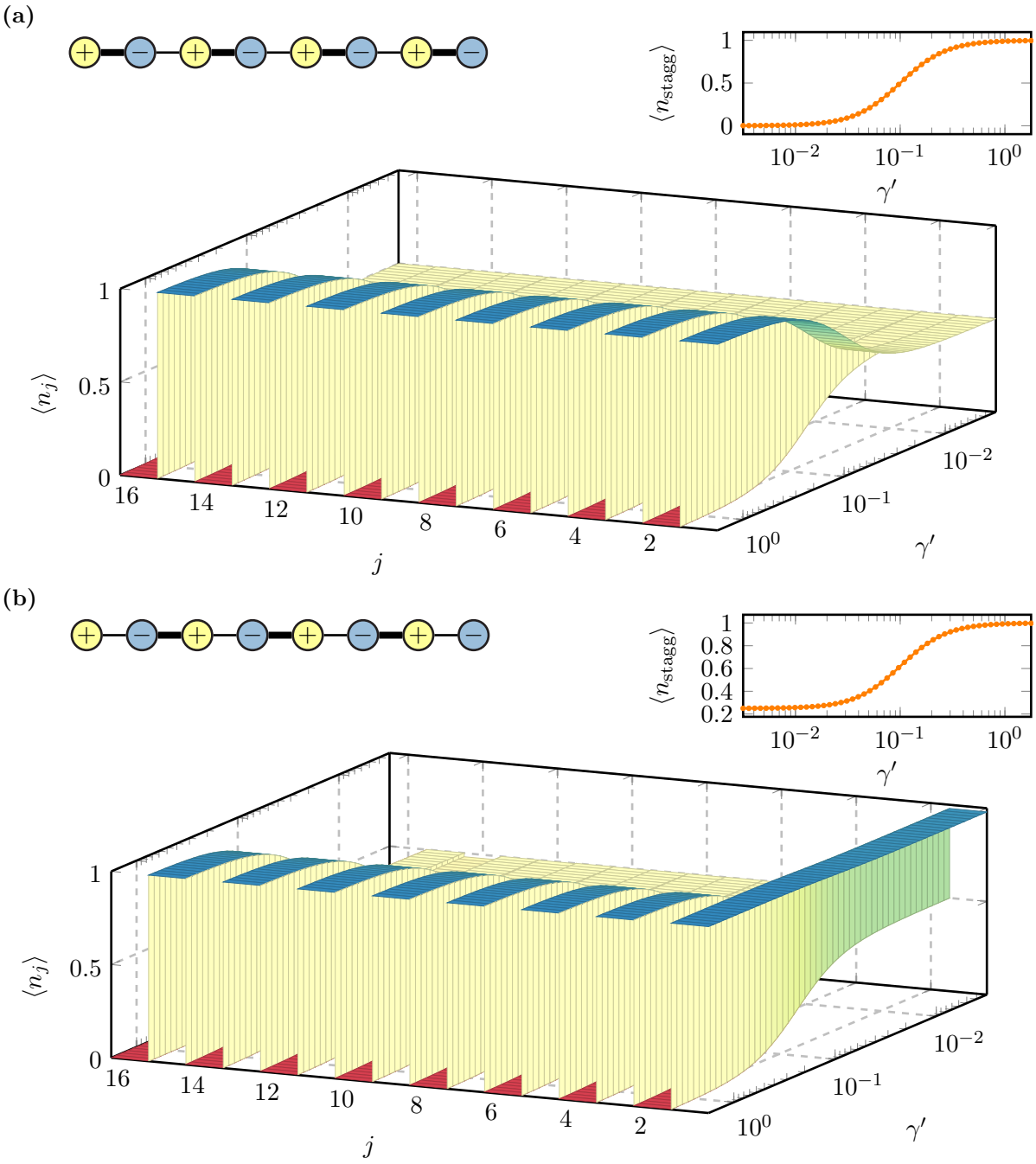

Figure 8.2.: Lattice occupation of open SSH chains ($L = 16$) subject to U_2. In the case of strong dissipation, gain sites are filled up entirely while loss sites do not contain any particles such that the NESS is staggered. To follow the transition, the quantity $\langle n_{\mathrm{stagg}}\rangle = -1/4\sum_{j=1}^{4}(-1)^j(\langle n_j\rangle - 1/2)$ providing a measure of the staggering at the left boundary of the system is also shown. (a) The trivial chain is driven from a flat to a staggered NESS. (b) In the nontrivial chain, edge modes are present while the steady state is still represented by a flat bulk. For large dissipative couplings however, the edge mode cannot be distinguished from the staggered bulk.

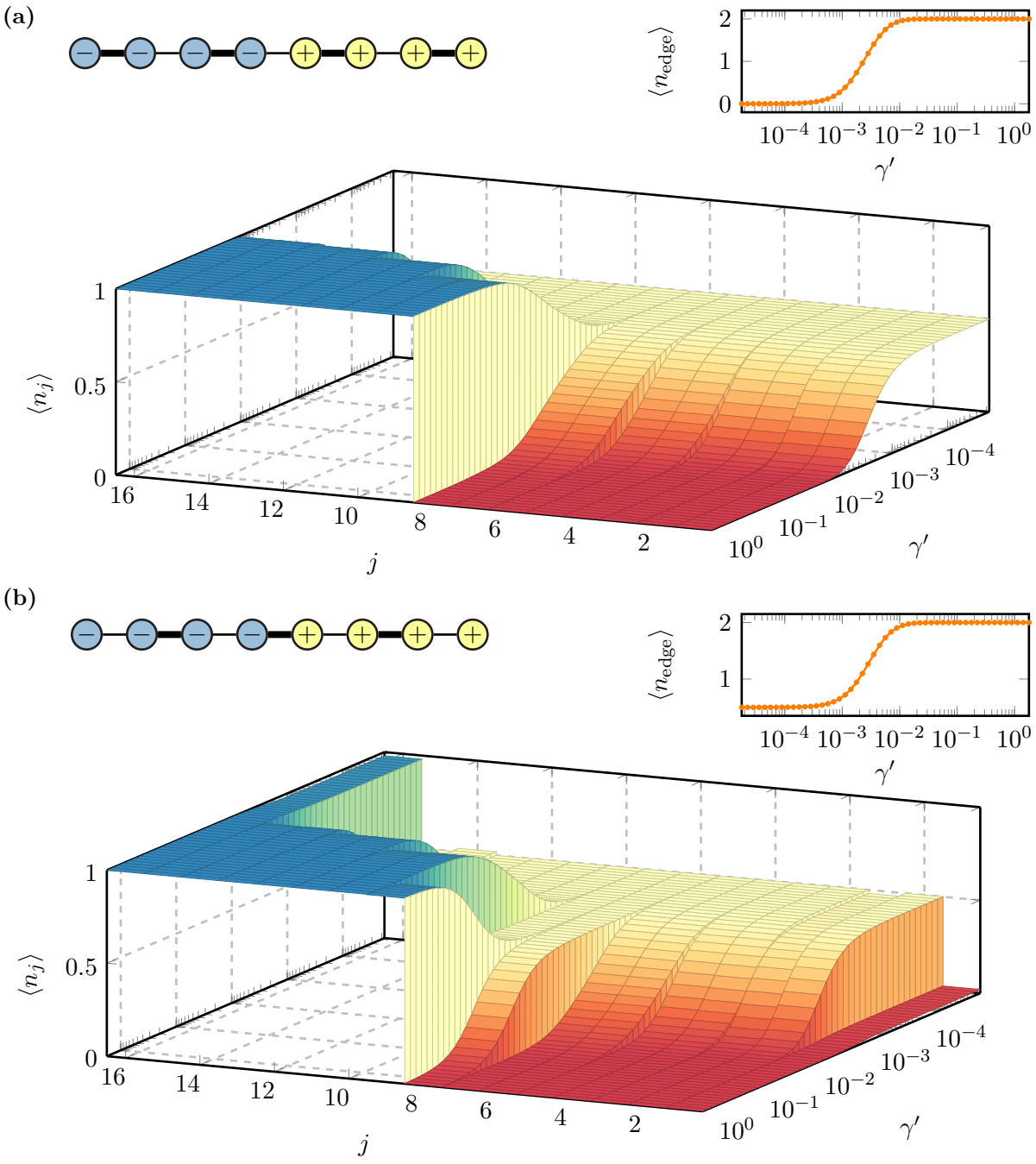

Figure 8.3.: Steady state lattice occupation and difference $\langle n_{\mathrm{edge}} \rangle$ between the occupation of the four outer sites at the gain boundary and a half-filled bulk of an open SSH chain with a dissipative pattern similar to U_3. (a) In the steady state of the trivial chain currents introduced by dissipation can be balanced up to a value of $\gamma' \approx 0.002$ before gain sites are completely filled up while loss sites are unoccupied. (b) The same holds for the nontrivial chain, except for the occurrence of edge states in the regime of weak dissipation.

Note that by using the steady state condition (8.15) for fermionic (hard-core bosonic) systems derived in the last section, it is easy to show that the steady state for the dissipative profiles represented by U_2 and U_3 without any sites unaffected by gain and loss is *always* at half-filling, while interestingly this statement holds as well for the case of U_1 where the coupling to the environment can be considered to lead to *balanced* gain and loss.

Results for the steady state occupation of the remaining dissipation pattern similar to U_3 are shown in figure 8.3. Similar to the previous scenarios, the system is able to balance the currents introduced by gain and loss up to a critical value of $\gamma' \approx 0.002$, which however is much smaller for U_3 compared to the other configurations. This is not surprising as the same process of in- or outcoupling of particles takes place at a large number of adjacent lattice sites and currents that stabilize the particle number can only be exchanged over the central bond. In fact, for an infinite system subject to U_3 the system would not be able to compensate the imposed currents for finite values of γ' leading to an immediate filling of gain sites with loss sites simultaneously emptying. This statement is consistent with the observation in chapter 6 that the spectrum of U_3 is immediately $\mathcal{PT}$-broken for finite γ'. Nevertheless, the small system size allows for a compensation of currents for small gain/loss strengths. The transition to the expected steady state configuration can be tracked by $\langle n_{\text{edge}} \rangle$, which is also shown for both the topologically trivial (figure 8.3a) and nontrivial (figure 8.3b) chain.

The dependency on the system size in the case of U_3 introduces another interesting degree of freedom that already expressed itself in the exact diagonalization study, where complex on-site potentials were employed and the state with largest imaginary part in

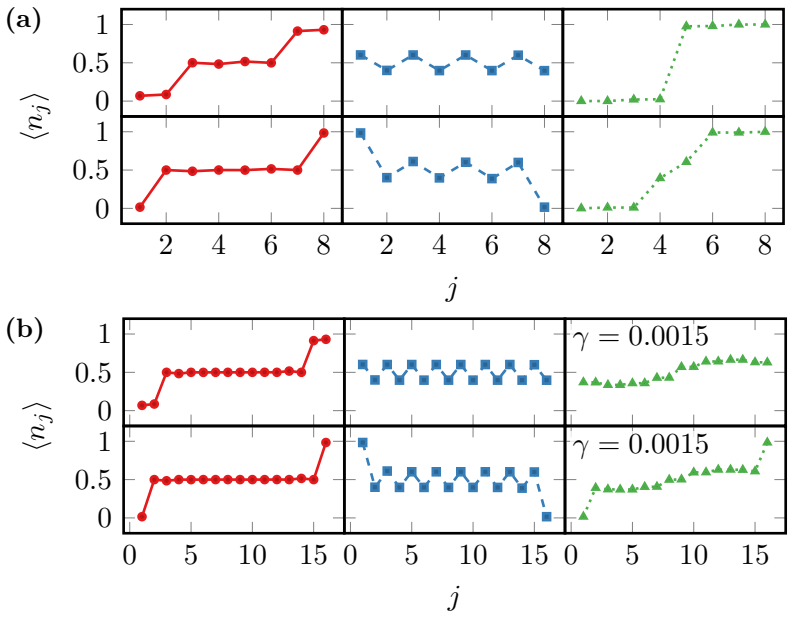

Figure 8.4.: Lattice occupation of the NESS of an open SSH chain with trivial (top rows) and nontrivial (bottom rows) dimerization obtained by the method of third quantization. The gain/loss parameter is $\gamma' = 0.05$ unless stated different, and the dissipation patterns implement U_1 (left column), U_2 (center column) and U_3 (right column). It is emphasized that the states resemble the results shown in figure 6.11. The system length is (a) $L = 8$ and (b) $L = 16$.

the low-energy regime was computed (compare figure 6.11). In this presentation, the observed lattice occupations were not sensible to the system size for the potentials U_1 and U_2, while the state of U_3 already showed a strong dependency on the chain length.

To conclude this section, a comparison between the description of dissipative effects with complex on-site potentials and a master equation in Lindblad form shall be given. Figure 8.4 shows the lattice occupations of NESS for the investigated dissipative patterns and dimerizations. The resemblance to the results shown in the course of the treatment of complex on-site potentials (compare figure 6.11) is *remarkable*. Only in the case of U_3 the gain/loss strength has to be tuned more carefully in order to obtain similar results, which is a consequence of the mentioned dependency on the system length.

8.3. Steady states of the non-interacting SL-BHM

In the last section, the similarity between the description of dissipative effects with $\mathcal{PT}$-symmetric on-site potentials and master equations in Lindblad form was outlined. A fundamental requirement for this comparison was given by the limitation of the occupation of a lattice site, realized by introducing the constraint to only consider the low-energy and strongly-interacting regime, where multiple occupations are avoided. If the latter is relaxed, thereby allowing for an arbitrary energy exchange between the reservoir and the system, one has to face the amplification problem bosonic systems suffer from.

To illustrate this, the non-interacting SL-BHM ($U = 0$) with Lindblad operators $L = \sqrt{\gamma'}a$, $L = \sqrt{r\gamma'}a^\dagger$ for single-particle loss and gain can be analyzed setting $\mu = 0$. Note that the gain amplitude is rescaled by a factor $0 \leq r < 1$, which will become clear in a moment. The NESS of non-interacting bosonic systems with linear Lindblad couplings to a reservoir can be investigated by means of the bosonic formulation of third quantization [22]. Employing this procedure for the non-interacting SL-BHM results in a problem. In most scenarios, the dissipative pattern imposed by carrying over the Lindblad operators of the last section does not lead to a steady state as the system infinitely fills up with particles. A first approach towards resolving the unbalanced gain and loss introduced by the choice of collapse operators involves a rescaling of the gain parameter by a factor r, such that the number of particles coupled into the system is effectively decreased. This method was used in reference [54] to construct a double-well system with gain and loss in one well each, exhibiting *balanced* gain and loss. The proper choice of r follows from a similar reasoning for the conservation of the total particle number like in section 8.1. However, the intention of the mentioned publication only aimed at a description of balanced gain and loss for short times and therefore *cannot* be successfully applied to the construction of balanced steady states in the long-time limit.

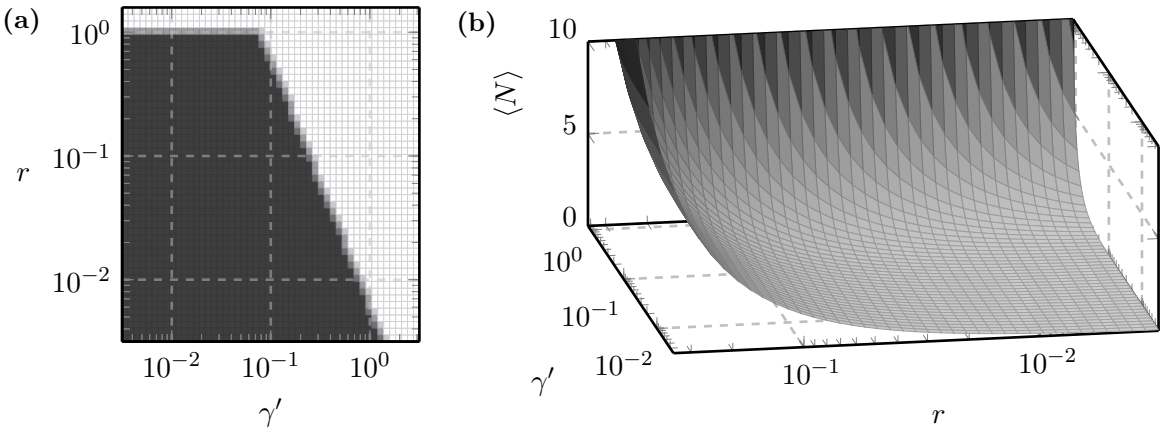

Figure 8.5.: Behavior of the steady state of a non-interacting periodic SL-BHM system with $L = 16$ and collapse operators $L = \sqrt{\gamma'}a$, $L = \sqrt{r\gamma'}a^\dagger$ arranged in the fashion of the complex potential U_2 with alternating gain and loss. (a) The black areas mark the regime in which the existence of a steady state is guaranteed (see appendix C) while an infinite amplification of the system occurs in the white regions. (b) Total particle number $\langle N \rangle$ of the NESS in the same parameter region. The filling increases rapidly at the boundary between the area with an existing steady state and the amplification regime.

Figure 8.5 illustrates this explained difficulty of properly choosing a Lindblad operator setup that leads to no amplification of the system. The panel of figure 8.5a shows an extract of the parameter regime for an arrangement of Lindblad operators similar to the complex on-site potential U_2 with a scaled gain amplitude. For increasing values of γ' the critical value of r up to which the existence of a steady state is guaranteed decreases. The results for the total number of particles present in the system's steady state shown in figure 8.5b underlines the improper choice of Lindblad operators as the total filling of the system is very sensitive to r, γ' near the transition to the amplification regime.

Thus, an alternative way for the parameterization of *controlled* gain and loss has to be found. In this work, the latter will be realized by introducing both gain and loss processes on a single site j, such that the linear collapse operator L_j acting on that site is most generally described by two parameters $\gamma_j'^{(-)}, \gamma_j'^{(+)}$,

$$L_j = \sqrt{\gamma_j'^{(-)}}a_j + \sqrt{\gamma_j'^{(+)}}a_j^\dagger. \tag{8.18}$$

In order to relate this pattern to the notion of sites subject to particle gain and as like in previous chapters, two different choices for the two parameters are made. A *gain site* (yellow circles denoted by + in the model schemes) is described by the vector

$$\underline{\gamma}'_{\mathrm{g}} = \begin{pmatrix} \gamma_{\mathrm{g}}'^{(+)} \\ \gamma_{\mathrm{g}}'^{(-)} \end{pmatrix} \quad \text{with} \quad \gamma_{\mathrm{g}}'^{(+)} < \gamma_{\mathrm{g}}'^{(-)} \tag{8.19a}$$

and a *loss site* (blue circle labeled with a minus sign in sketches) is characterized by

$$\underline{\gamma}'_\ell = \begin{pmatrix} \gamma_\ell'^{(+)} \\ \gamma_\ell'^{(-)} \end{pmatrix} \quad \text{with} \quad \gamma_\ell'^{(+)} < \gamma_\ell'^{(-)}. \tag{8.19b}$$

In the following, the most common choice of equal loss on all dissipative sites, $\gamma_\mathrm{g}'^{(-)} = \gamma_\ell'^{(-)}$, is adopted, simultaneously setting $\gamma_g'^{(+)} \geq \gamma_\ell'^{(+)}$. Consequently, effective controlled gain is then imposed by the difference between the strength of the gain processes on the loss and gain sites. In the case of $\underline{\gamma}'_\mathrm{g} = \underline{\gamma}'_\ell$ one speaks of *symmetric reservoirs*.

For the parameterization (8.19) there already exist some statements derived in [83], which also hold for the interacting scenario in some cases. For the purpose of this work, those results can be summed up as follows:

- In the non-interacting case ($U = 0$) of a *homogeneous chain* ($t_1 = t_2$) with a setup of Lindblad operators (8.19) arranged on the most outer sites in the fashion of U_1, an *exact* solution for the occupation of the interior sites $2, \ldots, L-1$ and the edge sites $1, L$ can be derived. The bulk is always flat in this configuration and only the edge occupations are influenced by bath parameters. With the onset of interactions ($U \neq 0$), the flat bulk tends to deform into a linear profile.

- In both the interacting ($U = 0$) and non-interacting ($U \neq 0$) model with *only one* or many *symmetric* reservoirs the steady state is completely uncorrelated and can be written as a product state. The entire system is filled with an identical number of particles per site given by the expression

$$\langle n_j \rangle = \left(\frac{\gamma_\ell'^{(-)}}{\gamma_\ell'^{(+)}} - 1 \right)^{-1} = \left(\frac{\gamma_\mathrm{g}'^{(-)}}{\gamma_\mathrm{g}'^{(+)}} - 1 \right)^{-1}, \tag{8.20}$$

  which is solely determined by the ratio of gain and loss on the reservoir(s). Note that this behavior of the model in this certain configuration is *independent* of the choice of the tunneling amplitudes, which may be chosen randomly (but non-zero).

With that said, the dissipation patterns of the complex on-site potentials U_1, U_2 and U_3 are transferred to the parameterization (8.19) of gain and loss sites allowing for a controlled way of introducing dissipative effects without suffering from an infinite amplification of the system.

Figure 8.6 shows the steady states of non-interacting SL-BHM chains with trivial ($t_1 = 0.1, t_2 = 0.02$, left panel), nontrivial ($t_1 = 0.02, t_1 = 0.1$, top right panel) and no ($t_1 = t_2 = 0.06$, bottom right panel) dimerization for a dissipative pattern in U_1 form. Note that the symmetric configuration (red circles) shown in all plots is in accordance with the analytical result (8.20) for the chosen reservoir parameters. As expressed above, the

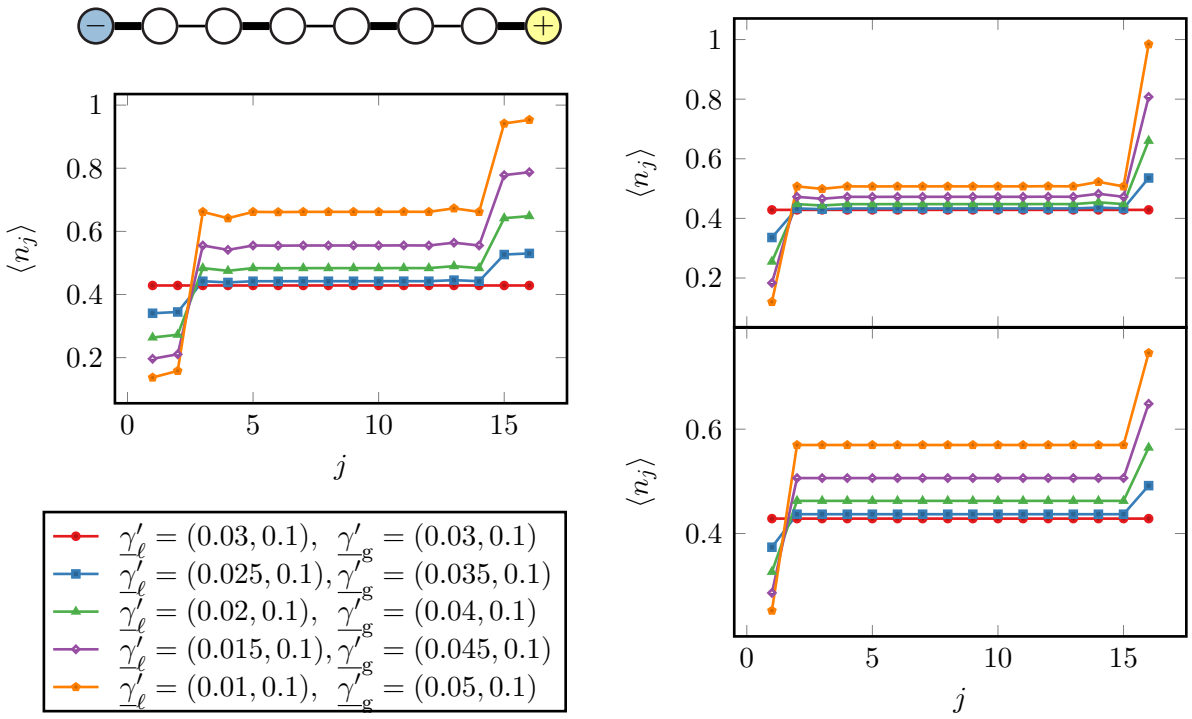

Figure 8.6.: Steady states of open non-interacting SL-BHM chains with different dimerizations subject to a dissipation pattern similar to the complex on-site potential U_1 for different reservoir preparations obtained by third quantization. Left: trivial chain ($t_1 = 0.1, t_2 = 0.02$), top right: nontrivial chain ($t_1 = 0.02, t_2 = 0.1$), bottom right: homogeneous chain ($t_1 = t_2 = 0.06$). Although the steady state is not at half filling anymore as in the hard-core bosonic (fermionic) scenario, edge features similar to those described in chapter 6 appear.

homogeneous chain possesses a flat bulk with only the occupation of the dissipative sites showing a different filling. In contrast to this, the trivial and nontrivial chain do not exhibit an entirely flat bulk, but rather show exactly the same effects that were already discussed in chapter 6. In the trivial chain the sites strongly coupled to the dissipative boundaries are also affected by a particle gain or loss that also weakly invades the next-neighboring sites. However, the described edge effects cannot be understood as degrees of freedom in terms of a single particle located at the edge and the NESS is generally not at half filling as can be seen from the condition (8.10) derived in section 8.1. The latter condition can also be verified to hold for the occupation of the symmetric configuration. Inserting (8.20) into the left side of (8.10) leads to (dropping the subscripts as both parameters are equal)

$$\sum_{j_{\text{gain}}} \gamma_{j_{\text{gain}}} \left(1 + \langle n_{j_{\text{gain}}} \rangle\right) = 2\gamma'^{(+)} \left[1 + \left(\frac{\gamma'^{(-)}}{\gamma'^{(+)}} - 1\right)^{-1}\right] = \frac{2\gamma'^{(+)}\gamma'^{(-)}}{\gamma'^{(-)} - \gamma'^{(+)}}. \tag{8.21a}$$

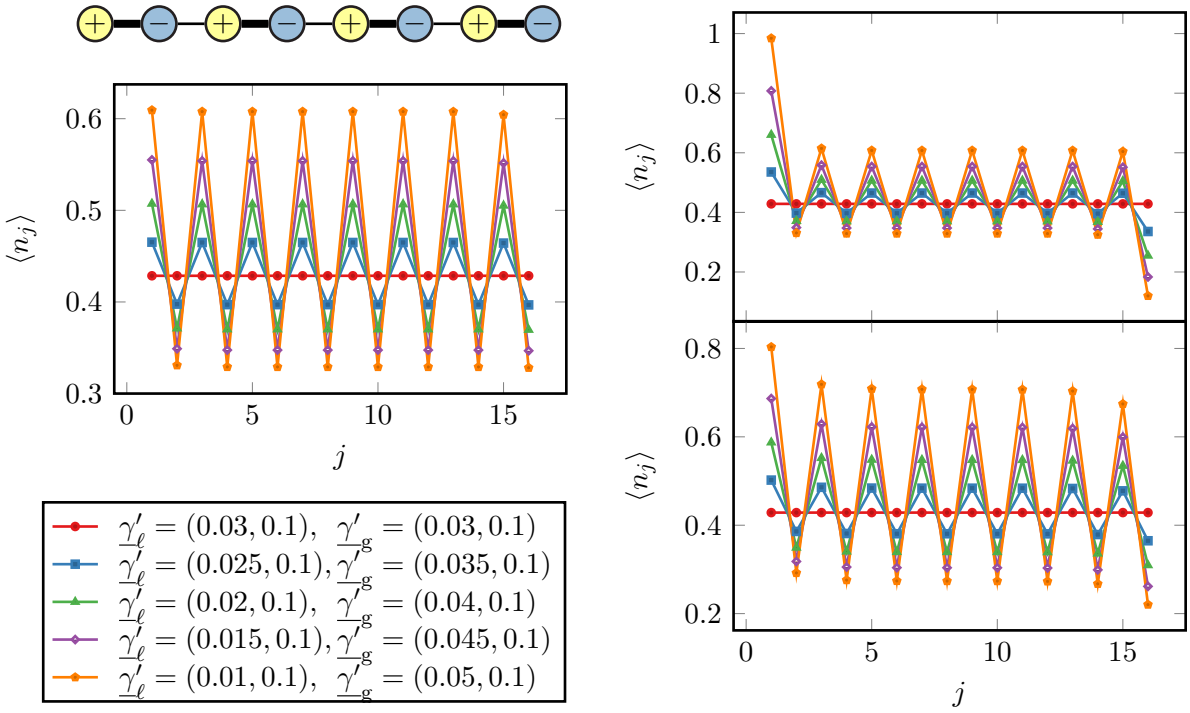

Figure 8.7.: Lattice occupation of the steady states of non-interacting SL-BHM chains ($L = 16$) exposed to a dissipative pattern similar to U_2 for varying reservoir couplings. Top left: trivial chain, top right: nontrivial chain, bottom right: homogeneous chain. The staggering of the bulk is a generic feature of the dissipative pattern, but nevertheless edge features are most pronounced for the nontrivially dimerized system.

Similarly, for the right side the same result follows,

$$\sum_{j_{\mathrm{loss}}} \gamma_{j_{\mathrm{loss}}} \langle n_{j_{\mathrm{loss}}} \rangle = 2\gamma'^{(-)} \left(\frac{\gamma'^{(-)}}{\gamma'^{(+)}} - 1 \right)^{-1} = \frac{2\gamma'^{(-)}\gamma^{(+)}}{\gamma'^{(-)} - \gamma'^{(+)}}. \tag{8.21b}$$

In contrast to the almost completely flat bulk, the dissipative pattern imposed by an arrangement of the controlled gain/loss Lindblad operators similar to U_2 leads to a staggering in the interior of the system regardless of the dimerization, compare figure 8.7. The staggering is rather a consequence of alternating gain and loss. While the staggering of the trivial and homogeneous chain continues to the system boundaries without major deviations from the interior, the nontrivial system shows clear edge features stemming from the weakly coupled boundary site that only allows for weak particle currents into the interior. Since the explained sensitivity of the nontrivial chain to edge effects can be explained by properties of the geometry of the chain (a weakly coupled site at the boundary), it remains an open question whether this can be considered a topological property of the system and, if so, how the latter can be classified.

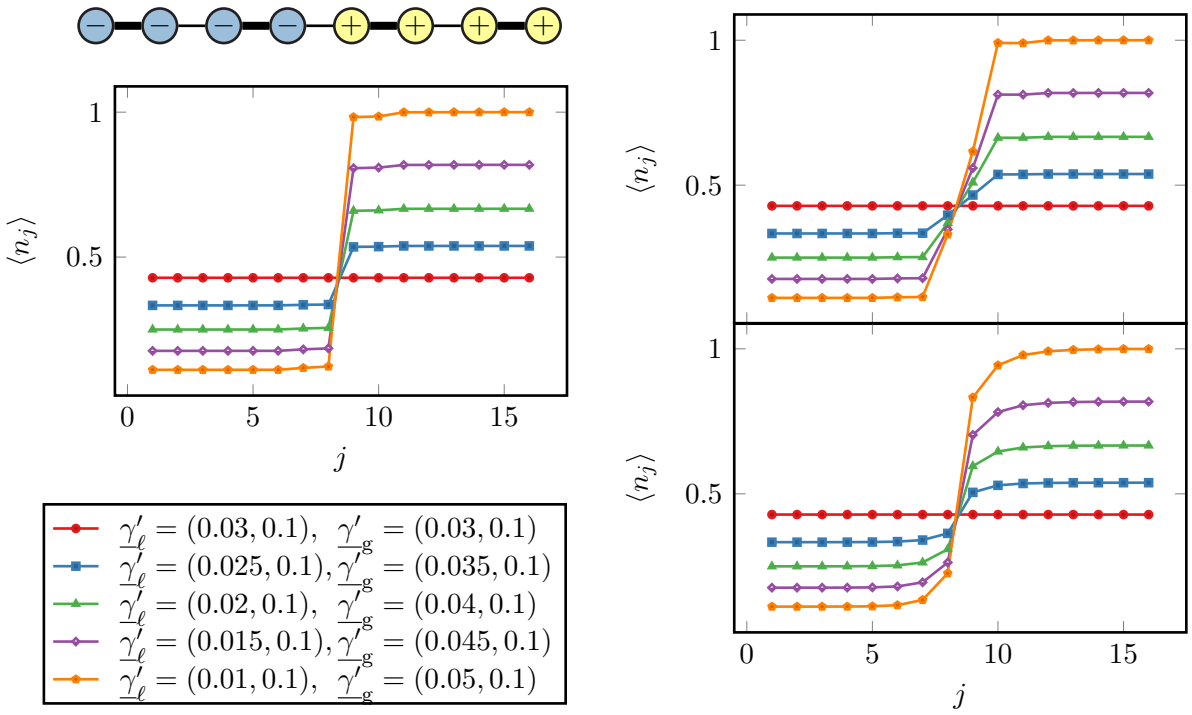

Figure 8.8.: Steady state lattice occupations obtained by third quantization for different non-interacting SL-BHM chains with $L = 16$ and a dissipative structure similar to the complex on-site potential U_3. Top left: trivial chain, top right: nontrivial chain, bottom right: homogeneous chain. The occupation of the two halfs subject to only loss or gain is described well by the symmetric configuration with the respective bath configuration.

Another illustration of the occupation number in the symmetric configuration (equation (8.20)) is given by an arrangement of Lindblad operators in the fashion of U_3 shown in figure 8.8. Except for the boundary between gain and loss sites, the occupation in one of the two halfs subject to only controlled gain or loss is properly described by the occupation number in the symmetric configuration. The fact that the sites $j = L/2+1, \ldots, L$ are filled up with particles until $\langle n_j \rangle \approx 1$ in the case of $\underline{\gamma}'_{\mathrm{g}} = (0.05, 0.1)$ is *not* a consequence of Pauli's exclusion principle as in the effective fermionic case discussed in the previous section, but follows directly from the choice of the bath couplings and equation (8.20), as $\langle n_j \rangle = (0.1/0.05 - 1)^{-1} = 1$ for $j = L/2+1, \ldots, L$. Only at the intermediate boundary particle currents lead to deviations from this expectation.

Following this reasoning, one could start from each of the presented dissipative patterns in a symmetric configuration with $\gamma'^{(-)}_{\mathrm{g},\ell}/\gamma'^{(+)}_{\mathrm{g},\ell} - 1 = 2$ thus leading to an entirely flat occupation at $\rho = 1/2$, no matter how all other model parameters (*including* interactions)

are chosen. Moving away from this configuration, for instance by the parameterization

$$\begin{aligned} \gamma_{\mathrm{g}}'^{(+)} &\rightarrow \gamma_{\mathrm{g}}'^{(+)} + \Delta\gamma', \\ \gamma_{\ell}'^{(+)} &\rightarrow \gamma_{\ell}'^{(+)} - \Delta\gamma', \end{aligned} \tag{8.22}$$

which was also applied in the shown results, one could increase the dissipative effects to obtain lattice occupations resembling the states of the hard-core bosonic (fermionic) case even more. The remaining effects to be studied for the dissipative SL-BHM involves influences of particle interactions, which are discussed in the next section.

8.4. Truncated interacting SL-BHM

Proceeding further, the non-interacting SL-BHM with controlled gain and loss described by Lindblad operators of the form of equations (8.18) is now extended by the interaction term determined by the on-site interaction U. For studying the entire SL-BHM Hamiltonian (3.1), all on-site potentials ε_j and the chemical potential μ are set to zero.

As the Liouvillean of the system is not quadratic anymore, the method of third quantization cannot be applied. Instead, the non-Hermitian DMRG algorithm presented in section 5.4 is employed to study the steady state. The major restriction of the algorithm on a regular workstation is given by the amount of memory required for the storage of the sparse superblock Liouvillean matrix. Recap that the dimension of the latter for two blocks with m basis states that are both enlarged by a single lattice site with dimension D^2, where D denotes the degrees of freedom of the single site's Hilbert space, is given by m^2D^4. Even if the Liouvillean matrix is extremely sparse this requires a storage of $\mathcal{O}(m^2D^4)$ elements. In contrast, the superblock Hamiltonian in the Hilbert space DMRG algorithm is only of dimension m^2D^2. Fortunately, the dissipative systems under investigation are close to the symmetric configuration whose steady state is *exactly* given by a product of single site density operators (see reference [83]), which in principle requires $m = 1$ for an exact representation within DMRG. Thus, it seems reasonable that the number of states to be kept in a block for a proper description of its basis is also small. In the following figures the DMRG strategy proceeds by keeping the truncation error $\varepsilon < 10^{-7}$ with a maximum of $m_{\max} = 32$ states.

Moreover, the bosonic Liouville space has to be truncated by allowing a maximum particle number of $D - 1$ per site, that is a local site dimension of D^2. However, it is evident that the maximum number of allowed bosons required for properly converged results depends heavily on the setup of the reservoirs. In order to choose the truncation parameter D, the symmetric configuration of which the result is analytically known, is simulated with the non-Hermitian DMRG method with different bosonic cutoffs for a comparison. As mentioned above, the number of basis states m for this case can be

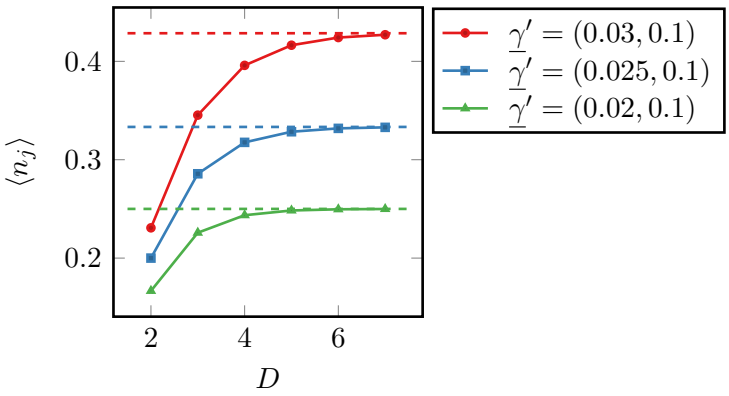

Figure 8.9.: Occupation of the symmetric non-interacting U_2 SL-BHM chain for different reservoirs obtained by non-Hermitian DMRG in Liouville space and different bosonic cut-offs. Lines are guides to the eye and dashed lines represent analytical results. Additional parameters are $L = 8$ and $t_1 = t_2 = 0.1$ but may in principle be chosen randomly.

kept *very* small, which allows accessible values up to $D = 7$. Figure 8.9 shows the occupation of the flat profile obtained by simulating a non-interacting SL-BHM chain with symmetric reservoirs for different bath couplings. The convergence behavior is connected to the filling of the steady state, that is the inverse of the ratio $\gamma'^{(-)}/\gamma'^{(+)} - 1$ (compare equation (8.20)). In the case of $\underline{\gamma}' = (0.03, 0.1)$, in which the occupation is largest, a proper convergence requires $D > 5$ while the other two configurations with less dominant gain already converge to a good extent for $D \geq 5$. Hence, convergence errors are best eliminated by choosing a large ratio $\gamma'^{(-)}/\gamma'^{(+)}$, which can then be modified by the parameterization (8.22). For the remaining part of this section, the symmetric bath configuration $\underline{\gamma}' = (0.02, 0.1)$ will therefore be adapted to investigate the dissipative patterns of the complex on-site potentials in the presence of particle interactions.

The results of both the non-interacting and interacting scenario of the dissipative SL-BHM for both dimerizations and the different gain/loss patterns are summarized in figure 8.10. Generally, the steady state for $U = 0$ is reproduced to a very good accuracy by the non-Hermitian DMRG procedure for $D = 5$. The open chains subject to U_1 (figures 8.10a, 8.10b) and U_3 (figures 8.10e, 8.10f) show small visible deviations from the result of third quantization. Moreover, the onset of interactions has a similar effect on the NESS occupation in the bulk as increasing the gain amplitude, while interestingly the nontrivial boundaries are mostly unaffected. The staggering of the steady state for the case of U_2 (figures 8.10c, 8.10d) is amplified by interactions. Similarly, filling/emptying of the sites at the boundary between gain and loss in the U_3 setup becomes more pronounced with the onset of particle interactions. It is not known whether the results for the interacting case are properly converged. Thus, the explained effect of U leading to similar consequences as an increase in the gain amplitude could be even more explicit when more particles are allowed on a single site. To conclude this section, it shall be stressed once more that the effects identified in chapter 6 are quite generic to dimerized dissipative chains regardless of the nature of the particles – fermionic or bosonic, interacting or non-interacting – which is a *remarkable* result.

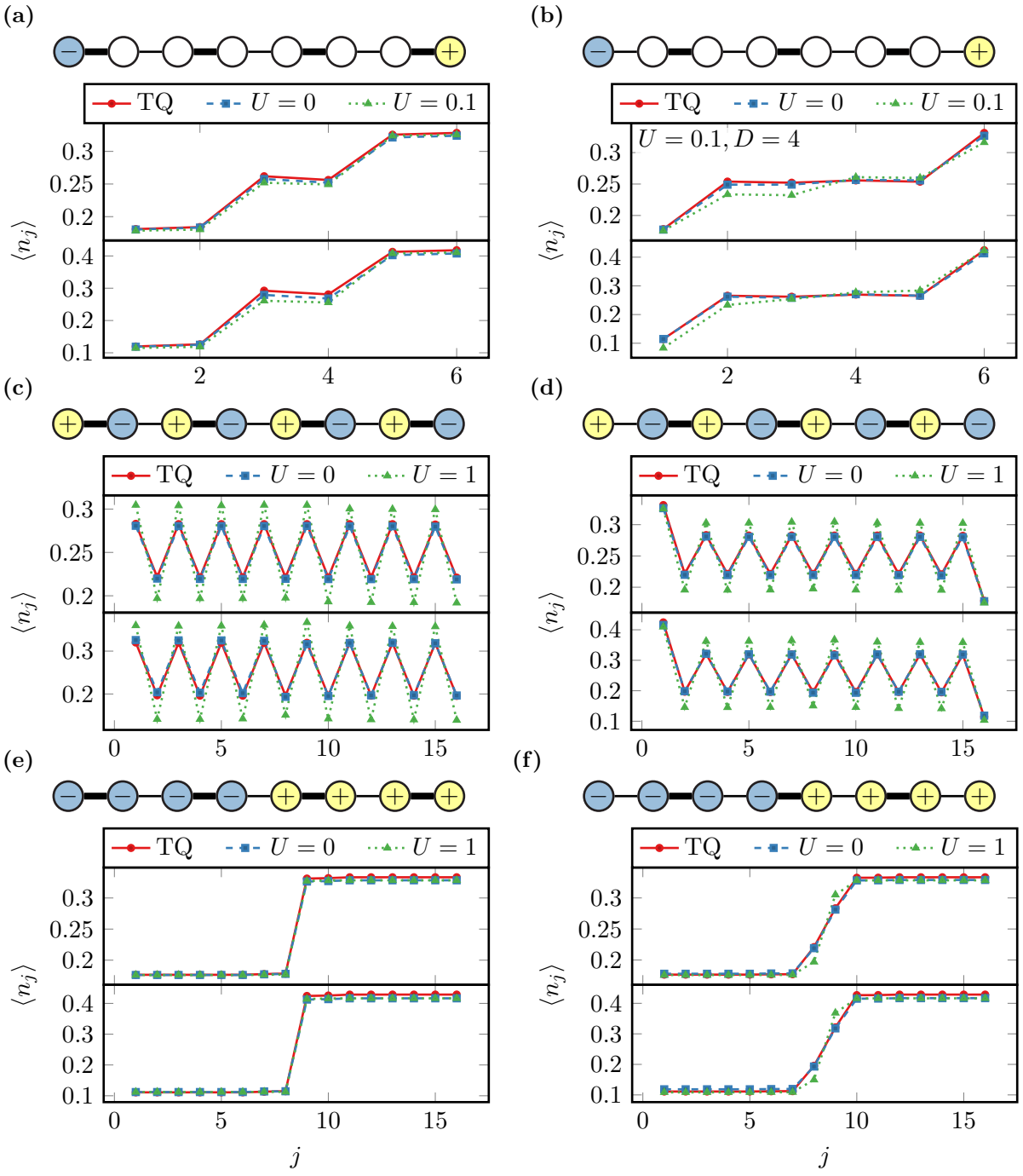

Figure 8.10.: Comparison of the NESS in the non-interacting (third quantization (TQ, red circles) and DMRG ($D = 5$, blue squares)) and interacting regime ($D = 5$ if not stated different, green triangles) for different dissipative patterns and bath setups. Reservoir configuration in top subfigure panels: $\underline{\gamma}'_\ell = (0.015, 0.1), \underline{\gamma}'_\mathrm{g} = (0.025, 0.1)$, bottom panels: $\underline{\gamma}'_\ell = (0.01, 0.1), \underline{\gamma}'_\mathrm{g} = (0.03, 0.1)$. The left half shows the trivial chain ($t_1 = 0.1, t_2 = 0.02$) for (a) U_1, (c) U_2 and (e) U_3 while the right side contains results of the nontrivial chain ($t_1 = 0.02, t_1 = 0.1$) with (b) U_1, (d) U_2 and (f) U_3.

Chapter review

- The total particle number expectation value of the non-equilibrium steady state (NESS) of a system with a particle-conserving Hamiltonian and linear Lindblad couplings obeys relations (equations (8.10) and (8.15)) that enforce the NESS of the fermionic (hard-core bosonic) dissipative SSH model to be at half filling for U_2, U_3. Interestingly, this also holds for U_1.
- A description of dissipation in the SL-BHM by complex on-site potentials leads to results that are in accordance to the formulation with master equations in Lindblad form. Identified effects stemming from the decoupling of dissipative sites from the rest of the system explained in chapter 6 can also be observed in the dissipative SSH model. It is remarkable that the approach of using complex on-site potentials to effectively describe dissipative processes reproduces the result of the Lindblad master equation steady state when the imaginary parts of the energies are interpreted as decay rates.
- Relaxing the restrictions of no multiple occupations, the choice of Lindblad operators has to be modified to impose controlled gain and loss on lattice sites avoiding an amplification of the bosonic system (equation (8.19)). Also for the dissipative non-interacting SL-BHM edge effects similar to those in the dissipative SSH and $\mathcal{PT}$-symmetric SL-BHM model can be identified, although the NESS is not generally at half filling.
- Quadratic master equations can be treated within the formalism of third quantization [21, 22] for both fermionic and bosonic systems. For interacting systems, no semi-analytic approach is available. The non-Hermitian DMRG algorithm introduced in section 5.4 is successfully applied to study the effects of particle interactions in the dissipative SL-BHM. The onset of interactions leads to effects in the NESS occupation that are similar to those obtained from increasing the gain amplitude.
- The presented method can be applied to arbitrary *local* non-quadratic Liouvilleans, that is models with a local Hamiltonian joined by local Lindblad operators.

9. Conclusion and outlook

One of the main goals in this work was the investigation of one-dimensional quantum many-body systems whose Hamiltonians yield topologically nontrivial phases and which are subject to dissipative effects. The study was done in order to identify generic effects that may give rise to topological effects also appearing in the case of dissipation, in which the development of a complete classification scheme is still an open problem. To do so, two different approaches of imposing gain and loss were taken – the introduction of complex on-site potentials and a description with master equations in Lindblad form [12]. Interestingly, both descriptions that have two mostly independent communities behind them lead to similar effects, which states one of the most outstanding results of this work.

The studied systems were given by extensions of the paradigmatic Su-Schrieffer-Heeger (SSH) model [10] for non-interacting spin-polarized fermions on a superlattice structure with alternating tunneling amplitudes, whose treatment allows for the illustration of topological effects such as edge states and the classification of topological invariants such as adiabatic phases originally introduced by Berry [14]. A straightforward implementation of the SSH model for bosons leads to the superlattice Bose-Hubbard model (SL-BHM) by incorporation of on-site potentials, on-site interactions and a grand-canonical ensemble described by its chemical potential. In the hard-core limit, that is for infinite particle interactions, the SL-BHM can be mapped onto the SSH model by a Jordan-Wigner transformation [40] in the case of vanishing on-site potentials and zero chemical potential. As a consequence, the topological properties of the SSH model's Bloch bands are inherited by the bosonic counterpart in this regime, also leading to a nontrivial topology, which is still present in the strongly-interacting regime of the model. This triggered efforts to generalize the topological classification scheme from the non-interacting to the interacting scenario [43]. For the SL-BHM, a generalization of the SSH bulk winding number, which is equivalent to the Berry phase picked up by the lower Bloch band after a transport through the Brillouin zone, also known as Zak phase [13], is achieved by introducing a magnetic flux threading the system [15, 46], which also builds the foundation for a generalization to the dissipative (non-Hermitian) case.

Introducing single-particle gain and loss effects, the first approach under investigation was realized by imposing $\mathcal{PT}$-symmetric on-site potentials on the SL-BHM leading to a non-Hermitian Hamiltonian with, in principle, complex energies. This can be motivated

as the introduction of a complex on-site potential $\overset{(+)}{-}\mathrm{i}\gamma/2$ leads to the same behavior of the particle number on a single site in the mean-field limit, when dissipation is introduced by Lindblad operators $\sqrt{\gamma}a$ ($\sqrt{\gamma}a^\dagger$) with the gain/loss strength γ. Different dissipative patterns given by the complex potentials U_i were studied in both the single- and many-particle (non-interacting and interacting) picture. To avoid infinite amplifications of the system, the analysis was restricted to the low-energy regime where multiple fillings of sites are refused. In the single-particle picture a limited number of bulk states is deformed towards energy real part zero for increasing gain/loss in the configurations $U_1, U_1^{(\mathrm{c})}$ and U_3, which can be identified in the many-particle picture to correspond to (i) localized particles at dissipative sites and (ii) zero-energy edge modes of the remaining Hermitian subsystem. The effect of gain/loss on a dissipative site leads to its *decoupling* from the rest of the system, thereby inducing the occurrence of edge states in the remaining subsystem when the latter possesses nontrivial boundaries. Interpreting the imaginary part of the energy of a state as a *decay rate* with a positive imaginary part leading to a favored occupation of the state while the opposite holds for a negative imaginary part, results in lattice occupations of the most contributing state (largest imaginary part) being *astonishingly* similar to that of the steady state of an equivalent master equation.

A very interesting arrangement of gain and loss in an alternating way, represented by the complex potential U_2 which exhibits a $\mathcal{PT}$-unbroken regime, has already attracted both theoretical [33, 80, 88–90] and experimental [4, 93] works for the realization and classification of topological phases in non-Hermitian non-interacting systems. In this work, the quantized topological invariant ν of the *interacting* SL-BHM (equation (3.17)) was generalized to the non-Hermitian $\mathcal{PT}$-unbroken case (equation (7.17)) formulated in a biorthogonal basis leading to a complex Berry phase ν. Following the argumentation of Hatsugai [46], the quantization of $\mathrm{Re}(\nu)$ in integer units of π was shown to be protected by the $\mathcal{PT}$ symmetry of the system. A simple method for the numerical computation of ν was presented in equation (7.18) and a different algorithm for the computation of the complex Berry phase, leading to similar results, established by a co-worker and the author of this thesis is to be published [33]. Moreover, the existence of topologically protected edge states at interfaces between two non-Hermitian $\mathcal{PT}$-unbroken systems characterized by different complex Berry phases was successfully illustrated, borrowing the system configuration from [4]. In fact, the formulation of the mentioned quantities for the extended SL-BHM gives rise to topological order in interacting systems even in the presence of dissipation.

The interpretation of the complex Berry phase as a topological invariant in the $\mathcal{PT}$-broken regime is spoiled as the assumptions of the adiabatic theorem have to be modified in the presence of complex energies [86, 87]. Nevertheless, the generalized winding number ν can be employed as a *local order parameter* encoding entanglement between adjacent sites even in the $\mathcal{PT}$-broken and non-quantized case, which is a consequence of the product form of the SL-BHM ground state in terms of singlet configurations located

along strong bonds in the fully-dimerized limit. In fact, the non-quantized values of ν in an open dissipative SL-BHM chain are close to the strictly quantized values in the periodic Hermitian system. The process of dissipative sites decoupling from the rest of the system in the limit of strong gain/loss can be tracked by a change of $\nu \approx \pi$ to $\nu \approx 0$. Thus, dissipative effects lift the correlations/entanglement in a state for increasing gain/loss strengths. Eventually, in the limit of strong dissipation, the winding numbers of all bonds in the system that are affected by gain or loss are driven to $\nu \approx 0$, which can be understood from the viewpoint of a reservoir frequently performing measurements on the system, thereby resolving entanglement in the affected regions.

To compare the results of the description with complex on-site potentials, the second approach towards describing dissipation was achieved by means of master equations in Lindblad form with collapse operators $\sqrt{\gamma'}a^\dagger, \sqrt{\gamma'}a$ accounting for single-particle gain and loss, respectively. The interesting object is then given by the non-equilibrium steady state (NESS) towards which the system converges in the long-time limit. A condition for the lattice occupation of the NESS was derived for the dissipative scenarios U_2 and U_3, stating that the NESS is always at half filling. The application of third quantization [21] allows for an easy extraction of NESS observables for the dissipative SSH model leading to lattice occupations that are in accordance with the interpretation of the spectra of non-Hermitian Hamiltonians. Both the descriptions of dissipation with complex on-site potentials and master equations in Lindblad form are in correspondence when the number of particles is restricted, as is the case for the fermionic (hard-core bosonic) model or the extended SL-BHM in the strongly-interacting low-energy regime. The outlined correspondence is best illustrated by the resemblance of figures 6.11 and 8.4. In the same fashion as for complex potentials, the decoupling of dissipative sites leading to Hermitian remnants that may host additional edge modes is observed. This triggering of edge modes in an interior Hermitian subsystem happens only for large enough dissipative strengths, when the imposed currents cannot be balanced by the system anymore. Thus one can deliberately prepare edge modes in a Hermitian subsystem, which may be referred to as edge modes *driven by dissipation*.

If the restrictions of avoided multiple occupations of a single site are relaxed, the problem of an infinite amplification bosonic systems may suffer from has to be circumvented by a modified choice of Lindblad operators that realizes *controlled gain and loss*. The parameterization with $\gamma'^{(\pm)}_{\mathrm{g},\ell}$ has already been investigated by reference [83] for a homogeneous Bose-Hubbard chain with reservoirs attached to the open boundaries as U_1 where also analytical results were obtained. Moving on to the treatment of the non-interacting SL-BHM by carrying over this choice of Lindblad operators realizing controlled gain and loss sites to the dissipative patterns of the U_i, the same effects occurring in the $\mathcal{PT}$-symmetric description and the dissipative SSH model could be identified by means of third quantization [22], namely the effective decoupling of dissipative lattice sites from the rest of the system leading to interior edge modes whenever the remnant possesses nontrivial boundaries.

Numerical methods have pushed the frontiers of accessible system dimensions for interacting models in recent years and one of the most prominent methods for treating one-dimensional quantum many-body systems is given by density matrix renormalization group algorithms (DMRG) [16, 17], whose understanding and formalization in the language of tensor network states (especially matrix product states (MPS)) [18, 60] requires quite an effort to become familiar with. In this work, a formulation of a DMRG algorithm in the traditional language was given, avoiding the terminology of MPS. This description is not restricted to Hermitian operators, but has also been extended to non-Hermitian operators, which allows for the study of both $\mathcal{PT}$-symmetric Hamiltonians and Liouvilleans. The technique resembles recently developed MPS-based algorithms [72]. Thus the outlined procedure may provide a very comprehensible approach for readers familiar with DMRG that do not (yet) want to get involved with MPS. It shall be emphasized that all adaptions can be included in a working Hermitian DMRG code without much effort. To the best of the author's knowledge, this is the first time a non-Hermitian DMRG method was deliberately employed to study $\mathcal{PT}$-symmetric Hamiltonians.

Turning on particle interactions, the Liouville operator in the master equation in Lindblad form is not quadratic anymore and the method of third quantization cannot be applied. To investigate the influence of particle interactions on the NESS, a DMRG algorithm for the treatment of non-Hermitian operators was developed to optimize the representation of the steady state in the Liouville space, whose dimension quickly exceeds numerical limitations when all degrees of freedom are kept in the description. The method reproduces the results obtained from third quantization in the non-interacting limit to high accuracy and aforementioned typical effects are also found in the interacting dissipative SL-BHM with particle interactions leading to similar effects on the NESS as an increase in the gain amplitude.

Outlook: In fact, the observed effects have not been rigorously related with a topological classification scheme. This however could be achieved by embedding the observed effects for the dissipative SSH model into the context of the topological classification of steady states of quadratic master equations presented in [9, 97]. Pushing this further, it is an open question whether the generalization of the winding number to the interacting case by introducing a $U(1)$ twist in a tunneling element can also be employed to classify the NESS of an interacting system. Moreover, a deeper understanding of how dissipative effects influence the Hermitian subsystem in the U_1 dissipation pattern could be gained by computing an effective Hamiltonian for the subsystem. It would be interesting to see whether the outer gain/loss effectively leads to a lowering raising of the edge states' energies leading to the observed favored/avoided occupation of the latter. Another analytically approachable task involved the derivation of analytical results for the dimerized Bose-Hubbard model out of equilibrium similar to the computation performed in [83].

A. Zusammenfassung (German)

Die vorliegende Arbeit mit dem Titel „Bosonische Vielteilchensysteme mit topologisch nichttrivialen Phasen unter Gewinn und Verlust“ befasste sich mit der Untersuchung eindimensionaler quantenmechanischer Vielteilchensysteme, deren Hamilton-Operatoren topologisch nichttriviale Phasen aufweisen, in der dissipativen Erweiterung. Insbesondere sollten allgemeine Effekte beschrieben werden, die Anlass für das Auftreten topologischer Effekte in offenen Quantensystemen geben, deren vollständige Charakterisierung ein ausstehendes Problem darstellt. Im Rahmen der Arbeit wurden zwei unterschiedliche Ansätze zur Beschreibung dissipativer Effekte realisiert – das Einführen komplexer Gitterplatzpotentiale und eine Beschreibung der Systemdynamik mit Hilfe von Master-Gleichungen in Lindblad-Form [12]. Insgesamt konnte gezeigt werden, dass beide Wege ähnliche Effekte aufweisen.

Als Modelle wurden verallgemeinerte Varianten des bekannten Su-Schrieffer-Heeger-Modells (SSH) [10] untersucht, welches nicht-wechselwirkende Spin-polarisierte Fermionen auf einem eindimensionalen Übergitter mit alternierenden Tunnelamplituden beschreibt und eine Vielzahl von Eigenschaften topologisch nichttrivialer Systeme illustriert, beispielsweise das Auftreten von topologisch geschützten Randzuständen und die Klassifizierung solcher Systeme mit Hilfe einer adiabatischen Phase, welche ursprünglich von Berry eingeführt wurden [14]. Im bosonischen Fall gelangt man durch Hinzunahme von kontaktartigen Teilchenwechselwirkungen, externen Gitterplatzpotentialen und einem großkanonischen Ensemble, das durch ein chemisches Potential charakterisiert wird, zum Übergitter-Bose-Hubbard-Modell (SL-BHM). Im Grenzfall unendlich starker Kontaktwechselwirkung, verschwindenden externen Potentialen und verschwindendem chemischem Potential können SL-BHM und SSH-Modell durch eine Jordan-Wigner-Transformation [40] ineinander überführt werden, weshalb die topologischen Eigenschaften der Bloch-Bänder im SSH-Modell in diesem Grenzfall direkt vom SL-BHM geerbt werden und sogar für endliche Teilchenwechselwirkungen erhalten bleiben. Daraus folgte das Bestreben, eine topologische Charakterisierung wechselwirkender Systeme durch Verallgemeinerung der Konzepte für nicht-wechselwirkende Systeme zu erhalten [43]. Für das SL-BHM kann die Windungszahl des Komponentenvektors des Hamilton-Operators in Bloch-Gestalt, welche äquivalent zur adiabatischen Phase, die ein Zustand des tiefer gelegenen Bloch-Bandes im SSH-Modell beim Transport durch die Brillouin-Zone aufnimmt – der Zak-Phase [13] – verallgemeinert werden, indem ein externer magnetischer

Fluß eingeführt wird [15]. Dieser Ansatz wird im Folgenden ebenfalls zur Verallgemeinerung der Begriffe im nicht-hermiteschen Fall benutzt.

Zuerst wurden $\mathcal{PT}$-symmetrische Potentiale im SL-BHM eingeführt, was zu einem nicht-hermiteschen Hamilton-Operator führt. Dieser Ansatz wird motiviert durch die Tatsache, dass das Verhalten der Teilchenzahl auf einem Gitterplatz mit Lindblad-Operatoren $\sqrt{\gamma}a, (\sqrt{\gamma}a^\dagger)$ im Mean-Field-Grenzfall identisch mit dem Verhalten durch Einführen eines komplexen Potentials $\overset{(+)}{-}\mathrm{i}\gamma/2$ ist. Eine Vielzahl von Reservoiranordnungen U_i wurde im Ein- und Vielteilchenbild untersucht. In ersterem stellte sich bei den Potentialen $U_1, U_1^{(\mathrm{c})}$ und U_3 heraus, dass der Realteil der Energie einer geringen Anzahl von Volumenzuständen verschwindet, welche im Vielteilchenbild als (i) komplett an dissipativen Gitterplätzen lokalisierte oder (ii) Randzustände des verbleibenden hermiteschen Teilsystems identifiziert werden konnten. Mit steigender Bad-Kopplung entkoppeln die dissipativen Gitterplätze zunehmend vom Rest des Systems, das wiederum Randzustände aufweisen kann, falls eine nichttrivale Grenze vorliegt. Interpretiert man den Imaginärteil der Energie als Zerfallsrate, so werden Zustände mit positivem Realteil aufgefüllt, wohingegen solche mit negativem entleert werden. Diese Interpretation führt zu Zuständen, welche gut mit den stationären Zuständen einer Master-Gleichung übereinstimmen.

Eine interessante Anordnung von Bädern stellt das Alternieren von Gewinn- und Verlusteffekten in der Form von U_2 dar, das eine $\mathcal{PT}$-ungebrochene Phase aufweist. In dieser Arbeit konnte die topologische Invariante des SL-BHM mit Hilfe einer biorthogonalen Basis formuliert und auf den $\mathcal{PT}$-ungebrochenen Bereich erweitert werden. Weiterhin wurde unter Zuhilfenahme der Argumentation in [46] gezeigt, dass der Realteil dieser komplexen Berry-Phase (order Windungszahl) $\mathrm{Re}(\nu)$ im genannten Bereich strikt quantisiert in ganzzahligen Vielfachen von π ist. Mit Gleichung (7.18) erfolgte eine numerische Berechnung und die Veröffentlichung eines weiteren Algorithmus zur Berechnung der komplexen Berry-Phase, zu dem der Autor beigetragen hat, steht bevor [33]. Weiterhin wurde das Auftreten von topologischen Randzuständen an Grenzflächen zweier nicht-hermitescher Systeme unterschiedlicher Berry-Phase illustriert.

Die Interpretation der komplexen Berry-Phase als topologische Invariante kann nicht auf den $\mathcal{PT}$-gebrochenen Bereich erweitert werden, da grundlegende Annahmen des adiabatischen Theorems bei Anwesenheit komplexer Energien zu berücksichtigen sind [41, 87]. Dennoch kann die Windungszahl ν als lokaler Ordnungsparameter zur Auflösung von Verschränkung zwischen benachbarten Gitterplätzen in Zuständen verwendet werden. Sogar im nicht-quantisierten Fall geringer Bad-Kopplungen verbleiben die Werte von ν bei den zu erwartenden Ergebnissen des periodischen hermiteschen Systems. Die Entkopplung nicht-dissipativer Plätze bei zunehmender Kopplung erfolgt durch einen Übergang von $\nu \approx \pi$ nach $\nu \approx 0$. Bei starker Dissipation werden letztendlich alle Bindungen, die von dissipativen Effekten betroffen sind nach $\nu \approx 0$ getrieben. Dies

steht in Übereinstimmung mit der Anschauung, dass ein Reservoir ununterbrochen Messungen am System ausführt, welche Korellationen/Verschränkung auflösen.

Zum Vergleich der Ergebnisse der nicht-hermiteschen Quantenmechanik erfolgte ebenfalls die Untersuchung von stationären Zuständen (NESS) zu Master-Gleichungen in Lindblad-Form mit linearen Lindblad-Operatoren $\sqrt{\gamma'}a^\dagger, \sqrt{\gamma'}a$. Für das fermionische dissipative SSH-Modell mit U_2, U_3 konnte abgeleitet werden, dass die Teilchenzahl des NESS stets bei halber Füllung des Gitters liegt. Mit Hilfe der Methode der dritten Quantisierung [21] können Observablen des stationären Zustandes leicht berechnet werden. Die resultierenden Gitterbesetzungen stimmen mit der Beschreibung mit nicht-hermiteschen Potentialen überein, was durch die beiden Abbildungen 6.11 und 8.4 illustriert wird. Diese Korrespondenz bedarf jedoch der Beschränkung maximal pro Gitterplatz zugelassener Teilchen. Es ist dennoch erstaunlich, dass beide Beschreibungen zu den selben Beobachtungen führen. Mit dem Wissen, dass dissipative Gitterplätze ab einer kritischen Badkopplung vom Rest des Systems entkoppeln, lassen sich gezielt Randzustände im verbleibenden Untersystem induzieren.

Falls die Einschränkung der Besetzungszahl pro Gitterplatz aufgehoben wird, besteht bei bosonischen Systemen die Möglichkeit, dass das System kontinuierlich mit Teilchen aufgefüllt wird. Dies kann durch eine geeignete Parametrisierung der Lindblad-Operatoren umgangen werden, sodass durch die Beschreibung mit den Parametern $\gamma'^{(\pm)}_{\mathrm{g},\ell}$ kontrolliert (ohne Überlaufen) Teilchen ein- und ausgekoppelt werden. Für den Fall solcher Bad-Konfigurationen existieren bereits analytische und numerische Untersuchungen einer homogenen Bose-Hubbard-Kette [83]. Mit Hilfe der dritten Quantisierung [22] wurde nun das nicht-wechselwirkende dissipative SL-BHM untersucht, wobei die identischen Effekte identifiziert werden konnten – das Auftauchen interner Randzustände durch Entkopplung von dissipativen Gitterplätzen im Fall eines nichttrivialen Teilsystems.

Das Behandeln wechselwirkender Systeme erfordert ein hohes Maß an Aufwand, da analytische Zugänge meist scheitern. Numerische Methoden haben in den vergangenen Jahren den Bereich zugänglicher Systeme deutlich erweitert. Eine äußerst populäre Methode zur Behandlung wechselwirkender quantenmechanischer Systeme stellen Dichtematrix-Renormierungs-Gruppen-Algorithmen (DMRG) [16, 17] dar, deren Verständnis und Formalisierung in der Sprache von Tensor-Netzwerken (insbesondere Matrix-Produkt-Zuständen (MPS)) [18, 60] eine gewisse Einarbeitung erfordert. Die Formulierung der Methode in dieser Arbeit verzichtet auf die Begriffe dieses Gebiets und bedient sich der traditionellen Sprache, in welcher DMRG ursprünglich eingeführt wurde. Weiterhin erfolgte eine Erweiterung der Methode, um nicht-hermitesche Operatoren zu behandeln, wie beispielsweise $\mathcal{PT}$-symmetrische Hamilton-Operatoren oder Liouville-Operatoren. Für Leser, die über Kenntnisse von DMRG für hermitesche Operatoren verfügen, bietet die vorliegende Darstellung eine verständliche Erweiterung ohne Begriffe aus dem Bereich der Tensor-Netzwerk-Formulierung. Die nötigen Veränderungen eines Programms, welches hermitesche DMRG implementiert, sind leicht durchzuführen.

Nach bestem Wissen des Autors ist die Untersuchung $\mathcal{PT}$-symmetrischer Operatoren mit DMRG in dieser Arbeit erstmalig erfolgt.

Um Auswirkungen von Teilchenwechselwirkungen zu studieren, konnte die Methode der dritten Quantisierung nicht verwendet werden, da der das System beschreibende Liouville-Operator nicht mehr von quadratischer Ordnung in den bosonischen Erzeugern/Vernichtern ist. Hierzu wurde ein DMRG-Algorithmus entwickelt, der eine endlichdimensionale Darstellung des stationären Zustands im Liouville-Raum optimiert, da die Dimension des letzteren dramatisch mit der Anzahl der zugelassenen Teilchen und der Systemlänge zunimmt. Diese Methode reproduziert die Ergebnisse der dritten Quantisierung im nicht-wechselwirkenden Fall mit hoher Genauigkeit. Auswirkungen der Teilchenwechselwirkung auf die Gestalt des NESS liefern ähnliche Ergebnisse wie ein leichtes Erhöhen der Einkoppelrate.

B. Third quantization for fermions

B.1. General method

This chapter will walk through a brief summary of what has already been worked out in a very comprehensive way in reference [21] – a method for the solution of steady state properties of dissipative quadratic fermionic systems. Instead of only replicating the main results of the latter work, the emphasis of this appendix is to drop some aspects in order to illustrate the application of *third quantization* to the dissipative SSH model. As most of the figures in section 8.2 have been obtained by this procedure, a practical numerical approach that may be helpful for setting up a code implementing the method of third quantization is included.

One of the major drawbacks in the numerically exact treatment of a dissipative fermionic system consisting of L lattice sites is the exponential growth of the dimension of the total system's Liouville space $\mathscr{L}_{\text{tot}}$ spanned by the the tensor product of single-site Liouville spaces $\mathscr{L}_i$ $(i = 1, \ldots, L)$,

$$\mathscr{L}_{\text{tot}} = \bigotimes_{i=1}^{L} \mathscr{L}_i, \tag{B.1}$$

required to express its density matrix. As the single-site Hilbert space $\mathscr{H}_i$ of each lattice site i possesses two degrees of freedom, $|0\rangle_i$ and $|1\rangle_i$, the single-site Liouville space $\mathscr{L}_i$ is spanned by four states, namely $|0\rangle_i\langle 0|_i$, $|0\rangle_i\langle 1|_i$, $|1\rangle_i\langle 0|_i$ and $|1\rangle_i\langle 1|_i$. Then, an exact representation of the total system's density matrix $\rho \in \mathscr{L}_{\text{tot}}$ requires the storage of 4^L coefficients $c_{i_1 j_1, i_2 j_2, \ldots, i_L j_L}$, the density matrix ρ reading as follows in the standard tensor product basis,

$$\rho = \sum_{i_1, j_1} \sum_{i_2, j_2} \cdots \sum_{i_L, j_L} c_{i_1 j_1, i_2 j_2, \ldots, i_L j_L} \, |i_1\rangle_1\langle j_1|_1 \otimes |i_2\rangle_2\langle j_2|_2 \otimes \ldots \otimes |i_L\rangle_L\langle j_L|_L \,, \tag{B.2}$$

where each of the summed indices takes values of 0 or 1. By setting up the system's Liouville operator (a $4^L \times 4^L$ matrix) one can compute the steady state's density matrix of equation (B.2), which yields all physical properties like expectation values of observables. However, system lengths are heavily restricted due to the exponential increase in the problem dimension.

The method of third quantization allows for the computation of steady state properties by diagonalizing a matrix of dimension $4L \times 4L$, called *shape matrix* $\boldsymbol{A}$, pushing the limit of accessible system sizes further.

The master equation in Lindblad form representing the equation of motion of the density matrix ρ of a dissipative quantum system of length L is given by

$$\frac{\mathrm{d}\rho}{\mathrm{d}t} = -\mathrm{i}\,[H,\rho] + \sum_{\mu} \left(2L_\mu \rho L_\mu^\dagger - \left\{L_\mu^\dagger L_\mu, \rho\right\}\right) \equiv \hat{\mathcal{L}}\rho, \tag{B.3}$$

where $\hbar = 1$ was set. While the Hermitian Hamilton operator H generates a unitary evolution, the Lindblad operators L_μ acccount for a coupling to a reservoir introducing dissipation. Together, they form the system's *Liouville operator* (or *Liouvillean*) $\hat{\mathcal{L}}$.

It is convenient to express the Hamiltonian and Lindblad operators in terms of $2L$ *abstract Hermitian Majorana operators* w_j, which satisfy the anticommutation relation

$$\{w_j, w_k\} = 2\delta_{jk}, \qquad j,k = 1,2,\ldots,2L. \tag{B.4}$$

For canonical fermions, the latter are related to the fermionic annihilation (creation) operators c_j ($c_j^\dagger$), annihilating (creating) a fermion at the lattice site labeled j,

$$\begin{aligned} w_{2j-1} &= c_j + c_j^\dagger, \\ w_{2j} &= \mathrm{i}\left(c_j - c_j^\dagger\right), \end{aligned} \quad \Leftrightarrow \quad \begin{aligned} c_j &= \frac{1}{2}\left(w_{2j-1} - \mathrm{i}w_{2j}\right), \\ c_j^\dagger &= \frac{1}{2}\left(w_{2j-1} + \mathrm{i}w_{2j}\right). \end{aligned} \tag{B.5}$$

Assuming a quadratic system and linear couplings to the environment, the operators of equation (B.3) can be expanded as

$$H = \sum_{j,k=1}^{2L} w_j H_{jk}^{(w)} w_k = \underline{w} \cdot \boldsymbol{H}^{(w)} \underline{w}, \tag{B.6a}$$

$$L_\mu = \sum_{j=1}^{2L} l_{\mu,j}^{(w)} w_j = \underline{l}_\mu^{(w)} \cdot \underline{w}, \tag{B.6b}$$

with $\underline{w} = \left(w_1, w_2, \ldots\right)^T$ and a matrix $\boldsymbol{H}^{(w)} = -\boldsymbol{H}^{(w)}$ that is chosen to be antisymmetric because of the anticommutation relations (B.4).

Instead of considering the situation in second quantization with, (un-)occupied Fock states of each lattice site, one introduces a Hilbert space structure on the 4^L dimensional space of operators w_j, referred to as $\mathcal{K}$. $\mathcal{K}$ is spanned by basis vectors $|P_{\underline{\alpha}}\rangle$ made up of different configurations $\underline{\alpha} = \left(\alpha_1, \alpha_2, \ldots, \alpha_{2L}\right)$ of the w_j,

$$P_{(\alpha_1,\alpha_2,\ldots,\alpha_{2L})} = w_1^{\alpha_1} w_2^{\alpha_2} \cdots w_{2L}^{\alpha_{2L}}, \tag{B.7}$$

with $\alpha_j \in \{0, 1\}$ representing the absence (or presence) of the operator w_j. The inner product of two elements of the Hilbert space $|x\rangle, |y\rangle \in \mathcal{K}$ is defined by

$$\langle x \,|\, y \rangle \equiv \frac{1}{4^L} \mathrm{Tr}\{x^\dagger y\}, \tag{B.8}$$

such that the basis vectors are orthonormal, $\langle P_{\underline{\alpha}} \,|\, P_{\underline{\alpha}'} \rangle = \delta_{\underline{\alpha}\underline{\alpha}'}$. This can be seen by considering the anticommutation relation (B.4) of the w_j and their relation to the fermionic annihilation and creation operators in equation (B.5), from which it is easy to see that $\mathrm{Tr}\{w_j\} = 0$ as w_j is a superposition of annihilation and creation operators and the trace is performed over the Fock space of second quantization. In addition, one finds $w_j^2 = \mathbb{1}$. Explicitly performing the inner product of two basis vectors described by $\underline{\alpha}$ and $\underline{\alpha}'$ is done by pulling through each of the w_j using the anticommutation relation until meeting another w_j thus canceling to $\mathbb{1}$. The only possibility for a non-zero contribution in the trace is given when there are no w_j left in the end, which implies $\underline{\alpha} = \underline{\alpha}'$.

Note the analogy to the notion of second quantization: instead of elements of the Fock space that are for instance counting particles, $|n_1, n_2, \ldots, n_L\rangle$, it is now Majorana operators one is dealing with, $|\alpha_1, \alpha_2, \ldots, \alpha_{2L}\rangle$. However, the operator Fock space $\mathcal{K}$ is not too different at all. There is an inner product and there are orthogonal basis states – only the interpretation is unfamiliar. Moreover, a density matrix of the form of equation (B.2) can be converted into a representation in abstract Majorana operators (B.7) by expressing the local operator basis in terms of the w_j. Therefore, ρ can be interpreted as a superposition of $P_{\underline{\alpha}}$.

In analogy to introducing fermionic annihilation (creation) operators c_j ($c_j^\dagger$), reference [21] defines their equivalents on $\mathcal{K}$ that add or remove a Majorana operator in the representation of equation (B.7) by $4L$ annihilation (creation) linear maps $\hat{c}_j$ ($\hat{c}_j^\dagger$), $j = 1, 2, \ldots, 2L$, called *adjoint Fermi maps* (or *a-fermions*),

$$\hat{c}_j \,|P_{\underline{\alpha}}\rangle = \delta_{\alpha_j 1} \,|w_j P_{\underline{\alpha}}\rangle, \tag{B.9a}$$

$$\hat{c}_j^\dagger \,|P_{\underline{\alpha}}\rangle = \delta_{\alpha_j 0} \,|w_j P_{\underline{\alpha}}\rangle, \tag{B.9b}$$

satisfying canonical anticommutation relations

$$\{\hat{c}_j, \hat{c}_k\} = 0, \tag{B.10a}$$

$$\left\{\hat{c}_j, \hat{c}_k^\dagger\right\} = \delta_{jk}. \tag{B.10b}$$

With that said, it is now possible to rewrite the equation of motion of the density matrix (B.3) in terms of a-fermions. This task decomposes into two subtasks as

$$\frac{\mathrm{d}\rho}{\mathrm{d}t} = \hat{\mathcal{L}}_0 \rho + \sum_\mu \hat{\mathcal{L}}_\mu \rho, \tag{B.11}$$

where the Liouvillean was split up in a unitary term $\hat{\mathcal{L}}_0$ and the dissipative terms $\hat{\mathcal{L}}_\mu$. Expressing the unitary Liouville term $\hat{\mathcal{L}}_0\rho = -\mathrm{i}\,[H,\rho]$ requires the computation of terms of the form $|w_j w_k P_{\underline{\alpha}}\rangle - |w_k w_j P_{\underline{\alpha}}\rangle$ (see equation (B.6a)). Using the properties (B.9), (B.10) of the adjoint Fermi maps results in

$$|w_j w_k P_{\underline{\alpha}}\rangle - |w_k w_j P_{\underline{\alpha}}\rangle = 2\left(\hat{c}_j^\dagger \hat{c}_k - \hat{c}_k^\dagger \hat{c}_j\right)|P_{\underline{\alpha}}\rangle\,, \tag{B.12}$$

and by linearity it follows immediately that

$$\hat{\mathcal{L}}_0 = -4\mathrm{i}\sum_{j,k=1}^{2L} \hat{c}_j^\dagger H_{jk}\hat{c}_k = -4\mathrm{i}\underline{\hat{c}}^\dagger \cdot \boldsymbol{H}^{(w)}\underline{\hat{c}} \tag{B.13}$$

with $\underline{\hat{c}} = \left(\hat{c}_1, \hat{c}_2, \ldots, \hat{c}_{2L}\right)^T$ and $\underline{\hat{c}}^\dagger = \left(\hat{c}_1^\dagger, \hat{c}_2^\dagger, \ldots, \hat{c}_{2L}^\dagger\right)^T$.

Similarly, the dissipative term of equation (B.11),

$$\hat{\mathcal{L}}_\mu\rho = 2L_\mu\rho L_\mu^\dagger - \left\{L_\mu^\dagger L_\mu, \rho\right\} = \sum_{j,k=1}^{2L} l_{\mu,j}^{(w)} l_{\mu,k}^{(w)*}\hat{\mathcal{L}}_{j,k}\rho \tag{B.14}$$

is found to be [21]

$$\begin{aligned}\hat{\mathcal{L}}_{j,k} = &\left(1 + \mathrm{e}^{\mathrm{i}\pi\hat{\mathcal{N}}}\right)\left(2\hat{c}_j^\dagger\hat{c}_k^\dagger - \hat{c}_j^\dagger\hat{c}_k - \hat{c}_k^\dagger\hat{c}_j\right)\\ &+ \left(1 - \mathrm{e}^{\mathrm{i}\pi\hat{\mathcal{N}}}\right)\left(2\hat{c}_j\hat{c}_k - \hat{c}_j\hat{c}_k^\dagger - \hat{c}_k\hat{c}_j^\dagger\right)\end{aligned} \tag{B.15}$$

with $\hat{\mathcal{N}} = \sum_j \hat{c}_j^\dagger\hat{c}_j$ being the operator counting the total number of a-fermions (the similarity of $\hat{\mathcal{N}}$ and the total particle number operator $N = \sum_j c_j^\dagger c_j$ in second quantization is not accidental). It is crucial to note that both terms of the Liouvillean, equations (B.13) and (B.14), consist only of *even* products of adjoint Fermi maps. Therefore, the *parity* of a-fermions is conserved and $\mathcal{K} = \mathcal{K}^+ \oplus \mathcal{K}^-$ can be decomposed in a space $\mathcal{K}^+$ spanned by basis vectors with an even sum $\sum_j \alpha_j$ of the vector $\underline{\alpha}$ and another space $\mathcal{K}^-$ hosting odd sums of a-fermions.

For the purpose of this work, the main interest lies on the computation of occupation numbers, that is observables consisting of an *even* number of Majorana fermions. Therefore, the Liouvillean can be restricted to $\mathcal{K}^+$. The resulting Liouvillean $\hat{\mathcal{L}}\big|_{\mathcal{K}^+} \equiv \mathcal{L}^+$ is given by [21]

$$\mathcal{L}^+ = -2\underline{\hat{c}}^\dagger \cdot \left(2\mathrm{i}\boldsymbol{H}^{(w)} + \boldsymbol{M}^{(w)} + \boldsymbol{M}^{(w)T}\right)\underline{\hat{c}} + 2\underline{\hat{c}}^\dagger \cdot \left(\boldsymbol{M}^{(w)} - \boldsymbol{M}^{(w)T}\right)\underline{\hat{c}}^\dagger, \tag{B.16}$$

where the matrix $\boldsymbol{M}^{(w)}$ is obtained from the Lindblad operators (B.6b) as follows,

$$M_{jk}^{(w)} = \sum_\mu l_{\mu,j}^{(w)} l_{\mu,k}^{(w)*}. \tag{B.17}$$

The true beauty of equation (B.16) is revealed after applying a linear transformation from adjoint Fermi maps $\hat{c}_j, \hat{c}_j^\dagger$ $(j = 1, 2, \ldots, 2L)$ to so-called *adjoint Hermitian Majorana maps* $\hat{a}_j = \hat{a}_j^\dagger$ $(j = 1, 2, \ldots, 4L)$,

$$\begin{aligned} \hat{a}_{2j-1} &= \frac{1}{\sqrt{2}}\left(\hat{c}_j + \hat{c}_j^\dagger\right) \\ \hat{a}_{2j} &= \frac{\mathrm{i}}{\sqrt{2}}\left(\hat{c}_j - \hat{c}_j^\dagger\right) \end{aligned} \quad \Leftrightarrow \quad \begin{aligned} \hat{c}_j &= \frac{1}{\sqrt{2}}\left(\hat{a}_{2j-1} - \mathrm{i}\hat{a}_{2j}\right) \\ \hat{c}_j^\dagger &= \frac{1}{\sqrt{2}}\left(\hat{a}_{2j-1} + \mathrm{i}\hat{a}_{2j}\right), \end{aligned} \tag{B.18}$$

which also account for anticommutation relations $\{\hat{a}_j, \hat{a}_k\} = \delta_{jk}$. Finally, the Liouvillean collapses into a compact form,

$$\hat{\mathcal{L}}^+ = \underline{\hat{a}} \cdot \boldsymbol{A} \underline{\hat{a}} - 2\mathrm{Tr}\{\boldsymbol{M}\}\,\hat{\mathbb{1}}, \tag{B.19}$$

with $\underline{\hat{a}} = \left(\hat{a}_1, \hat{a}_2, \ldots, \hat{a}_{4L}\right)^T$ and the aforementioned antisymmetric $4L \times 4L$ shape matrix $\boldsymbol{A} = -\boldsymbol{A}^T$ that eventually allows for the computation of the steady state properties straightforwardly.

Assuming the shape matrix to be diagonalizable, the $4L$ eigenvectors of $\boldsymbol{A}$ come up in pairs of eigenvalues,

$$\boldsymbol{A}\underline{v}_{2j-1} = \beta_j \underline{v}_{2j-1}, \qquad \boldsymbol{A}\underline{v}_{2j} = -\beta_j \underline{v}_{2j}, \qquad j = 1, 2, \ldots, 2L. \tag{B.20}$$

The *rapidities* β_j are sorted according to $\mathrm{Re}(\beta_1) \geq \mathrm{Re}(\beta_2) \geq \cdots \geq \mathrm{Re}(\beta_{2L})$. Moreover, it can be shown that it is always possible to normalize the eigenvectors to respect the following property (in case of degenerate rapidities, one has to choose appropriate superpositions in the degenerate subspace, see subsection B.2.2),

$$\underline{v}_k \cdot \underline{v}_\ell = J_{k\ell}, \qquad \boldsymbol{J} = \begin{pmatrix} \left(\begin{smallmatrix} 0 & 1 \\ 1 & 0 \end{smallmatrix}\right) & \left(\begin{smallmatrix} 0 & 0 \\ 0 & 0 \end{smallmatrix}\right) & \\ \left(\begin{smallmatrix} 0 & 0 \\ 0 & 0 \end{smallmatrix}\right) & \left(\begin{smallmatrix} 0 & 1 \\ 1 & 0 \end{smallmatrix}\right) & \\ & & \ddots \end{pmatrix}. \tag{B.21}$$

In the notion of reference [21] one can dervive the following statements assuming a quadratic Hamiltonian H, linear Lindblad couplings L_μ, diagonalizability of the shape matrix $\boldsymbol{A}$ and normalized eigenvectors according to equation (B.21):

- ➢ The non-equilibrium steady state (NESS) of a system described by equation (B.3) is *unique* if and only if none of the rapidities equals zero.
- ➢ Any initial density operator $\rho_0 \in \mathcal{K}^+$ converges towards the NESS if and only if all real parts of the rapidity spectrum are strictly positive, $\mathrm{Re}(\beta_j) > 0$.
- ➢ If the NESS is unique, quadratic observables $\langle w_j w_k \rangle_{\mathrm{ness}}$ are computed by

$$\begin{aligned} \langle w_j w_k \rangle_{\mathrm{ness}} = \delta_{jk} + \frac{1}{2}\sum_{m=1}^{2L} \big(&v_{2m,2j-1} v_{2m-1,2k-1} - v_{2m,2j} v_{2m-1,2k} \\ &- \mathrm{i} v_{2m,2j} v_{2m-1,2k-1} - \mathrm{i} v_{2m,2j-1}, v_{2m-1,2k}\big). \end{aligned} \tag{B.22}$$

B.2. Application to the dissipative SSH model

Having introduced and discussed main aspects of third quantization for quadratic fermionic open systems with linear Lindblad operators, this section shall dive more into detail when it comes to the implementation of the method in order to have numerical results at hand. In this work, the focus lies on employing the procedure of section B.1 for the computation of expectation values of particle numbers $\langle n_j \rangle_{\text{ness}} = \langle c_j^\dagger c_j \rangle_{\text{ness}}$.

B.2.1. Obtaining the shape matrix

As an example, consider the SSH model presented in chapter 2 subject to dissipation with alternating gain and loss in the spirit of the complex on-site potential U_2 proposed in chapter 6,

$$H = -\sum_{j=1,3,\dots}^{L-1} \left(t_1 c_j^\dagger c_{j+1} + \text{h. c.} \right) - \sum_{i=2,4,\dots}^{L-1} \left(t_2 c_j^\dagger c_{j+1} + \text{h. c.} \right), \tag{B.23a}$$

$$L_\mu = \begin{cases} \sqrt{\gamma'} c_\mu^\dagger, & \text{for } \mu = 1, 3, \dots \\ \sqrt{\gamma'} c_\mu, & \text{for } \mu = 2, 4, \dots, \end{cases} \tag{B.23b}$$

assuming $t_1, t_2 \in \mathbb{R}$. From the treatment of the model by means of exact diagonalization, the Hamiltonian matrix $\boldsymbol{H}^{(c)}$ in the basis of fermionic annihilation and creation operators is already accessible,

$$H = \underline{c}^\dagger \cdot \boldsymbol{H}^{(c)} \underline{c}, \qquad \boldsymbol{H}^{(c)} = \underbrace{\begin{pmatrix} 0 & -t_1 & 0 & & \\ -t_1 & 0 & -t_2 & \ddots & \\ 0 & -t_2 & 0 & \ddots & \\ & \ddots & \ddots & & \end{pmatrix}}_{L \times L}, \tag{B.24}$$

gathering the fermionic operators in vectors $\underline{c} = \left(c_1, c_2, \dots, c_L\right)^T, \underline{c}^\dagger = \left(c_1^\dagger, c_2^\dagger, \dots, c_L^\dagger\right)^T$. With the representation of H in the basis of $c_j, c_j^\dagger$ it is simple to obtain the matrix $\boldsymbol{H}^{(w)}$ in the basis of abstract Majorana fermions (equation (B.6a)). Numerically, one can rewrite the relation (B.5) between both bases in matrix form,

$$\begin{aligned} \underline{c} &= \frac{1}{2} \underbrace{\begin{pmatrix} 1 & -\mathrm{i} & 0 & 0 & & & \\ 0 & 0 & 1 & -\mathrm{i} & 0 & 0 & \\ & & 0 & 0 & 1 & -\mathrm{i} & \ddots \\ & & & & \ddots & \ddots & \ddots \end{pmatrix}}_{L \times 2L} \underline{w} \equiv \boldsymbol{B} \underline{w}, \\ \underline{c}^\dagger &= \boldsymbol{B}^* \underline{w} \qquad \text{or} \qquad \underline{c}^{\dagger T} = \underline{w}^T \boldsymbol{B}^\dagger. \end{aligned} \tag{B.25}$$

Inserting both relations into (B.24), comparing with (B.6a), one finds

$$\boldsymbol{H}^{(w)} = \boldsymbol{B}^\dagger \boldsymbol{H}^{(c)} \boldsymbol{B}. \tag{B.26}$$

Before proceeding, note that $\boldsymbol{H}^{(w)}$ obtained this way is not necessarily antisymmetric, which is however possible due to the anticommutation relation (B.4) of abstract Majorana fermions. Hence, an explicit antisymmetrization is required,

$$\boldsymbol{H}^{(w)} \to \frac{1}{2}\left(\boldsymbol{H}^{(w)} - \boldsymbol{H}^{(w)T}\right). \tag{B.27}$$

Doing the calculus for the example Hamiltonian (B.24) leads to

$$\boldsymbol{H}^{(w)} = \frac{\mathrm{i}}{4}\underbrace{\begin{pmatrix} \left(\begin{smallmatrix}0&0\\0&0\end{smallmatrix}\right) & \left(\begin{smallmatrix}0&t_1\\-t_1&0\end{smallmatrix}\right) & \left(\begin{smallmatrix}0&0\\0&0\end{smallmatrix}\right) & \\ \left(\begin{smallmatrix}0&t_1\\-t_1&0\end{smallmatrix}\right) & \left(\begin{smallmatrix}0&0\\0&0\end{smallmatrix}\right) & \left(\begin{smallmatrix}0&t_2\\-t_2&0\end{smallmatrix}\right) & \ddots \\ \left(\begin{smallmatrix}0&0\\0&0\end{smallmatrix}\right) & \left(\begin{smallmatrix}0&t_2\\-t_2&0\end{smallmatrix}\right) & \left(\begin{smallmatrix}0&0\\0&0\end{smallmatrix}\right) & \ddots \\ & \ddots & \ddots & \ddots \end{pmatrix}}_{2L\times 2L}. \tag{B.28}$$

In the same manner, the Lindblad operators (B.23b) are expressed as

$$L_\mu = \sqrt{\gamma'}\begin{cases} \underline{l}_\mu^{(c)T}\underline{c}^\dagger = \underbrace{\underline{l}_\mu^{(c)T}\boldsymbol{B}^*}_{\underline{l}_\mu^{(w)}}\underline{w} & \text{for } \mu = 1,3,\ldots \\ \underline{l}_\mu^{(c)T}\underline{c} = \underbrace{\underline{l}_\mu^{(c)T}\boldsymbol{B}}_{\underline{l}_\mu^{(w)}}\underline{w} & \text{for } \mu = 2,4,\ldots \end{cases} \quad \text{with } \underline{l}_{\mu,j}^{(c)} = \delta_{\mu j}, \tag{B.29}$$

which, in terms of the example, results in

$$\begin{aligned} \underline{l}_1^{(w)} &= \frac{\sqrt{\gamma'}}{2}\big(1,\mathrm{i},0,0,\ldots\big)^T, \\ \underline{l}_2^{(w)} &= \frac{\sqrt{\gamma'}}{2}\big(0,0,1,-\mathrm{i},0,0,\ldots\big)^T, \\ &\vdots \end{aligned} \tag{B.30}$$

The last thing to deal with is the construction of the matrix $\boldsymbol{M}^{(w)}$ parameterized by the Lindblad operators. Arranging all Lindblad vectors in a matrix,

$$\boldsymbol{L}^{(w)} = \underbrace{\begin{pmatrix} \underline{l}_1^{(w)T} \\ \underline{l}_2^{(w)T} \\ \vdots \end{pmatrix}}, \tag{B.31}$$

equation (B.17) can be interpreted as a simple matrix multiplication,

$$\boldsymbol{M}^{(w)T} = \boldsymbol{L}^{(w)}\boldsymbol{L}^{(w)\dagger}. \tag{B.32}$$

For the example model one obtains

$$\boldsymbol{M}^{(w)} = \frac{\gamma'}{4}\underbrace{\begin{pmatrix} \left(\begin{smallmatrix}1&-\mathrm{i}\\\mathrm{i}&1\end{smallmatrix}\right) & \left(\begin{smallmatrix}0&0\\0&0\end{smallmatrix}\right) & \\ \left(\begin{smallmatrix}0&0\\0&0\end{smallmatrix}\right) & \left(\begin{smallmatrix}1&\mathrm{i}\\-\mathrm{i}&1\end{smallmatrix}\right) & \ddots \\ & \ddots & \ddots \end{pmatrix}}_{2L\times 2L}. \tag{B.33}$$

Now that all matrices required for the computation of the Liouvillean restricted to the space of even-number Majorana fermions have been transformed into the appropriate bases, the last task requiring some effort in order to obtain the aspired shape matrix is to implement the transformation from Fermi maps to adjoint Hermitian Majorana maps. The corresponding relation (B.18) translates into

$$\begin{aligned} \hat{\underline{c}} &= \frac{1}{\sqrt{2}} \underbrace{\begin{pmatrix} \boldsymbol{B} & \mathbf{0}_{2L\times 2L} \\ \mathbf{0}_{2L\times 2L} & \boldsymbol{B} \end{pmatrix}}_{2L\times 4L} \hat{\underline{a}} \equiv \hat{\boldsymbol{B}}\hat{\underline{a}}, \\ \hat{\underline{c}}^\dagger &= \hat{\boldsymbol{B}}^* \hat{\underline{a}} \qquad \text{or} \qquad \hat{\underline{c}}^{\dagger T} = \hat{\underline{a}}^T \hat{\boldsymbol{B}}^\dagger. \end{aligned} \tag{B.34}$$

Inserting the latter into equation (B.16) ultimately yields the shape matrix,

$$\begin{aligned} \mathcal{L}^+ &= -2\hat{\underline{a}}^T \hat{\boldsymbol{B}}^\dagger \left(2\mathrm{i}\boldsymbol{H}^{(w)} + \boldsymbol{M}^{(w)} + \boldsymbol{M}^{(w)T}\right) \hat{\boldsymbol{B}}\hat{\underline{a}} \\ &\quad + 2\hat{\underline{a}}^T \hat{\boldsymbol{B}}^\dagger \left(\boldsymbol{M}^{(w)} - \boldsymbol{M}^{(w)T}\right) \hat{\boldsymbol{B}}^* \hat{\underline{a}} \\ &= \hat{\underline{a}} \cdot \boldsymbol{A}\hat{\underline{a}}, \end{aligned} \tag{B.35}$$

which is guaranteed to be antisymmetric by another antisymmetrization,

$$\boldsymbol{A} \to \frac{1}{2}\left(\boldsymbol{A} - \boldsymbol{A}^T\right), \tag{B.36}$$

In terms of the example model the final result reads

$$\boldsymbol{A} = \frac{1}{2} \begin{pmatrix} \gamma'\boldsymbol{\Gamma}_1 & -t_1\boldsymbol{T} & & \\ -t_1\boldsymbol{T} & \gamma'\boldsymbol{\Gamma}_2 & -t_2\boldsymbol{T} & \\ & -t_2\boldsymbol{T} & \gamma'\boldsymbol{\Gamma}_1 & \ddots \\ & & \ddots & \ddots \end{pmatrix}, \tag{B.37a}$$

where the 4×4 matrices $\boldsymbol{\Gamma}_1, \boldsymbol{\Gamma}_2, \boldsymbol{T}$ have been introduced for abbreviation,

$$\boldsymbol{\Gamma}_1 = \begin{pmatrix} -1 & \mathrm{i} & -\mathrm{i} & 1 \\ -\mathrm{i} & -1 & 1 & \mathrm{i} \\ \mathrm{i} & -1 & -1 & \mathrm{i} \\ -1 & -\mathrm{i} & -\mathrm{i} & -1 \end{pmatrix}, \quad \boldsymbol{\Gamma}_2 = \begin{pmatrix} -1 & \mathrm{i} & \mathrm{i} & -1 \\ -\mathrm{i} & -1 & -1 & -\mathrm{i} \\ -\mathrm{i} & 1 & -1 & -\mathrm{i} \\ 1 & \mathrm{i} & -\mathrm{i} & -1 \end{pmatrix}, \quad \boldsymbol{T} = \begin{pmatrix} 0 & 0 & -1 & 0 \\ 0 & 0 & 0 & -1 \\ 1 & 0 & 0 & 0 \\ 0 & 1 & 0 & 0 \end{pmatrix}. \tag{B.37b}$$

Two remarks are in order: First of all, note that the shape matrix of the example is a band matrix which is not that different from the Hamiltonian matrix obtained by adding a complex on-site potential to the SSH model. Generalizing the method of Fourier expansion presented in chapter 2, one is capable of deriving an equivalent of the Bloch Hamiltonian – a "Bloch Liouvillean" represented by an 8×8 matrix. An interesting question to be posed is whether a topological invariant can be assigned to the steady state by investigation of such a matrix in a similar way than in the Hamiltonian framework. For further information, the interested reader is referred to reference [9] presenting a framework for topology in dissipative systems and a thesis currently in progress in the author's group [90]. Second, the actual purpose of obtaining NESS observables requires dealing with the eigenvalues and appropriate eigenvectors of the shape matrix. It turns out that for the investigated system configurations degeneracies in the rapidity spectrum arise frequently, demanding additional treatment that is commented on now.

B.2.2. Dealing with degeneracies

Once the shape matrix has been obtained by following the explained steps above, the calculation of NESS observables is almost straight ahead. In case of a non-degenerate rapidity spectrum, the normalization convention (B.21) is straightforwardly implemented by simple sorting and scaling of the eigenvectors. However, the degenerate case takes some more effort.

Consider only one subspace of a k-fold degenerate eigenvalue $\beta \neq 0$ with eigenvectors $\underline{v}_1^{(+)}, \underline{v}_2^{(+)}, \ldots, \underline{v}_k^{(+)}$ and the equivalents $\underline{v}_1^{(-)}, \underline{v}_2^{(-)}, \ldots \underline{v}_k^{(-)}$ belonging to the eigenvalue $-\beta$. To simplify notation, one defines $\underline{v}_j^{(+)} \equiv |\beta, j\rangle$ and $\underline{v}_\ell^{(-)} \equiv |-\beta, \ell\rangle$ and introduces

$$\langle \beta, j \,|\, -\beta, \ell \rangle \equiv \underline{v}_j^{(+)} \cdot \underline{v}_\ell^{(-)}. \tag{B.38}$$

Because of the antisymmetry of the shape matrix $\boldsymbol{A} = -\boldsymbol{A}^T$ it is easy to show the following properties of the eigenvectors of the degenerate subspace,

$$\begin{aligned} \langle \beta, i \,|\, \beta, j \rangle &= 0, \\ \langle -\beta, i \,|\, -\beta, j \rangle &= 0, \qquad \text{where } i, j = 1, 2, \ldots, k. \end{aligned} \tag{B.39}$$

Only two vectors of different eigenvalue have nonzero overlap,

$$\langle \beta, j \,|\, -\beta, i \rangle \equiv c_{ij}, \tag{B.40}$$

so one set of eigenvectors can be kept unchanged while the eigenvectors in the remaining set have to be properly superimposed to satisfy the normalization condition (B.21). Picking the set of eigenvectors of eigenvalue β to stay unmodified one has to find linear superpositions $\left|-\beta, \tilde{j}\right\rangle$ (distinguished by tilde indices) such that

$$\left\langle \beta, i \,\middle|\, -\beta, \tilde{j} \right\rangle = \delta_{ij}. \tag{B.41}$$

An expansion of the original eigenvectors in the sought basis,

$$|-\beta, i\rangle = \sum_j \alpha_{ij} \left|-\beta, \tilde{j}\right\rangle, \tag{B.42}$$

in combination with the demanded property (B.41) leads to

$$\alpha_{ij} = \langle \beta, j \,|\, -\beta, i \rangle = c_{ij} \tag{B.43}$$

and implies

$$|-\beta, i\rangle = \sum_j c_{ij} \left|-\beta, \tilde{j}\right\rangle, \tag{B.44a}$$

$$\begin{pmatrix} |-\beta, 1\rangle \\ \vdots \\ |-\beta, k\rangle \end{pmatrix} = \boldsymbol{c} \begin{pmatrix} \left|-\beta, \tilde{1}\right\rangle \\ \vdots \\ \left|-\beta, \tilde{k}\right\rangle \end{pmatrix}. \tag{B.44b}$$

Thus, finding valid superpositions can be implemented by computing the overlap matrix $\boldsymbol{c}$ according to equation (B.40) followed by inverting the system of linear equations (B.44b). The desired superpositions satisfying (B.41) are obtained by

$$\begin{pmatrix} \left|-\beta, \tilde{1}\right\rangle \\ \vdots \\ \left|-\beta, \tilde{k}\right\rangle \end{pmatrix} = \boldsymbol{c}^{-1} \begin{pmatrix} |-\beta, 1\rangle \\ \vdots \\ |-\beta, k\rangle \end{pmatrix}. \tag{B.45}$$

With that said, all requirements for the application of equation (B.22) are met.

C. Third quantization for bosons

The approach towards extending the method of third quantization to bosonic systems is somewhat different from the previous one outlined in appendix B. Nevertheless, the fermionic method has been included in this work as it gently introduces the idea of working in an operator Fock space rather than in the more familiar Fock space of second quantization, not to mention the various results presented in section 8.2 that have been obtained by the fermionic method.

Moreover, the generalization performed in this chapter is helpful for understanding how a Liouville operator describing a dissipative bosonic system can be represented numerically in a similar way to that presented in section 5.1. In fact, it has triggered the generalization of the non-Hermitian DMRG code of section 5.4 to systems described by a Liouvillean.

The following discussion is taken from references [22, 98] whose approach is motivated by the treatment of non-dissipative bosonic systems in the framework of second quantization. There, the representation of a basis of the many-body state, $|n_1, n_2, \ldots, n_L\rangle \equiv |\underline{n}\rangle$, living on a one-dimensional lattice of length L requires two ingredients: (i) a *vacuum state* $|\psi_0\rangle = |0, 0, \ldots\rangle$ and (ii) *ladder operators* $\{a_j, a_k^\dagger, \quad j, k = 1, 2, \ldots, L\}$ obeying canonical commutation relations $[a_j, a_k^\dagger] = \delta_{jk}, [a_j, a_k] = [a_j^\dagger, a_k^\dagger] = 0$, that allow for the creation or annihilation of a boson at a certain lattice site, which leads to the familiar construction of the Fock basis,

$$|\underline{n}\rangle = \prod_{j=1}^{L} \frac{1}{\sqrt{n_j!}} \left(a_j^\dagger\right)^{n_j} |\psi_0\rangle \,. \tag{C.1}$$

C.1. General aspects

In contrast to the fermionic case, the bosonic counterpart requires two vector spaces $\mathcal{K}$ and $\mathcal{K}'$ satisfying some properties that shall not be discussed here (see [22]). While $\mathcal{K}$ contains trace class operators (density matrices) denoted as kets $|\rho\rangle$, $\mathcal{K}'$ contains unbounded operators such as a physical observable A, denoted as bras $(A|$, with the expectation value of an observable $(A| \in \mathcal{K}$ evaluated on a density matrix $|\rho\rangle \in \mathcal{K}'$,

$$(A|\,\rho\rangle = \mathrm{Tr}\{A\rho\} \,. \tag{C.2}$$

Following the notion of second quantization one introduces $2L$ left and right annihilation and creation *operator maps* $\hat{b}^{\mathrm{L}}, \hat{b}^{\mathrm{R}}, b \in \{a_j, a_k^\dagger, \quad j,k = 1,2,\ldots,L\}$, whose action onto a density matrix $|\rho\rangle \in \mathcal{K}$ is defined by

$$\begin{aligned} \hat{b}^{\mathrm{L}} &= |b\rho\rangle\,, \\ \hat{b}^{\mathrm{R}} &= |\rho b\rangle\,, \end{aligned} \tag{C.3}$$

which, by equation (C.2), implies the action onto an observable $(A| \in \mathcal{K}'$,

$$\begin{aligned} (A|\,\hat{b}^{\mathrm{L}} &= (Ab|\,, \\ (A|\,\hat{b}^{\mathrm{R}} &= (bA|\,. \end{aligned} \tag{C.4}$$

From the set of left and right annihilation (creation) operator maps one constructs $4L$ maps $\hat{a}_{\nu,j}, \hat{a}'_{\nu,j}, j = 1,2,\ldots,L, \nu = 0,1$, as follows,

$$\begin{aligned} \hat{a}_{0,j} &= \hat{a}_j^{\mathrm{L}}, & \hat{a}'_{0,j} &= \hat{a}_j^{\dagger\mathrm{L}} - \hat{a}_j^{\dagger\mathrm{R}}, \\ \hat{a}_{1,j} &= \hat{a}_j^{\dagger\mathrm{R}}, & \hat{a}'_{1,j} &= \hat{a}_j^{\dagger\mathrm{L}} - \hat{a}_j^{\dagger\mathrm{R}}. \end{aligned} \tag{C.5}$$

The latter satisfy almost canonical commutation relations,

$$\begin{aligned} \left[\hat{a}_{\nu,j}, \hat{a}'_{\mu,k}\right] &= \delta_{\mu\nu}\delta_{jk}, \\ \left[\hat{a}'_{\nu,k}, \hat{a}'_{\mu,k}\right] &= [\hat{a}_{\nu,k}, \hat{a}_{\mu,k}] = 0. \end{aligned} \tag{C.6}$$

At this point, note the similarity to second quantization: while the bosonic annihilation (creation) operators annihilate the right (left) vacuum state, $\langle\psi_0|\, a_j^\dagger = 0$ and $a_j\,|\psi_0\rangle = 0$, their equivalents in third quantization left-annihilate the identity operator $(\mathbb{1}|\,\hat{a}'_{\nu,j}$ and right-annihilate the vacuum density matrix $|\rho_0\rangle = ||\psi_0\rangle\langle\psi_0|\rangle$ such that $\hat{a}_{\nu,j}\,|\rho_0\rangle = 0$. In complete analogy to equation (C.1) the construction of basis states $|\underline{m}\rangle \in \mathcal{K}, (\underline{m}| \in \mathcal{K}'$ where $\underline{m} = \left(m_{0,1}, m_{1,1}, \ldots, m_{L,0}, m_{L,1}\right)$ follows,

$$\begin{aligned} |\underline{m}\rangle &= \prod_{j=1}^{L} \prod_{\nu=0,1} \frac{1}{\sqrt{m_{\nu,j}!}} \left(\hat{a}'_{\nu,j}\right)^{m_{\nu,j}} |\rho_0\rangle\,, \\ (\underline{m}| &= (\mathbb{1}| \prod_{j=1}^{L} \prod_{\nu=0,1} \frac{1}{\sqrt{m_{\nu,j}!}} \left(\hat{a}_{\nu,j},\right)^{m_{\nu,j}}\,, \end{aligned} \tag{C.7}$$

as well as the biorthogonality relation $(\underline{m}|\,\underline{m}'\rangle = \delta_{\underline{m}\underline{m}'}$ guaranteed by (C.6) (which is also the case in second quantization, where only an orthogonal basis is required).

C.2. Quadratic bosonic open systems

Having introduced the mathematical foundation, especially the $4L$ maps (C.3) that allow for a construction of basis states similar to the notion of second quantization, consider

a one-dimensional system of L lattice sites subject to dissipation, which is properly modeled by a master equation in Lindblad form (setting $\hbar = 1$),

$$\frac{\mathrm{d}\rho}{\mathrm{d}t} = -\mathrm{i}\,[H,\rho] + \sum_{\mu}\left(2L_\mu \rho L_\mu^\dagger - \left\{L_\mu^\dagger L_\mu, \rho\right\}\right) \equiv \hat{\mathcal{L}}\,|\rho\rangle\,. \tag{C.8}$$

For the purpose of this work, the assumptions about the form of the system Hamiltonian H are chosen to be more restrictive than in the original outline [22] in order to avoid clutter. In fact, a quadratic Hamiltonian of the form

$$H = \sum_{i,j=1}^{L} a_i^\dagger H_{ij} a_j = \underline{a}^\dagger \cdot \boldsymbol{H}\underline{a}, \tag{C.9a}$$

where $\underline{a} = \left(a_1, a_2, \ldots, a_L\right)^T$ and $\boldsymbol{H}^\dagger = \boldsymbol{H}$ is assumed, joined by linear Lindblad operators parameterized as follows,

$$L_\mu = \underline{l}_\mu \cdot \underline{a} + \underline{k}_\mu \cdot \underline{a}^\dagger. \tag{C.9b}$$

Then, for $|\rho\rangle \in \mathcal{K}$, the Liouvillean $\hat{\mathcal{L}}$ in (C.8) can be expressed in terms of the $4L$ maps (C.5). Gathering the maps in vectors $\underline{\hat{a}}'_0 = \left(\hat{a}'_{0,1}, \hat{a}'_{0,2}, \ldots, \hat{a}'_{0,L}\right)^T$ and, in the same fashion, $\underline{\hat{a}}'_1, \underline{\hat{a}}_0, \underline{\hat{a}}_1$, some lengthy algebra yields [22]

$$\begin{aligned}
\hat{\mathcal{L}} &= -\mathrm{i}\hat{H}^{\mathrm{L}} + \mathrm{i}\hat{H}^{\mathrm{R}} + \sum_{\mu}\left(2\hat{L}_\mu^{\mathrm{L}}\hat{L}_\mu^{\dagger\mathrm{R}} - \hat{L}_\mu^{\dagger\mathrm{L}}\hat{L}_\mu^{\mathrm{L}} - \hat{L}_\mu^{\mathrm{R}}\hat{L}_\mu^{\dagger\mathrm{R}}\right) \\
&= -\mathrm{i}\underline{\hat{a}}'_0 \cdot \boldsymbol{H}\underline{\hat{a}}_0 + \mathrm{i}\underline{\hat{a}}'_1 \cdot \boldsymbol{H}^*\underline{\hat{a}}_1 \\
&\quad + \underline{\hat{a}}'_0 \cdot \left(\boldsymbol{N} - \boldsymbol{M}^*\right)\underline{\hat{a}}_0 + \underline{\hat{a}}'_1 \cdot \left(\boldsymbol{N}^* - \boldsymbol{M}\right)\underline{\hat{a}}_1 \\
&\quad + \underline{\hat{a}}'_0 \cdot \left(\boldsymbol{L}^\dagger - \boldsymbol{L}^*\right)\underline{\hat{a}}_1 + \underline{\hat{a}}'_1 \cdot \left(\boldsymbol{L}^T - \boldsymbol{L}^*\right)\underline{\hat{a}}_0 \\
&\quad - \underline{\hat{a}}'_0 \cdot \boldsymbol{L}^*\underline{\hat{a}}'_0 - \underline{\hat{a}}'_1 \cdot \boldsymbol{L}\underline{\hat{a}}'_1 + 2\underline{\hat{a}}'_0 \cdot \boldsymbol{N}\underline{\hat{a}}'_1,
\end{aligned} \tag{C.10}$$

with $L \times L$ matrices $\boldsymbol{M} = \boldsymbol{M}^\dagger, \boldsymbol{N} = \boldsymbol{N}^\dagger$ and $\boldsymbol{L}$ defined by

$$\begin{aligned}
\boldsymbol{M} &= \sum_\mu \underline{l}_\mu \otimes \underline{l}_\mu^* \equiv \sum_\mu \boldsymbol{M}_\mu, \qquad (\boldsymbol{M}_\mu)_{ij} = l_{\mu,i} l^*_{\mu,j}, \\
\boldsymbol{N} &= \sum_\mu \underline{k}_\mu \otimes \underline{k}_\mu^* \equiv \sum_\mu \boldsymbol{N}_\mu, \qquad (\boldsymbol{N}_\mu)_{ij} = k_{\mu,i} k^*_{\mu,j}, \\
\boldsymbol{L} &= \sum_\mu \underline{l}_\mu \otimes \underline{k}_\mu^* \equiv \sum_\mu \boldsymbol{L}_\mu, \qquad (\boldsymbol{L}_\mu)_{ij} = l_{\mu,i} k^*_{\mu,j}.
\end{aligned} \tag{C.11}$$

A remark about the way equation (C.10) is obtained is in order. First, recall that the $4L$ maps $\hat{a}_{\nu,j}, \hat{a}'_{\nu,j}$ are related to the left and right creation (annihilation) maps $\hat{a}^{\mathrm{L,R}}, \hat{a}^{\dagger\mathrm{L,R}}$

by equation (C.5) which translates into

$$\begin{aligned} \hat{\underline{a}}^{\mathrm{L}} &= \hat{\underline{a}}_0, & \hat{\underline{a}}^{\mathrm{R}} &= \hat{\underline{a}}'_1 + \hat{\underline{a}}_0, \\ \hat{\underline{a}}^{\dagger\mathrm{L}} &= \hat{\underline{a}}'_0 + \hat{\underline{a}}_1, & \hat{\underline{a}}^{\dagger\mathrm{R}} &= \hat{\underline{a}}_1. \end{aligned} \tag{C.12}$$

In order to shed some more light on equation (C.10), consider each term separately, for instance $\mathrm{i}\hat{H}^{\mathrm{R}} |\rho\rangle$ arising from $\mathrm{i}\rho H$ in (C.8). Expressing the latter in terms of $\hat{a}^{\mathrm{L,R}}, \hat{a}^{\dagger\mathrm{L,R}}$ and using equation (C.12) leads to

$$\begin{aligned} \mathrm{i}\rho H &= \mathrm{i} \sum_{i,j=1}^{L} \rho a_i^\dagger H_{ij} a_j \\ &= \mathrm{i} \sum_{i,j} H_{ij} \left| \rho a_i^\dagger a_j \right\rangle = \mathrm{i} \sum_{i,j} H_{ij} \hat{a}_j^{\mathrm{R}} \left| \rho a_i^\dagger \right\rangle = \mathrm{i} \sum_{i,j} H_{ij} \hat{a}_j^{\mathrm{R}} \hat{a}_i^{\dagger\mathrm{R}} |\rho\rangle \\ &= \mathrm{i} \sum_{i,j} H_{ji}^* \hat{a}_j^{\mathrm{R}} \hat{a}_i^{\dagger\mathrm{R}} |\rho\rangle = \mathrm{i} \hat{\underline{a}}^{\mathrm{R}} \cdot \boldsymbol{H}^* \hat{\underline{a}}^{\dagger\mathrm{R}} |\rho\rangle = \mathrm{i} \left(\hat{\underline{a}}'_1 + \hat{\underline{a}}_0 \right) \cdot \boldsymbol{H}^* \hat{\underline{a}}_1 |\rho\rangle \\ &\equiv \mathrm{i}\hat{H}^{\mathrm{R}} |\rho\rangle . \end{aligned} \tag{C.13}$$

Performing this kind of computation for each of the terms occuring in the Lindblad equation, adding up all terms, simplifying them by using the commutation relations (C.8) and collecting terms of identical pattern finally results in the longish expression for the Liouvillean $\hat{\mathcal{L}}$.

A more compact form is achieved when all operators are arranged in a $4L$ component vector $\hat{\underline{b}} = \left(\hat{\underline{a}}_0, \hat{\underline{a}}_1, \hat{\underline{a}}'_0, \hat{\underline{a}}'_1 \right)^T$ reading

$$\hat{\mathcal{L}} = \hat{\underline{b}} \cdot \boldsymbol{S} \hat{\underline{b}} - S_0 \hat{\mathbb{1}} \tag{C.14}$$

with a constant $S_0 = \mathrm{Tr}\{\boldsymbol{M}\} - \mathrm{Tr}\{\boldsymbol{N}\}$ and the $4L \times 4L$ matrix $\boldsymbol{S}$,

$$\boldsymbol{S} = \begin{pmatrix} \boldsymbol{0}_{2L\times 2L} & -\boldsymbol{X} \\ -\boldsymbol{X}^T & \boldsymbol{Y} \end{pmatrix} = \boldsymbol{S}^T, \tag{C.15}$$

consisting of $2L \times 2L$ matrices $\boldsymbol{X}, \boldsymbol{Y}$ parameterized by the matrices of (C.11),

$$\boldsymbol{X} = \frac{1}{2} \begin{pmatrix} \mathrm{i}\boldsymbol{H}^* - \boldsymbol{N}^* + \boldsymbol{M} & -\boldsymbol{L} + \boldsymbol{L}^T \\ -\boldsymbol{L}^* - \boldsymbol{L}^\dagger & -\mathrm{i}\boldsymbol{H} - \boldsymbol{N} + \boldsymbol{M}^* \end{pmatrix}, \tag{C.16a}$$

$$\boldsymbol{Y} = \frac{1}{2} \begin{pmatrix} -\boldsymbol{L}^* - \boldsymbol{L}^\dagger & 2\boldsymbol{N} \\ 2\boldsymbol{N}^T & -\boldsymbol{L} - \boldsymbol{L}^T \end{pmatrix} = \boldsymbol{Y}^T. \tag{C.16b}$$

Similar to the fermionic case, the $2L$ eigenvalues β_j of the matrix $\boldsymbol{X}$ which is assumed to be diagonalizable in the following, are referred to as *rapidities*.

By using the properties of $\boldsymbol{S}$, reference [22] expands the Liouvillean in terms of left and right eigenvectors (so called *normal master-mode maps*) of the latter in order to

derive expressions for properties of the NESS, which is right-annihilated by $\hat{\mathcal{L}}$, that is $\hat{\mathcal{L}}\,|\rho_{\text{ness}}\rangle = 0$ in order to be a stationary solution of equation (C.8).

Following the notion of this reference, everything finally reduces to solving for a complex $2L \times 2L$ symmetric matrix $\boldsymbol{Z} = \boldsymbol{Z}^T$ satisfying a *continuous Lyapunov* or *Sylvester equation*,

$$\boldsymbol{X}^T\boldsymbol{Z} + \boldsymbol{Z}\boldsymbol{X} = \boldsymbol{Y}. \tag{C.17}$$

A unique solution of equation (C.17) is known to exist if there are no rapidities $\beta_j, \beta_{j'}$ that add up to zero, $\beta_j + \beta_{j'} = 0$. Since $\boldsymbol{X}$ is unitary similar to a real matrix, the eigenvalues β_j always come in complex conjugate pairs β_j, β_j^*, requiring all rapidities to have a non-vanishing real part $\text{Re}(\beta_j) \neq 0$ in order to achieve the condition for the solution of the continuous Lyapunov equation to be unique.

Contrary to the fermionic case, the existence of a NESS in a bosonic system is not guaranteed and depends on the choice of Lindblad operators as the system is not finite-dimensional and may never stop filling up with excitations from the reservoir (infinite *amplification*). However, if this is not the case, or equivalently if $\text{Re}(\beta_j) > 0$ for all j, the following statements hold (see reference [22] for a more complete listing):

- ➢ A unique NESS exists and is right-annihilated by the Liouvillean, $\hat{\mathcal{L}}\,|\rho_{\text{ness}}\rangle = 0$.
- ➢ Expectation values of two-point correlators $\langle :\, b_i b_j \,: \rangle_{\text{ness}} = \text{Tr}\{:\, b_i b_j \,: \rho_{\text{ness}}\}$ of the NESS, where $: \circ :$ denotes normal ordering and $\underline{b} = \left(\underline{a}, \underline{a}^\dagger\right)^T$, are easily read off from the matrix $\boldsymbol{Z}$,

$$\langle :\, b_i b_j \,: \rangle_{\text{ness}} = Z_{ij}. \tag{C.18}$$

To conclude, some comments on the implementation of the presented method as well as the extraction of physical observables of the NESS, especially the computation of lattice site occupations $\langle a_j^\dagger a_j \rangle_{\text{ness}}$, are in order. Generally, it does not take much effort to extract the Hamiltonian matrix $\boldsymbol{H}$ and Lindblad vectors $\underline{l}_\mu, \underline{k}_\mu$ (see equation (C.9)) of a certain system setup. Next, those quantities are used to construct the matrices $\boldsymbol{M}, \boldsymbol{N}, \boldsymbol{L}$ (see (C.11)) followed by the build-up of $\boldsymbol{X}, \boldsymbol{Y}$ (equation (C.16)). Assuring all assumptions made on the rapidities β_j to hold, one then solves equation (C.17) for $\boldsymbol{Z}$ to yield the desired observable expectation values as $\langle a_j^\dagger a_j \rangle_{\text{ness}} = Z_{L+j,j}$. There are already existing standard algorithms to solve equations of such a form. For instance, the Python library **SciPy** [99, 100] provides a solver method **scipy.linalg.solve_sylvester**.

D. Generalized Gell-Mann matrices

This appendix is devoted to further pushing the performance and reliability of the non-Hermitian DMRG algorithm presented in section 5.4 that targets the steady state of a dissipative system described by a master equation in Lindblad form.

So far, the local basis for a single-site density matrix allowing for at most $D-1$ particles is spanned by the standard basis $|i\rangle\langle j|$, where $i,j = 0,1,\ldots,D-1$. Such a D-dimensional quantum system is also referred to as *qudit*. Besides the fact that all operators required for the construction of the Liouville operator are already at hand from the Hermitian DMRG algorithm, requiring only little adaption of the code, the basis is trace-orthogonal,

$$\mathrm{Tr}_{\mathscr{H}}\Big\{\left(|i\rangle\langle j|\right)^{\dagger}|k\rangle\langle\ell|\Big\} = \delta_{ik}\delta_{j\ell}, \tag{D.1}$$

where the trace is performed over the basis of the qudit Hilbert space $\mathscr{H}$. This is a practical property when it comes to evaluating overlaps or computing reduced density operators like in the truncation procedure of the algorithm.

The algorithm itself allows for complex expansion coefficients $c_{ij} \in \mathbb{C}$ leading to (possibly non-physical) operators in the single-site's Liouville space,

$$\rho = \sum_{i,j} c_{ij}\,|i\rangle\langle j|\,. \tag{D.2}$$

It is essential to note that the space of expansion coefficients can easily be reduced by the Hermiticity of ρ implying $c_{ij} = c_{ji}^{*}$. However, such a restriction cannot be straightforwardly implemented, because handing over such kind of information to the large sparse eigensolver employed during the optimization of the steady state density matrix is difficult.

This problem can be overcome by choosing a basis that is Hermitian, given by the *generalized Gell-Mann matrices* (GGM). For a single qudit, whose Liouville space is spanned by the standard basis $|j\rangle\langle k|$ with $j,k = 0,1,\ldots,D-1$ the D^2-1 generalized Gell-Mann matrices read as follows:

➢ $D(D-1)/2$ symmetric GGM:

$$\Lambda_{(\mathrm{s})}^{jk} = |j\rangle\langle k| + |k\rangle\langle j|\,, \qquad 1 \leq j < k \leq D. \tag{D.3a}$$

➢ $D(D-1)/2$ antisymmetric GGM:

$$\Lambda_{(\mathrm{a})}^{jk} = -\mathrm{i}\,|j\rangle\langle k| + \mathrm{i}\,|k\rangle\langle j|\,, \qquad 1 \leq j < k \leq D. \tag{D.3b}$$

➢ $D-1$ diagonal GGM:

$$\Lambda^{\ell} = \sqrt{\frac{2}{\ell(\ell+1)}}\left(\sum_{j=1}^{\ell} |j\rangle\langle j| - \ell\,|\ell+1\rangle\langle \ell+1|\right), \quad 1 \leq \ell \leq D-1. \tag{D.3c}$$

For a qubit ($D = 2$), the GGM (D.3) reduce to the familiar Pauli matrices. In fact, the GGM are a generalization of the qubit case to arbitrary dimension.

Including the identity matrix $\mathbb{1}$, the set of GGM forms a basis that is Hermitian and trace-orthogonal in the sense of equation (D.1) with only a little deviation: if an arbitrary enumeration is assigned to the elements of the basis $\{\{\Lambda_{(\mathrm{s})}^{jk}\}, \{\Lambda_{(\mathrm{a})}^{jk}\}, \{\Lambda^{\ell}\}, \mathbb{1}\}$ such that it reads $\{A^i,\ i = 1, 2, \ldots, D^2\}$, the trace-orthogonality translates into

$$\mathrm{Tr}_{\mathscr{H}}\{A^{i\dagger}A^j\} = \mathrm{Tr}_{\mathscr{H}}\{A^iA^j\} = D\delta_{ij}. \tag{D.4}$$

Proving this statement is straightforward and explicitly worked out in reference [101]. Note that the constant does not cause trouble for the steps of DMRG to work properly.

Reference [101] also provides a useful relation for the expansion of standard basis elements $|j\rangle\langle k|$ in GGM,

$$|j\rangle\langle k| = \begin{cases} \frac{1}{2}\left(\Lambda_{(\mathrm{s})}^{jk} + \mathrm{i}\Lambda_{(\mathrm{a})}^{jk}\right), & \text{for } j < k \\ \frac{1}{2}\left(\Lambda_{(\mathrm{s})}^{kj} - \mathrm{i}\Lambda_{(\mathrm{a})}^{kj}\right), & \text{for } j > k \\ -\sqrt{\frac{j-1}{2j}}\Lambda^{j-1} + \sum_{n=0}^{D-j-1} \frac{1}{\sqrt{2(j+n)(j+n+1)}}\Lambda^{j+n} + \frac{1}{D}\mathbb{1}, & \text{for } j = k. \end{cases} \tag{D.5}$$

Equation (D.5) simplifies the procedure of expressing operators and density matrices in the total Liouville space, which is composed of products of single-site Liouville spaces.

The performance of the non-Hermitian DMRG algorithm presented in section 5.4 can be improved by expanding all operators and density matrices in such a basis. To see

this, reconsider the single-site density matrix of equation (D.2), but now expanded in the basis of $\{A^i\}$,

$$\rho = \sum_{i,j} c_{ij} \left|i\right\rangle\!\left\langle j\right| = \sum_i \tilde{c}_i A^i, \tag{D.6}$$

with $\tilde{c}_i$ $(i = 1, 2, \ldots, D^2)$ denoting the expansion coefficents of ρ in the GGM basis. Consequently, the Hermiticity of ρ and the basis, $A^{i\dagger} = A^i$, implies $\tilde{c}_i^* = \tilde{c}_i$ and thus $\tilde{c}_i \in \mathbb{R}$. Therefore, once all operators and Liouvilleans have been expressed in the GGM basis, it is sufficient to only target states in the sparse eigensolver with entirely real coefficients. Alternatively, this condition can be employed as an assertion for guaranteeing the target density matrix to be Hermitian.

The idea of using GGM as a practical basis, in which the density matrix of a system can be expressed, has already been realized in an MPS-based formalism to optimize the steady state of a dissipative system [83]. However, in this reference an initial state is evolved in time by means of MPS algorithms until it has converged towards the steady state.

There are also other MPS-based formalisms targeting steady states by time evolution [69, 70] or directly [72] (and the algorithm presented in this work) besides further variational principles [71] for obtaining steady state properties of dissipative quantum many-body systems.

Assuring Hermiticity of the density matrix of the steady state is one important challenge in order to obtain physically valid results. Another crucial property of the density matrix is *positivity*, which turns out to be either difficult to impose on the target state ansatz (as is the case for the code presented in this work) or computationally more costly (see [72] and references within).

At least, by introducing operators in the GGM basis, the algorithm of section 5.4 can be extended such that the problem of accidentally targeting non-Hermitian density matrices can be circumvented. Nevertheless, as the algorithm's output is consistent with results obtained from the **QuTiP** [102, 103] library's steady state solver **qutip.steadystate.steadystate** for small systems and does not produce physically counter-intuitive data for larger systems, the author leaves this extension of the code for future work considering it to already perform fine for most scenarios investigated in this work.

Bibliography

[1] M. Nakahara. *Geometry, topology and physics*. CRC Press (2003).

[2] K. von Klitzing. The quantized Hall effect. *Rev. Mod. Phys.* 58, 519–531 (1986).

[3] M. Z. Hasan and C. L. Kane. Colloquium: Topological insulators. *Rev. Mod. Phys.* 82, 3045–3067 (2010).

[4] Weimann S., Kremer M., Plotnik Y., Lumer Y., Nolte S., Makris K. G., Segev M., Rechtsman M. C., and Szameit A. Topologically protected bound states in photonic parity-time-symmetric crystals. *Nat. Mat.* 16, 433–438 (2017).

[5] A. Stern and N. H. Lindner. Topological Quantum Computation — from basic concepts to first experiments. *Science* 339, 1179–1184 (2013).

[6] V. Lahtinen and J. K. Pachos. A short introduction to topological quantum computation. *SciPost Phys.* 3, 021 (2017).

[7] S. Ryu, A. P. Schnyder, A. Furusaki, and A. W. W. Ludwig. Topological insulators and superconductors: Tenfold way and dimensional hierarchy. *N. J. Phys.* 12, 065010 (2010).

[8] S. Diehl, E. Rico, M. A. Baranov, and P. Zoller. Topology by dissipation in atomic quantum wires. *Nat. Phys.* 7, 971 (2011).

[9] C.-E. Bardyn, M. A. Baranov, C. V. Kraus, E. Rico, A. İmamoğlu, P. Zoller, and S. Diehl. Topology by dissipation. *N. J. Phys.* 15, 085001 (2013).

[10] W. P. Su, J. R. Schrieffer, and A. J. Heeger. Solitons in Polyacetylene. *Phys. Rev. Lett.* 42, 1698–1701 (1979).

[11] C. M. Bender and S. Boettcher. Real spectra in non-Hermitian Hamiltonians having $\mathcal{PT}$ symmetry. *Phys. Rev. Lett.* 80, 5243–5246 (1998).

[12] G. Lindblad. On the generators of quantum dynamical semigroups. *Comm. Math. Phys.* 48, 119–130 (1976).

[13] J. Zak. Berry's phase for energy bands in solids. *Phys. Rev. Lett.* 62, 2747–2750 (1989).

[14] M. V. Berry. Quantal phase factors accompanying adiabatic changes. *Proc. Roy. Soc. L. A* 392, 45–57 (1984).

[15] F. Grusdt, M. Höning, and M. Fleischhauer. Topological edge states in the one-dimensional superlattice Bose-Hubbard model. *Phys. Rev. Lett.* 110, 260405 (2013).

[16] S. R. White. Density matrix formulation for quantum renormalization groups. *Phys. Rev. Lett.* 69, 2863–2866 (1992).

[17] U. Schollwöck. The density matrix renormalization group. *Rev. Mod. Phys.* 77, 259–315 (2005).

[18] U. Schollwöck. The density matrix renormalization group in the age of matrix product states. *Ann. Phys.* 326, 96 – 192 (2011). January 2011 Special Issue.

[19] C. M. Bender. Introduction to $\mathcal{PT}$-symmetric quantum theory. *Cont. Phys.* 46, 277–292 (2005).

[20] C. M. Bender. Making sense of non-Hermitian Hamiltonians. *Rep. Prog. Phys.* 70, 947 (2007).

[21] T. Prosen. Third quantization: A general method to solve master equations for quadratic open Fermi systems. *N. J. of Phys.* 10, 043026 (2008).

[22] T. Prosen and T. H. Seligman. Quantization over boson operator spaces. *J. Phys. A* 43, 392004 (2010).

[23] A. J. Heeger, S. Kivelson, J. R. Schrieffer, and W.-P. Su. Solitons in conducting polymers. *Rev. Mod. Phys.* 60, 781–850 (1988).

[24] J. K. Asbóth, L. Oroszlány, and A. Pályi. *A short course on topological insulators: Band structure and edge states in one and two dimensions.* Lecture Notes in Physics. Springer International Publishing (2016).

[25] R. Resta. *Berry phase in electronic wavefunctions.* Troisième Cycle de la Physique. Université de Lausanne (1996).

[26] D. Jaksch and P. Zoller. The cold atom Hubbard toolbox. *Ann. Phys.* 315, 52 – 79 (2005).

[27] M. Lewenstein, A. Sanpera, and V. Ahufinger. *Ultracold atoms in optical lattices: Simulating quantum many-body systems.* OUP Oxford (2012).

[28] F. Bloch. Über die Quantenmechanik der Elektronen in Kristallgittern. *Z. Phys.* 52, 555–600 (1929).

[29] L. Li, C. Yang, and S. Chen. Winding numbers of phase transition points for one-dimensional topological systems. *E. Phys. Lett.* 112, 10004 (2015).

[30] X. Chen, Z.-C. Gu, and X.-G. Wen. Classification of gapped symmetric phases in one-dimensional spin systems. *Phys. Rev. B* 83, 035107 (2011).

[31] M. Born and V. Fock. Beweis des Adiabatensatzes. *Z. Phys.* 51, 165–180 (1928).

[32] J. C. Budich and B. Trauzettel. From the adiabatic theorem of quantum mechanics to topological states of matter. *Phys. Stat. Sol.* 7, 109–129 (2013).

[33] M. Wagner, F. Dangel, H. Cartarius, J. Main, and G. Wunner. Numerical calculation of the complex berry phase in non-Hermitian systems. *arXiv preprint arXiv:1708.03230 (to be published in Acta Polytechnica)* (2017).

[34] Atala M., Aidelsburger M., Barreiro J. T., Abanin D., Kitagawa T., Demler E., and Bloch I. Direct measurement of the Zak phase in topological Bloch bands. *Nat. Phys.* 9, 795–800 (2013).

[35] T. D. Kühner and H. Monien. Phases of the one-dimensional Bose-Hubbard model. *Phys. Rev. B* 58, R14741–R14744 (1998).

[36] D. Muth, A. Mering, and M. Fleischhauer. Ultracold bosons in disordered superlattices: Mott insulators induced by tunneling. *Phys. Rev. A* 77, 043618 (2008).

[37] J. K. Freericks and H. Monien. Strong-coupling expansions for the pure and disordered Bose-Hubbard model. *Phys. Rev. B* 53, 2691–2700 (1996).

[38] P. Buonsante, V. Penna, and A. Vezzani. Strong-coupling expansions for the topologically inhomogeneous Bose-Hubbard model. *Phys. Rev. B* 70, 184520 (2004).

[39] Greiner M., Mandel O., Esslinger T., Hansch T. W., and Bloch I. Quantum phase transition from a superfluid to a Mott insulator in a gas of ultracold atoms. *Nat.* 415, 39–44 (2002). 10.1038/415039a.

[40] P. Jordan and E. Wigner. Über das Paulische Äquivalenzverbot. *Z. Phys.* 47, 631–651 (1928).

[41] Q. Niu, Ds J. Thouless, and Y.-S. Wu. Quantized Hall conductance as a topological invariant. *Phys. Rev. B* 31, 3372 (1985).

[42] V. Gurarie. Single-particle Green's functions and interacting topological insulators. *Phys. Rev. B* 83, 085426 (2011).

[43] X. Chen, Z.-C. Gu, Z.-X. Liu, and X.-G. Wen. Symmetry-protected topological orders in interacting bosonic systems. *Science* 338, 1604–1606 (2012).

[44] Y.-Y. He, H.-Q. Wu, Z. Y. Meng, and Z.-Y. Lu. Topological invariants for interacting topological insulators. II. Breakdown of single-particle Green's function formalism. *Phys. Rev. B* 93, 195164 (2016).

[45] Y.-Y. He, H.-Q. Wu, Z. Y. Meng, and Z.-Y. Lu. Topological invariants for interacting topological insulators. I. Efficient numerical evaluation scheme and implementations. *Phys. Rev. B* 93, 195163 (2016).

[46] Y. Hatsugai. Quantized Berry phases as a local order parameter of a quantum liquid. *J. Phys. Soc. J.* 75, 123601 (2006).

[47] R. Peierls. On the theory of the diamagnetism of conduction electrons. *Sci. Pap.* pp. 97–120 (1997).

[48] Goldman N., Budich J. C., and Zoller P. Topological quantum matter with ultracold gases in optical lattices. *Nat. Phys.* 12, 639–645 (2016).

[49] A. Mering and M. Fleischhauer. One-dimensional Bose-Fermi-Hubbard model in the heavy-fermion limit. *Phys. Rev. A* 77, 023601 (2008).

[50] H. P. Breuer and F. Petruccione. *The theory of open quantum systems.* OUP Oxford (2007).

[51] D. C. Brody. Biorthogonal quantum mechanics. *J. Phys. A* 47, 035305 (2014).

[52] G. Kordas, D. Witthaut, P. Buonsante, A. Vezzani, R. Burioni, A. I. Karanikas, and S. Wimberger. The dissipative Bose-Hubbard model. *E. Phys. J.* 224, 2127–2171 (2015).

[53] K. Mølmer, Y. Castin, and J. Dalibard. Monte Carlo wave-function method in quantum optics. *J. Opt. Soc. Am. B* 10, 524–538 (1993).

[54] D. Dast, D. Haag, H. Cartarius, and G. Wunner. Quantum master equation with balanced gain and loss. *Phys. Rev. A* 90, 052120 (2014).

[55] D. Dast. *Bose-Einstein condensates with balanced gain and loss beyond mean-field theory.* Ph.D. thesis, University of Stuttgart (2017).

[56] N. Moiseyev. *Non-Hermitian Quantum Mechanics.* Cambridge University Press (2011).

[57] A. Mostafazadeh. Pseudo-Hermiticity versus $\mathcal{PT}$ symmetry: The necessary condition for the reality of the spectrum of a non-Hermitian Hamiltonian. *J. Math. Phys.* 43, 205–214 (2002).

[58] A. Mostafazadeh. Pseudo-Hermiticity versus $\mathcal{PT}$ symmetry II. A complete characterization of non-Hermitian Hamiltonians with a real spectrum. *J. Math. Phys.* 43, 2814–2816 (2002).

[59] A. Mostafazadeh. Pseudo-Hermiticity versus $\mathcal{PT}$ symmetry III: Equivalence of pseudo-Hermiticity and the presence of antilinear symmetries. *J. Math. Phys.* 43, 3944–3951 (2002).

[60] R. Orus. A practical introduction to tensor networks: Matrix product states and projected entangled pair states. *Ann. Phys.* 349, 117 – 158 (2014).

[61] A. L. Malvezzi. An introduction to numerical methods in low-dimensional quantum systems. *B. J. Phys.* 33, 55 – 72 (2003).

[62] A. O. Mitrushenkov, G. Fano, R. Linguerri, and P. Palmieri. On the possibility to use non-orthogonal orbitals for density matrix renormalization group calculations in quantum chemistry. *arXiv preprint* (2003).

[63] G. K.-L. Chan and T. Van Voorhis. Density matrix renormalization group algorithms with nonorthogonal orbitals and non-Hermitian operators, and applications to polyenes. *J. Chem. Phys.* 122, 204101 (2005).

[64] Y. Hieida. Application of the density matrix renormalization group method to a non-equilibrium problem. *J. of the Phys. Soc. J.* 67, 369–372 (1998).

[65] M. Kaulke and I. Peschel. A DMRG study of the q-symmetric Heisenberg chain. *E. Phys. J. B* 5, 727–734 (1998).

[66] E. Carlon, M. Henkel, and U. Schollwöck. Density matrix renormalization group and reaction-diffusion processes. *Europ. Phys. J. B* 12, 99–114 (1999).

[67] I. Peschel and M. Kaulke. Non-Hermitian problems and some other aspects. In *Density matrix renormalization*, pp. 279–285. Springer (1999).

[68] M. Henkel and M. Pleimling. *Non-qquilibrium phase transitions: Ageing and dynamical scaling far from equilibrium*, volume 2. Springer, Heidelberg (2010).

[69] M. Zwolak and G. Vidal. Mixed-state dynamics in one-dimensional quantum lattice systems: A time-dependent superoperator renormalization algorithm. *Phys. Rev. Lett.* 93, 207205 (2004).

[70] F. Verstraete, J. J. García-Ripoll, and J. I. Cirac. Matrix product density operators: Simulation of finite-temperature and dissipative systems. *Phys. Rev. Lett.* 93, 207204 (2004).

[71] H. Weimer. Variational principle for steady states of dissipative quantum many-body systems. *Phys. Rev. Lett.* 114, 040402 (2015).

[72] J. Cui, J. I. Cirac, and Mari C. Bañuls. Variational matrix product operators for the steady state of dissipative quantum Systems. *Phys. Rev. Lett.* 114, 220601 (2015).

[73] R. Lehoucq, D. Sorensen, and C. Yang. *Arpack users' guide: Solution of large scale eigenvalue problems with implicitly restarted Arnoldi methods* (1997).

[74] A. E. Feiguin. The time-dependent density matrix renormalization group. In *Strongly Correlated Systems*, pp. 131–152. Springer (2013).

[75] J. Eisert, M. Cramer, and M. B. Plenio. Colloquium: Area laws for the entanglement entropy. *Rev. Mod. Phys.* 82, 277–306 (2010).

[76] X. Chen, Z.-C. Gu, and X.-G. Wen. Local unitary transformation, long-range quantum entanglement, wave function renormalization, and topological order. *Phys. Rev. B* 82, 155138 (2010).

[77] C. Lanczos. An iteration method for the solution of the eigenvalue problem of linear differential and integral operators. *J. Res. Natl. Bur. Stand. B* 45, 255–282 (1950).

[78] B. Zhu, R. Lü, and S. Chen. $\mathcal{PT}$ symmetry in the non-Hermitian Su-Schrieffer-Heeger model with complex boundary potentials. *Phys. Rev. A* 89, 062102 (2014).

[79] C. Yuce. Topological phase in a non-Hermitian $\mathcal{PT}$ symmetric system. *Phys. Lett. A* 379, 1213 – 1218 (2015).

[80] H. Menke and M. M. Hirschmann. Topological quantum wires with balanced gain and loss. *Phys. Rev. B* 95, 174506 (2017).

[81] M. Klett, H. Cartarius, D. Dast, J. Main, and G. Wunner. Relation between $\mathcal{PT}$-symmetry breaking and topologically nontrivial phases in the Su-Schrieffer-Heeger and Kitaev models. *Phys. Rev. A* 95, 053626 (2017).

[82] T. Prosen and I. Pižorn. Quantum phase transition in a far-from-equilibrium steady state of an XY spin chain. *Phys. Rev. Lett.* 101, 105701 (2008).

[83] I. Pižorn. One-dimensional Bose-Hubbard model far from equilibrium. *Phys. Rev. A* 88, 043635 (2013).

[84] L. Jin, P. Wang, and Z. Song. Su-Schrieffer-Heeger chain with one pair of $\mathcal{PT}$-symmetric defects. *Sci. Rep.* 7 (2017).

[85] A. Mostafazadeh. A new class of adiabatic cyclic states and geometric phases for non-Hermitian Hamiltonians. *Phys. Lett. A* 264, 11 – 17 (1999).

[86] G. Nenciu and G. Rasche. On the adiabatic theorem for nonself-adjoint Hamiltonians. *J. Phys. A* 25, 5741 (1992).

[87] J. C. Garrison and E. M. Wright. Complex geometrical phases for dissipative systems. *Phys. Lett. A* 128, 177–181 (1988).

[88] K. Esaki, M. Sato, K. Hasebe, and M. Kohmoto. Edge states and topological phases in non-Hermitian systems. *Phys. Rev. B* 84, 205128 (2011).

[89] M. Klett. *Nichttriviale topologische Phasen in quantenmechanischen Vielteilchensystemen mit Gewinn- und Verlusteffekten.* Master thesis (2016).

[90] M. Wagner. *Characterization and investigation of topologically nontrivial states in $\mathcal{PT}$-symmetric fermionic many-body systems.* Master thesis (2017).

[91] Lu L., Joannopoulos J. D., and Soljačić M. Topological photonics. *Nat. Phot.* 8, 821 (2014).

[92] M. Ornigotti and A. Szameit. Quasi $\mathcal{PT}$ symmetry in passive photonic lattices. *J. Opt.* 16, 065501 (2014).

[93] Julia M. Zeuner, Mikael C. Rechtsman, Yonatan Plotnik, Yaakov Lumer, Stefan Nolte, Mark S. Rudner, Mordechai Segev, and Alexander Szameit. Observation of a topological transition in the bulk of a non-Hermitian system. *Phys. Rev. Lett.* 115, 040402 (2015).

[94] O. Viyuela, A. Rivas, and M. A. Martin-Delgado. Uhlmann phase as a topological measure for one-dimensional fermion systems. *Phys. Rev. Lett.* 112, 130401 (2014).

[95] J. C. Budich and S. Diehl. Topology of density matrices. *Phys. Rev. B* 91, 165140 (2015).

[96] F. Grusdt. Topological order of mixed states in correlated quantum many-body systems. *Phys. Rev. B* 95, 075106 (2017).

[97] C.-E. Bardyn, M. A. Baranov, E. Rico, A. İmamoğlu, P. Zoller, and S. Diehl. Majorana modes in driven-dissipative atomic superfluids with a zero Chern number. *Phys. Rev. Lett.* 109, 130402 (2012).

[98] T. H. Seligman and T. Prosen. Third quantization. *AIP Conf. Proc.* 1323, 296–300 (2010).

[99] E. Jones, T. Oliphant, P. Peterson, et al. SciPy: Open source scientific tools for Python (2001).

[100] S. van der Walt, S. C. Colbert, and G. Varoquaux. The NumPy array: A structure for efficient numerical computation. *Com. Sci. En.* 13, 22–30 (2011).

[101] R. A. Bertlmann and P. Krammer. Bloch vectors for qudits. *J. Phys. A* 41, 235303 (2008).

[102] J. R. Johansson, P. D. Nation, and F. Nori. QuTiP: An open-source Python framework for the dynamics of open quantum systems. *Com. Phys. Comm.* 183, 1760 – 1772 (2012).

[103] J. R. Johansson, P. D. Nation, and F. Nori. QuTiP 2: A Python framework for the dynamics of open quantum systems. *Com. Phys. Comm* 184, 1234 – 1240 (2013).

Danksagung (German)

Hiermit möchte ich allen danken, die mich beim Verfassen dieser Masterarbeit und während meines Studiums unterstützt haben.

Ich danke Herrn Prof. Günter Wunner dafür, dass ich diese Arbeit am 1. Institut für Theoretische Physik anfertigen durfte, sowie Herrn Prof. Udo Seifert für die Übernahme des Mitberichts dieser Masterarbeit. Mein besonderer Dank gilt Herrn Dr. Holger Cartarius für die ausgezeichnete Betreuung, hilfreiche Denkanstöße und Diskussionen, sowie die gewissenhafte Lektüre dieses Dokuments mit zahlreichen Korrekturvorschlägen.

Für die produktive Zusammenarbeit und angenehme Kaffeepausen danke ich ebenfalls meinem Kollegen Herrn Marcel Wagner. Weiterhin möchte ich mich bei allen Mitarbeitern des Instituts für das äußerst angenehme Arbeitsklima bedanken.

Ich danke auch meiner Familie, die mich während meines gesamten Studiums unterstützt hat, insbesondere meinen Eltern, meiner Schwester und meinen Großeltern.

Erklärung

Ich versichere,

- dass ich diese Masterarbeit selbständig verfasst habe,
- dass ich keine anderen als die angegebenen Quellen benutzt und alle wörtlich oder sinngemäß aus anderen Werken übernommenen Aussagen als solche gekennzeichnet habe,
- dass die eingereichte Arbeit weder vollständig noch in wesentlichen Teilen Gegenstand eines anderen Prüfungsverfahrens gewesen ist,
- und dass das elektronische Exemplar mit den anderen Exemplaren übereinstimmt.

Stuttgart, den 27. Oktober 2017 *Felix Dangel*